UNIVERSITY OF GENOA
POLYTECHNIC SCHOOL

DIME - Department of Mechanical, Energy, Management and Transportation Engineering

PhD in Machine and Systems Engineering for Energy, the Environment and Transport
Curriculum Mathematical Engineering and Simulation

PhD Thesis
XXXIII Course

"Performance analysis and dynamics of innovative SOFC hybrid systems based on turbocharger-derived machinery"

Supervisors:
Prof. Patrizia Bagnerini
Prof. Alberto Traverso

Candidate:
Luca Mantelli

May 2021

UNIVERSITÀ DEGLI STUDI DI GENOVA
SCUOLA POLITECNICA

DIME - Dipartimento di Ingegneria Meccanica, Energetica, Gestionale e dei Trasporti

Dottorato di Ricerca in Ingegneria delle Macchine e dei Sistemi per l'Energia, l'Ambiente e i Trasporti
Curriculum Ingegneria Matematica e Simulazione

Tesi di Dottorato
XXXIII Ciclo

"Analisi di prestazioni e dinamica di innovativi sistemi ibridi a SOFC basati su dispositivi derivati da turbocompressori"

Supervisori:
Chiar.ma Prof.ssa Patrizia Bagnerini
Chiar.mo Prof. Alberto Traverso

Candidato:
Luca Mantelli

Maggio 2021

Contents

Abstract

The growing awareness on climate change and pollution has brought to national and international policies aimed at promoting the development of innovative and environmentally sustainable energy systems. Among these systems, fuel cells are one of the most promising technologies, characterized by high energy conversion efficiencies and low emissions. In particular, hybrid systems based on the integration of a high temperature fuel cell with turbocharger-derived machinery have drawn the interest of academia and industry over the past decades. However, the complexity, fragility and high cost of these plants have slowed down their development, and only a few big companies were able to build complete prototypes. The technological challenges faced by the scientific community have highlighted the importance of simulations to design, test, control and analyse fuel cell hybrid systems.

Based on this experience, this thesis wants to expand the current knowledge on solid oxide fuel cell hybrid systems, with a particular focus on an innovative small-scale biofueled turbocharged layout, which was introduced recently within the Bio-HyPP European project. The main goal of this thesis is to determine if this kind of system can be a viable alternative to micro gas turbine-based systems, analysing its steady-state and transient behaviour in various operating conditions. To do this, it is necessary to define the system operative constraints, and to develop a control system capable of ensuring their compliance, while optimizing the plant performance. The possibility of increasing the reliability of solid oxide fuel cell hybrid systems is finally investigated, considering the implementation of surge prevention techniques and diagnostic tools.

All these activities strongly relying on simulation tools. This was possible thanks to the collaboration between the Laboratory of Applied Mathematics, Simulation and Mathematical Modelling with the Thermochemical Power Group of the University of Genoa.

After introducing the layout of the turbocharged fuel cell system, a detailed steady-state model of the plant is developed in Matlab®-Simulink® and used to design a strategy, based on the control of valves installed on the plant, able to comply with its many operative constraints. Then, an off-design performance analysis of the system is performed, considering simultaneously various conditions of power load and ambient temperature. This analysis is used to confirm the effectiveness of the proposed control strategy and to assess the capabilities of the turbocharged system.

A dynamic model is created using the TRANSEO tool to study the transient behaviour of the system. Having adopted a control strategy based on the cold bypass valve, the response of the system to a valve opening step change is analysed in order to design an effective and responsive control system, able to keep the fuel cell maximum temperature constant while complying with the system constraints. Four different controllers are designed, tested on two different load variation scenarios and compared on the basis of many parameters.

The final part of the thesis regards the development of innovative tools aimed at improving the reliability of solid oxide fuel cell hybrid system, in particular surge prevention techniques and Bayesian belief network-based diagnosis systems.

A simplified dynamic model of the turbocharged SOFC system is developed in TRANSEO, and various surge prevention techniques are tested on it: intake air conditioning, water spray at compressor inlet, air bleed and recirculation, and installation of an ejector at the compressor intake. The most effective procedures are integrated with the controller of the hybrid system and tested during a transient scenario to prevent the compressor operative point from approaching a surge condition.

Bayesian belief networks aimed at diagnosing the status of SOFC hybrid systems are developed thanks to a collaboration between the University of Genoa and the Mälardalens Högskola of Västerås, Sweden. A micro gas turbine

– solid oxide fuel cell system is considered for this study, but the methodology could be easily extended to turbocharged plants. The activity is carried out simulating the system on Matlab®-Simulink® and designing the Bayesian networks on Hugin Expert. Two different diagnosis systems, one for the turbomachinery and one for the fuel cell stack, are developed and tested on stationary conditions. The second one is also tested during transients and integrated with the control system to prevent degradation of the fuel cells.

In conclusion, this thesis highlighted the great potential of turbocharged SOFC hybrid systems, showing high energy conversion efficiencies in a wide operative range in terms of load and ambient conditions. It also showed that the proper operation of the system is possible during various transient scenarios, implementing cascade controllers designed to act on a cold bypass valve to control the SOFC maximum temperature. Regarding the possibility of improving the reliability of these systems, surge prevention techniques based on compressor recirculation appeared as the most effective ones. Simulation results suggest that their integration with a surge precursors detection tool could avoid the occurrence of many potentially dangerous scenarios. The final part of this thesis showed that the durability of SOFC hybrid systems could be further improved thanks to Bayesian belief networks, which were proved to effectively diagnose the status of SOFC-MGT systems but could be applied to turbocharged plants as well.

Sommario

La crescente consapevolezza su temi quali il cambiamento climatico e l'inquinamento atmosferico ha portato a politiche nazionali ed internazionali mirate allo sviluppo di sistemi energetici innovativi e sostenibili. Tra di essi, le fuel cell sono uno dei più promettenti, essendo caratterizzate da alte efficienze e basse emissioni. In particolare, i sistemi ibridi basati sull'integrazione di fuel cell ad alta temperatura con dispositivi derivati da turbocompressori hanno attirato l'attenzione del mondo accademico e dell'industria negli ultimi decenni. Tuttavia, la complessità, la fragilità e l'alto costo di questi impianti ha rallentato il loro sviluppo, e solo poche grandi aziende sono state in grado di realizzare prototipi completi. Le difficoltà tecniche affrontate dalla comunità scientifica hanno messo in luce l'importanza delle simulazioni per progettare, testare, controllare e analizzare i sistemi ibridi a fuel cell.

Sulla base di tale esperienza, questa tesi mira ad espandere la attuale conoscenza sui sistemi ibridi a fuel cell a ossidi solidi, ponendo una particolare attenzione su un innovativo sistema turbocompresso di piccola taglia, alimentato con biogas e recentemente introdotto all'interno del progetto europeo Bio-HyPP. Lo scopo principale della tesi è determinare se questo tipo di sistema possa essere una valida alternativa ai sistemi basati su microturbine a gas, analizzando il suo comportamento in relazione a diversi scenari, sia stazionari, sia transitori. Per fare ciò, è necessario definire i vincoli operativi del sistema e sviluppare un sistema di controllo in grado di rispettarli, ottimizzando al tempo stesso le prestazioni dell'impianto. Inoltre, l'affidabilità dei sistemi ibridi può essere migliorata grazie all'implementazione di strumenti diagnostici e di procedure per prevenire il pompaggio del compressore. La parte finale della tesi è mirata allo studio di tali strumenti, al loro sviluppo e alla loro integrazione con il sistema di controllo.

Tutte le attività presentate in questa tesi sono state svolte facendo affidamento su strumenti di simulazione. Ciò è stato possibile grazie alla collaborazione tra

il Laboratorio di Matematica Applicata, Simulazione e Modellistica Matematica e il Thermochemical Power Group dell'Università degli Studi di Genova.

Dopo aver presentato il layout del sistema a fuel cell con turbocompressore, un dettagliato modello stazionario dell'impianto sviluppato in Matlab®-Simulink® è stato utilizzato per progettare una strategia, basata sul controllo di valvole installate sull'impianto, in grado di rispettare tutti i suoi vincoli operativi. Successivamente, è stata svolta un'analisi di prestazioni in off-design, considerando allo stesso tempo diverse condizioni di carico di potenza e di temperatura ambiente. Tale analisi è stata utilizzata per confermare l'efficacia della strategia di controllo proposta, e per valutare le capacità del sistema con turbocompressore.

Successivamente è stato creato un modello dinamico utilizzando lo strumento TRANSEO, in modo da studiare il comportamento del sistema durante i transitori. Avendo adottato una strategia di controllo basata sulla valvola di cold bypass, è stata analizzata la risposta del sistema ad una sua apertura a gradino, al fine di progettare un sistema di controllo efficace e reattivo, in grado di mantenere la massima temperatura di cella costante e, allo stesso tempo, di rispettare i vincoli del sistema. Sono stati progettati quattro diversi controllori, che successivamente sono stati testati su due diversi scenari di variazione di carico e confrontati sulla base di vari parametri operativi.

La parte finale della tesi ha riguardato lo sviluppo di innovativi strumenti che possano aumentare l'affidabilità dei sistemi ibridi a fuel cell a ossidi solidi, in particolare tecniche di prevenzione del pompaggio e sistemi di diagnostica basati su reti Bayesiane. Un modello semplificato del sistema con turbocompressore è stato sviluppato in TRANSEO e sono state testate diverse tecniche di prevenzione del pompaggio: condizionamento del flusso d'aria, iniezione di acqua, ricircolo e bleed, installazione di un eiettore all'imbocco del compressore. Le soluzioni più efficaci sono state integrate con il controllore del sistema ibrido e sono state testate durante un transitorio per evitare che il punto operativo del compressore si avvicinasse al pompaggio.

Infine, grazie ad una collaborazione tra l'Università degli Studi di Genova e la Mälardalens Högskola di Västerås, in Svezia, sono state sviluppate delle reti Bayesiane per la diagnostica di sistemi ibridi a fuel cell a ossidi solidi con microturbina a gas. Questa attività è stata svolta simulando il sistema su Matlab®-Simulink® e creando le reti Bayesiane su Hugin Expert. Due sistemi di diagnostica, uno per la microturbina e uno per la fuel cell, sono stati sviluppati e testati in condizioni stazionarie. Il secondo è stato anche testato in condizioni dinamiche e integrato con il sistema di controllo per prevenire l'usura della cella.

In conclusione, questa tesi ha messo in luce il grande potenziale dei sistemi ibridi SOFC-turbocompressore, mostrando la loro alta efficienza in un ampio intervallo di condizioni operative in termini di carico elettrico e temperatura ambiente. La tesi ha anche dimostrato che è possibile garantire il corretto funzionamento di questi sistemi durante diversi scenari transitori, implementando controllori a cascata progettati per agire sulla valvola di bypass freddo per controllare la massima temperatura della cella. Per quanto riguarda la possibilità di migliorare l'affidabilità di tali sistemi, le tecniche basate sul ricircolo del compressore sono risultate essere le più efficaci per allontanare il sistema da una condizione di pompaggio. I risultati delle simulazioni mostrano come la loro integrazione con strumenti di monitoraggio possa prevenire diverse situazioni di pericolo. La parte finale della tesi ha mostrato come il deterioramento dei sistemi ibridi a SOFC possa essere limitato grazie a reti Bayesiane, che sono state utilizzate per diagnosticare accuratamente le condizioni di un sistema SOFC-microturbina a gas, ma potrebbero ugualmente essere applicate su impianti con turbocompressore.

Acknowledgements

I would like to thank all the people I had the pleasure to work with during all these years.

Patrizia, Alberto, Mario and Angelo gave me the opportunity to work on various challenging projects, and their mentorship was a fundamental contribution to my professional growth. I would have never thought to work on so many different topics at the beginning of this journey!

Working both at the TPG and at the Laboratory of Applied Mathematics, Simulation and Mathematical Modelling I met a lot of wonderful colleagues and friends, and it would be hard to make a list. I just want to say it was great to spend these years with all of them, and that I will always remember our time together at the office, at the bar, at the restaurant, on the football field.

Living abroad for my international collaborations was one of the best experiences I had during my PhD, and I am really glad I could work with so many people with different backgrounds and cultures. From elementary school to master's degree, I have always been within walking distance from home, so this was a huge step! A special thanks to the Hyper gang of NETL in Morgantown and to the SOFIA group of the Mälardalens Högskola in Västerås, for making me feel at home while being so far from it.

Finally, I would like to thank mom, dad and Alex for their love and support. Your faith in me made every obstacle much easier to overcome.

Nomenclature

Abbreviations and Acronyms

AFC	Alkaline fuel cell
APH	Air pre-heater
BBN	Bayesian belief network
BL	Blower
BV	Bleed valve
CBV	Cold bypass valve
CHP	Combined heat and power
DLR	German Aerospace Centre
DMFC	Direct methanol fuel cell
EU	European Union
FF	Feed-forward
FPH	Fuel pre-heater
GE	General Electric
GEN	Generator
HE	Heat Exchanger
ICE	Internal Combustion Engine
LGFCS	LG Fuel Cell Systems
MCFC	Molten carbonate fuel cell
MGT	Micro gas turbine
MHPS	Mitsubishi-Hitachi Power Systems
MPC	Model Predictive Control
NETL	National Energy Technology Laboratory
OGB	Off-gas burner
PAFC	Phosphoric acid fuel cell
PEMFC	Proton exchange membrane fuel cell
PI	Proportional-integral

PID	Proportional-integral-derivative
REC	Recuperator
REF	Reformer
SMR	Steam methane reforming
SOFC	Solid oxide fuel cell
TPG	Thermochemical power group
RV	Recirculation valve
USA	United States of America
WGS	Water gas shift
WGV	Wastegate valve

Variables

A	Area [m^2]
$A_{HE,el}$	Discretization element heat exchange area [m^2]
B	Ratio between gas-solid heat exchange area and cell area [-]
C	Actuator disk contribution to momentum [Pa]
C_{dis}	Ejector discharge coefficient (primary duct) [-]
CAW	Flow correction factor [-]
c	Velocity [m/s]
c_p	Specific heat at constant pressure [J kg^{-1} K^{-1}]
$c_{p,mol}$	Molar specific heat [J mol^{-1} K^{-1}]
c_s	Specific heat of solid material [J kg^{-1} K^{-1}]
c_v	Specific heat at constant volume [J kg^{-1} K^{-1}]
D	Gas diffusivity [m^2 s^{-1}]
D_h	Hydraulic diameter [m]
DAE	Efficiency delta [-]
E	Energy [J mol^{-1}]
F	Faraday constant [C mol^{-1}]
FO	fractional opening [-]
F_V	voltage reduction factor [-]
f	Friction factor [-]

ΔG	Gibbs free energy change on overall reaction [J mol^{-1}]
ΔG^0	Standard Gibbs free energy change on overall reaction [J mol^{-1}]
H	Enthalpy [J kg^{-1}]
ΔH	Overall reaction enthalpy change [J mol^{-1}]
h	Convective heat coefficient [W m^{-2} K^{-1}]
i_{cell}	Fuel cell electric current [A]
J	Rotational inertia [kg m^2]
j_0	Exchange electric current density [A m^{-2}]
j_{cell}	Fuel cell electric current density [A m^{-2}]
K^{eq}	Reaction equilibrium constant [-]
K_p	Surge margin [-]
k	Pressure loss coefficient [-]
k_v	Valve friction factor [-]
L	Length [m]
LHV	Lower heating value [J kg^{-1}]
l	Pressure loss coefficient [-]
M	Mass [kg]
$\dot{m}$	Mass flow rate [kg/s]
N_{cells}	Number of cells in the SOFC stack [-]
Nu	Nusselt number [-]
$\dot{n}$	Molar flow [mol s^{-1}]
n^*	Molar flow rate [mol m^{-2} s^{-1}]
n_e	Number of electrons transferred in the electrochemical reaction [-]
P	Power [W]
p	Pressure [Pa]
p_X	Partial pressure of the substance X [Pa]
Δp	Pressure loss [Pa]
Pr	Prandtl number [-]
Δq	Heat exchange [W]
$\dot{q}$	Heat flux [W]
R	Overall reaction rate [mol s^{-1}]

Re	Reynolds number [-]
R_{el}	Electrical resistance [Ω m^2]
R_g	Gas constant [J mol^{-1} K^{-1}]
R_{pred}	Exact prediction rate [-]
R_{sg}	Specific gas constant [J kg^{-1} K^{-1}]
RR	Recirculation ratio [-]
R_{sg}	Specific gas constant [J kg^{-1} K^{-1}]
r	Reaction rate [mol m^{-3} s^{-1}]
S/C	Steam to carbon ratio [-]
T	Temperature [K]
T_I	Integral time [-]
T_D	Derivative time [-]
ΔT	Temperature gradient [K]
t	Thickness [m]
U_f	Fuel utilization factor [-]
V_{Nernst}	Nernst ideal electric potential [V]
V_{real}	Fuel cell real electric potential [V]
ΔV	Fuel cell electric potential loss [V]
w	Velocity [m/s]
X	Molar fraction [-]
x	Cell coordinate [m]
ß	Pressure ratio [-]
γ	Activation losses coefficient [A m^{-2}]
η	Efficiency [-]
θ_a,θ_c	Charge transfer coefficients [-]
κ	Concentrated pressure losses coefficient [-]
Λ	Volume [m^3]
λ	Thermal conductivity [W m^{-1} K^{-1}]
ν	Stoichiometric coefficient [-]
μ	Dynamic viscosity [Pa·s]
ρ	Density [kg/m^3]

τ	Time [s]
Ψ	Concentrated pressure losses coefficient [-]
ω	Turbocharger shaft rotational speed [rpm]
Ω	Section area [m^2]

Subscripts and Superscripts

1	Component inlet
2	Actuator disk outlet/duct inlet
3	Component outlet
act	Activation
amb	Ambient
an	Fuel cell anode
aux	Auxiliary systems
avg	Average
C	Compressor
C,fuel	Fuel compressor
ca	Fuel cell cathode
cell	Fuel cell
ch	Fuel cell channel
cold	Heat exchanger cold side
conc	Concentrated
des	Design value
distr	Distributed
eff	Effective
f	Fluid
fg	Feeding gas
g	Gas
hot	Heat exchanger hot side
i	i-th component or substance
in	Inlet
inv	Inverter

j	j-th section of the heat exchanger
k	k-th reaction
ld	Larger duct
loss	Thermal losses
max	Maximum
ohm	Ohmic
out	Outlet
pl	Heat exchanger plate
prim	Ejector primary inlet
R	Reaction (MSR,WGS)
Red	Reduced
ref	Reference condition
SP	Setpoint
s	Solid
sd	Smaller duct
sec	Ejector secondary inlet
sens	Sensor
surge	Surge condition
s	Solid
T	Turbine
tot	Total
ZN	According to the Ziegler-Nichols method

1 Introduction

1.1 Background

Since the industrial revolution, the world's energy demand, and therefore the fossil fuels consumption, have increased progressively. As a direct consequence, the concentration of greenhouse gases has reached alarming levels, impacting onto the climate of our planet [1–3]. From 1901 the average surface temperature (which definition and measurement is anyway controversial) of Earth has been increasing with 0.7 – 0.9 °C/century, reaching values of 1.5 – 1.8 °C/century after 1975 [2]. These alterations have potentially endangered the equilibrium of the planet in many ways, e.g. causing a significant worldwide reduction of glaciers [4] and accelerating desertification of drylands [5]. Climate change, combined with emission and deposition of pollutants has impacted both aquatic and terrestrial ecosystems due to their detrimental effect on vegetation and wildlife [6].

Thanks to a growing awareness on these topics, energy policies have addressed decarbonization and reduction of pollutant emissions, shifting the focus of both industries and researchers working in the energy systems field on the development of environmentally sustainable power generation systems. The European Union (EU) research programme Horizon 2020, which had run from 2014 to 2020, put close attention on climate action and development of clean and efficient energy systems and transports [7]. The European Green Deal, a set of measures launched by the European Commission in 2019, has the ambitious goal of achieving zero net greenhouse gas emissions within the EU by 2050, replacing fossil power plants with renewable energy systems [8]. The Green Deal will drive the EU towards a sustainable, climate-neutral, and circular economy [9]. In the United States (US), renewable energy policies are often promoted individually by the states themselves, more than by the federal government, leading to very different scenarios. In general, the strongest clean

energy policies are promoted by the most progressive states. For example, California set the goals of producing 60% of clean energy by 2030 and of reaching 100% electric retail sales from clean energy systems by 2045. Similarly, the New York government planned to achieve a carbon-neutral economy by 2040, widely adopting clean energy systems [10]. China has also promoted clean energy systems through five-year plans [10], and, according to [11] it could reach 35% of clean energy production by 2030, becoming the biggest user of clean energy in the world.

For these reasons, in the last decades the installed capacity of renewable energy systems showed a strong growing trend [12]. However, wind and solar power plants, which have a lead role in this process, introduce several technical challenges regarding the management of the power grid, due to their non-controllable variability and unpredictability [13].

1.2 Fuel Cells

In order to improve the flexibility of renewable systems, there has been an increasing interest in batteries, hydrogen storages and hydrogen-based power plants [14]. In fact, if there is an energy surplus produced by renewable plants, it can be stored in batteries or used to power electrolysers and produce hydrogen. When the energy demand exceeds the production, it is then possible to discharge the batteries or to generate power with hydrogen-based systems [15].

Regarding hydrogen-based systems, fuel cells are one of the most promising technologies, thanks to their high energy conversion efficiencies, which can theoretically reach values >75% [16]. A fuel cell is an electrochemical reactor, which generates electric and thermal power directly from the oxidation of hydrogen, without combustion. The only by-products of this process are water and heat. However, fuel cells can also be fuelled by hydrocarbons, from which hydrogen is obtained within the cell or in an external reformer. In this case, carbon dioxide is produced by the system, but the high efficiencies of the fuel

cell, combined with the possibility of using a biofuel [17], make this setup more attractive than a traditional energy system [18]. Other advantages of fuel cells are modularity and low noise emissions [19], making them feasible both for distributed generation applications and power plants generating several MW of electric power.

Many different kinds of fuel cells have been developed over the years, which can be classified in six main categories, based on the type of electrolyte [20]:

- Proton exchange membrane fuel cells (PEMFC);
- Alkaline fuel cells (AFC);
- Solid oxide fuel cells (SOFC);
- Molten carbonate fuel cells (MCFC);
- Phosphoric acid fuel cells (PAFC);
- Direct methanol fuel cells (DMFC).

They differ in terms of materials, operating temperatures, fuels that can be used to feed them and tolerance to impurities, as well as efficiency and power density. However, they share the same working principle and have a similar structure, based on two electrodes, an electrolyte and an external electric connection. Figure 1 shows the main structure and basic working principles of a solid oxide fuel cell. The hydrogen fuel enters the fuel cell on the side of the anode electrode (A), while the oxidant, typically oxygen, on the side of the cathode electrode (B). The hydrogen molecules decompose into positive ions, releasing electrons, while the oxygen molecules decompose into negative ions. The electrolyte is an insulator for the electrons, but, based on the technology, it allows positive or negative ions to flow from one side of the fuel cell to the other (C) to form water (D). In order to reach the cathode side, the electrons must flow through the anode and the external electric connection, generating the electric power (E). Multiple fuel cells are electrically connected with each other and arranged in a stack.

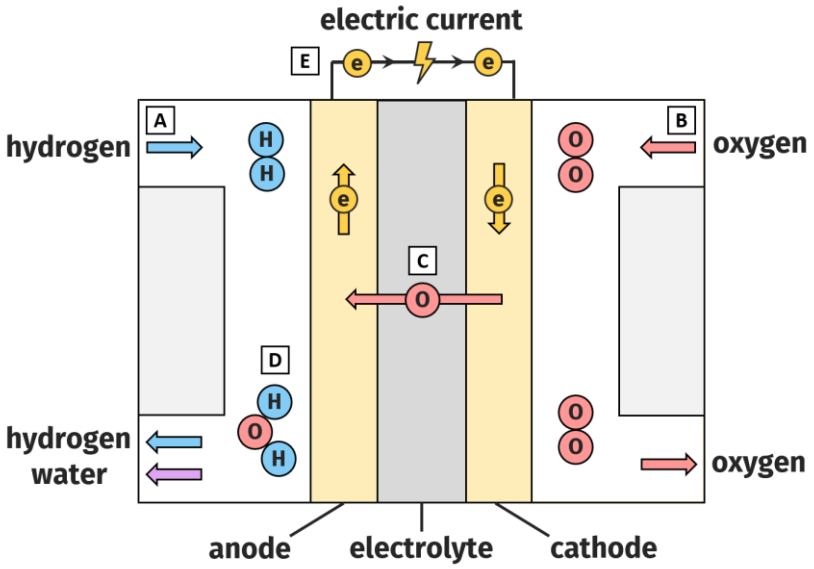

Figure 1. *Main structure and basic working principles of a solid oxide fuel cell.*

Many reports highlight the strong growth of fuel cell applications during the last two decades [21–28]. The European Commission's Joint Research Centre observed that the global installed capacity of stationary large scale fuel cells systems, i.e. with a power above 200 kW, has been growing constantly since 2007, exceeding 800 MW in 2017 [21], as shown in Figure 2.

Figure 3 shows that most of these plants were installed in USA and South Korea, while European companies have been focusing of small and medium size energy systems [21]. Several demonstration projects for fuel cell combined heat and power small scale systems were carried out in the EU over the past years, and more than 1500 plants were installed within their framework [22]. According to [23], the global fuel cell market size was estimated around 10.48 billion USD in 2019, of which 70% due to stationary systems.

The diffusion of fuel cell systems has been accompanied by a reduction of both fixed and variable costs. The total installed costs per MW of stationary fuel cell systems in 2017 were on average around 30% of those in 2009, while the operation and maintenance costs were slightly over 40% [24].

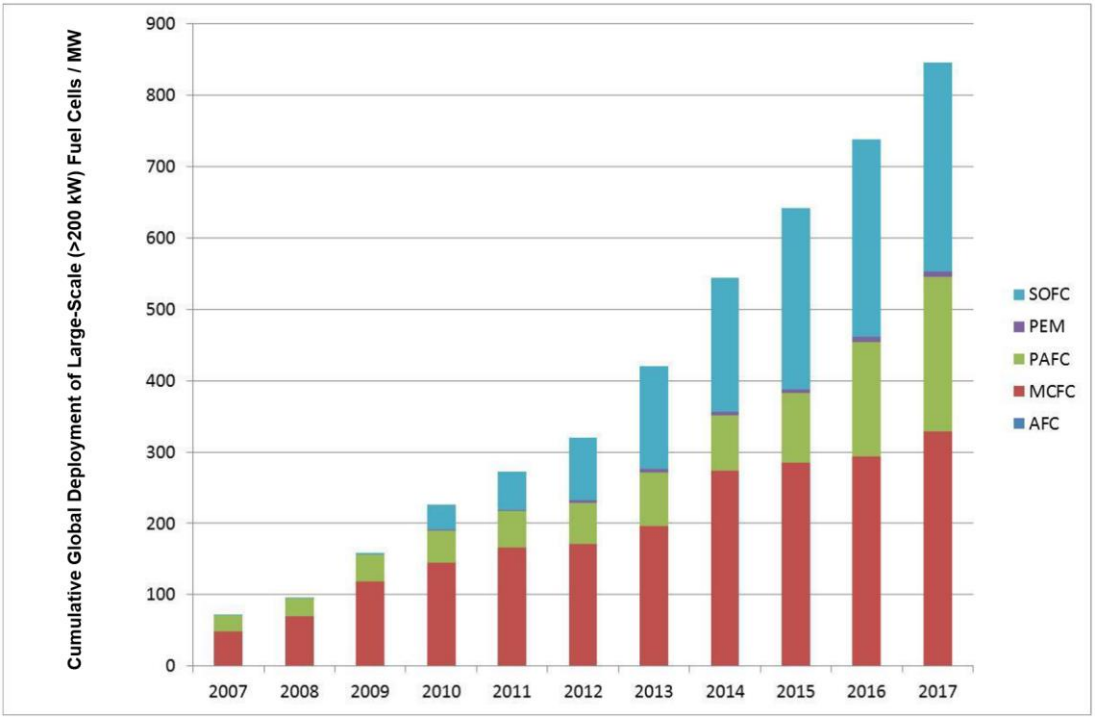

Figure 2. *Cumulative global deployment of stationary fuel cells systems over 200 kW, displayed per technology [21].*

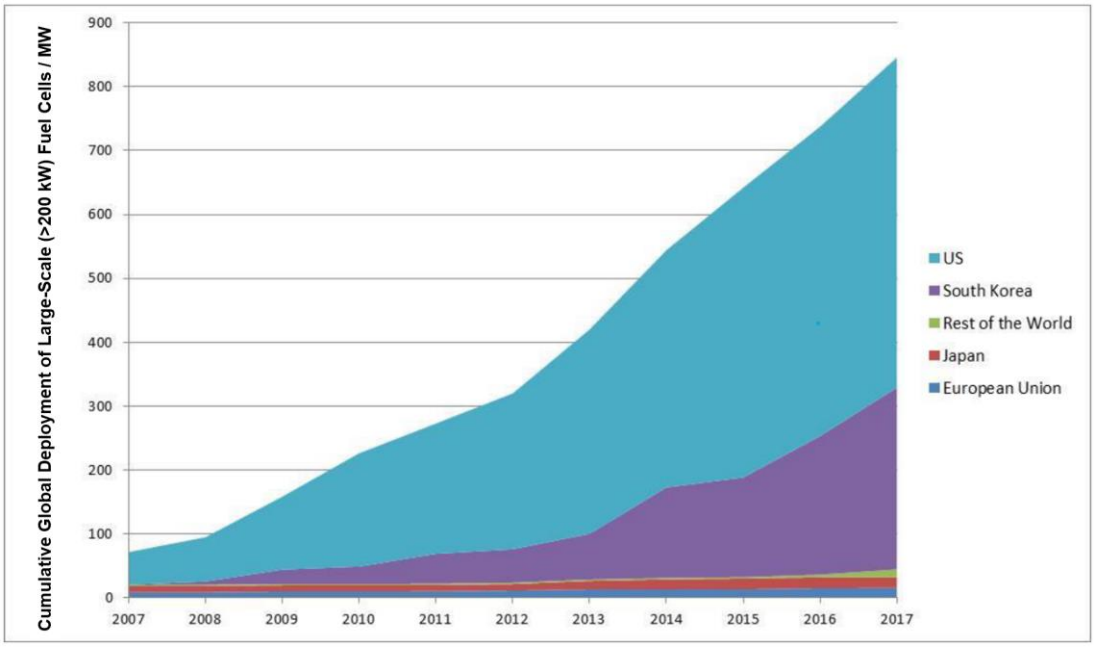

Figure 3. *Cumulative global deployment of stationary fuel cells systems over 200 kW, displayed per geographical location [21].*

Various big companies decided to rely on fuel cells to power their facilities during the last decade. The first 100 kW commercial SOFC by Bloom Energy was sold to Google in 2008 and already in 2011 the company declared that 200 of these systems had been installed at the facilities of some of the biggest American corporations and research institutions, such as Coca-Cola, Adobe, Bank of America and the California Institute of Technology [25]. In 2013 the e-commerce multinational corporation eBay opened in Salt Lake City, Utah, USA the first data centre primarily powered by fuel cells, specifically Bloom Energy SOFCs fuelled by natural gas and generating up to 6 MW of electric power [29]. In 2020 Microsoft claimed to have powered for 48 hours a data centre with a 250 kW hydrogen fuel cell system, again in Salt Lake City [30]. Today Amazon, Walmart, Carrefour and BMW use hydrogen fuel cells produced by Plug Power Inc. for stationary power generation and to operate forklifts in their warehouses [31]. The biggest fuel cell installation in the world is currently the Desan Hydrogen Fuel Cell Power Plant in Seosan, South Korea , a 50 MW PAFC system which is also the first one to use hydrogen generated as by-product of petrochemical processes [32].

Even if this thesis is focused on stationary systems, it is worth mentioning the most relevant applications of fuel cells in the transportation field. The main advantages of fuel cells with respect to internal combustion engines regard efficiency, size, noise and pollutant emissions [26]. Various automotive companies, such as Honda, Toyota and Volkswagen, presented vehicles powered by fuel cells during the last years [33]. They are generally powered entirely by a fuel cell or by a fuel cell – battery hybrid system and use hydrogen as energy source. For this application PEMFC are usually used, due to their low temperature, high power density and slow corrosion. The interest towards fuel cells has been growing also in the naval sector, for vessels of various sizes. Many research projects, investigating maritime applications of fuel cells, have been carried out over the last few decades [27]. One of the latest accomplishments in this field is the creation by the Italian shipbuilding company Fincantieri of the ZEUS experimental vessel, equipped with a 130 kW fuel cell system powered by

hydrogen. In order to reduce CO_2 emissions, also the aviation sector has shown interest in fuel cells, mainly PEMFC and SOFC [28,34]. Some of the main manufacturers, such as Boeing and Airbus, are developing hydrogen fuel cell systems to provide electrical power to non-propulsion systems on the airplane. Regarding propulsion applications, fuel cells have been installed mainly on unmanned aerial vehicles and small manned aircrafts. One of the latest accomplishments in this field is the successful test of the HY4 aircraft by the DLR German Aerospace Center in 2016. The HY4 is equipped by a hydrogen PEMFC and a lithium battery to assist during peak power loads, has space for four passengers and can reach a speed of about 200 km/h [35].

In this thesis, attention is focused on stationary solid oxide fuel cells (SOFCs), which are characterized by an electrolyte constituted by metallic oxide ceramic material [36]. Due to their high operating temperatures [19,37], SOFCs present a high tolerance to impurities, and expensive catalysts are not needed, with a positive impact on the production cost [19,37]. They have higher efficiencies compared to other fuel cells [38], and can be fed with biofuels (typically reformed in specific reactors [39]), combining the advantages of a high efficiency generation with the use of a renewable resource. This solution allows for mitigation of the pollutant emissions [40] and the ability to increase the system flexibility for operations with renewable resources in a smart grid application.

1.3 Fuel cell hybrid systems

Thanks to the high operating temperatures (600-1000°C), SOFC exhausts have a significant energy content, which can be used to provide heat in a cogeneration setup [41,42], or to drive turbocharger-derived machinery (i.e. turbochargers and micro gas turbines) [43,44]. The latter option is particularly interesting for pressurized systems: the stack exhausts expand in a turbine, providing the mechanical power necessary to drive a compressor, pressurizing the SOFC without need for an additional power consumption. The pressurization of the

cell has a beneficial effect on the SOFC performance, which, according to the analysis presented in [45], influences both power density and efficiency.

As mentioned before, two different types of turbomachinery can be used for pressurizing the SOFC: a micro gas turbine (MGT) or a turbocharger.

MGTs are small size turbine generators, typically able to generate power in the range of 25-250 kW. Some of the first devices were derived from automotive turbochargers or aircraft auxiliary power units [46], and they are generally based on a simple or a recuperated layout. A simple MGT has low energy conversion efficiency, typically around 15%, while a recuperated one has values between 20% and 30% [46]. Figure 4 shows the main components of a recuperated MGT by Capstone.

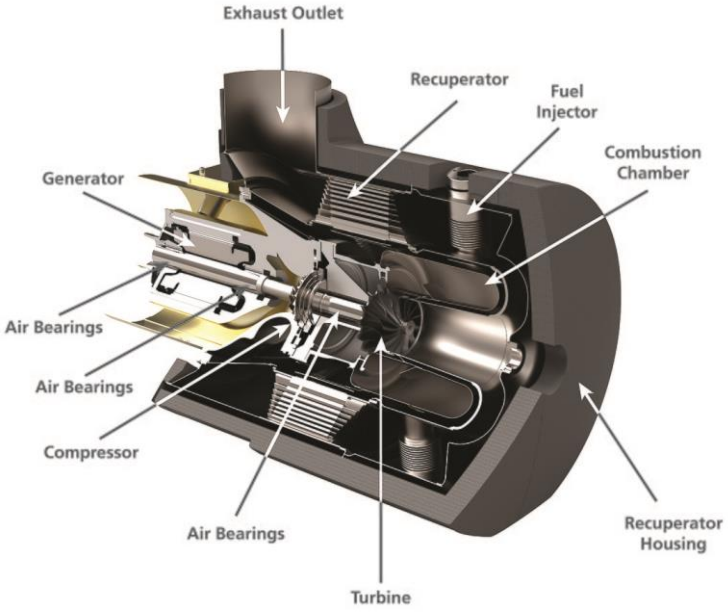

Figure 4. *Cross-section cutaway of a Capstone C65 micro gas turbine* [47].

Today MGTs are adopted as combined heat and power (CHP) systems for distributed generation applications, being able to reach overall efficiencies around 80% and, at the same time, to reduce transmission and distribution power losses [48]. Many innovative MGT-based solutions have been studied by the research community to achieve high energy conversion efficiency, power

density and low emissions. Other than SOFC-MGT hybrid systems, it is worth mentioning MGT-based humid air turbine cycles [49], MGT systems combined with concentrated solar power technology [50], MGT systems with exhaust gas recirculation for carbon capture[51], and externally fired layouts for usage of alternative fuels, such as solid biomass [52]. Among all these solutions, the SOFC-MGT layout is particularly interesting, being independent from intermittent energy sources and being characterized by lower exergy destruction, thanks to the absence of combustion.

Integrating a SOFC with an MGT (Figure 5), which is equipped with an alternator, additional electric power is generated by the system, increasing its global efficiency.

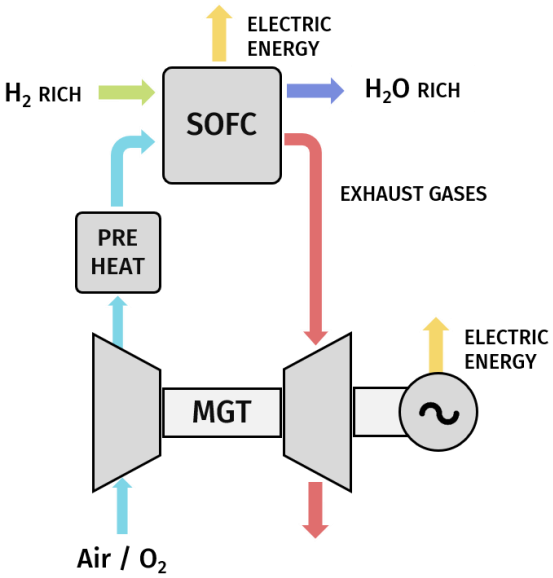

Figure 5. *Simplified layout of a SOFC-MGT hybrid system.*

The alternator is also useful for control purposes: thanks to the presence of the alternator, it is possible to control the turbomachinery rotational speed [53], which determines the air flow entering the system. Since the cathode air flow is the main responsible of the SOFC cooling, the rotational speed control can be decisive to comply with the fuel cell temperature constraints.

Thanks to these features, the SOFC-MGT layout has drawn the interest of researchers and companies in the energy systems field over the last decades.

The biggest results on the development of fully operational SOFC-MGT systems were accomplished by industry, due to the high capital required.

The first SOFC-MGT system (Figure 6) was developed by Siemens-Westinghouse and tested at National Fuel Cell Center of the University of California in Irvine, California in the year 2000. It was composed by a 180 kW tubular SOFC and a 40 kW MGT, and it was able to produce an electrical power of 220kW, reaching an efficiency of 53% [54,55]. However, it could not run for more than one hundred hours during its first test due to some malfunctions. In the early 2000s Siemens-Westinghouse was also working on the development of a 300 kW and the installation of two demonstrator plants in Germany and Italy was planned at the end of 2002. Moreover, Siemens-Westinghouse was part of a consortium aimed at developing the first 1MW SOFC-MGT hybrid system in Europe, that should have started its operation in 2003 [54]. However, despite their great involvement in this field, Siemens-Westinghouse was never able to overcome some technical issues and eventually they decided to interrupt their research programs.

Figure 6. *Siemens-Westinghouse SOFC-MGT system* [56].

General Electric (GE) first activities on fuel cells date back to the 1950s and they led to the invention of the first PEM in 1953 [57]. Thereafter the company

continued the research on fuel cells taking part in various projects and developing their own MCFC in 1982. In 2013 they started to work on an innovative fuel cell – combined cycle and in 2014 they launched GE-Fuel Cells to develop a 1.3 MW SOFC demonstration project and eventually commercialize it. This system is based on the integration of an SOFC and a Janbacher gas engine, and it is designed to generate both electric and thermal power in a combined heat and power setup. The hydrogen necessary to power the SOFC is obtained from natural gas by an external reformer and the gas engine is fuelled by the stack tail gas, generating additional heat end electrical power. According to GE, the expected electrical efficiency of this system should be around 65%, while its CHP efficiency could reach 90% [57].

Rolls-Royce Fuel Cell Systems, that later became LG Fuel Cell Systems (LGFCS), started their activities on SOFC-MGT systems in 1992, with the goal of developing a 1 MW hybrid system [55]. A prototype of their system, which was composed by 250 kW modules (240 kW fuel stack + 10 kW MGT), was run for the first time in 2008 (Figure 7). In 2018 a product-like demonstrator was successfully operated for more than 1800 hours on load, generating 250 kW of electrical power (alternated current) with an efficiency of 55% [58].

Mitsubishi Heavy Industries was one of the first companies involved into the development of SOFC-MGT systems, since the 1980s. They started designing and manufacturing a 200 kW system in 2004, which was successfully tested in 2007 for more than 1500 hours reaching an efficiency of 52.1% in nominal conditions [55].

The most recent advancements on the development of a fully operational SOFC-MGT system were achieved in industry by Mitsubishi-Hitachi Power Systems (MHPS), a company jointly established by Mitsubishi Heavy Industries and Hitachi. A 250kW SOFC-MGT demonstration plant was designed by MHPS and installed at the Ito Campus of Kyushu University (Japan), where it was able to operate for more than 10,000 hours between 2015 and 2017. Today the company website lists the SOFC-MGT system between their products [60].

Figure 7. *The 250 kW test rig of Rolls-Royce Fuel Cell Systems at Derby, UK* [59].

All these companies had to make significant investments and to face many complex technical challenges related to the integration of an MGT with the SOFC. The main difficulties concern the coupling of SOFC and MGT, especially due to the difference in operating conditions from the standard gas turbine operation [61]. As a direct consequence, the design of control systems is particularly critical, as highlighted in [62,63], also due to the many operative limits of the SOFC, which must be respected to avoid its degradation. Regarding the costs, the MGT and the SOFC are very expensive components, that, when both included together, limit the economic feasibility of the system [64].

Due to the novelty of these systems, and their many operative constraints, most of the current literature regards numerical simulation results. In fact, fuel cells are expensive and delicate components, which can be easily damaged by mechanical or thermal stress [65], and the mutual interactions with the MGT, make the behaviour of the system less predictable compared to a standalone fuel cell stack. During transient operations, temperature and pressure operative limits could be exceeded if the control strategy had not been designed properly, while fluid-dynamic instabilities (e.g. surge) may arise in the compressor, due

to the presence of the stack volume in the plant [66]. Moreover, SOFC pressurization requires advanced sealing technologies, such as wet sealing and hard sealing, to limit gas leakages. Adopting these techniques introduces new technological challenges, mainly related to the requirements of sealing materials [67]. Pressurization also negatively affects the cell degradation, with, as consequence, a reduction of its lifetime. According to [45], operating the SOFC at higher pressures facilitates nickel oxidation at the anode, and it has a strong influence on carbon deposition that must be considered when the system operating strategies are designed. For this reason, the research community has often relied on emulator plants more than on complete prototypes for what concern experimental studies.

An emulator plant is a system where the most critical and delicate components are not present but emulated by other devices on the basis of a real-time model running in parallel. Measurements from the system sensors are used as inputs of the models and, based on its results, the actions to be performed on the emulator actuators are determined. Typically, it is the SOFC system to be emulated, operating a burner to simulate its thermal output, and including one or more vessels to consider the effect of its volume and thermal capacity.

Emulator plants based on this logic were built at the laboratories of the Thermochemical Power Group (TPG) of the University of Genoa (Italy) (Figure 8) [68], National Energy Technology Laboratory (NETL, USA) [69] and German Aerospace Center (DLR, Germany) (Figure 9) [70]. The DLR facilities also include an emulator plant based on a different approach, where the SOFC system is actually present and the micro gas turbine is emulated [71].

For the reasons mentioned above, turbocharged SOFC systems have begun to generate a growing interest in the research community [74,75]. Turbochargers are turbine-driven devices which are commonly integrated with internal combustion engines (ICE), in order to increase the engine inlet air mass flow and pressure.

Figure 8. *The SOFC-MGT emulator plant of TPG* [72].

Figure 9. *The SOFC-MGT emulator plant of DLR (emulated SOFC, real MGT) – now dismantled* [73].

This setup is typically referred to as turbocharged engine or forced induction engine and it is schematically displayed in Figure 10. In this way it is possible to enhance the ICE power output, without altering the volume of its cylinders. Adopting a turbocharger, rather than an MGT, to pressurize the SOFC stack, is an effective solution to obtain a similar performance improvement and, at the same time, to reduce the system capital cost.

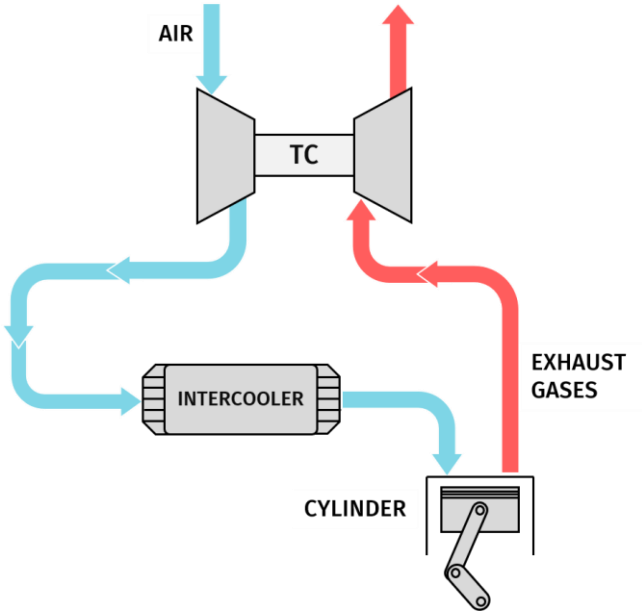

Figure 10. *Scheme of a turbocharged internal combustion engine.*

This cost reduction is mostly due to the mass production of turbochargers for the automotive industry and due to the lower number of components: electric alternator and other power electronic devices are not present in a turbocharged system. These features are expected to accelerate the pressurized SOFC systems market entry.

The drawbacks of this solution are the reduction of generated power (around 10-15% in comparison with a SOFC-MGT system), and the loss of control on the turbomachinery rotational speed. When the SOFC is pressurised by an MGT, the alternator plays an important role in the system control during the off-design and part load operations. Specifically, the air flow rate is controlled by the shaft rotational speed acting on the electrical generator. This leads to the possibility of keeping the fuel cell operating parameters acceptable for a wide range of operating conditions, because the air mass flow is used to cool down the SOFC. For a turbocharger, this possibility is no longer available, because the rotational speed depends only on the power balance between compressor and turbine, so an alternative control strategy must be defined (e.g. acting on valves installed on the system, as will be explained in Chapter 3).

Due to the novelty of this solution, the studies on SOFC-turbocharger systems are very scarce when compared with the literature available on SOFC-MGT systems and rely exclusively on simulation tools. The Thermochemical Power Group (TPG) of the University of Genoa has started to investigate the potential of innovative biofueled turbocharged SOFC systems within the Bio-HyPP European project in 2015. Many studies had been carried out during this project, including some of the activities of this thesis. The first existing SOFC-turbocharger emulator plant was designed and built at the Innovative Energy Systems Laboratory of the University of Genoa for the Bio-Hypp project (Figure 11).

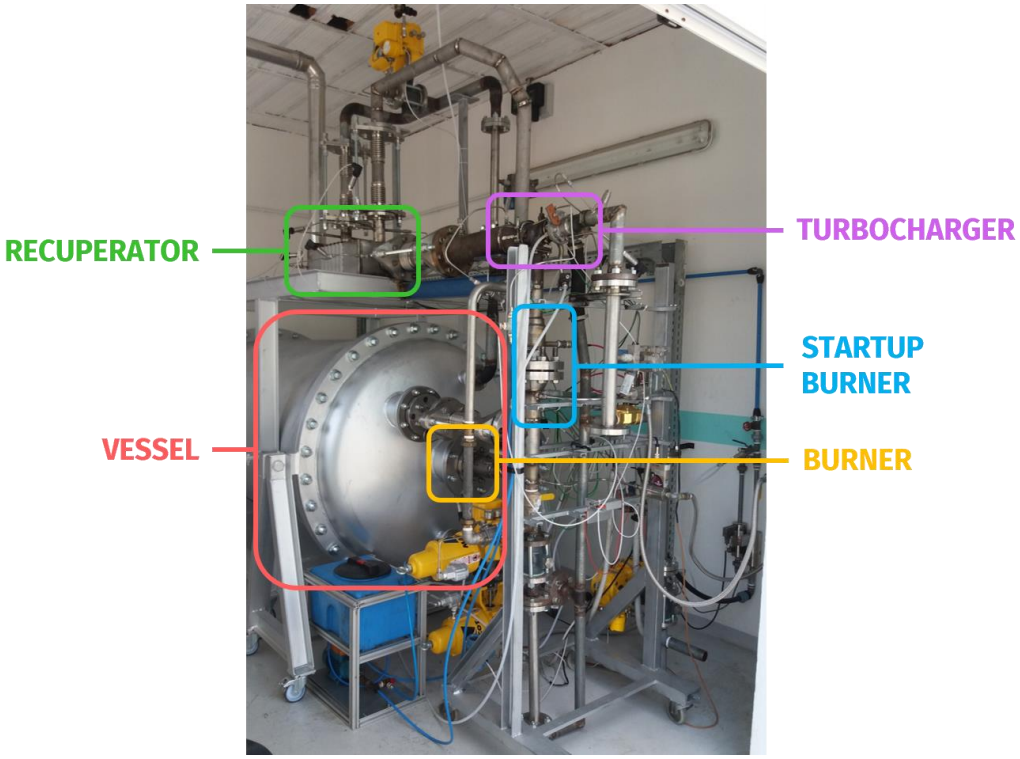

Figure 11. *The SOFC-turbocharger emulator plant of TPG, which was built for the Bio-HyPP European project (the main components are highlighted).*

1.4 Work motivation and thesis highlights

The main goal of this thesis is to expand the knowledge on pressurized SOFC systems, analysing their performance and addressing the most critical

technological challenges. Most of the research activities carried out over the past years focused on an innovative plant layout based on the integration of a SOFC with a turbocharger. The turbocharged layout is novel, and it is particularly interesting to investigate its potential as a viable alternative to SOFC-MGT systems. Some of the activities focused on SOFC-MGT systems too, but the results obtained can be generally extended to turbocharged layouts.

On these premises, the main questions this thesis wants to answer are:

- Can turbocharged SOFC systems run in a wide operative range, generating electrical power with high efficiency, to become a viable alternative to MGT-based hybrid systems?
- What kind of control system should be designed to guarantee the proper operation of turbocharged SOFC systems, both in stationary conditions and during transients?
- Which solutions and tools can be implemented on SOFC hybrid systems, to reduce the risk of potentially detrimental scenarios, increasing their reliability and extending their service life?

However, it is not viable to answer directly these questions analysing the performance of these plants. In fact, it was emphasised in this chapter that, despite their great potential, the development of SOFC-MGT systems has been particularly difficult due to their high cost and many technical challenges. Even companies that reached impressive results, such as Siemens-Westinghouse and LGFCS, decided eventually to close their programs. Based on this experience, the early development of turbocharged-SOFC systems must strongly rely on numerical simulations, in order to increase the knowledge of these systems without the need of huge investments. For this reason, the activities carried out during the PhD were focused on developing detailed numerical models, analysing the results of their simulations, and testing effective control systems in a software-in-the-loop setup. In the future, the results obtained in this thesis could be validated on emulator plants and, eventually, on real prototypes.

The research presented here is the outcome of a collaboration between the Laboratory of Applied Mathematics, Simulation and Mathematical Modeling with the TPG.

At first, the layout of the turbocharged SOFC system considered in this thesis is presented. The studies conducted and their outcomes are presented and discussed in separate chapters, according to the following list:

- **Off-design performance analysis of a turbocharged SOFC system**

  The aim of this study is to analyse the off-design performance of an innovative turbocharged solid oxide fuel cell system fed by biogas. To perform this analysis, a steady-state model was created using a modular tool developed in Matlab®-Simulink® including off-design models of the system components. The model was used to compare different control strategies, then the most suitable one, based on wastegate and cold bypass valves, was adopted, obtaining compliance with the operative constraints and effect on the system efficiency. Afterward, the system steady-state operation was simulated for various electric power loads and ambient temperatures.

- **Dynamics and control of turbocharged SOFC system**

  This study regards design and test of control systems for a 30kW turbocharged solid oxide fuel cell system fuelled by biogas. The control of this kind of system is a novel topic, characterized by many technical challenges, that were not addressed before. To regulate the stack temperature, a cold bypass valve was included, connecting the compressor outlet to the turbine inlet. A dynamic model of this system was developed in Matlab-Simulink® using the TRANSEO simulation tool by TPG. This model was used to analyse the response of the turbocharged solid oxide fuel cell system to a cold bypass valve opening step change. System information obtained from this analysis was used to design and tune four controllers: a conventional proportional integral controller and three

different cascade controllers. The controller performance was evaluated under two different scenarios, considering quite aggressive power ramps.

- **Surge Prevention and Recovery Techniques for a SOFC-Turbocharger Hybrid System**

  The aim of this study is to investigate different techniques to drive the operative point of the compressor far from the surge condition when needed, reducing the risks related to transients and increasing its reliability. By means of a system dynamic model, developed using Matlab-Simulink® and TRANSEO, the effect of different anti-surge solutions is simulated: (i) intake air conditioning, (ii) water spray at compressor inlet, (iii) air bleed and recirculation, and (iv) installation of an ejector at the compressor intake. The pressurized fuel cell system is simulated with two different control strategies, i.e. constant fuel mass flow and constant turbine inlet temperature. Different solutions are evaluated based on surge margin behaviour, both in the short and long terms, but also monitoring other relevant physical quantities of the system, such as compressor pressure ratio and turbocharger rotational speed.

- **Application of Bayesian Networks for Degradation Diagnosis on SOFC-MGT Hybrid Systems**

  This study aims to develop and test Bayesian belief network-based diagnosis methods, which can be used to predict the most likely degradation levels of turbine, compressor and fuel cell in a SOFC-MGT hybrid system on the basis of different sensors measurements. The capability of the diagnosis systems to understand if an abnormal measurement is caused by a component degradation or by a sensor fault is also investigated. The data used both to train and to test the networks is generated from a deterministic model and later modified to consider noise or bias in the sensors. Similarly to the previous study on surge

prevention techniques, the purpose of this research activity is to develop a tool able to increase the plant reliability and avoid potentially detrimental scenarios.

The choice of Bayesian belief networks to diagnose the system status is based on their many existing applications for turbomachinery diagnosis. However, their application to fuel cell – gas turbine hybrid systems is novel, thus the results obtained from this analysis could be a significant starting point to understand their potential.

A different layout is considered in this case, because this work was part of a bi-lateral collaboration project between Università degli Studi di Genova and Mälardalens Högskola, focused on SOFC-MGT hybrid systems. However, the approach adopted here could be extended to different plants and applied to develop diagnostic systems for a turbocharged SOFC system. The project was funded by the Italian Minister of Education and the Swedish Research Council, and the research activity was carried out by the author of this thesis in 2019, during a period of 4 months with the SOFIA Group of Mälardalens Högskola in Västerås, Sweden.

2 Turbocharged SOFC system

The focus of this thesis is on an innovative small-scale turbocharged SOFC system that could be used for distributed generation applications. This plant was designed within the BioHyPP European project to generate about 30 kW of net electric power when fuelled with biogas. The design choices of the turbocharged SOFC system are based on [77]. As mentioned in Chapter 1, the adoption of a turbocharger and the use of a standard recuperator are aimed to reduce the investment costs and to increase the reliability of the plant. The use of biogas and not methane, instead, has the purpose of reducing the environmental impact of the system. The design parameters of the system (e.g. fuel utilization factor, SOFC pressure and current density) were set to guarantee the proper integration of turbocharger and SOFC, while achieving high efficiency and power density. The layout of this plant, which will be described in more detail in Section 2.2, is based on the integration of a fuel cell stack containing planar SOFCs and a turbocharger: the stack exhausts expand in the turbine, providing the mechanical energy necessary to drive the compressor. The compressor, on its turn, pressurizes the air flow entering the fuel cell, affecting positively its performance.

2.1 Biogas

Typically, biogas is mostly composed by CH_4 and CO_2, with molar percentages in the range of 50-75% for CH_4 and of 50-25% for CO_2 [78,79]. According to [80], the third most abundant substance in biogas is N_2, with a content <1% for biogas produced by sewage digesters and organic waste digesters, and values between 5% and 15% for biogas produced form landfill waste. Since N_2 is also an inert gas concerning the reactions occurring in a pressurized SOFC system, it appears reasonable to neglect its effect on the system performance. To study the turbocharged SOFC system, a constant molar composition of 50% CH_4 and 50%

CO_2 is considered. To keep the system costs as low as possible, at this stage, no CO_2 separation system was included. In the future, CO_2 separation from the biofuel would increase the power density of the system, reducing at the same time emissions of greenhouse gases.

2.2 Plant layout

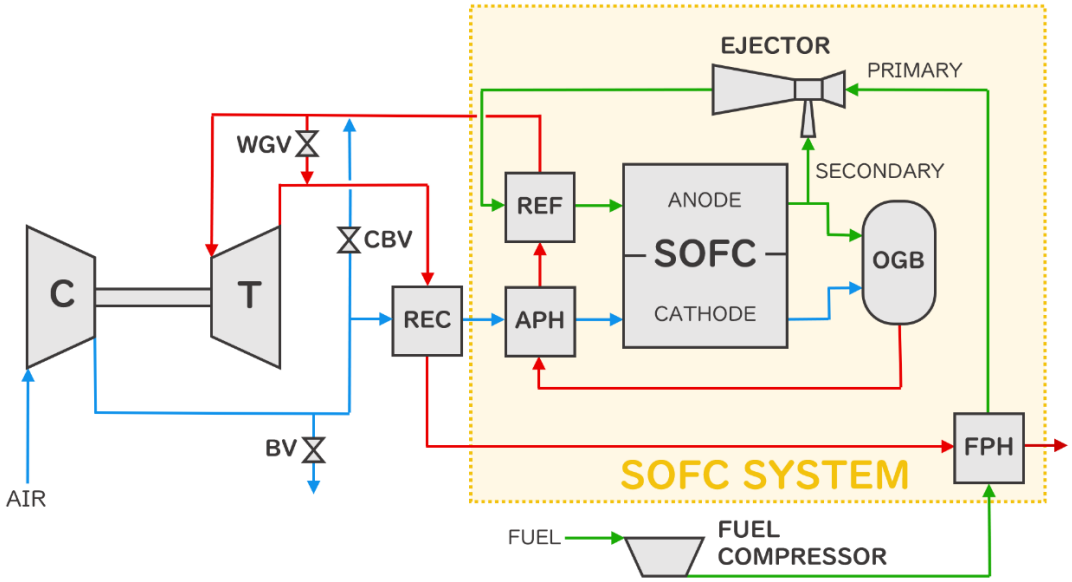

Figure 12. *Turbocharged SOFC plant layout; in blue the cathode side air flow, in green the anode side fuel flow and in red the exhaust flow.*

Contrary to pressurised systems equipped with an expensive MGT, the proposed layout benefits from the SOFC pressurization using a standard component, subject to mass production, with a consequent reduction in capital costs. Moreover, when compared with MGTs, turbochargers are components with a high degree of technological maturity thanks to their extensive use in the automotive field. However, there is a non-negligible decrement in power and efficiency due to the use of a turbocharger (10-15% in comparison with a SOFC-MGT system). Therefore, the main motivation for this solution is the cost reduction, thanks to the lower cost of the turbocharger (a couple hundreds of

euros for a turbocharger [81] compared to more than 1000 €/kW for an MGT [82,83]) and to the lower number of components (electric alternator and power electronics are no longer necessary). It is possible to further limit the costs of the system (whether it is MGT or turbocharger based) using a standard stainless-steel recuperator, that must operate at temperatures below 650°C. These design choices, aimed to reduce the investment costs and to increase the reliability of the plant, are crucial to facilitate penetration of turbocharged SOFC systems in the energy market and to attract potential investors.

Figure 12 presents the plant layout of the innovative turbocharged SOFC system. On the cathode side, the air flow is pressurized by the compressor and pre-heated by the turbine exhausts while flowing through a standard stainless-steel recuperator (REC). Some additional heat is provided by an SOFC system internal heat transfer, represented in Figure 12 by the air pre-heater (APH). On the anode side, the biogas is compressed, and heated through the fuel pre-heater (FPH) before entering the ejector primary duct. Similarly to the APH, the FPH is not an actual heat exchanger, but it represents an internal heat transfer between nearby ducts. The fuel flow drives the partial recirculation of the stack anode outlet flow to the secondary nozzle of the ejector. Primary and secondary flows are then mixed within the ejector before entering the external reformer (REF). The anode recirculation guarantees the minimum steam amount necessary to drive the chemical reactions occurring in the REF and to avert carbon deposition inside the SOFC [84]. The reformer produces hydrogen through the steam methane reforming (SMR) Eq. (1) and the water gas shift (WGS) Eq. (2) reactions [85], feeding the SOFC anode with the reformed fuel flow.

$$CH_4 + H_2O \rightarrow CO + 3H_2 \quad (1)$$

$$CO + H_2O \leftrightarrow CO_2 + H_2 \quad (2)$$

Inside the SOFC, oxygen and hydrogen participate in the electrochemical reaction Eq. (3) to generate electric power. For this reaction to take place, O^{2-}

ions have to migrate through the electrolyte from the cathode to the anode, where water is produced and electrons (e^-) are released from the electrochemical oxidation of H_2. Since the two sides of the SOFC are linked by an electrical connection, the electrons are able to flow to the cathode, generating the electric power.

$$H_2 + O^{2-} \rightarrow H_2O + 2e^- \quad (3)$$

The portion of anodic outlet flow which is not recirculated into the secondary duct of the ejector, is mixed with the cathodic outlet air flow and oxidized inside the off-gas burner (OGB). Therefore, the unused fuel in the SOFC produces the surplus heat useful to pre-heat the cathodic air and to drive the endothermic chemical reactions inside the REF. The combustion of the SOFC exhausts is also necessary to prevent the emission of pollutants into the atmosphere. The exhaust flow reaches the turbine inlet generating, through its expansion, the mechanical power necessary for the turbocharger operation. The turbine exhaust gases are then used to pre-heat the compressed air in the REC and the biogas in the FPH, before being released into the atmosphere.

The system must run under many constraints, which will be described in more detail in the next paragraphs. For this reason, it was equipped with a set of valves, whose openings are determined to guarantee correct operation of the system, both in nominal and off-design conditions. In Figure 12, cold bypass (CBV), bleed (BV) and wastegate (WGV) control valves are visible with their pipelines. The CBV diverts part of the compressed air flow to upstream of the turbine, lowering the turbine inlet temperature and reducing the air mass flow entering the REC. The BV discharges part of the compressed air into the atmosphere, reducing the cathode inlet mass flow. The WGV is used to direct part of the SOFC system exhaust flow directly to the REC entrance, bypassing the turbine.

The system components will be described more in detail in the following paragraphs.

2.3 SOFC

The SOFC stack considered in this thesis is composed by 1500 planar cells with an active area of 127.8 cm^2 each. Its specifications are based on the technical datasheet of a Staxera GmbH system, characterized by high electrical efficiencies, low pressure drops and parasitic losses [86].

In nominal conditions it operates with a current density of 0.237 A/cm^2 and a fuel utilization factor of 0.8. In part load operation the current density would vary, while the fuel utilization could vary or be kept constant, depending on the system control strategy. This SOFC has a broad operation range in terms of current density, fuel flow rate and fuel utilization factor, as showed by the performance map in [86]. A particularly interesting behavior which can be observed on such map, is the efficiency increase at part load and constant fuel utilization factor. For a system operating with constant fuel utilization factor equal to 0.8, the efficiency changes from a value of about 43% when the current is 46 A, to a value of about 50% when the current is 24 A.

This phenomenon is typical of SOFCs and it was addressed many times in literature [37,87,88]. The results discussed in [87] are particularly interesting: in this study a standalone SOFC operating with constant utilization factor showed higher efficiency at lower loads. The influence on the turbocharged system of the performance enhancement at part load will be further discussed.

The SOFC is a delicate component, which could be permanently damaged if its operational limits were not complied. The characteristic parameters and operational limits of the SOFC are showed in Table 1.

Table 1. *Operational limits of the SOFC* [86].

Parameter	Unit	Value
Max temperature	°C	850-860
Max anode-cathode inlet ΔT	°C	250
Max anode ΔT	°C	250
Max cathode ΔT	°C	250
Max anode-cathode Δp	bar	0.03
Max fuel utilization factor	-	0.85
Max cell $\Delta T/\Delta\tau$	°C/s	5

2.4 Reformer

The reformer, necessary to obtain hydrogen from the methane present in the biogas, is installed in co-flow configuration in the present layout. It is designed to transfer the proper amount of heat from the cathode to the anode flow, and to drive the SMR and WGS reactions. The characteristic parameters chosen in the present study, determined on the basis of [77], are shown in Table 2.

If the heat provided or the steam mass flow recirculated from the anode outlet are not sufficient, these reactions would be incomplete. As a consequence, concentrations of carbon monoxide and methane entering the SOFC would increase, causing carbon deposition on the fuel cells. To monitor if the molar flow ($\dot{n}$) of steam is sufficient, a steam to carbon ratio (S/C) is defined according to Eq. (4) based on the reformer inlet flow composition.

$$S/C = \frac{\dot{n}_{H_2O}}{\dot{n}_{CH_4} + \dot{n}_{CO}} \tag{4}$$

According to [89], in order to ensure the correct operation of the system, S/C should be higher than 1.8.

Table 2. *Characteristic parameters of the reformer.*

Parameter	Unit	Value
Mass	kg	18
Single plate length	m	0.280
Single plate width	m	0.008
Single plate thickness	m	0.001
Number of plates	-	80
Plate area correction factor (due to geometry)	-	2
Plate thermal conductivity	W/m·K	20
Reference hydraulic diameter	m	0.004
Nusselt for laminar flow	-	4

2.5 Recuperator

The recuperator is a primary surface heat exchanger, installed in counter-flow configuration and designed to transfer a proper amount of heat, in agreement with [77]. The characteristic parameters of the REC are shown in Table 3. According to these specifications, the recuperator effectiveness should be ~0.79 in the nominal conditions of the hybrid plant.

As explained in Section 2.2, if the turbine outlet temperature is always kept under 650°C, it is possible to install a standard stainless-steel heat exchanger as recuperator, reducing the plant capital cost. Since the main goal of the turbocharged layout is the cost reduction, the compliance with this limit is considered a system constraint and it is included in Table 3.

Table 3. *Characteristic parameters and operative limits of the recuperator.*

Parameter	Unit	Value
Mass	kg	12
Single plate length	m	0.235
Single plate thickness	m	0.001
Plate thermal conductivity	W/m·K	20
Solid specific heat	J/kg·K	750
Number of plates	-	350
Heat exchange area	m^2	8.03
Total flow section	m^2	0.04
Maximum temperature	°C	650

2.6 Off-gas burner

The off-gas burner is a catalytic combustor installed at the fuel cell stack outlet to burn any residuals of fuel. As explained in Section 2.2, it has the purpose of providing additional thermal energy to turbine, reformer, APH, REC and FPH, while consuming any pollutants that would be discharged by the system. In fact, partial combustion in the OGB should be considered not acceptable because of environmental regulations regarding the release of H_2, CH_4, and CO into the atmosphere. Therefore, complete combustion is considered a constraint that must be verified during the off-design operation of the system.

The geometry of this combustor was designed specifically for the Bio-HyPP project by the German Aerospace Center (DLR), in order to burn the SOFC gas exhausts, which are characterized by low calorific value [90]. The air flow enters the combustor axially and it is split into a series of nozzles. The combustor is surrounded circumferentially by a plenum, which is filled by the off-gas. From this plenum, the off-gas enters the burner though another series of nozzles, which are coaxial to the air nozzles. Then, the flows of air and off-gas enter a

liner, where they take part into the combustion before going through the outlet. More details about the off-gas burner can be found in [90].

2.7 Ejector

The ejector is composed by a primary nozzle, connected to the fuel line, a secondary nozzle, recirculating from the SOFC anode outlet, a mixing chamber, and an outlet diffuser, connected to the REF inlet, as shown in Figure 13.

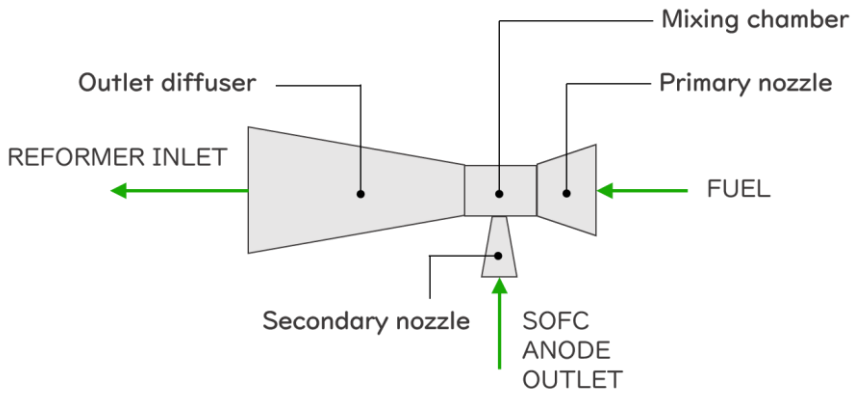

Figure 13. *Main structure of the ejector installed on the turbocharged SOFC system.*

The ejector is designed in order to guarantee a proper recirculation during design conditions, as in [77,91], to provide the correct amount of steam and heat at the REF. Its characteristic parameters are shown in Table 4.

Table 4. *Characteristic parameters of the ejector.*

Parameter	Unit	Value
Primary nozzle diameter	m	0.0025
Secondary nozzle diameter	m	0.0191
Mixing chamber diameter	m	0.0191
Diffuser outlet diameter	m	0.0264
Diffuser angle	°	6
Nozzle discharge coefficient	-	0.95

In comparison with natural gas based anodic recirculation, the biogas forces important modifications in the anodic ejector geometry because of the additional mass flow rate in the fuel flow (the composition includes also 50% CO_2) [91].

2.8 Turbocharger

An automotive turbocharger is considered for integration with the SOFC. The specifications of compressor and turbine are based on real devices manufactured by Garrett Advancing Motion, but they were scaled in terms of mass flow to properly fit the pressurized SOFC system requirements. The performance maps of these devices in terms of pressure ratio β, reduced mass flow $\dot{m}^{red}$ and efficiency η are displayed in Figure 14. The values on the axis are omitted due to confidentiality requirements.

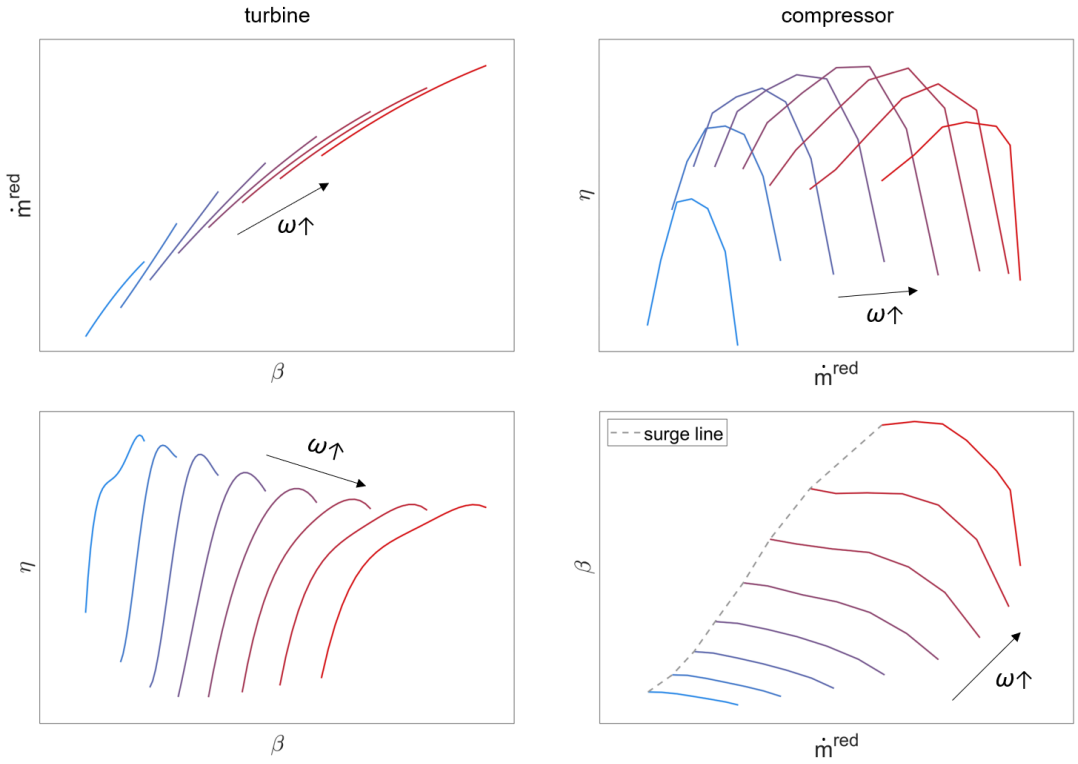

Figure 14. *Steady-state performance maps of the turbocharger; iso-speed lines are represented with a blue colour for lower speeds and with a red colour for higher speeds (the black arrow shows along which direction the rotational speed increases).*

A speed limit equal to 2.9 10^5 rpm is considered, based on the manufacturer specifications: exceeding such speed may cause severe damage of the turbocharger components. Another phenomenon that can be detrimental for the system is compressor surge, a fluid-dynamic instability occurring at low mass flow rates, that consists of fluctuations of mass flow rate and pressure. Surge is characterized by unbalanced forces on the compressor rotor, causing vibrations and increasing its mechanical stress level [92]. Moreover, compressor surge is particularly dangerous when a turbocharger is part of a pressurized SOFC system. In fact, the abrupt pressure oscillations could easily break the ceramic supports of the fuel cells, damaging them permanently [93]. Generally, compressor maps display the surge line, a line that delimits the normal operation region of the component, where surge is avoided. To quantify how safe an operative point is from a surge event, the surge margin K_p is generally used in the literature on SOFC hybrid systems [62,94]. The surge margin is proportional to the distance between the operative point and the surge line, but many different definitions of this parameter can be found in literature. In this thesis K_p is computed using Eq. (5), one of the most common expressions according to [95], which depends on both $\dot{m}$ and β.

$$K_p = \frac{\dot{m}/\beta}{\dot{m}_{surge}/\beta_{surge}} \tag{5}$$

In Eq. (5), $\dot{m}_{surge}$ and β_{surge} are the values of the operative point where the current iso-speed line intersects the surge line, as shown in Figure 15.

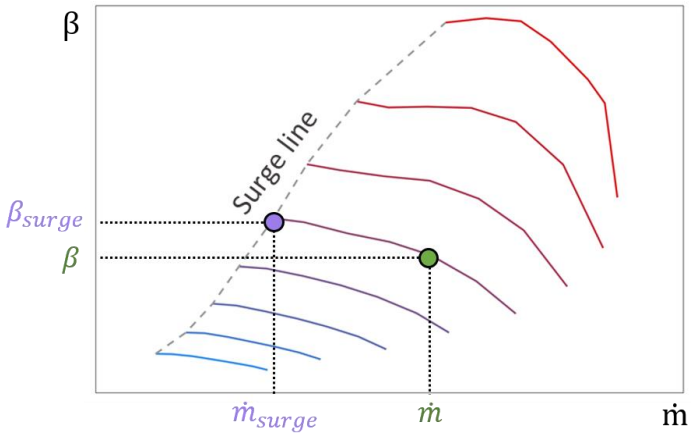

Figure 15. *Position of the operative point of the compressor (in green) and of the point where the iso-speed line intersects the surge line (in purple).*

Surge conditions are characterized by $K_p < 1.00$, but a K_p lower than 1.10 is already representative of dangerous operating conditions [96]. In fact, even if the compressor operative point is stable for $1.00 < K_p < 1.10$, it could be easily moved to surge by a small variation in the system. On the other hand, higher values of K_p represent a safer condition, where the compressor operative point is far from the surge line and therefore the risk for the compressor to enter the unstable region during a transient is low.

3 Off-design performance analysis of a turbocharged SOFC system

Many researchers have investigated the potential of pressurized SOFC systems and analysed their performance in different conditions, mostly relying on numerical simulations of an SOFC-MGT layout [44,97–100]. In [44] the behaviour of such a system was analysed at part-load and over-load conditions, determining the condition ranges where stable system operation is possible. This analysis showed that the system operative range is limited by the fuel utilization factor and by the flue gas temperature. The assessment of the thermodynamic performance of internal reforming SOFC-MGT systems was presented in [97], showing system efficiencies of 65-70% for atmospheric SOFCs and 74-76% for pressurized SOFCs. An off-design performance analysis was carried out in [98], for an SOFC-MGT plant equipped with ejectors for the anode and cathode recirculation. This study showed that ejectors can effectively replace blowers for recirculation. The optimal size of the gas turbine was determined to be equal to the fuel cell power in [99], relying on a genetic algorithm to limit the SOFC degradation while also optimizing the plant internal rate of return and extending its lifetime to 21 years. A study about multi-objective configuration optimization of a SOFC – gas turbine cogeneration system was presented in [100], considering the effect of design parameters of the compressor, turbine, combustion chamber and heat exchangers on the system performance. The optimal setup determined by this analysis was characterized by an exergy efficiency around 47% and a total cost rate of 748.1 $/h.

The use of biofuels to run SOFC systems is a topic of great interest and was addressed in many different studies. The performance evaluation in [101] was presented for an SOFC-MGT system that directly fed its fuel cell with biogas for an application of combined heat and power generation. This study showed that proper operation of the system is possible using biogas, but the performance of

the SOFC must be carefully monitored to avoid thermal stress and carbon deposition. The focus of [102] was the performance at different power loads of a system fuelled with wood chip gas. Considering various operational modes, the power generated could vary between 20% and 134% of the system nominal power. The potential of a SOFC-MGT system fed by hydrothermally gasified waste biomass was presented in [103], showing a first law efficiency of 63%. In [104], the behaviour of a pressurized SOFC system was analysed for various compositions of biofuel, finding that methane is the best fuel in terms of energy and exergy efficiency. A detailed analysis of a SOFC system fueled by gasified biomass, where the authors relied on 3D fluid-dynamic electrochemical model of the SOFC was presented in [105]. It was found that this system needs an integration heat flux equal to the 21% of the low heating value at the SOFC inlet to work properly and it can reach an overall efficiency of 45.8% in nominal conditions.

Most of the studies considered only the nominal value of the ambient temperature, typically 15°C, with only few works taking into account the effect of this parameter. However, previous works on ambient temperature effects were all devoted to pressurized systems based on a microturbine, not on the innovative turbocharged configuration proposed in this work. In [56] the effect of ambient perturbations on the performance of an SOFC-MGT system was analysed, based on experimental data and dynamic simulation results. Additionally, simple control loops were tested to limit internal temperature fluctuations. The effect of the ambient temperature was also investigated in [106], which tested a model predictive control strategy on a power-load ramp simulation. Other studies focusing on both system performance and control strategies are presented in [63,107–109].

However, a complete performance analysis of a pressurized SOFC system at different ambient temperature conditions and power load is missing from literature. Moreover, the focus of the community has been on SOFC-MGT systems, with few studies on turbocharged SOFC systems, such as [75] and [74].

In [75], a turbocharged SOFC system was compared with two different standalone SOFC system layouts, showing that the highest values of electrical efficiency were obtained by the turbocharged solution. The study presented in [74] provided information regarding the performance of two different layouts, i.e. integrating a single spool and a dual spool turbocharger. This analysis also included a sensitivity analysis of key variables, as well as a dynamic analysis for load transitions.

The study presented in this chapter aims at filling the literature gap on biofueled turbocharged SOFC systems and, simultaneously, to provide a completely new off-design performance analysis of pressurized SOFC systems with varying power load and ambient temperature. The novel results obtained from this activity are expected to help both to academia and industry in the research and development of pressurized SOFC systems.

To analyse the performance of the turbocharged SOFC system the author has developed a modular off-design steady-state model in Matlab®-Simulink®. The system layout, which is strictly related to the one introduced in [91], was designed assuming a small-scale application and the use of biogas as fuel. Based on simulation results, three different control strategies were tested and the most suitable one for operating the system at part-load conditions was selected. Then a complete mapping of the system performance was carried out, with consideration for variations in power load and ambient temperature. Great attention was paid to the system constraints, pointing out potential limitations to its operation.

This study was published in the article “Off-design performance analysis of a turbocharged solid oxide fuel cell system” on the journal Applied Thermal Engineering [96].

3.1 Steady-state model

A steady-state off-design model of the system was developed in Matlab®-Simulink® to study its behaviour at part load and at different ambient temperature conditions. The plant model was created by assembling 0D and 1D component models from Steady-State library that was previously developed at TPG by other researchers. The component of this library are described subsequently in this section. The validation of this tool is discussed in Section 3.1.8. The development of the full hybrid system model required to interface correctly all the components, defining constraints and boundary conditions, as well as to set the characteristic parameters of each one of them in accordance with the system specifications.

Each component model interfaces are based on mass flow ($\dot{m}$), pressure (p), temperature (T) and composition (X). Only H_2, H_2O, CH_4, CO_2, CO, N_2, O_2 and Ar are considered in the fluid compositions. All the gases are assumed to be ideal: following the perfect gas law, but with thermo-physical properties dependant on the temperature. It is important to remind that the ideal gas model is unsuitable when the pressure is very high and when the temperature is very low (the closer to the critical point of the substance, the higher is the error) [110]. However, a pressurized SOFC system is expected to have maximum pressures of a few bars, and a minimum temperature around the ambient conditions, making the ideal gas assumption perfectly reasonable to model the plant performance. The thermo-physical properties, such as enthalpy (H), specific heat (c_p) dynamic viscosity (μ) and thermal conductivity (λ), are calculated from single species properties via polynomial functions of temperature [111].

Pressure losses (Δp) across each component (if non-negligible) are calculated as a function of flow inlet conditions, starting from a user defined reference condition of pressure loss, mass flow, pressure, temperature and composition as follows Eq. (6) [112]:

$$\Delta p = \frac{\mu_{in}^{k} R_{sg,in} T_{in} \dot{m}_{in}^{j}}{p_{in}} \cdot \frac{\Delta p_{ref} p_{ref}}{\mu_{ref}^{k} R_{sg,ref} T_{ref} \dot{m}_{ref}^{j}} \quad (6)$$

where R_{sg} is the specific gas constant, the subscripts *in* and *ref* refer to flow inlet and reference conditions (nominal operating point) respectively, k and j are coefficients depending on the flow condition (k=1 and j=1 laminar flow and k=0.25 and j=1.75 for turbulent flow).

3.1.1 Heat Exchanger

The 1D heat exchanger model [113–115] can simulate either a co-flow or a counter-flow plate heat exchanger. The model parameters are physical and geometrical properties of the heat exchanger such as mass, specific heat, thermal conductivity, number of plates, length and thickness of each plate, as well as heat exchange areas and flow section areas. Each plate is discretized along its longitudinal direction according to finite difference scheme, and it is possible to set the number of discretization elements of it. For this study, this number was set equal to 10, which, according to the author's experience, obtains a good precision in the results without increasing excessively the model computational time. The heat exchanger is discretized in the direction along which the fluids flow and, in each element of a single plate, the heat exchange (Δq) is determined according to Eq. (7)

$$\Delta q = \frac{T_{hot} - T_{cold}}{\frac{1}{h_{hot}\, A_{HE,el}} + \frac{1}{h_{cold}\, A_{HE,el}} + \frac{\lambda_{pl}\, A_{HE,el}}{t_{pl}}} \quad (7)$$

where A_{el} is the heat exchange area of the discretization element, λ_{pl} and t_{pl} are the thermal conductivity and the thickness of the plate, respectively, and the subscripts *hot* and *cold* refer to the flow with the highest and the lowest inlet temperature, respectively. The convective heat exchange coefficients h are computed at each discretization point of the single plate, using Eq. (8)

$$h = \frac{Nu \cdot \lambda_f}{D_h} \tag{8}$$

where λ_f is the thermal conductivity of the fluid and D_h is the hydraulic diameter of the section between plates. The Nusselt number Nu is calculated for both the hot and the cold sides of the heat exchanger as follows in Eq. (9) [116]

$$Nu = \begin{cases} 3.66 + \dfrac{0.0668 \, \frac{D_h}{L_{pl}} \, Re \, Pr}{1 + 0.04 \left(\frac{D_h}{L_{pl}} \, Re \, Pr \right)^{\frac{2}{3}}} & Re < 2400 \\ 0.023 \, Re^{\frac{4}{5}} \, Pr^{\frac{2}{5}} & Re \geq 2400 \end{cases} \tag{9}$$

Where L_{pl} is the plate length, Re is the Reynolds number and Pr is the Prandtl number, which are determined from the geometry of the heat exchanger and the physical properties of flow.

Considering the convective heat exchange on both sides and the conductive heat exchange through the solid matrix (both across the plates and along the flow direction), temperatures of the fluids and of the solid are calculated iteratively until convergence is reached. Heat losses towards the atmosphere are neglected.

Regarding the layout considered in this study, only the REC is an actual heat exchanger, while FPH and APH represent heat exchanges between nearby ducts. Since the counter-flow configuration always guarantees higher values of effectiveness than the co-flow, the REC was designed as a counter-flow heat exchanger, and the model is set accordingly. The REC model parameters were set accordingly to the heat exchanger specifications in Table 3. FPH and APH models were set to be equivalent to counter-flow heat exchangers with effectiveness equal to ~0.2. This value was assumed by the author and could be calibrated on real data in the future for better accuracy.

3.1.2 Reformer

The 1D reformer model can simulate either a co-flow or a counter-flow reformer: for the scope of this work it was used in co-flow configuration, according to the system layout. The model is characterized setting its physical and geometrical properties such as mass, thermal conductivity, number of plates, dimensions of each plate, hydraulic diameter and Nusselt number for laminar flow. It is possible to set the number of discretization points for a single plate, which was set equal to 50 for this analysis.

The model solves the methane reforming and water-gas shift reactions occurring in the fuel stream.

To compute the reaction rates R_{MSR} and R_{WGS}, corresponding to the decrease of CH_4 molar fraction and to the increase of CO_2 molar fraction respectively, it is necessary to compute the equilibrium constants K^{eq} (Eqs. (10) and (11)) as functions of the local temperature, according to Eq. (12) [97,117]. However, it should be highlighted that the model does not include kinetics and assumes that the output is at equilibrium condition because of the high temperatures of the SOFC system, therefore the reaction rates are those necessary to achieve such output conditions. The validity of this assumption was proved comparing the results of this model against experimental data in [117]. Moreover, the study presented in [118] showed similar results on SOFC systems adopting equilibrium or kinetic models, even if the most reliable results can be obtained considering SMR kinetics.

$$K_{SMR}^{eq} = \frac{p_{CO}\, p_{H_2}^3}{p_{CH_4}\, p_{H_2O}} \tag{10}$$

$$K_{WGS}^{eq} = \frac{p_{H_2}\, p_{CO_2}}{p_{CO}\, p_{H_2O}} \tag{11}$$

$$K_R^{eq} = A_R\, T^4 + B_R\, T^3 + C_R\, T^2 + D_R\, T + E_R \qquad with \quad R = SMR, WGS \tag{12}$$

The values of the coefficients used in Eq. (12) depend on the considered reaction and can be found in Table 5.

Table 5. *Coefficients used to compute the equilibrium constants in Eq. (12)* [97].

Coefficient	SMR	WGS
A_R	$-2.6312 \cdot 10^{-11}$	$5.47 \cdot 10^{-12}$
B_R	$1.2406 \cdot 10^{-7}$	$-2.574 \cdot 10^{-8}$
C_R	$-2.2523 \cdot 10^{-4}$	$4.6374 \cdot 10^{-5}$
D_R	$1.95027 \cdot 10^{-1}$	$-3.91500 \cdot 10^{-2}$
E_R	-66.139488	13.209723

The partial pressures of the substances taking part in the MSR and WGS reactions, and the reaction rates, can be obtained from the equilibrium constants. Thus, the molar flow of the i-th substance involved in the k-the reaction can be updated using Eq. (13).

$$\dot{n}_i^{out} = \dot{n}_i^{in} + \sum_k v_{i,k} R_k \tag{13}$$

where $\dot{n}$ is the molar flow and v is the stoichiometric coefficient.

Regarding the heat exchange between the air and the fuel flows, the reformer performance is simulated with the same approach presented in Section 3.1.1 for the heat exchanger. For each discretization element, values of T_{air} and T_{fuel} in the next section of the reformer are computed iteratively in order to respect the thermal balance of the cathodic and of the anodic flows.

The characteristic parameters of the reformer model are set in accordance with Table 2.

3.1.3 Burner

A 0D burner model is used to simulate the off-gas burner. The model assumes complete combustion of fuel if O_2 content is enough, otherwise progressive partial or complete combustion of H_2, CH_4, and CO is calculated, always assuming equilibrium of the reactions. Partial combustion in the off-gas burner should be considered not acceptable because of environmental regulations regarding the release of H_2, CH_4, and CO into the atmosphere. Therefore, complete combustion is considered a system constraint (guaranteed with the adoption of a catalytic combustor in the system) that must be verified during the off-design analysis. The outlet temperature is determined with Eq. (14) as a function of the inlet temperature and the enthalpy change ΔH due to the k oxidations [117].

$$T^{out} = \frac{\sum_i \dot{n}_i^{in}\, c_{p,i}\, T^{in} + \sum_k R_k(-\Delta H_k)}{\sum_i \dot{n}_i^{out}\, c_{p,i}} \tag{14}$$

Pressure drops along the burner are computed according to Eq. (6), as explained at the beginning of this section.

3.1.4 Ejector

This 0D model, which was already presented in [119], is used to simulate the ejector. The ejector is characterized by geometrical parameters (primary, secondary, mixing chamber and diffuser outlet diameters, diffuser angle) and performance parameters. The main sections of the ejector are the same shown in Figure 13.

From the primary and secondary streams and from the imposed secondary pressure, this model computes the ejector recirculation ratio, the diffuser outlet stream, the primary inlet pressure and other operating parameters, such as Mach numbers, in relevant sections. To do these calculations, the model solves

the continuity Eq. (15), momentum Eq. (16) and energy Eq. (17) equations, as explained in [119].

$$\dot{m}_{prim} + \dot{m}_{sec} = \rho_{out}\, c_{out}\, \Omega_{out} \tag{15}$$

$$p_{out}\Omega_{out} - p_{prim}\Omega_{prim} - p_{sec}\Omega_{sec} - \int_{prim-sec}^{out} p\, d\Omega = \dot{m}_{prim} C_{dis} c_{prim} + \dot{m}_{sec}\, c_{sec} - \dot{m}_{out}\, c_{out} \tag{16}$$

$$\dot{m}_{prim}\left(H_{prim} + \frac{1}{2}\, c_{prim}^2\right) + \dot{m}_{sec}\left(H_{sec} + \frac{1}{2}\, c_{sec}^2\right) = \dot{m}_{out}\left(H_{out} + \frac{1}{2}\, c_{out}^2\right) \tag{17}$$

Section areas are represented by the symbol Ω, c is the velocity, and C_{dis} is the nozzle discharge coefficient, included to consider the effect of ejector discharge losses. The subscripts *prim*, *sec* and *out* refer to the ejector primary duct, secondary duct and outlet, respectively. The recirculation ratio RR is calculated in the ejector model as follows Eq. (18):

$$RR = \frac{\dot{m}_{sec}}{\dot{m}_{prim}} \tag{18}$$

As explained in Section 2.7, the ejector must supply the reformer with a proper amount of steam to drive the MSR and WGS chemical reactions and avoid carbon deposition inside the SOFC. The steam to carbon ratio (S/C), defined according to Eq. (4), is computed by the model at each time step based on the ejector outlet flow composition.

According to [89], in order to ensure the correct operation of the system, S/C should be higher than 1.8. The ejector is designed in order to guarantee a proper recirculation during design conditions, as in [77,91]. The characteristic parameters of the reformer model are set in accordance with Table 4.

3.1.5 Fuel Compressor

The fuel compressor is modelled assuming perfect gas behaviour and isentropic efficiency equal to 0.8. The variables of this function are the fuel inlet conditions, such as pressure, temperature and composition. In Section 2.2 it was explained how, through SMR and WGS reactions, 4 molecules of H_2 can be obtained from one CH_4 and two H_2O molecules. The fuel molar flow required to feed the system with the proper amount of H_2, was obtained from the system fuel utilization factor U_f [120] and operating current with Eq. (19)

$$\dot{n}_{fuel} = \frac{i_{cell}\, N_{cells}}{U_f\ 2\ F} \cdot \frac{1}{4\ X_{CH_4}} \tag{19}$$

where i_{cell} is the fuel cell electric current, N_{cells} is the number of cells in the stack and F is the Faraday constant. The outlet pressure is calculated from the values of ejector primary pressure and pressure losses; the outlet temperature is calculated based on inlet temperature, pressure ratio and isentropic efficiency [121]. The power absorbed by the fuel compressor $P_{C,fuel}$ is calculated according to Eq. (20).

$$P_{C,fuel} = \dot{m}_{fuel}\ (H_{fuel,out}\ - H_{fuel,in}) \tag{20}$$

3.1.6 Turbocharger

The turbocharger model is based on the coupling of 0D models of turbine and compressor. Both models interpolate and extrapolate the maps of rotational speed, reduced mass flow, pressure ratio and efficiency presented in Section 2.8 and displayed in Figure 14. The compressor maps also include data regarding the position of the surge line.

Inlet conditions of pressure, temperature, composition and rotational speed are inputs to both models whereas mass flow, outlet temperature calculated via interpolated efficiency and power are model outputs. The turbine outlet

pressure, which is equal to the ambient pressure plus the REC pressure losses, is used as an input of the model to compute the turbine inlet pressure from the value of pressure ratio. The computation of K_p is performed by the model according to Eq. (5), assuming that values higher than 1.1 represent a safe operative condition.

Compressor and turbine power are calculated using Eq. (21).

$$P = \dot{m}_{out} \, (H_{out} - H_{in}) \tag{21}$$

The matching between compressor and turbine is obtained by verifying two conditions at each simulation step:

- No power output: the compressor power is equal to the turbine power, minus the mechanical losses (assumed to be 1%): any imbalance is used to correct the turbocharger rotational speed ω;
- Turbine mass flow balance: the mass flow interpolated from the maps must be equal to the mass flow entering the turbine from the rest of the system; any difference is used to correct the compressor pressure ratio β to vary the interpolated air flow at the next step.

3.1.7 SOFC

This 1D model is used to simulate the SOFC. Setting the number of cells in the stack N_{cell}, the current density j_{cell}, the geometric characteristics of the SOFC and the thermal losses, the fuel cell is characterized. To solve numerically the SOFC equations, a finite difference scheme is adopted, and each single cell is discretized in a certain number of points along the longitudinal direction. In this study the number of points was set equal to 10. This value was determined in order to achieve a good precision without increasing the computational time of the model too much. It was observed that a lower number of points altered the model outputs. Instead, a higher resolution did not significantly improve the accuracy of the model: setting the number of points to 20, the values of cathode

outlet temperature and power in nominal conditions changed only of 0.003% and 0.0004% respectively. This number is set according to the experience of the author and other members of the TPG with this model, which was used in previous studies and verified against experimental data, as will be discussed in the next section. The characteristic parameters and the operational limits for the modelled SOFC, are set in the model according to the specifications of the Staxera GmbH system in [86]. The input data of the model are the anode and cathode inlet flows, and the operating current. The outputs are the outlet flows physical properties, the electric power generated, the cell voltage, and the temperature and current density distributions along the cell. To simulate the behaviour of the SOFC the method proposed in [117] was followed. It is assumed that all the fuel cells in the stack are connected in parallel and have the same behavior. The distribution of current density in the cell is computed on the basis of electrochemical reactions and local temperature. Even if this model is used for steady-state simulations, it was developed as a dynamic representation of an SOFC. The time constant of the solid structure thermal transient is much bigger than those of the other transitory phenomena happening in an SOFC, such as fluid dynamics and electrochemical reactions. Thus, the solid energy balance is the only equation in the model with time derivative terms.

The model follows five main steps to simulate the SOFC performance:

a) Based on electrical cell current, physical properties and chemical composition of the inlet flows, the equations governing the electrochemical kinetics are solved to determine the amounts of O_2 and H_2 reacting in the SOFC. The cell voltage is computed subtracting all the cell losses from the Nernst's reversible voltage [122]. The characteristic losses of a SOFC are ohmic, activation and concentration losses: ohmic losses are related to ionic and electrical resistances of the cell and of its electrical connections, activation losses are due to the voltage necessary to activate the electrochemical reaction, while concentration losses are caused by the slow diffusion of the substances through the electrodes.

b) If any residuals of CH_4 and CO are present at the SOFC inlet, they can take part in MSR and WGS reactions within the SOFC, considered at equilibrium and simulated with the same procedure used in the reformer model (Section 3.1.2).

c) Chemical compositions of the flows leaving the cathode and anode are updated on the basis of the electrochemical reactions occurring in the SOFC. If a fraction of CH_4 or CO was not completely consumed by the MSR and WGS reactions, their contribution to the electrochemical reactions is neglected.

d) Energy balance equations are solved for the gas flows and for the SOFC solid structure, taking into account the heat generated by the electrochemical oxidation, the thermal capacitance of the stack and the thermal losses to the ambient. In this way it is possible to find the temperature of the outlet anode and cathode gas flows, as well as the temperature distribution along the cell.

e) The real SOFC voltage is obtained computing the ideal Nernst's value and considering the effect of concentration, activation and ohmic losses.

The complete set of equations implemented in the SOFC model are shown in Table 6 (Eqs.(22)-(39)). The meaning of the symbols introduced in it can be found in the Nomenclature section.

It is worth pointing out that, even if MSR and WGS are simulated in the SOFC model, these reactions occur mostly in the external reformer. For this reason, their effect on the cell operation is limited and the influence on the concentration losses is negligible.

Table 6. SOFC model equations [117].

Local Electrochemical Kinetics	**Nernst Voltage**	$V_{Nernst} = -\frac{\Delta G}{n_e F} = -\frac{\Delta G^0}{n_e F} - \frac{R_g T_s}{n_e F} \cdot \ln\left(\prod_i p_i^{v_i}\right)$	(22)
	Cell Voltage	$V_{real} = V_{Nernst} - \Delta V^{tot}$	(23)
		$\Delta V^{tot} = \Delta V^{ohm} + \Delta V^{act} + \Delta V^{conc}$	(24)
	Ohmic Losses	$\Delta V^{ohm} = R^{ohm} \cdot j_{cell}$	(25)
	Activation Losses	$j_{cell} = j_0 \left[\exp\left(\theta_a \cdot \frac{F}{R_g T} \cdot \Delta V^{act}\right) - \exp\left(\theta_c \cdot \frac{F}{R_g T} \cdot \Delta V^{act}\right)\right]$	(26)
		$j_{0,an} = \gamma_{AN} \cdot \frac{p_{H_2}}{p_{ref}} \cdot \frac{p_{H_2O}}{p_{ref}} \cdot \exp\left(-\frac{E_{an}^{act}}{R_g T_s}\right)$	(27)
		$j_{0,ca} = \gamma_{ca} \cdot \left(\frac{p_{O_2}}{p_{ref}}\right)^{0.25} \cdot \exp\left(-\frac{E_{ca}^{act}}{R_g T_s}\right)$	(28)
	Concentration Losses	$\Delta V_{an}^{conc} = -\frac{R_g T}{n_e F} \cdot \ln\left(\frac{1 - \frac{j_{cell} R_g T t_{an}}{n_e F D_{an}^{eff} p X_{H_2}^{fg}}}{1 + \frac{j_{cell} R_g T t_{an}}{n_e F D_{an}^{eff} p X_{H_2O}^{fg}}}\right)$	(29)
		$\Delta V_{ca}^{conc} = -\frac{R_g T}{n_e F} \cdot \ln\left(\frac{1}{X_{O_2}^{fg}} - \left(\frac{1}{X_{O_2}^{fg}} - 1\right) \cdot exp\left(\frac{j_{cell} R_g T t_{ca}}{2 n_e F D_{ca}^{eff} p}\right)\right)$	(30)
Equilibrium Chemical Reactions		$K_{WGS}^{eq} = \frac{p_{CO_2} p_{H_2}}{p_{CO} p_{H_2O}}$	(31)
		$K_{SMR}^{eq} = \frac{p_{CO} p_{H_2}^3}{p_{CH_4} p_{H_2O}}$	(32)

Local Balances	**Mass**	Gases	$\frac{\partial n_i^*}{\partial x} = r_i$	(33)
	Energy	Gases	$\sum_i n_i^* \, c_{p,mol,i} \cdot \frac{\partial T_g}{\partial x} + \sum_i c_{p,mol,i} \cdot \frac{\partial n_i^*}{\partial x} \cdot \left(T_g - T_s\right) + +h \, B \cdot \frac{1}{t_{ch}} \cdot \left(T_g - T_s\right) = 0$	(34)
		Solid	$\frac{1}{t_{cell}} \cdot \sum_g h \, B \left(T_g - T_s\right) - \frac{1}{t_{cell}} \cdot \left(\frac{\Delta H}{n_e \, F} + V\right) \cdot j_{cell} + \lambda_s \cdot \frac{\partial^2 T_s}{\partial x^2} = = \rho_s \, c_s \cdot \frac{\partial T_s}{\partial \tau}$	(35)
	Momentum	Gases	$\Delta p_{distr} = \frac{4f}{D_h} \cdot L_{cell}$	(36)
			$f = \frac{14.2}{Re}$	(37)
			$\Delta p_{conc} = \kappa \cdot \frac{\rho \, V^2}{2}$	(38)
			$\kappa = \Psi \cdot \left(1 - \frac{A_{sd}}{A_{ld}}\right) \quad \begin{cases} \Psi = 1.0 & \text{for the inlet} \\ \Psi = 0.5 & \text{for the outlet} \end{cases}$	(39)

The electric power generated by the SOFC is determined on the basis of the cell current i_{cell}, the real voltage V_{real} and the number of cells in the stack N_{cell}. Since the SOFC generates a direct current, it is also necessary to consider the efficiency of an inverter device (η_{inv}), as shown in Eq. (40).

$$P_{cell} = \eta_{inv} \cdot V_{real} \cdot i_{cell} \cdot N_{cell} \tag{40}$$

The system net power output P_{net} is determined subtracting the power consumed by the auxiliary systems from the P_{cell}. In this specific layout the only power

consumption is the one of the fuel compressor $P_{C,fuel}$, thus the P_{net} can be computed according to Eq. (41).

$$P_{net} = P_{cell} - P_{C,fuel} \tag{41}$$

Thus, the net efficiency η_{net} of the system is determined according to Eq. (42) as the ratio between the P_{net} and the chemical power provided by the fuel, computed as the product of the fuel mass flow $\dot{m}_{fuel}$ and its lower heating value LHV_{fuel}.

$$\eta_{net} = \frac{P_{net}}{\dot{m}_{fuel}\, LHV_{fuel}} \tag{42}$$

Matlab code used to simulate the SOFC, the functions used to initialize the code and to compute various physical properties, as well as the values of the parameters set in the model can be found in Appendix.

3.1.8 Model validation

Each component model was validated against real steady-state data in previous publications by other researchers of TPG [77,113,117,123–125], devoted on activities involving SOFCs and other plant components. These publications offer a detailed description of the setup used to collect experimental data and of the validation process. Validation of the whole system is not possible, because a real plant based on the layout presented in Section 2 has not been built yet. Up to the present day, due to the component costs and the technical challenges, only a few big companies had appropriate means to develop fully operational SOFC-MGT systems [126], and no SOFC - turbocharger prototypes are known from literature.

Reformer and SOFC modelling tools were validated mainly in [117] and [123]. In [117], these models were validated comparing simulations results against experimental data collected running a Staxera GmbH SOFC system. These data included measurements of temperature, flow rate, pressure drop and electrical

power. The calibration of the models was performed referring to the design operating conditions. To validate models, various operating points were considered. The validation of the SOFC was carried out comparing the values of voltage, current density and temperature on five different power output conditions. Comparing simulations and experimental data for different levels of current density (low, medium and high), it was possible to obtain a good agreement for the temperature distribution along the cell, with an average model error of ~1.4%. The error between experimental and simulated solid temperature was maximum at the end point of the cell, where the model error reached ~3.4% for high current density. This discrepancy was caused by the adiabatic hypothesis adopted in the model, while in the real system the temperature decreased due to heat dispersion at the cell borders. The reformer was validated comparing experimental and simulated compositions of the fuel at the outlet. An average error of about 10% was found in this case, which was considered reasonably good to confirm the assumption of equilibrium on the MSR and WGS reactions. Moreover, the concentration of hydrogen, which is the substance with the most significant effect on the system, was computed with a much higher precision (error around 2.5%).

The reliability verification of the other plant component models was carried out in the following works: [113] for the recuperator, [125] for the ejector and [77] for the turbocharger devices. In [113] the recuperator was part of an externally fired micro-gas turbine system and the model validation was based on experimental data collected running the system at different electric power loads. The validation of the whole model showed an error of the compressor mass flow around 2%, while the maximum deviation from the measured generated power was ~5%. In [125] an ejector based anodic test rig developed within the TPG was presented. Many tests were run on this rig using air or CO_2, at room temperature and at 150°C. The data collected during these tests were used to validate the ejector model based on pressure difference at the secondary and recirculation factor. The differences between the real values of pressure and the ones computed by the model are always low, with maximum error values of ~3%

during steady state operations. In [77] the turbocharger model was validated on data collected running two different turbochargers on a test rig. Regarding the values of pressure ratio and mass flow, the deviation of the simulation from the experimental data was always within the measurement uncertainty range (3-5%).

3.2 Definition of the control strategy

The model described in the previous section was used to simulate the behaviour of the plant in different operating conditions. The first set of simulations was carried out with the purpose of defining an effective strategy to control the valves and comply with the system operational constraints at different power loads. After achieving this result, it was possible to carry out a deeper analysis of the off-design performance of the turbocharged system, running simulations under different conditions of power load and ambient temperature.

The system design point was calculated at j_{cell} equal to 0.237 A/cm^2 and 15°C ambient temperature. This choice was based on previous studies on similar layouts [77,127,128]. Recalling that j_{cell} is defined as the ratio between i_{cell} and the fuel cell area A_{cell}, it is is clear from Eqs.(40) and (41) that its value directly impacts the SOFC power (P_{cell}) and the system net power (P_{net}). In the simulations performed to investigate the effects of different control strategies, a j_{cell} between 100% and 60% of the nominal value was considered. The ambient temperature was instead kept constant. The results obtained from this analysis are expected to be valuable in future works focused on a rigorous optimization of the design point.

The first strategy considered was based on the opening of the only wastegate valve (WGV). The system has many constraints that must be complied to guarantee its proper operation. The most critical one is on the SOFC maximum temperature, because, if this limit were exceeded, the cell could be permanently damaged. As reported in Table 1, this value should be between 850°C and 860°C.

Since a higher operational temperature has a beneficial effect on the SOFC performance, this analysis, assumed 860°C to be a desirable value. Opening the WGV, a more significant percentage of the SOFC exhausts is driven directly downstream of the turbine without expansion. In this way, when the exhaust gases enter the REC hot side, they are characterized by a higher temperature and therefore they transfer more thermal energy to the air flow. Since the cathode flow is the main contributor to the SOFC temperature control, heating it is an effective way of raising the cell temperature. The fraction of mass flow $\dot{m}_{f,WGV}$ bypassed through the WGV, which is shown in , is determined in order to reach 860°C as maximum temperature of the SOFC.

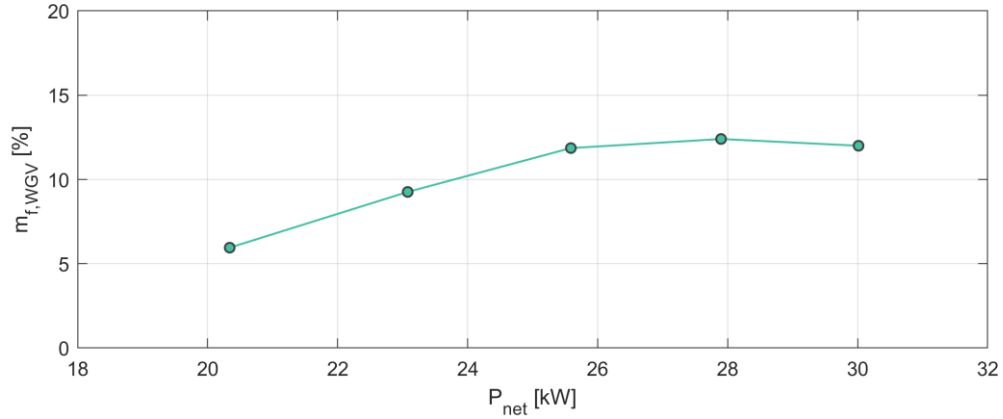

Figure 16. *Fraction of mass flow bypassed through the WGV, using the WGV control strategy.*

However, as shown in Figure 17, the higher values of turbine outlet temperature, caused by the WGV opening, were higher than the temperature limit of 650°C for the REC.

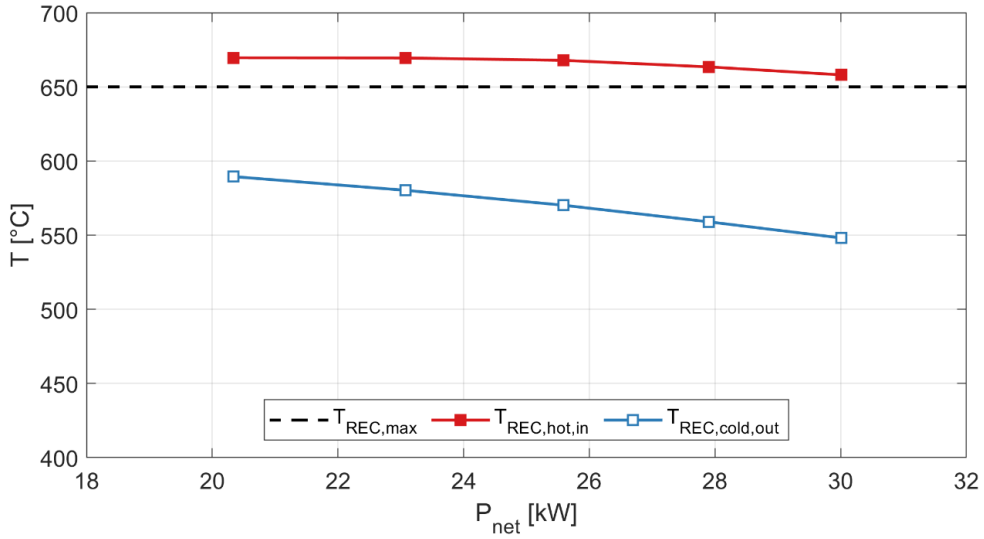

Figure 17. *REC maximum temperatures at the hot and cold side, using the WGV control strategy.*

As stated in Sections 2.2 and 2.5, this limit was dictated by the choice of installing a stainless steel standard heat exchanger in the SOFC system, in order to reduce the plant capital cost. Since cost reduction is considered crucial in this study, the control strategy based on the WGV was determined to be unsuitable.

The second strategy considered is based on the opening of the only cold bypass valve (CBV). Opening the CBV, a higher percentage of the compressed air flow is driven directly upstream of the turbine, bypassing completely the SOFC system. This procedure has two effects: reducing the cold mass flow entering the REC and cooling down the turbine inlet flow (and, consequently, the outlet flow). From the simulations, it can be observed that, even if both flows entering REC are subject to a temperature decrease when the CBV is opened, the air mass flow of the REC is reduced. Consequently, the air flow has a lower heat capacity rate ($\dot{m} \cdot c_p$), and its temperature at the outlet is higher. For this reason, the SOFC temperature can be effectively controlled acting on the CBV opening. Moreover, because of the turbine outlet temperature decrease, this procedure is beneficial in terms of thermal stress on the REC. Figure 18 shows how the mass flow bypassed through the CBV changes at various power loads. Figure 19 shows

that, controlling the mass flow through the CBV, the REC maximum temperature never exceeded the 650°C limit at part load conditions.

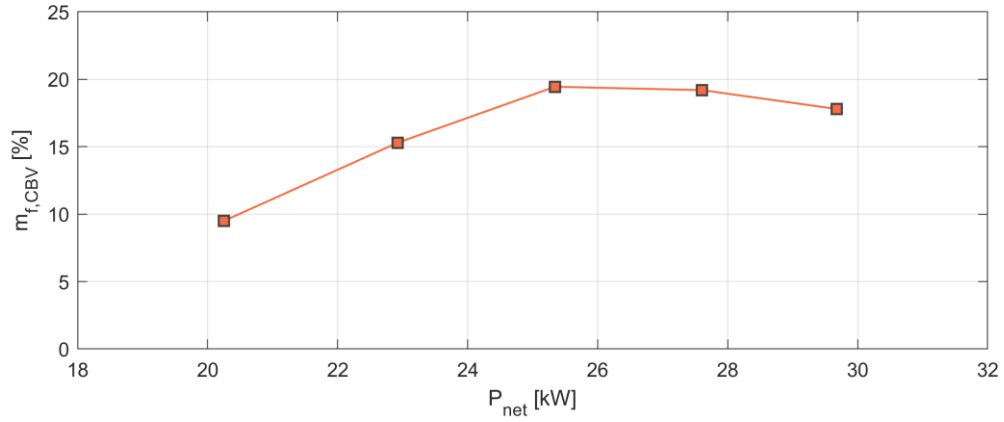

Figure 18. *Fraction of mass flow bypassed through the CBV, using the CBV control strategy.*

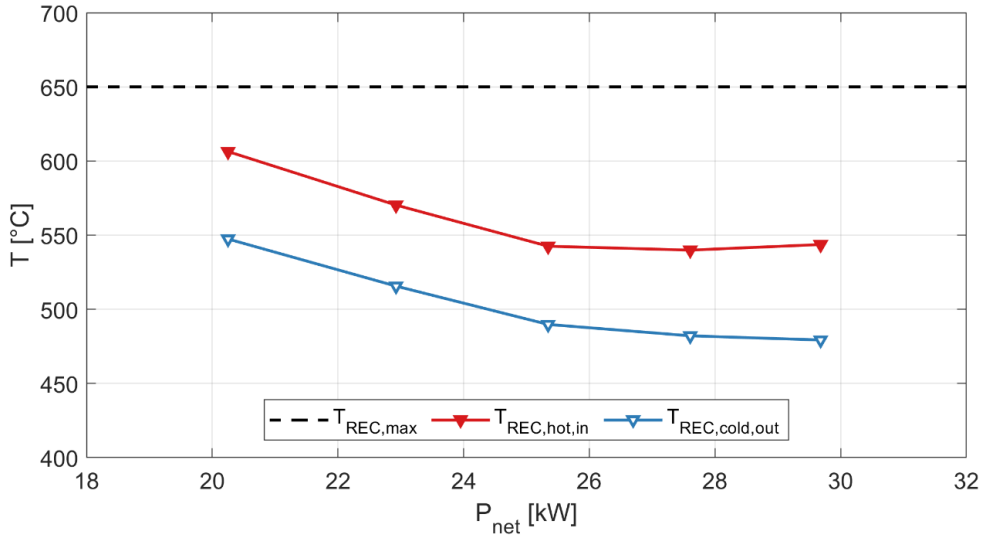

Figure 19. *REC maximum temperatures at the hot and cold side, using the CBV control strategy.*

The comparison between the impact of the WGV and the CBV control strategies on the performance of the system (Figure 20) shows that the latter generated a net efficiency (η_{net}) reduction. In fact, using the CBV control strategy, the cathode air flow entering the SOFC has a lower temperature, negatively

affecting the fuel cell performance. With the purpose of optimizing the system efficiency, a third control strategy was proposed, acting at the same time on WGV and CBV to comply with the SOFC and the REC maximum temperature constraints, without unnecessary reductions in efficiency.

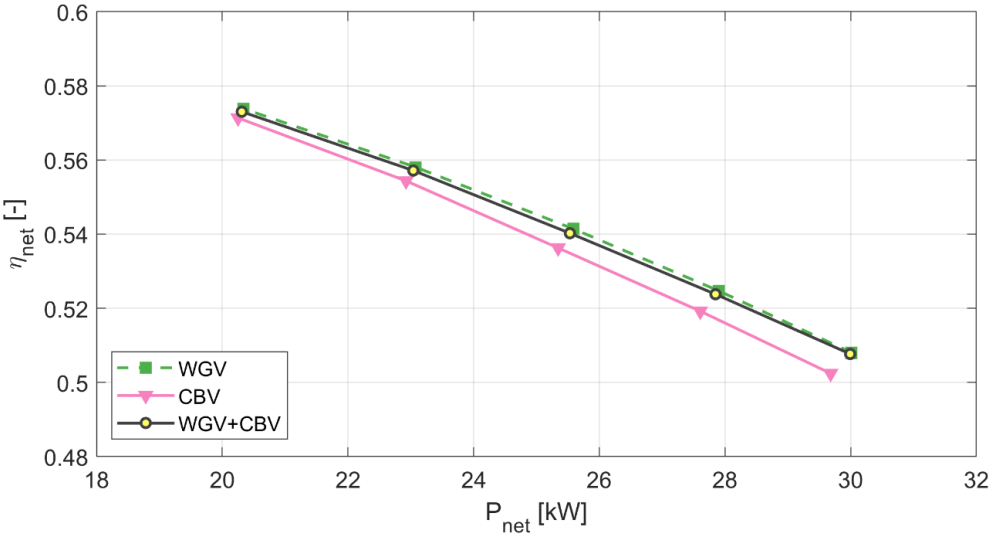

Figure 20. *Efficiency-load plot for different control strategies (WGV, CBV, WGV+CBV).*

The mass flow to be bypassed through the valves (shown in Figure 21) is determined in order to have a SOFC maximum temperature equal to 860°C and a REC maximum temperature as close as possible to 650°C. In Figure 22, it is possible to observe the values of maximum temperature in REC and SOFC for this set of simulations, and to verify that the maximum temperature limit was never exceeded. Figure 20 shows that, controlling simultaneously the WGV and the CBV, the efficiency trend of the system deviated only minimally from the one obtained controlling only the WGV.

Being able to comply with all the operational constraints without significant sacrifices in terms of performance, the control strategy based on WGV and CBV is considered for the off-design analysis of this turbocharged SOFC system.

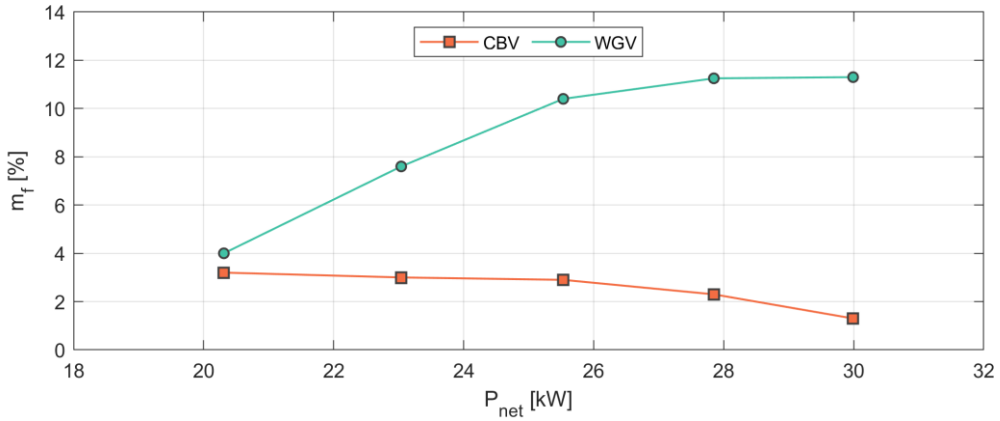

Figure 21. *Fraction of mass flow bypassed through the CBV and WGV, using the WGV+CBV control strategy.*

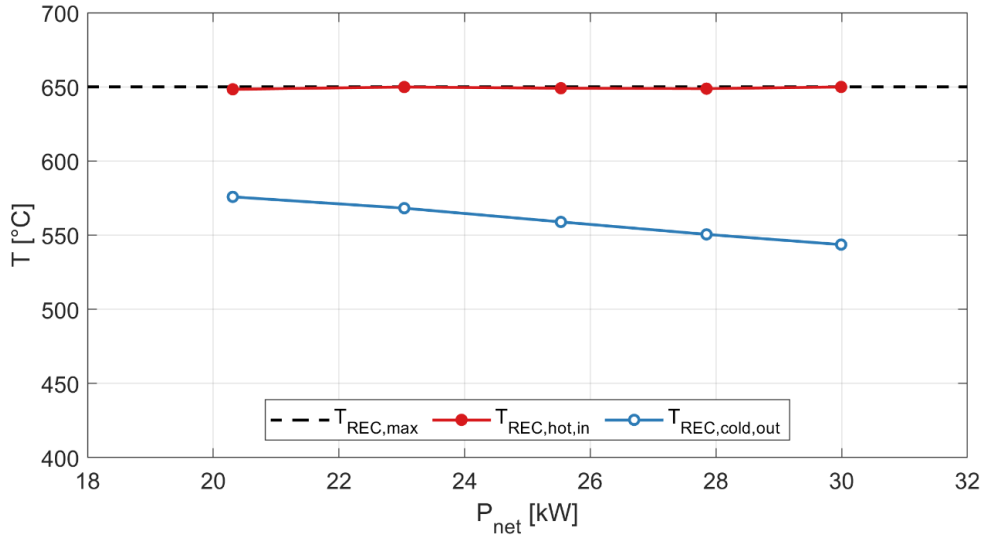

Figure 22. *REC maximum temperatures at the hot and cold side, using the WGV+CBV control strategy.*

3.3 Performance analysis

A set of 25 simulations was performed, considering different combinations of current density (j_{cell}) and ambient temperature (T_{amb}) conditions. During this analysis, the SOFC density current, which impacts directly on P_{cell} and P_{net}, was

changed between the 100% and the 60% of its nominal value. The considered ambient temperatures were 0°C, 10°C, 15°C (design value), 20°C and 30°C.

In design conditions, the system generated a P_{net} equal to 29.99 kW with a net efficiency of 50.77%. The nominal value of j_{cell} was set as 0.237 A/cm^2 and the U_f [120], which was not altered for the entire set of simulations, was equal to 0.8.

Figure 23 shows the P_{net} and the η_{net} of the system versus different ambient temperatures (the trends shown in this diagram will be discussed in more detail later). For all the considered operative points, the system requirements were always respected. More specifically, the results show that it is possible to comply with all the SOFC limits reported in Table 1, while never exceeding the REC maximum temperature 650°C, as shown in Figure 24.

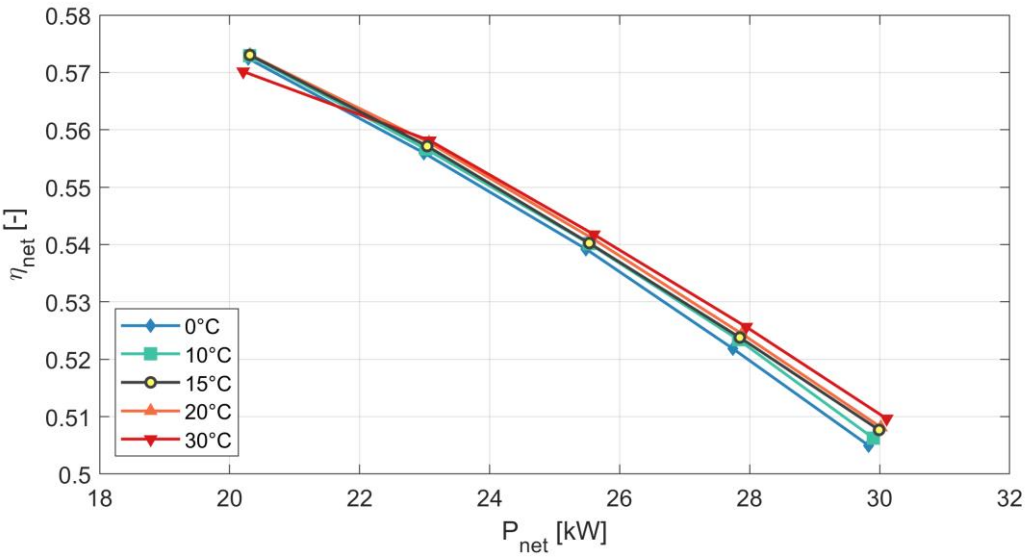

Figure 23. *Efficiency-load curves for different ambient temperature values, using the WGV+CBV control strategy.*

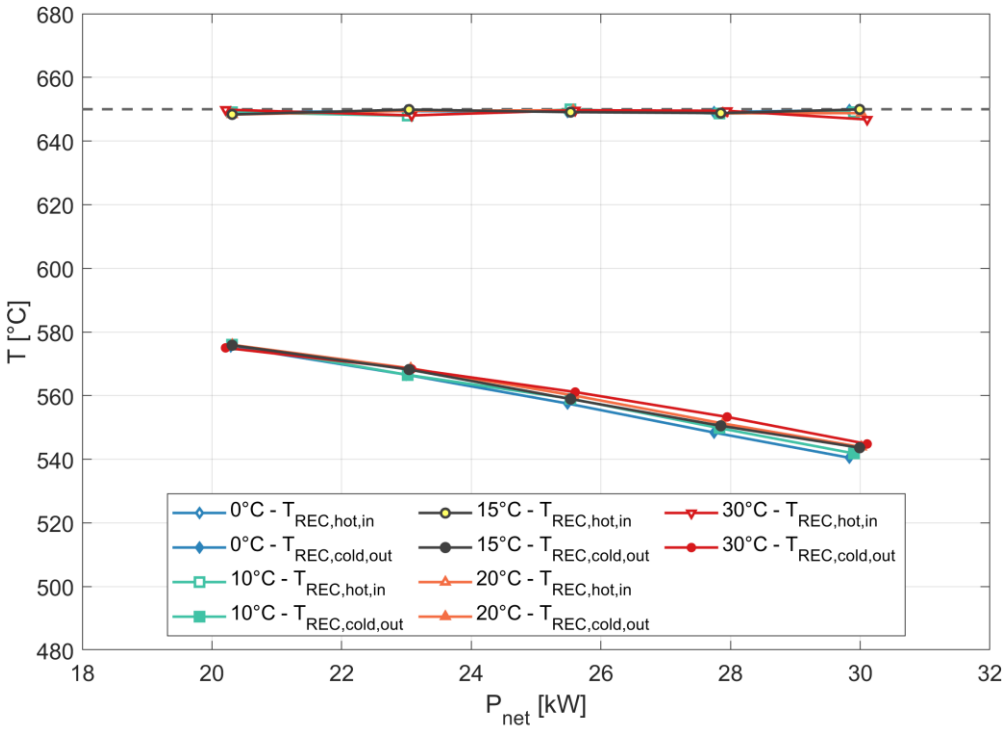

Figure 24. *REC maximum temperatures at the hot and cold side for different ambient temperature values, using the WGV+CBV control strategy.*

3.3.1 Off-design analysis in part-load conditions

To understand how part-load operations affect the system behaviour, the following part of the study focused mainly on the simulations performed at 15°C of ambient temperature (nominal value). Starting from the design point, five different conditions were simulated imposing values of j_{cell} between the nominal value (0.237 A/cm²) and 60% of the nominal value. The results of this set of off-design simulations are reported in Table 7. From the plots shown in this Section, it is easy to extend the observations regarding the system behaviour at 15°C to other values of the ambient temperature. As explained in Section 3.2, the CBV and WGV valves were controlled in order to keep the SOFC temperature at 860°C and the REC maximum temperature as close as possible to 650°C.

Lowering the current density, the power generated by the fuel cell decreases (Table 7), thus the total net power of the plant drops. Since the internal losses

are smaller, the fuel cell efficiency is higher at lower values of current density (in accordance with the Staxera GmbH system specifications [86] and typical fuel cells behaviour [37,87,88]). On the other hand, when the fuel cell power drops, the amount of energy available for the turbocharger is lower and the shaft rotational speed decreases. Therefore, the compression ratio is lower and, consequently, also the SOFC pressure. Even if a lower pressure negatively affects the SOFC performance [45], the beneficial effect of the ohmic losses reduction has a stronger impact than the lack of pressurization. Because of these reasons, and also for the reduction of the power absorbed by the auxiliary (Table 7), the net global efficiency is higher at part-load (Figure 23). At part-load conditions, the auxiliary power decreases because the fuel mass flow to be compressed is smaller, but also because the system pressure, and thus the required pressure ratio, is lower. It can be observed that, in all the operating points reported in Table 7, the constraints of the system are always respected. At 60% of the nominal current density, η_{net} reaches the remarkable value of 57.3% (+6.5% in absolute value over the design efficiency). However, this result does not lead to the conclusion that such a system should always operate at low current density. As reported in [129], operating SOFCs at maximum efficiency can make these systems not economically viable. In fact, this solution would require a large size SOFC, with a high capital cost, to work at minimum load to achieve high efficiencies. In this setup, the SOFC would generate a low electrical power, limiting the financial incomes of the plant.

At part load, the compressor air mass flow $\dot{m}_{air}$ and pressure ratio β decrease, as shown in Table 7, moving the compressor operational point closer to the surge line. Despite this fact, the values of K_p shown in Table 7, which are always significantly higher than 1.1, guarantee the correct operation of the compressor.

At lower values of j_{cell}, the fuel mass flow is smaller, because the fuel utilization factor U_f is constant. In details, it should be noted that, according to Eq. (19), given the composition of the fuel and the number of fuel cells, U_f determines the dependency between j_{cell} and $\dot{n}_{fuel}$.

Table 7. *Results of the part-load off-design simulations.*

Parameter	Symbol	Unit	$j_{cell}/j_{cell,design}$				
			100%	**90%**	**80%**	**70%**	**60%**
Fuel cell current density	j_{cell}	A/cm²	0.237	0.213	0.190	0.166	0.142
Nernst voltage	V_{Nernst}	mV	924	920	916	910	904
Fuel cell real voltage	V_{real}	mV	712	731	752	772	791
System net power	P_{net}	kW	29.99	27.85	25.53	23.04	20.31
Auxiliary systems power	P_{aux}	kW	1.06	0.87	0.70	0.54	0.40
System net efficiency	η_{net}	%	50.8	52.4	54.0	55.7	57.3
SOFC max temperature	$T_{cell,max}$	°C	860	860	860	860	860
SOFC inlet T difference (anode-cathode)	$\Delta T_{an\text{-}ca,in}$	°C	121	105	86	61	30
SOFC anode T difference (inlet-outlet)	ΔT_{an}	°C	103	106	111	117	127
SOFC cathode T difference (inlet-outlet)	ΔT_{ca}	°C	223	210	195	178	158
SOFC anode inlet p	$p_{an,in}$	bar	2.83	2.58	2.34	2.14	1.93
SOFC cathode inlet p	$p_{ca,in}$	bar	2.84	2.59	2.36	2.15	1.94
Fuel mass flow rate	$\dot{m}_{fuel}$	g/s	4.42	3.98	3.53	3.09	2.65
Inlet reformer steam to carbon ratio	S/C	-	2.40	2.36	2.30	2.24	2.15
Anode inlet molar %CH_4	$X_{CH4,an,in}$	%	0.06	0.06	0.06	0.07	0.08
OGB outlet molar %H_2	$X_{H2,OGB,out}$	%	0.00	0.00	0.00	0.00	0.00
OGB outlet molar %CH_4	$X_{CH4,OGB,out}$	%	0.00	0.00	0.00	0.00	0.00
OGB outlet molar %CO	$X_{CO,OGB,out}$	%	0.00	0.00	0.00	0.00	0.00
Recirculation Ratio	RR	-	7.26	6.92	6.53	6.08	5.53
Turbocharger rotational speed	ω	krpm	264	249	233	218	198
Compressor surge margin	K_p	-	1.75	1.76	1.71	1.61	1.53
Compressor mass flow rate	$\dot{m}_{air}$	g/s	72.7	65.1	57.4	49.1	40.8
Compressor pressure ratio	β	-	2.84	2.59	2.36	2.15	1.94
Compressor efficiency	η_C	%	72.2	72.4	72.6	72.1	71.4
Turbine efficiency	η_T	%	60.4	60.3	59.7	58.5	57.3

Parameter	Symbol	Unit	$j_{cell}/j_{cell,design}$				
			100%	90%	80%	70%	60%
Turbine inlet temperature	$T_{T,in}$	°C	762	749	738	729	716
Turbine outlet temperature	$T_{T,out}$	°C	636	636	638	643	646
WGV mass flow fraction	$\dot{m}_{f,WGV}$	%	11.3	11.3	10.4	3.0	3.2
CBV mass flow fraction	$\dot{m}_{f,CBV}$	%	1.3	2.3	2.9	7.6	4.0

Moreover, since the system pressure decreases, the ejector recirculation ratio RR decreases as well (Figure 25), and the recirculated steam flow is smaller. Among these two different effects, the steam recirculation reduction is more significant, and the steam to carbon ratio S/C at the reformer inlet decreases at part loads, as shown in Figure 26. However, even at 60% of the nominal j_{cell}, the value of the S/C is considerably higher than the limit of 1.8 reported in [89], ensuring the correct operation of the system. Referring to the design ambient temperature case, the CH_4 mass fraction is higher for lower values of j_{cell}, but since its values are always very low (Table 7), the fuel cell internal reforming is not significant and SOFC carbon deposition is prevented.

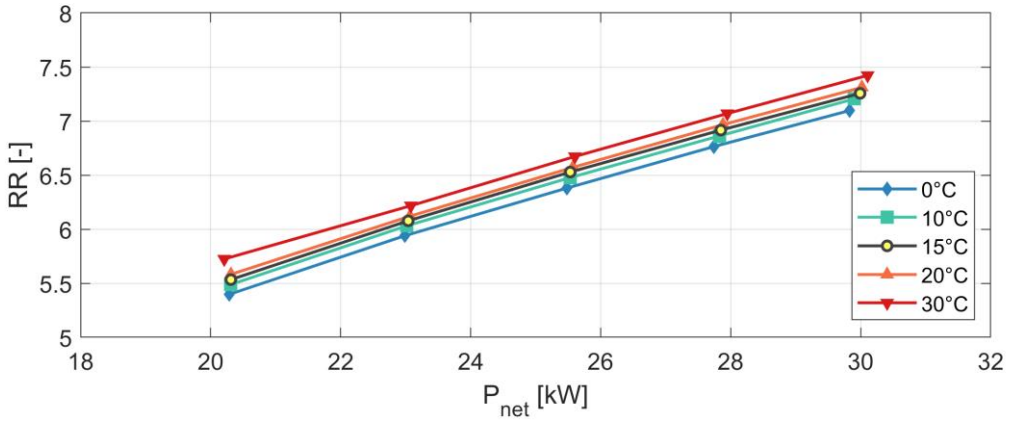

Figure 25. *Recirculation ratio of the anode ejector in off-design conditions.*

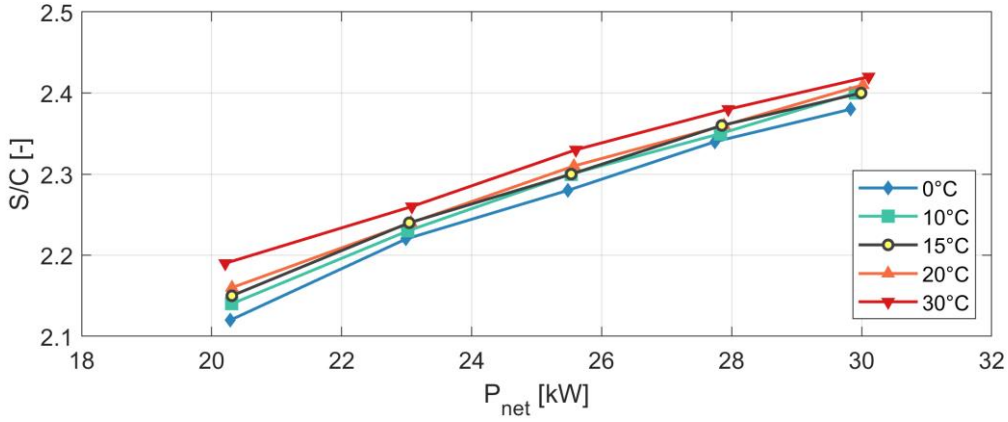

Figure 26. *Steam to carbon ratio at the reformer anode side inlet in off-design conditions. Values higher than 1.8 guarantee the correct operation of the system* [89].

3.3.2 Off-design analysis at different ambient temperatures

Running the simulations at part-load for different values of the ambient temperature is crucial to understanding the influence of this parameter on the system behaviour. In Table 8 it is possible to observe this effect for temperatures between 0°C and 30°C, in a full load condition.

Table 8. *Results of the design simulations for different ambient temperatures.*

Parameter	**Symbol**	**Unit**	**Ambient Temperature [°C]**				
			0	**10**	**15**	**20**	**30**
Fuel cell current density	j_{cell}	A/cm²	0.237	0.237	0.237	0.237	0.237
Nernst voltage	V_{Nernst}	mV	924	925	924	925	925
Fuel cell real voltage	V_{real}	mV	708	709	712	712	714
System net power	P_{net}	kW	29.83	29.90	29.99	30.02	30.11
Auxiliary systems power	P_{aux}	kW	1.05	1.05	1.06	1.06	1.06
System net efficiency	η_{net}	%	50.5	50.6	50.8	50.8	51.0
SOFC max temperature	$T_{cell,max}$	°C	860	860	860	860	860
SOFC inlet T difference (anode-cathode)	$\Delta T_{an\text{-}ca,in}$	°C	122	122	121	121	121
SOFC anode T difference (inlet-outlet)	ΔT_{an}	°C	105	104	103	103	102

Parameter	Symbol	Unit	Ambient Temperature [°C]				
			0	10	15	20	30
SOFC cathode T difference (inlet-outlet)	ΔT_{ca}	°C	225	224	223	222	221
SOFC anode inlet p	$p_{an,in}$	bar	2.73	2.79	2.83	2.86	2.94
SOFC cathode inlet p	$p_{ca,in}$	bar	2.73	2.79	2.84	2.88	2.94
Fuel mass flow rate	$\dot{m}_{fuel}$	g/s	4.42	4.42	4.42	4.42	4.42
Inlet REF steam to carbon ratio	S/C	-	2.38	2.39	2.40	2.41	2.42
SOFC anode inlet molar %CH_4	$X_{CH4,an,in}$	%	0.06	0.06	0.06	0.06	0.06
OGB outlet molar %H_2	$X_{H2,OGB,out}$	%	0.00	0.00	0.00	0.00	0.00
OGB outlet molar %CH_4	$X_{CH4,OGB,out}$	%	0.00	0.00	0.00	0.00	0.00
OGB outlet molar %CO	$X_{CO,OGB,out}$	%	0.00	0.00	0.00	0.00	0.00
Recirculation Ratio	RR	-	7.10	7.21	7.26	7.31	7.42
Turbocharger rotational speed	ω	krpm	253	260	264	268	276
Compressor surge margin	K_p	-	1.79	1.76	1.75	1.73	1.69
Compressor mass flow rate	$\dot{m}_{air}$	g/s	73.9	73.2	72.7	72.4	71.6
Compressor pressure ratio	β	-	2.74	2.81	2.84	2.88	2.95
Compressor efficiency	η_C	%	72.4	72.3	72.2	72.1	71.9
Turbine efficiency	η_T	%	61.1	60.7	60.4	60.2	59.6
Turbine inlet temperature	$T_{T,in}$	°C	751	757	762	764	770
Turbine outlet temperature	$T_{T,out}$	°C	630	632	636	636	639
Mass flow fraction through the WGV	$\dot{m}_{f,WGV}$	%	5.8	9.6	11.3	13.0	16.1
Mass flow fraction through the CBV	$\dot{m}_{f,CBV}$	%	0.0	0.9	1.3	1.9	2.8

Table 8 shows that at full load it is always possible to keep the SOFC maximum temperature at 860°C while complying with all the other system constraints. However, this compliance is not possible at 60% of the nominal value of j_{cell} and for T_{amb} = 30°C. In this case, due to higher temperatures in the whole system, the REC maximum temperature would exceed the 650°C limit if the SOFC maximum temperature were 860°C. To prevent this excess, the values of $\dot{m}_{f,WGV}$ and $\dot{m}_{f,CBV}$ are set to 0% and 1.1%, respectively, in order to have a SOFC maximum temperature equal to 851°C, which is still acceptable according to the

specifications in Table 1. The drawback of this solution is that, operating at a lower temperature (Figure 27), the SOFC is less efficient. Figure 23 shows that the leftmost point deviates from the trend of the 30°C curve because of this effect. From these results it is possible to deduce that some issues may arise running the system at higher ambient temperatures or lower loads and that specific countermeasures should be taken in that case. From Figure 24, it can be observed that, even if the $T_{T,out}$ increases with the ambient temperature, as shown in Table 8, the temperature at the hot side of the REC has minimum variations, which could be further reduced increasing the accuracy adopted to determine the valves openings.

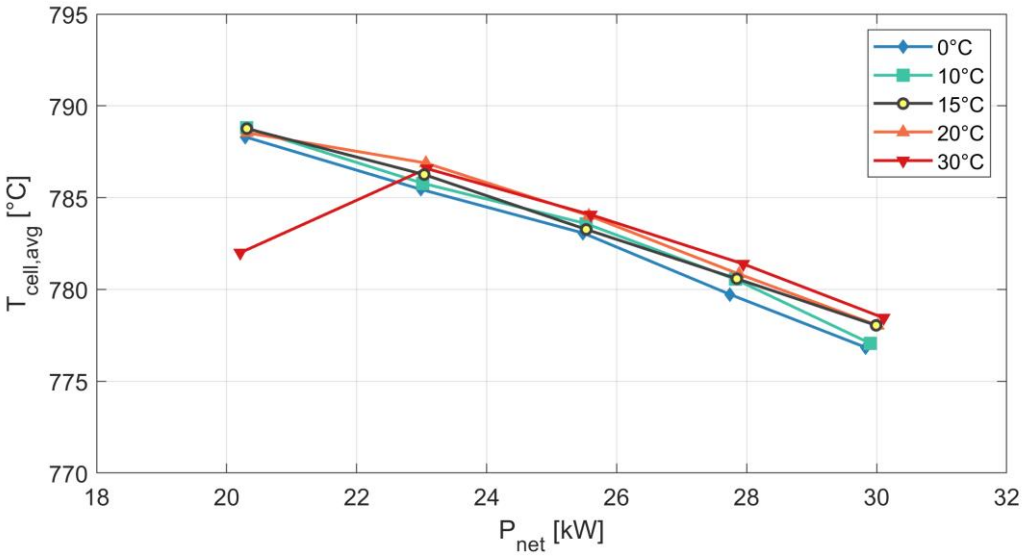

Figure 27. *Average temperature of the SOFC stack in off-design conditions.*

When the ambient temperature is higher, the $T_{T,in}$ is also higher, and more mechanical power can be obtained by the gas expansion in the turbine. This positive effect is prevalent on the fact that, working on lower density air, the compressor needs more mechanical power to achieve the same pressurization. Thus, the turbocharger rotational speed increases, and the compressor β and mass flow increase as well, as shown in Table 8. The consequential pressure and temperature increase in the SOFC (Figure 27 and Figure 28), has a beneficial effect on its performance [45], which causes the net efficiency increase shown in

Figure 23. The increase of mass flow and β in the compressor drives the operating point closer to the surge line, however Table 8 shows that it is always in a safe condition.

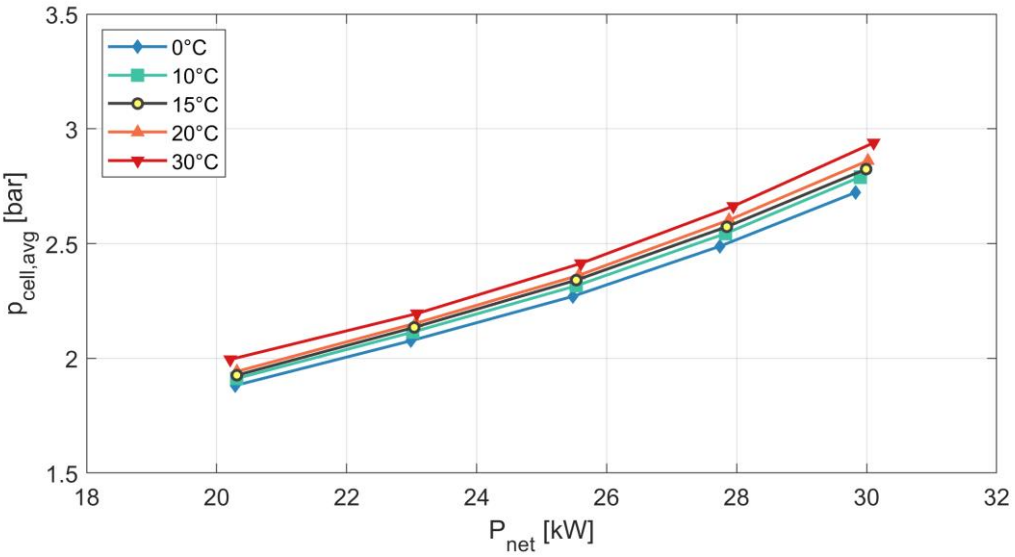

Figure 28. *Average pressure of the SOFC stack in off-design conditions.*

Figure 25 shows that the recirculation ratio RR follows the trend of the compressor pressure ratio (Table 8): when the cathode pressure increases at higher ambient temperature, the ejector primary pressure also increases to equalize the anode and cathode pressures. Therefore, more exhaust is recirculated from the SOFC outlet, producing an increase of S/C at the reformer inlet, as shown in Figure 26. It is worth noticing that, even for the lowest value of ambient temperature, the S/C is always above the limit of 1.8 reported in [89], guaranteeing the correct operation of the system. The percentage of CH_4 at the SOFC inlet is always very low, independently from the ambient temperature, as shown in Table 8. Therefore, carbon deposition inside the SOFC is prevented.

3.4 Concluding remarks

The off-design performance analysis of the turbocharged SOFC system was performed during the research activity presented in this chapter. A steady state model was created in Matlab-Simulink to simulate the system in different operating conditions. The novelty of this study is both related to the adoption of a turbocharger for the fuel cell pressurization, which was rarely considered in literature, and to the simultaneous variation of power load and ambient temperature, which is unprecedented even for MGT based layouts. The on-design simulation (j_{cell} = 100% of its nominal value, T_{amb} = 15°C) shows an interesting net efficiency value, equal to 50.8%, thanks to the pressurization. The performance of the system was analysed at values of the j_{cell} between 100% and 60% of its nominal value, varying the ambient temperature between 0°C and 30°C. Compliance with the operative constraints in off-design condition is effectively guaranteed by controlling the mass flows bypassed through WGV and CBV, which affects the temperatures in the SOFC and the REC. The main results obtained in this study are summarized in the following points.

- A control strategy based on the only WGV is not able to keep the REC temperatures under 650°C, even if the SOFC maximum temperature target is matched. Using the CBV both components can operate properly, but the system efficiency is affected negatively. Acting at the same time on WGV and CBV, it is possible to comply with all the constraints without significant reductions in the efficiency.
- With the WGV+CBV strategy it is possible to run the system properly in all the considered conditions. However, at 60% of the nominal j_{cell} and T_{amb} equal to 30°C, it is necessary to lower the SOFC temperature to avoid overheating in the REC. This affects negatively the system efficiency and, based on these observations, it may be necessary to define some additional strategy to run the system properly with a lower j_{cell} or a higher T_{amb}.

- Decreasing the cell current density, and thus the power load, the system net efficiency increases because of the ohmic losses reduction in the SOFC. For T_{amb} = 15°C, decreasing the j_{cell} from 100% to 60% of its nominal value causes η_{net} *to* grow from 50.8% to 57.3%.
- When the ambient temperature is higher, the $T_{T,in}$ is also higher and more mechanical power can be obtained by the gas expansion in the turbine. Providing more power to the compressor, the SOFC pressure raises, with a beneficial effect on the efficiency. At full load, increasing the T_{amb} from 0°C to 30°C causes η_{net} to grow from 50.5% to 51.0%.
- When the fuel cell power is lower, there is less energy available for the turbocharger and the shaft rotational speed decreases. Therefore, the compressor air mass flow decreases, and its operational points move closer to the surge line. This effect is enhanced by a higher ambient temperature because of the consequential pressure ratio increase. The analysis showed that, even for minimum load and the highest T_{amb}, the compressor is always working safely: in this case the value of K_p is equal to 1.52, way over the 1.1 value that was assumed in this study to be the safe operation threshold.
- At lower loads, the system pressure is lower, and the fuel mass flow is lower. Consequently, the ejector recirculates less steam at the REF anode inlet, and the S/C decreases. The pressure ratio reduction caused by a lower ambient temperature enhances this effect. However, according to the simulations, the values of S/C at the REF inlet and the fraction of CH_4 at the SOFC inlet always ensure proper operation of the system, even for minimum load and the lowest T_{amb}.

In conclusion, the analysis presented in this chapter shows that a turbocharged SOFC system can operate effectively in a wide range of power loads and ambient conditions, and that all the operative constraints can be respected by just acting on two valves, the WGV and the CBV. The global efficiency of the system is always between 50% and 58%, an impressive result considering the use of 50%

CH_4 - 50% CO_2 biogas, a renewable energy source with a low environmental impact.

These promising results can be a motivation for researchers, both in academia and industry, to investigate more deeply the potential of innovative turbocharged SOFC systems. Due to the lack of pre-existing literature currently, this topic offers many novel research opportunities, such as dynamic analysis, control system development and, eventually, experimental activities.

In the next chapter, the outcomes of this study will be used as starting point to analyse and improve the fuel flexibility of the turbocharged SOFC system. Then, the outcomes of this study will be used as starting point to study the dynamic behaviour of the plant and to design and test an effective control system.

4 Dynamics and control of turbocharged SOFC system

Many analyses regarding the control of pressurized SOFC systems have been presented over the past few decades. An insightful literature review on this topic is shown in [53], with various different control strategies that were considered by the research community: proportional-integral (PI), proportional-integral-derivative (PID), feed-forward (FF), model predictive controls (MPC), etc. The same analysis also highlighted that such controllers mostly act on turbomachinery rotational speed and bypass valves to ensure the proper operation of the SOFC-MGT system. In [63] the authors created a dynamic model of an SOFC-MGT system, and used it to test a multi-loop feedback control scheme under load changes. The effect of a cold-bypass valve on the performance of a SOFC-MGT cyber-physical emulator plant was investigated in [62] and the data collected were used to generate transfer functions of the system components, which can be used to develop a robust control system. In [130] a 6 loops control system based on PIDs was designed and tested on an SOFC-MGT system, in order to comply with its operational limits regarding temperatures, steam to carbon ratio, thermal stress and compressor surge margin.

In contrast with the many works regarding control of SOFC-MGT systems, the available literature addressing the control of turbocharged systems is very scarce. An MPC controller for an SOFC system integrated with a turbocharger was presented in [131]. However, in the layout considered for this study, the turbocharger is linked to a generator and thus the rotational speed can be easily controlled. Widening the attention on applications that are different from stationary power generation, a control system for an automotive turbocharged SOFC-internal combustion engine was presented in [132]. The technical challenges related to the absence of the electric generator have not been addressed by the research community yet, and a detailed procedure for the controller design is also missing from literature.

The goal of the study described in this chapter is to fill the literature gap on turbocharged SOFC system dynamics, and to present a control system design procedure. A dynamic model of a turbocharged SOFC system fed by biogas is created by the authors in Matlab®-Simulink® using TRANSEO, an original tool developed at TPG [114]. Such model is used to characterize dynamically the turbocharged SOFC system and to determine the physical quantities that should be monitored by the controller to have a fast response. Four different control systems are designed, tuned and tested on two different scenarios. Their performance is evaluated based on deviation from the SOFC temperature target, settling time, and compliance with the plant operative constraints.

This study was published in the article "Dynamics and control of a turbocharged solid oxide fuel cell system" on the journal Applied Thermal Engineering [133].

4.1 TRANSEO tool and dynamic model

To simulate the turbocharged SOFC system, analyse its transient behaviour and test control systems, a dynamic model was created using TRANSEO, an original tool developed by the Thermochemical Power Group (TPG) for the dynamic and transient performance of energy systems [114]. The tool exploits the Matlab®-Simulink® environment for the time management and the visual interface, but chemical compositions, thermodynamic and physical properties of the flows and components performance are determined by Fortran and C codes, both linked to Matlab®-Simulink® via C MEX functions.

TRANSEO was originally created to simulate microturbine-based systems, but, thanks to its modularity and flexibility, its application can be easily extended to many different kinds of advanced energy systems, including pressurized fuel cell systems. The dynamic behaviour of energy systems is mainly related to the mass and energy balances, while effects related to the momentum balance, such as pressure wave propagation, are normally neglected. Few TRANSEO components (i.e. pipe and ejector) can be set to simulate the complete dynamics,

however this option is very time consuming and it is not adopted in the present model, which simulates the transient behaviour of the components with a lumped-volume approach.

This section reports details and references about the dynamic model developed in TRANSEO tool of the turbocharged SOFC hybrid system, including the approach for lumped-volume representation, which proved to be particularly effective and efficient for energy system simulation. Here it is worthwhile to remark that single plant components in TRANSEO were validated against experimental and/or literature data in previous works carried out by other researchers working at TPG.

In this thesis the model of the whole plant was created, and the simulation workflow of the model was defined. This process is particularly critical, and it regards determining the setup of each component (i.e. active, inactive-forward or inactive-backwards, that will be explained in Section 4.1.2) necessary to determine correctly the physical properties of the working fluid in each point of the system. It was also necessary to calibrate the characteristic parameters to align the dynamic model with the steady-state one and match the turbocharged SOFC system specifications.

4.1.1 Lumped-volume models

A lumped-volume model is made up of two elements: an actuator disk, simulating the off-design performance of the component, and a duct, characterized by equivalent length and cross section area to take into account the fluid dynamic delay. The actuator disk reacts to component inlet and duct conditions, the duct delays its output on the basis of its geometrical properties. The duct transient behaviour is based on Eqs. (43) - (45).

$$\frac{d\dot{m}}{d\tau} = \frac{A_{duct}}{L_{duct}} \left(C - \left(p_3 - p_{1,tot}\right) - \dot{m}\left(w_3 - w_1\right)\right) \tag{43}$$

$$\frac{d(c_v\,\rho_{avg}\,\Lambda\,T_{tot})}{d\tau} = \dot{m}\left(H_{2,tot} - H_{3,tot}\right) - \dot{q}_s \tag{44}$$

$$\frac{d(c_{p,s}\,M_s\,T_s)}{d\tau} = \dot{q}_s - \dot{q}_{loss} \tag{45}$$

The meaning of the symbols used in the equations is shown in the Nomenclature section. The subscript *avg* means average, while *tot* refers to total physical quantities and *s* to the material constituting the pipe. The subscripts *1*, *2* and *3* refer to different sections of the component, as shown in Figure 29: 1 is the component inlet, 2 is the actuator disk outlet and duct inlet, 3 is the component outlet.

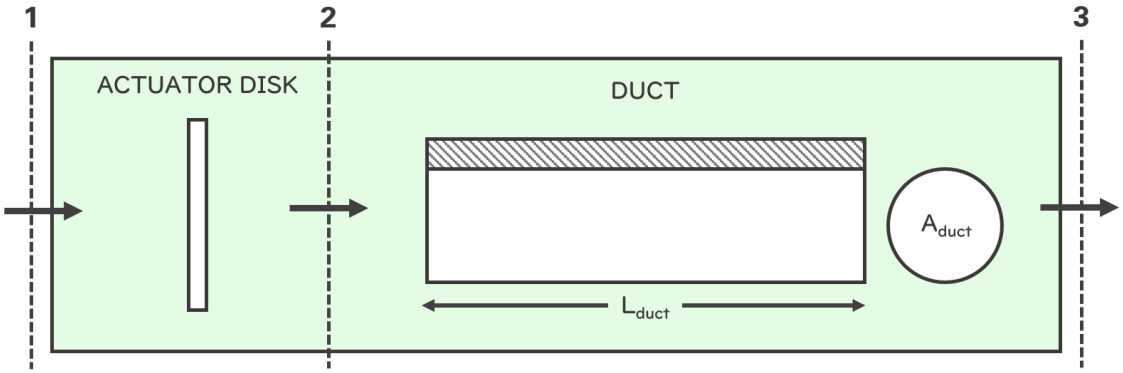

Figure 29. *Structure of a standard TRANSEO component based on the lumped volume approach (1: component input = actuator disk input, 2: actuator disk output = duct input, 3: duct output = component output)*

The duct is not discretized spatially, meaning that its equations are integrated over time, but not along its length. The mass flow is considered uniform along the duct and subject to the overall momentum equation (Eq. (7)).

4.1.2 Flow properties and component settings

The physical properties of a TRANSEO model are defined by mass flow, pressure, temperature and chemical composition, which can be expressed as

mass or molar fractions. Each component performs calculations on the basis of these properties, but it can be set in different ways:

- If a component is set as “mass flow active”, it computes the mass flow based on the pressures upstream and downstream of it.
- If a component is set as “mass flow inactive-forward”, it sets the mass flow downstream equal to the one upstream, and computes the pressure upstream based on the one downstream and the mass flow.
- If a component is set as “mass flow inactive-backward”, it sets the mass flow upstream equal to the one downstream, and computes the pressure downstream based on the one upstream and the mass flow.

Since all components are interconnected, the wrong setting of a single component can compromise the computation of pressures and mass flows in the whole plant model.

For all the components, temperatures and compositions at the outlet are always computed as a function of the inlet flow physical properties. Pressure losses between inlet and outlet are determined based on the current flow properties and a reference condition set by the user.

4.1.3 Heat exchanger

A 1D counter-flow heat exchanger model, which can be set as a primary surface or plate-fin heat exchanger, is used to simulate both REC and APH. However, as mentioned in Chapter 2, the APH actually represents an internal heat exchange, while the REC is a real primary surface heat exchanger. Considering that the fuel mass flow is significantly lower than the ejector secondary flow, small fluctuations of its temperature would have a negligible effect on system performance. For this reason, a model of the FPH is not included, but its effect is approximated setting directly the fuel temperature equal to 250 K, with the aim of reducing the model computational time. This value was derived from the steady-state simulations of the turbocharged SOFC system presented in

Chapter 3. The transient heat exchanger model was first presented in [134] and it considers four different sections of the component: the two channels where the hot and the cold fluids flow, the solid internal structure and the external solid shell (Figure 30). The model is based on a partial difference numerical scheme for the solution of the energy equation (Eq. (46)).

$$\rho_{j,i}\, c_{v_j} A_j \frac{\partial T_{j,i}}{\partial \tau} = - c_{p_j} \dot{m}_j \frac{\partial T_{j,i}}{\partial x} + \dot{q}_{j,i} \tag{46}$$

Where c_p is the specific heat at constant pressure, the subscript j refers to the four different sections (hot, cold, solid, shell) and the subscript i refers to the i-th discretization element (10 in total). The heat source $\dot{q}$ is different varying j, and it considers convection between solid walls and fluids, heat losses to the ambient (which are neglected in this specific study), and conduction along the longitudinal direction of the heat exchanger. The contributions to the heat source $\dot{q}$ are computed with standard conductive and convective heat exchange equations, using the parameters and physical properties set by the user for the heat exchanger.

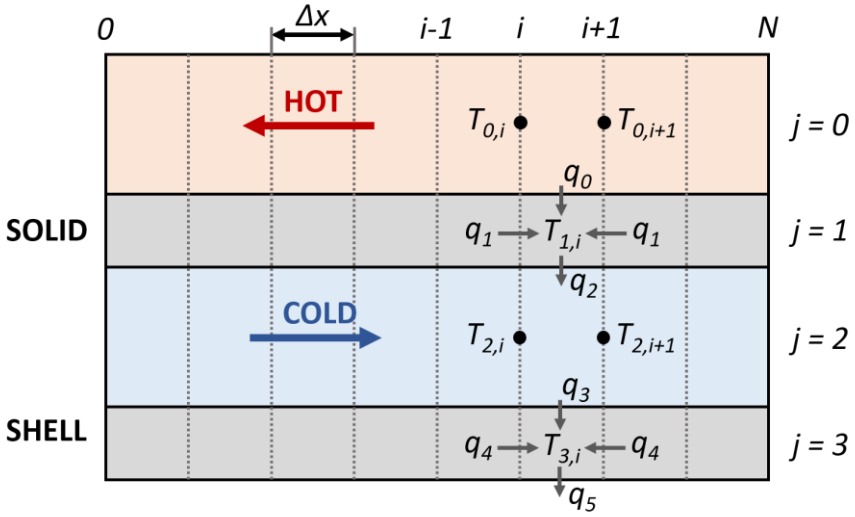

Figure 30. *Structure of the TRANSEO heat exchanger component.*

The REC parameters are determined in order to transfer a proper amount of heat, based on previous studies on pressurized SOFC systems [77] and according

to the steady-state model presented in the previous chapter. Details regarding the values set in the REC model are reported in Table 3 and [96]. According to the setup of the steady-state model, the APH is modelled as a counterflow heat exchanger and its parameters are set to obtain an effectiveness around 0.2.

4.1.4 Reformer

The 1D reformer model simulates a co-flow device. The chemical reactions, which are assumed to be at equilibrium, are simulated with the same steady-state equations implemented on the model described in Section 3.1.2. This set of equations constitute the actuator disk of the reformer lumped-volume model. However, compared to the steady-state model, the number of discretization points is lowered from 50 to 10, in order to reduce the computational time. The transient behaviour is simulated by a duct with geometrical properties equivalent to the reformer, following the approach presented in Section 4.1.1, and taking into account its thermal capacity.

4.1.5 Burner

The OGB is simulated with a 0D model of a burner, where all the flammable substances at the stack outlet (H_2, CO, CH_4) are mixed and burnt. Assuming complete oxidation of all these substances, the reaction rate of each oxidation reaction, which is considered at equilibrium, corresponds to the molar inlet flow of the fuel involved. The composition at the burner outlet is updated according to Eq. (13). The outlet temperature is determined as a function of the inlet temperature and the enthalpy change ΔH due to the k oxidations (Eq. (14)) [117]. Also for the burner, transients are simulated by a duct with equivalent geometrical properties, considering also the thermal capacity of its solid structure.

4.1.6 Ejector

The ejector model used for this study was introduced in [125] and it simulates the off-design behaviour of the component solving steady-state mass, energy and momentum equations. It considers the primary nozzle momentum loss, the viscous pressure losses in the diffuser and in the mixing chamber. It also takes into account the heat transfer between primary and secondary nozzles, and the pressure loss caused by the primary nozzle thickness. The transient behaviour is simulated by solving energy and momentum equations, considering the heat transfers between flows, solid structure and the ambient. More information regarding the equations implemented in the ejector model are shown in [125], while the characteristic parameters regarding geometry and performance that were used in the model are available in [96].

4.1.7 Turbocharger

A turbocharger is composed of three main components: compressor, turbine and shaft. This structure is reflected in the turbocharger model, which is formed by these 3 different components. The inputs of compressor and turbine models are flow conditions (different if the component is set as mass flow active or inactive) and turbocharger rotational speed. The outputs are the unknown flow properties and the mechanical power drawn or generated by the component, computed according to Eq. (21).

Both models are based on the steady-state performance maps introduced in Section 0. When the turbomachinery operating condition deviates from the reference condition, the models correct the results obtained from the maps by using similitude theory [135]. The compressor model also provides information about the distance between operating point and surge line, determining the surge margin K_p. The turbocharger model simulates the effect of the thermal capacity, while heat losses to the ambient and heat transfer from the turbine to the compressor are neglected.

The shaft model updates the rotational speed from the power imbalance between compressor and turbine, considering the effect of the turbocharger rotational inertia J and the mechanical power losses in bearings, according to Eq. (47)

$$P_T - P_C - P_{loss} = J \frac{d\left(\omega^2/2\right)}{d\tau} \tag{47}$$

where P is the power, ω is the rotational speed, and the subscripts T and C refer to turbine and compressor respectively. The power losses P_{loss} are computed based on their value at nominal rotational speed and the current ω, according to a quadratic law.

4.1.8 SOFC

The SOFC is simulated using a 1D model, which solves the same steady-state equations adopted for the off-design model in Section 3, with the parameters set according to the same Staxera GmbH system [86]. The transient behavior of the fuel cell is simulated considering the fluid-dynamic delay due to its large volume and its thermal capacity. The volume is set to 2.8 m^3, while the thermal capacity is computed assuming a total mass of 530 kg and a specific heat capacity of 660 J/kg K.

A complete dynamic model of the fuel compressor was not included to reduce the computational time of the model, since the performance of this component is expected to have a limited impact on the plant behavior. Its pressure ratio is imposed by the user and the fuel mass flow is automatically modified in off-design operation proportionally to the electrical current density, in order to keep the fuel utilization factor U_f at the constant value of 0.80. The outlet flow conditions are obtained assuming perfect gas behaviour and a compressor isentropic efficiency of 0.80. Therefore, fuel compressor power consumption is proportional to the fuel mass flow and it is computed according to Eq. (20).

4.1.9 Valve

The CBV and BV are simulated with the TRANSEO 0D valve model [115], assuming a linear relationship between valve fractional opening and mass flow at fixed pressure loss. The relationship between pressure loss and flow velocity is expressed by Eq. (48) [136].

$$\frac{\Delta p}{\rho} = \frac{1}{2} k_v w^2 \tag{48}$$

where the friction factor k_v is computed according to Eq. (49).

$$k_v = \frac{1}{FO^2} \tag{49}$$

Based on the plant specifications, the CBV was set to have a mass flow at full opening equal to 0.015 kg/s when the inlet pressure is 3 bar, while the BV was set to have a 0.01 kg/s mass flow at full opening, for the same inlet pressure. The model considers both the delay on fractional opening changes and the fluid dynamic delay on mass flow variations (0.1 s and 0.01 s respectively for the cold bypass valve).

4.1.10 Model validation

The components of the TRANSEO library were validated against experimental data in many previous studies conducted by other researchers at TPG [113,114,117,123,125]. In [117] the models of SOFC and reformer were validated referring to the values of electrical power, flow rates, pressures and temperatures obtained from an actual Staxera GmbH system [86]. The validation of the SOFC model in steady-state conditions was performed comparing the temperature profile along the cell for different values of current density. The model transient behaviour was validated on voltage and temperature distribution measurements, obtained while varying air inlet temperature and mass flow rate, electrical current and fuel utilization factor.

The reformer model was validated comparing the anode side outlet composition computed by the model with the compositions recorded during experimental test run at various operative temperatures. In [123] the SOFC model was validated on the basis of the trends of power, temperature and current during a reformer fault. In [125] a test-rig, built at the TPG laboratory to study the integration of ejectors with SOFC hybrid systems, was presented. The data collected from said test-rig were used to validate the ejector model, both in stationary and transient operations. In [114] the steady-state validation of turbomachinery components was performed on the basis of experimental data collected a recuperated MGT system in different part load conditions. The transient condition validation was performed as well, analyzing temperatures and rotational speed computed by the model during a machine shutdown scenario. The heat exchanger model was validated referring to the recuperator of an MGT system [113]. More in detail, the experimental data was collected while operating the system at loads between 20% and 100% of the MGT nominal power, and the validation was performed comparing values of efficiency, compressor outlet temperature, pressure in the external combustion chamber and at the expander outlet. The dynamic behavior of the component was validated referring to experimental data of rotational speed response to load step variations.

Similarly to the steady-state model, validation of the entire SOFC system model is not currently possible, because the layout considered in this study is still in a research stage, and no experimental prototypes have been developed yet.

4.2 Steady-state operation and transient characterisation

To design the control of the turbocharged SOFC system properly, it is first necessary to determine the steady-state operation of the system, identifying the best trajectories at part-load, to be tested later under dynamic conditions.

4.2.1 Steady-state operation

The dynamic model of the SOFC system was used to simulate its steady-state behaviour at different values of the cell electrical current density (j_{cell}) (100-90-80% of its nominal value, equal to 0.237 A/cm^2), and a constant ambient temperature of 15°C. According to [86,127], the maximum SOFC temperature set-point was set equal to 860°C, and the control system will be designed to follow this requirement with the lowest deviation possible. According to experimental data collected on the Staxera GmbH system referenced by this study, the temperature increases along the fuel cell. Thus, it is reasonable to consider the SOFC cathode outlet temperature ($T_{ca,out}$) as the SOFC maximum temperature. As mentioned in Section 3, the system is subject to many different constraints during its operation. The constraints that must be checked while designing the control strategy of the turbocharged SOFC system are shown in Table 9.

Table 9. *Operating limits of the turbocharged SOFC system* [86,137].

Parameter	**Unit**	**Value**
Max anode-cathode inlet ΔT	°C	250
Max anode-cathode Δp	Pa	3000
Max cell ΔT/Δτ	°C/s	5
Max turbocharger rotational speed	rpm	2.9 10^5
Min reformer inlet S/C	-	1.8

In Section 3.2 it was observed that control strategies based on CBV or CBV+WGV are able to comply with the system operative constraints in different conditions of current density and ambient temperature. Even if the CBV+WGV ensures a better performance of the system, CBV control is adopted for this study. In fact, this is the first study regarding the design of control strategies

for turbocharged SOFC systems known in literature and adopting a multi-output controller would increase unnecessarily the complexity of the problem. Differently from the previous off-design analysis, the fractional opening of the bleed valve (BV) is kept constant and equal to 30%, to increase the air temperature at the REC outlet and improve the performance of the system.

Opening the CBV, the portion of compressed air flow that is driven directly to the turbine inlet, bypassing the SOFC stack, increases, as shown in Figure 12. Moreover, the air mass flow entering the REC is smaller and its temperature increase within this component is higher. Since the air mass flow temperature affects the SOFC temperature, varying the CBV fractional opening can be an effective way of controlling the fuel cell temperature. The transient model developed in TRANSEO was aligned with good accuracy to the results of the steady-state model in full load, as shown in Table 10.

Table 10. *Comparison between simulations of the steady-state and the TRANSEO models in full load conditions, considering variable CBV opening and fixed BV.*

Parameter	**Symbol**	**Unit**	**Model**		**Error**
			TRANSEO	**Steady -state**	
SOFC max temperature	$T_{cell,max}$	°C	860	860	-
Fuel cell current density	j_{cell}	A/cm^2	0.237	0.237	-
System net power	P_{net}	kW	29.78	29.89	0.37%
System net efficiency	η_{net}	%	50.8	50.6	0.39%
Turbocharger rotational speed	ω	krpm	268	271	1.11%
Compressor outlet pressure	$p_{C,out}$	bar	2.95	3.01	1.99%
Turbine inlet temperature	$T_{T,out}$	°C	980	983	3°C

The results of system steady-state simulations performed with the TRANSEO model are displayed in Table 11, where the values of SOFC maximum temperature, matching their set-point for all the three operative conditions, are highlighted in green.

Table 11. *Results of the steady-state simulations.*

Parameter	**Symbol**	**Unit**	**$j_{cell}/j_{cell,des}$**		
			100%	**90%**	**80%**
SOFC max temperature	$T_{cell,max}$	°C	860	860	860
Fuel cell current density	j_{cell}	A/cm²	0.237	0.213	0.190
System net power	P_{net}	kW	29.78	27.54	25.18
Auxiliary system power	P_{aux}	kW	1.06	0.95	0.85
System net efficiency	η_{net}	%	50.8	51.8	53.3
SOFC inlet T difference (anode-cathode)	$\Delta T_{an\text{-}ca,in}$	°C	137	132	119
SOFC inlet p difference (anode-cathode)	$\Delta p_{an\text{-}ca,in}$	Pa	799	723	714
Fuel mass flow rate	$\dot{m}_{fuel}$	g/s	4.42	3.98	3.53
Turbocharger rotational speed	ω	krpm	268	249	227
Compressor surge margin	K_p	-	1.79	1.85	1.81
CBV fractional opening	FO_{CBV}	%	50.2	72.9	75.0
BV fractional opening	FO_{BV}	%	30.0	30.0	30.0

It is possible to observe that the operating limits of Table 9 are respected in all the three operative conditions, proving the effectiveness of the proposed control strategy.

As expected, the system P_{net} decreases proportionally reducing the j_{cell}. On the other hand, η_{net} has the opposite trend, increasing at lower values of current density and power, as shown in Figure 31.

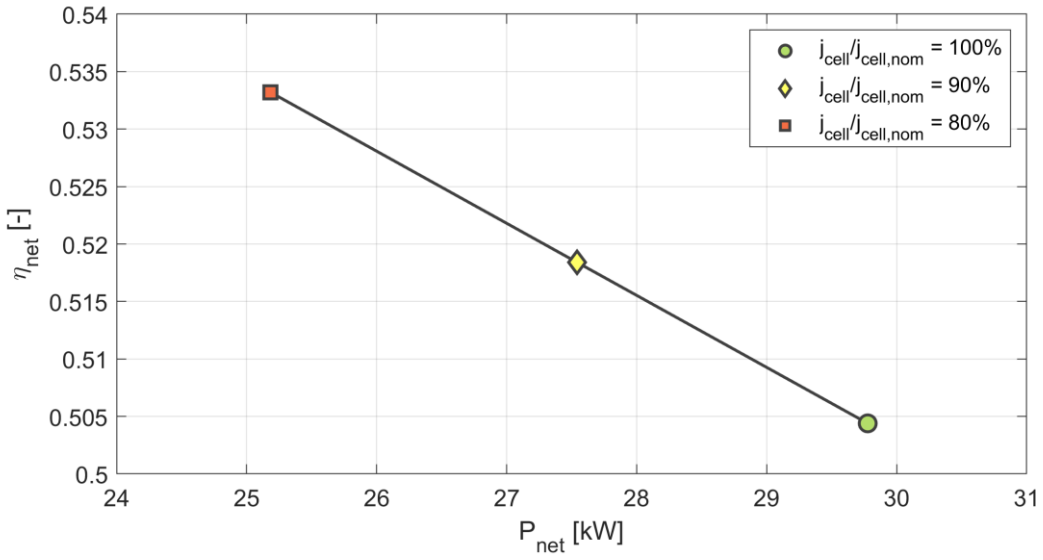

Figure 31. *Net efficiency versus net power output in three different conditions of cell current density.*

As explained during the off-design performance analysis, this can be explained by the SOFC performance improvement at part load [37,87]: when the electric current is lower, the impact of ohmic losses is also lower. Thus, the SOFC efficiency is higher, and the system net efficiency increases as well.

4.2.2 Step response

Since it is possible to comply with all the operative limits acting just on the CBV, the control system is designed to change the CBV fractional opening as the only control action. Therefore, the transient characterisation of the turbocharged SOFC system has to be performed via a CBV opening step response. More in detail, a dynamic simulation is performed over a time span of 7000 s, starting from a stable on-design condition. After 100 s, the FO command to the CBV is suddenly increased by 5%. After a small delay, due to the valve dynamics, the

bypassed mass flow grows. As explained in Section 4.2.1, this operation causes an increase of temperature at the REC outlet. Consequently, there is an increase of temperature at the SOFC cathode inlet and outlet, and at the OGB outlet. Figure 32 shows the variations of these physical quantities from the on-design values, while Figure 33 shows the trends of SOFC solid temperature in the 10 discretisation elements of the nodes.

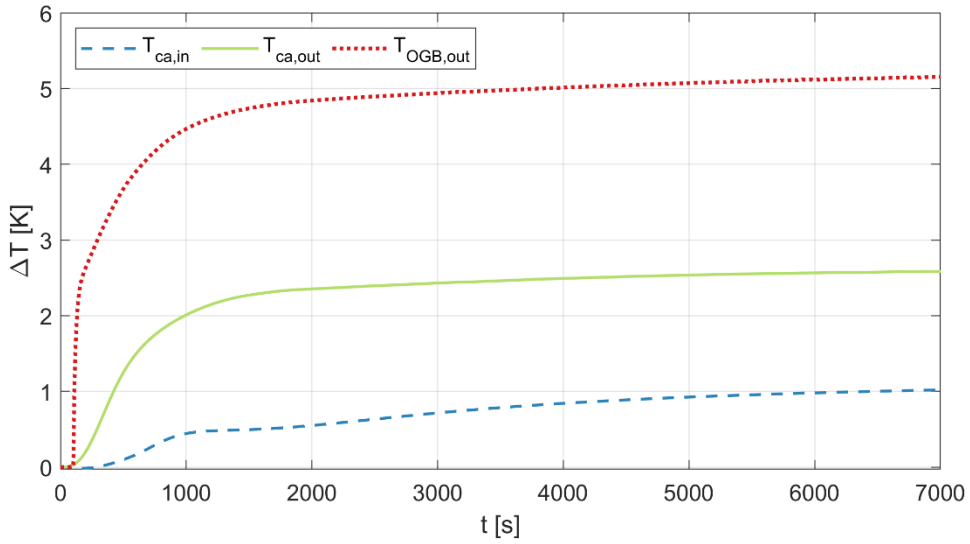

Figure 32. *Response after a CBV 5% opening step (time 0 s) of the turbocharged SOFC system, regarding the variations of* $T_{ca,in}$*,* $T_{ca,out}$ *and* $T_{OGB,out}$*.*

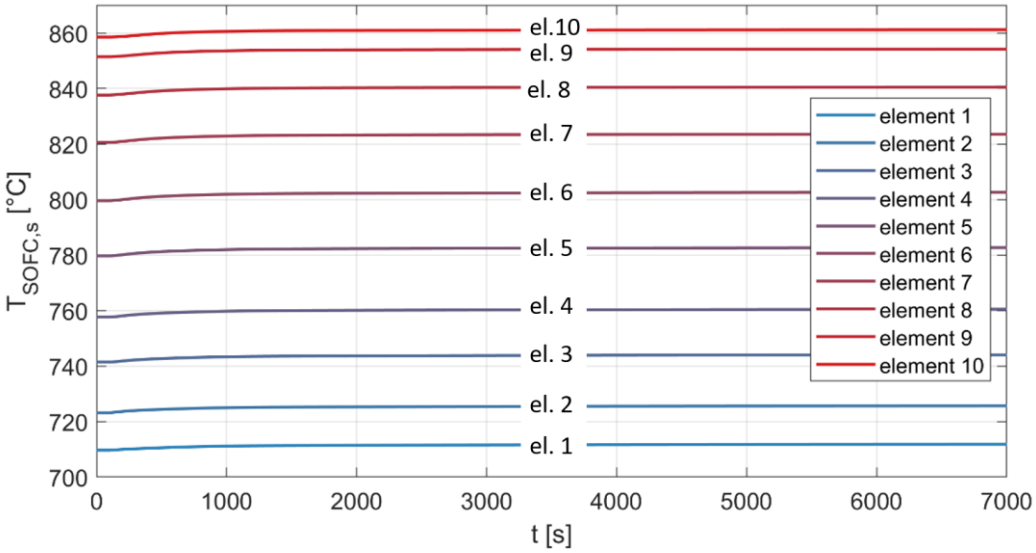

Figure 33. *Response after a CBV 5% opening step (time 0 s) of the turbocharged SOFC system, regarding trends of SOFC solid temperature ($T_{SOFC,s}$) in the 10 discretisation elements of the model. The elements are numbered from 1 to 10, going from the inlet to the outlet.*

It is possible to observe that the cathode inlet temperature $T_{ca,in}$ is the parameter with the slowest reaction to the CBV opening step: 50% of the total variation is reached after about 1600 s. Cathode outlet temperature $T_{ca,out}$, which is also the parameter to be kept constant in the system, has a faster variation, with 50% of its total variation reached about 420 s after the opening. The temperature of the OGB exhausts $T_{OGB,out}$ is the one that experiences the most abrupt change: 50% of the total variation occurs in just the first 90 s after the CBV opening.

It is important to highlight that the purpose of this test is just to analyse the transient behaviour of the system, therefore exceeding the maximum $T_{ca,out}$ (as shown in Figure 32) does not compromise the validity of these results.

Figure 33 shows that the SOFC temperature always increases from the inlet (element 1) to the outlet (element 10), even during the transient. This result is in accordance with the experimental results collected on the Staxera GmbH system and again confirms that the $T_{cat,out}$ can be reasonably considered as

SOFC maximum temperature. It is possible to notice that the temperature gradient at the inlet and at the outlet is smaller than inside the cell. At the inlet, this is mostly due to the MSR reaction consuming any CH_4 residual, which is strongly endothermic. At the end of the SOFC, the temperature increment is less significant because of heat losses to the atmosphere.

On the basis of these results, $T_{ca,out}$ and $T_{OGB,out}$ are considered as possible observed variables of the control system. The former because, being also the controlled parameter, it would allow for the design of a simple control system; the latter because, being the variable that reacts quickest to a CBV opening change, it would make it possible to develop a more responsive control system. The $T_{ca,in}$, instead, does not appear to be interesting as an observed variable of a control system, mostly due to its slow variation.

4.3 Control system design

Four different control systems are designed to keep the SOFC maximum temperature as close as possible to the 860°C setpoint. The control systems are evaluated based on their responsiveness and their capability to limit temperature variations, even if small temporary deviations from the setpoint are assumed to be acceptable.

At first, a very simple controller, i.e. a proportional-integrative (PI), is tested. The PI was selected due to its high reliability and wide use on industrial applications. Then a more sophisticated approach, based on a cascade controller, is proposed, and further improvements are gradually added to the system. Cascade controllers were considered for this study based on their previous applications as innovative control systems for fuel cell systems [138–141]. The controllers were tuned according to the Ziegler-Nichols method [142] and eventually modified to perform better during a reference transient scenario.

4.3.1 PI controller

The first control system to be designed was a proportional-integrative (PI) controller, acting on the CBV fractional opening to follow the $T_{ca,out}$ set point. The proportional gain and integral time (K and T_I respectively) were determined referencing the CBV opening step presented in Section 4.2.2. The PI tuning was refined observing the controller behaviour during a current density reduction simulation, lowering the value of j_{cell} from 100% to 90% of its nominal value with a ramp, over a time of 600 s. The test is performed on a ramp, and not on a step variation, because this scenario is more representative of the real operative conditions of a pressurized SOFC system.

Using the values of K and T_I obtained by the Ziegler-Nichols method (K_{ZN} = 0.197, $T_{I,ZN}$ = 180) without any modifications, resulted in an unstable control, with growing oscillations of FO_{CBV} and $T_{ca,out}$. As highlighted in [143], the Ziegler-Nichols method is widely used, but it uses insufficient information on the system and has various flaws, leading to poor robustness. Therefore, in this study the values of K_{ZN} and $T_{I,ZN}$ are empirically modified to improve the performance of the controller. A K reduction was considered to increase the controller stability and solve this issue: Figure 34 and Figure 35 show how the controller performed (with a current decrease ramp) dividing the K_{ZN} by 20, 30 and 50, referring to the cathode outlet temperature set-point ($T_{ca,out,SP}$).

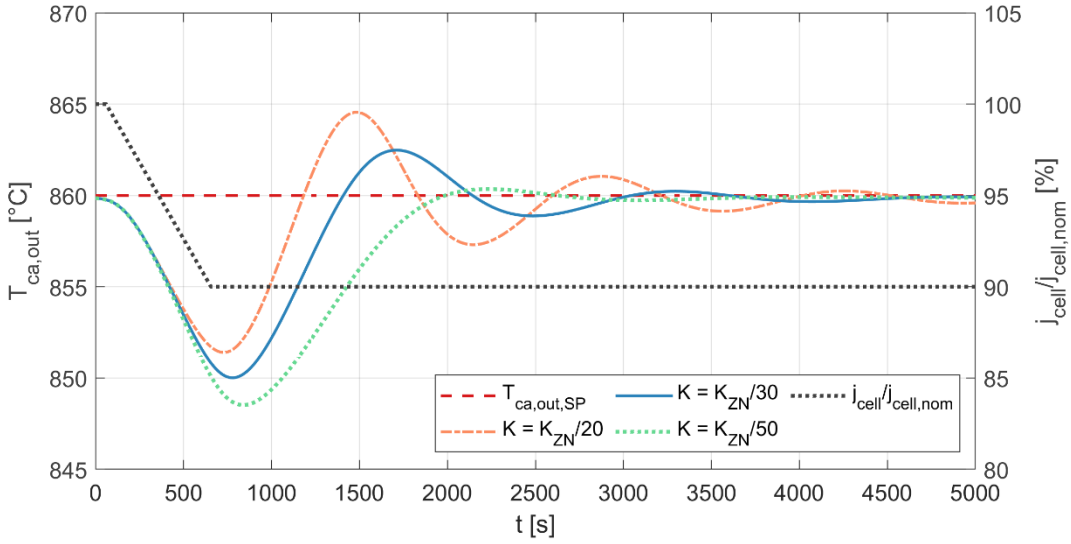

Figure 34. *SOFC cathode outlet temperature trends for different values of proportional gain in the PI acting on the* FO_{CBV} *(left axis). The black dotted line shows how the current density is modified during this scenario (right axis).*

All the PIs considered for this analysis were stable and provided acceptable results. Higher values of proportional gain increase system readiness, but they cause higher temperature oscillations. The $K = K_{ZN}/30$ was selected as a trade-off value, able to limit oscillation amplitude and to ensure good responsiveness.

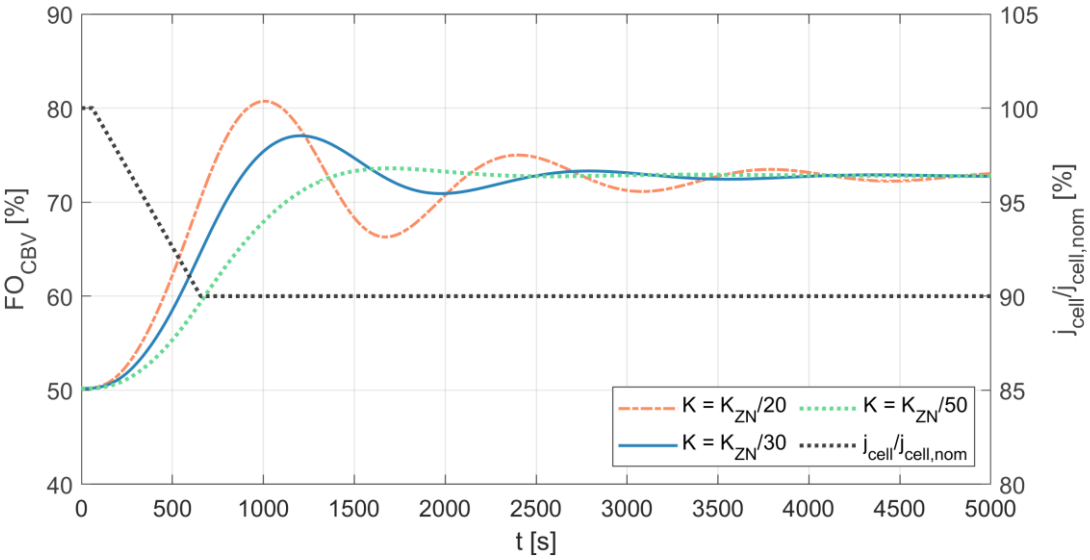

Figure 35. *FO_{CBV} trends for different values of proportional gain in the PI acting on the FO_{CBV} (left axis). The black dotted line shows how the current density is modified during this scenario (right axis).*

4.3.2 PI – PI cascade controller

In Section 4.2.2 it was pointed out that a control system taking into account the OGB outlet temperature variations might be more responsive than one monitoring only the $T_{ca,out}$. However, a simple PI is not feasible for this purpose, because it can monitor only the $T_{ca,out}$ to follow its set-point. To overcome this problem, a cascade control involving two PIs was designed and implemented on the system. In general, cascade control, which was introduced in [144], is based on two separate controllers, with the first determining the set-point of the second.

In this specific setup, the first PI compares the actual value of $T_{ca,out}$ with its set-point $T_{ca,out,SP}$ = 860°C, and determines the off-gas burner outlet temperature set-point ($T_{OGB,out,SP}$) based on their difference. The error between $T_{OGB,out,SP}$ and $T_{OGB,out,}$ is then used by the second PI to compute the fractional opening of the CBV. The structure of this controller is shown in Figure 36.

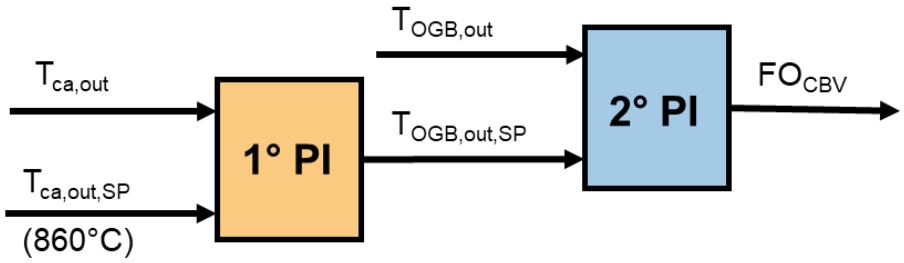

Figure 36. *Structure of the PI-PI cascade controller.*

The second PI was tuned following the same procedure described in Section 4.3.1 for the PI that determines the CBV fractional opening: K_{ZN} = 0.032 and $T_{I,ZN}$ = 22.5 were determined according to the Ziegler-Nichols method, and then

K_P was obtained dividing K_{ZN} by a factor of 30 to improve stability. To tune the first PI, a new simulation was run, including the second PI in the system and starting from a stable on-design condition, where the value of $T_{OGB,out,SP}$ was set equal to 1045.1°C. After 100 s, the $T_{OGB,out,SP}$ suddenly increased by 10°C, and the results on the dynamic response of the system (shown in Figure 37) were used to tune the first PI following the Ziegler-Nichols method (K_{ZN} = 12.9 and $T_{I,ZN}$ = 155.1). Figure 38 shows that, testing the cascade controller on the same j_{cell} reduction ramp used in Section 4.3.1 (from 100% to 90% of the nominal value over 600 s), it was not necessary to reduce the proportional gain of the first PI to increase controller stability, therefore the Ziegler-Nichols gains were kept in this case. Figure 39 shows how the controller acts on the CBV fractional opening. When the current density is reduced, the $T_{ca,out}$ decreases. To contrast this effect and bring the cathode outlet temperature back on its setpoint value, the controller opens the CBV.

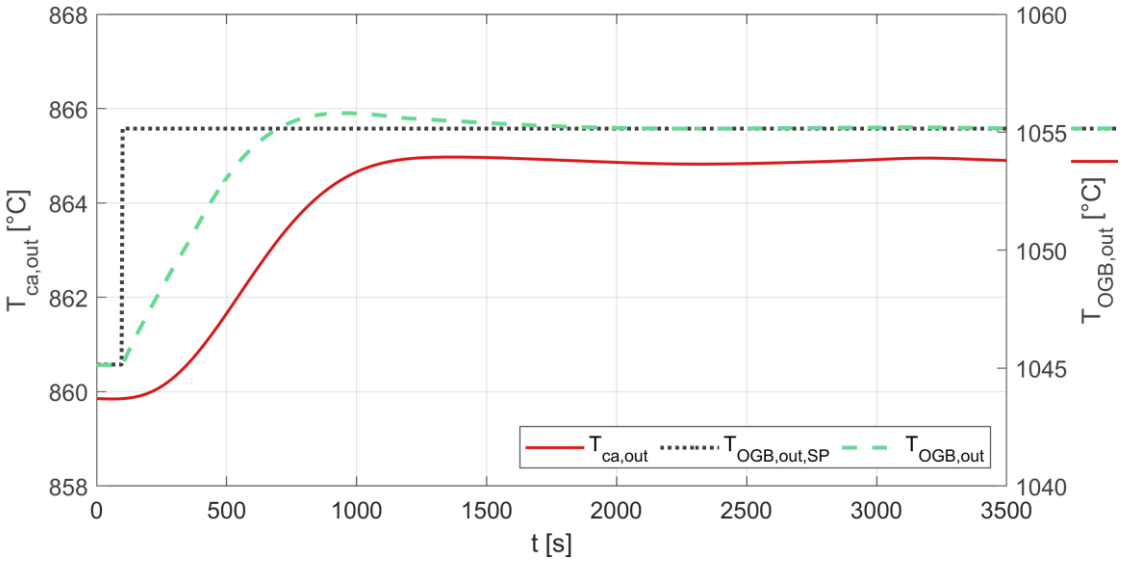

Figure 37. *Transient response of the SOFC cathode outlet temperature after a 10°C step increase of the OGB outlet temperature setpoint.*

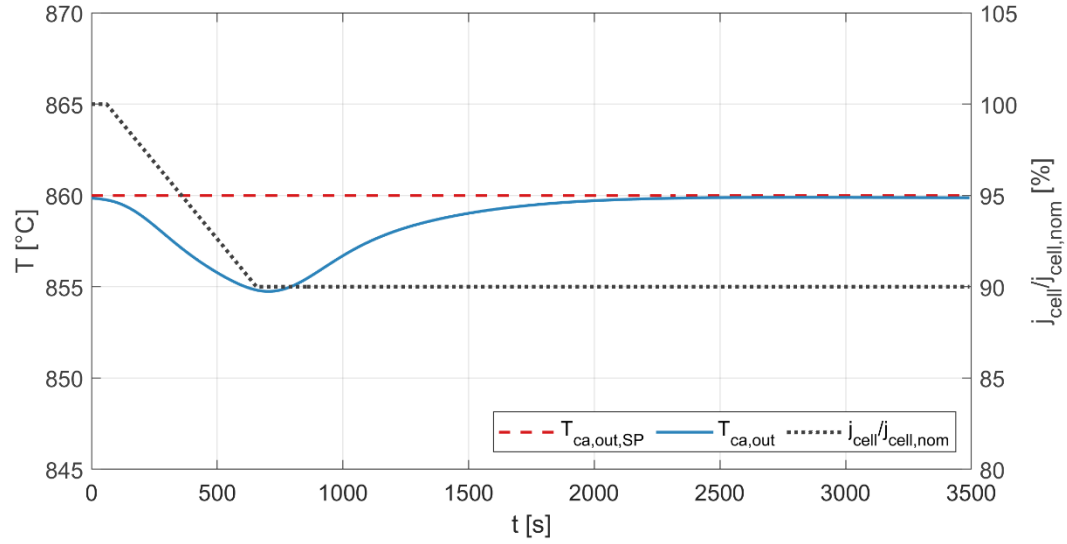

Figure 38. *SOFC cathode outlet temperature trend during a j_{cell} reduction ramp from 100% to 90% of its nominal value over 600 s, using a PI-PI cascade controller.*

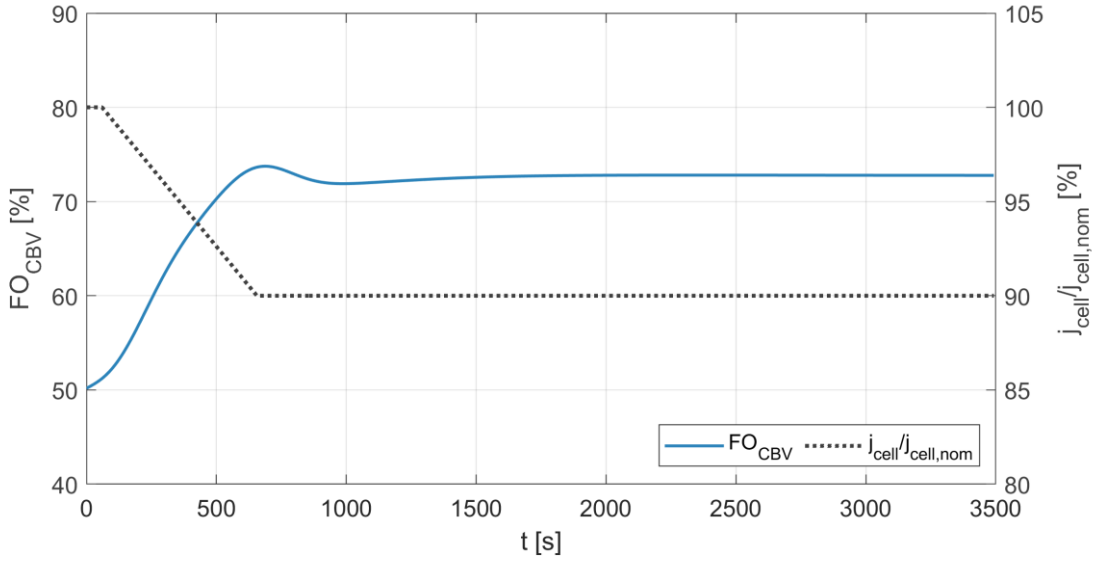

Figure 39. *FO_{CBV} trend during a j_{cell} reduction ramp from 100% to 90% of its nominal value over 600 s, using a PI-PI cascade controller.*

From Figure 38 it is evident how the PI-PI cascade controller performed better than the previous PI controller to keep the $T_{ca,out}$ as close as possible to its set-point. During the simulation no significant oscillations were present, and the maximum deviation from the set-point is equal to 5.1°C, significantly lower than the 9.8°C obtained controlling the system with the previous PI controller.

4.3.3 PI-PI cascade controller with FF approaches

The PI-PI cascade controller performance could be further improved taking advantage of the fact that the electrical current is a measured disturbance on the system. Therefore, the previous controller could be complemented with feed-forward (FF) approaches based on the electrical current drawn, using the information obtained from the steady-state simulations of the system (Section 4.2.1). From the steady-state simulation results, the regime values of FO_{CBV} and $T_{OGB,out}$ are known when the system is operating at $j_{cell}/j_{cell,des}$ equal to 100%, 90% and 80%. The FO_{CBV} and $T_{OGB,out}$ in the whole operative range of j_{cell} (100-80% of its nominal value) could be approximated by a lookup table interpolating linearly between the known data. Thus, the cascade control no longer determines the values of FO_{CBV} and $T_{OGB,out}$, but only the deviations from the lookup table output, which are necessary to follow the $T_{ca,out}$ set-point. The structure of this setup is shown in Figure 40. Such controller structures can be effective not only during transients but also to mitigate the effects of component degradation, thanks to the feedback loops that ensure, in any case, the constant observed temperature.

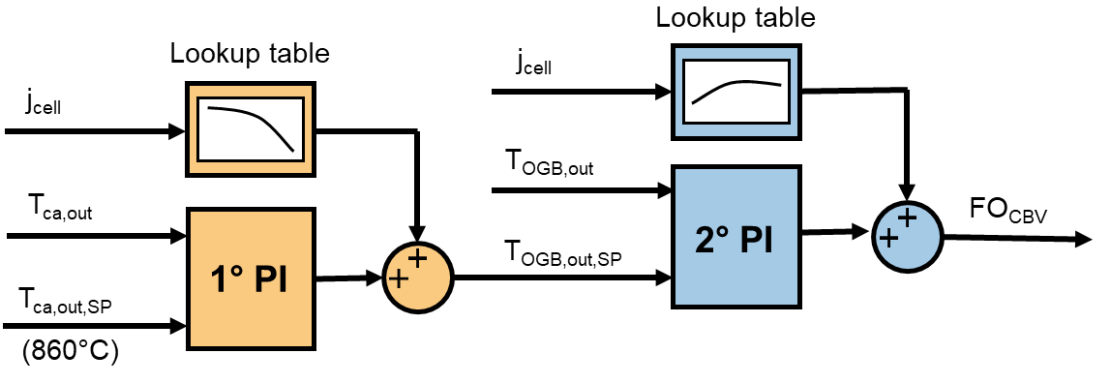

Figure 40. *Structure of the PI-PI cascade controller with feed-forward approaches.*

This controller was also tested on a j_{cell} reduction ramp, from 100% to 90% of its nominal value over 600 s. The $T_{ca,out}$ trend in Figure 41 shows an even lower

deviation from the set-point value for the whole simulation, with a maximum value of 2.5°C and no significant oscillations, proving very good set-point tracking capability and robustness. Compared to the PI-PI cascade controller, a $T_{ca,out}$ overshoot is present using this controller. However, the deviation from the setpoint is larger for the PI-PI and, in a j_{cell} increase ramp scenario, a more significant overshoot is expected. Figure 42 shows how the controller acts on the CBV fractional opening.

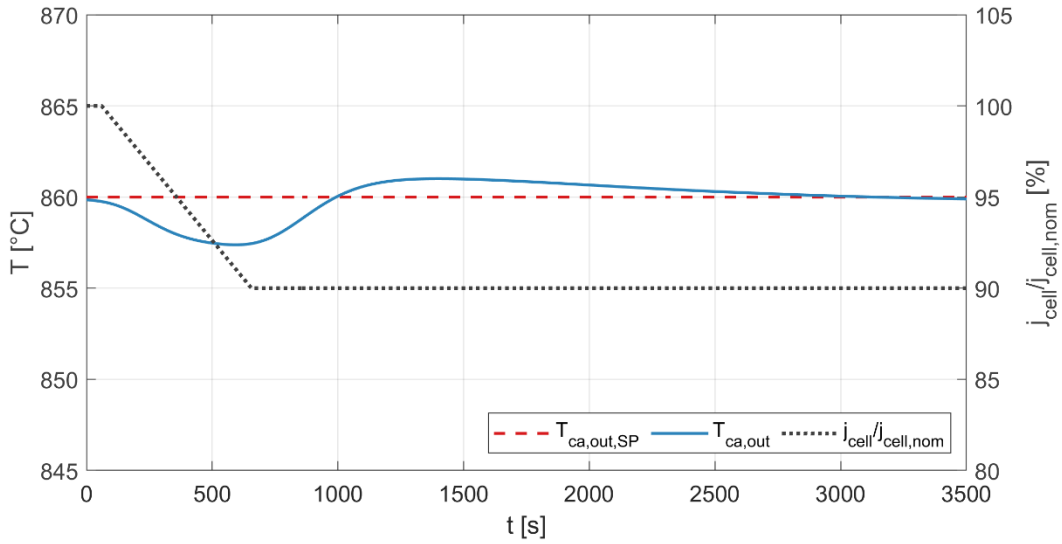

Figure 41. *SOFC cathode outlet temperature trend during a j_{cell} reduction ramp from 100% to 90% of its nominal value over 600 s, using a PI-PI cascade controller with feed-forward approaches.*

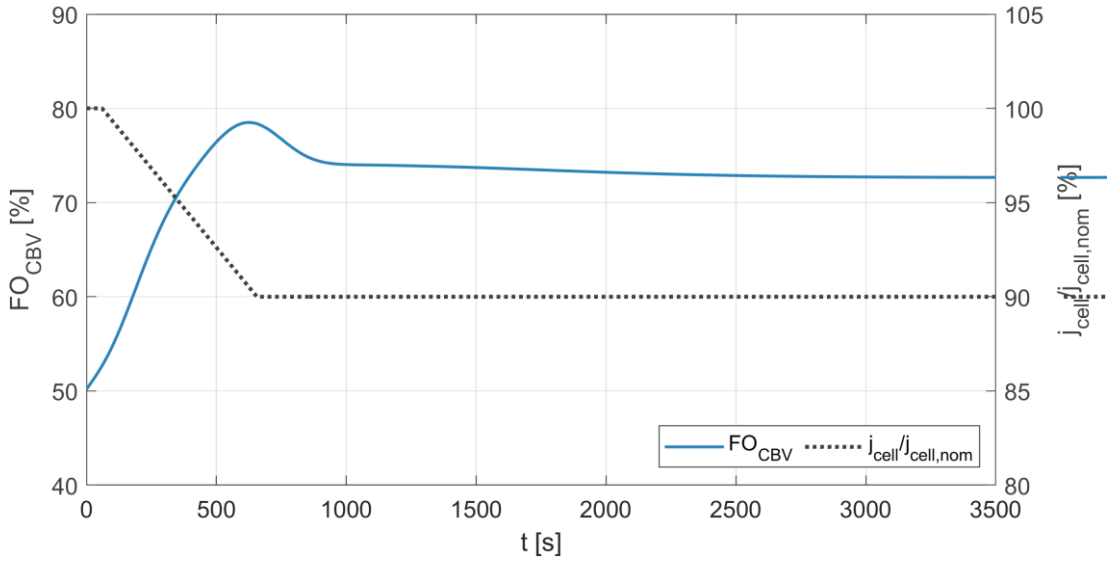

Figure 42. *FO_{CBV} trend during a j_{cell} reduction ramp from 100% to 90% of its nominal value over 600 s, using a PI-PI cascade controller with feed-forward approaches.*

4.3.4 PID-PI cascade control with FF approaches

The last control system analysed in this study is similar to the previous PI-PI cascade control with FF, but instead of a PI, a PID is used to determine the $T_{OGB,out,SP}$ based on the $T_{ca,out}$ error. While the PI considers only the error and its integral, the PID actuating signal is also computed as a function of the error derivative. Therefore, the control is partially based on the prediction of the future error. On a real application the drawback of including the derivative term is the amplification of high frequency sensor noise, and thus a filter should be implemented [145].

The PID proportional gain $K = 17.2$, integral time $T_I = 103.4$ and derivative time $T_D = 25.9$ were tuned according to the Ziegler-Nichols method [142], reducing the K by a factor of 30 for consistency with the previous controllers. Similarly to the tuning of the first PI in Section 4.3.2, the tuning of the PID was performed activating the PI acting on the CBV and observing the system transient

response to a $T_{OGB,SP}$ +10°C step variation. Figure 43 shows the variation of $T_{ca,out}$ during this simulation. Amongst the controllers considered in this study, the PID-PI cascade control with FF was the one able to provide the smallest maximum deviation from the $T_{ca,out,SP}$, equal to 2.1°C. Also this controller causes a small $T_{ca,out}$ overshoot, while the PI-PI cascade controller does not. However, a system with smaller deviation from the setpoint is preferrable because, in a j_{cell} increase ramp scenario, the PI-PI is expected to cause a more significant overshoot. Figure 44 shows how the controller acts on the CBV fractional opening.

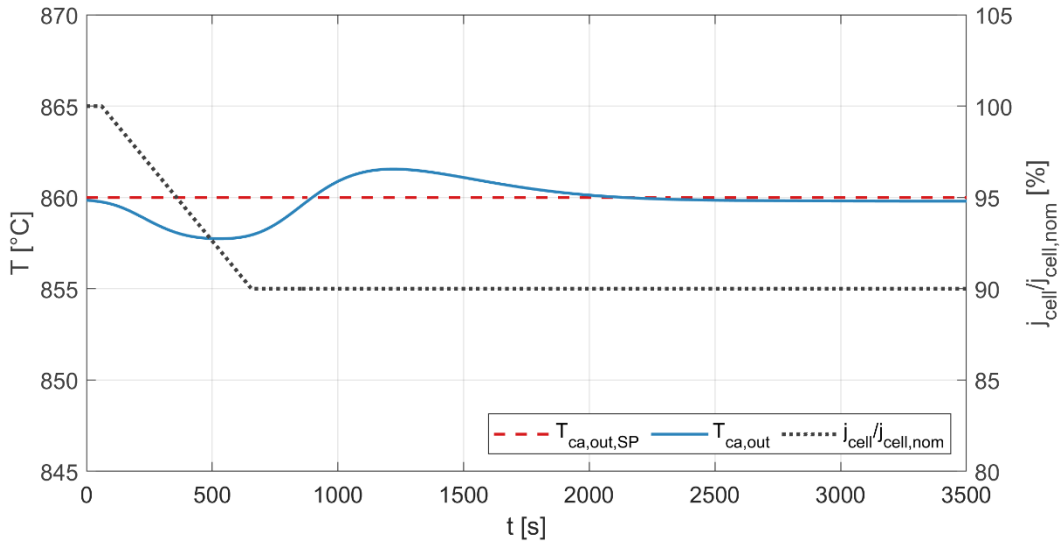

Figure 43. *SOFC cathode outlet temperature trend during a j_{cell} reduction ramp from 100% to 90% of its nominal value over 600 s, using a PID-PI cascade controller with feed-forward approaches.*

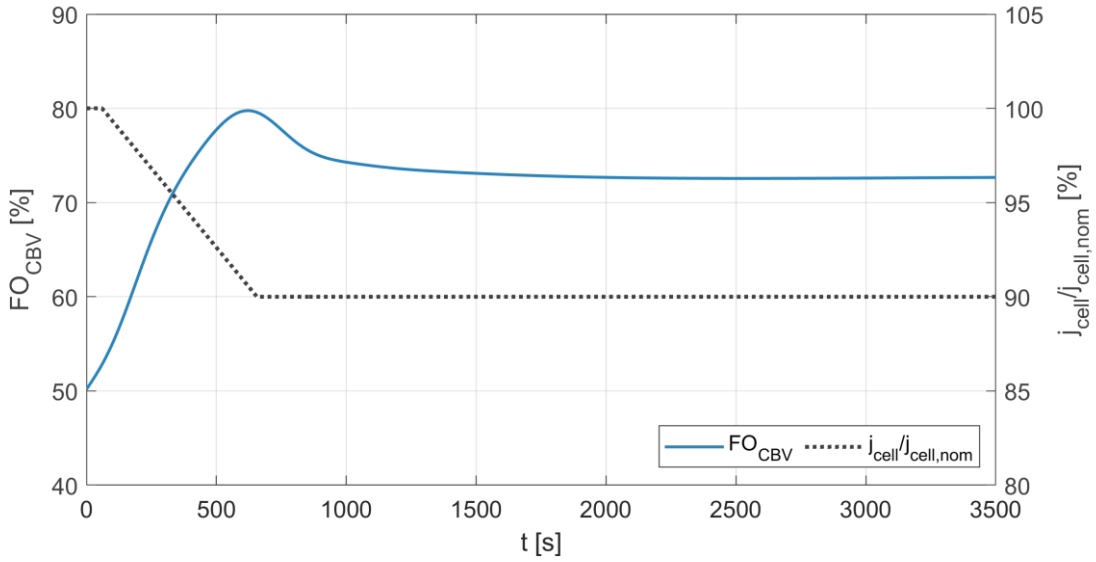

Figure 44. *FO_{CBV} trend during a j_{cell} reduction ramp from 100% to 90% of its nominal value over 600 s, using a PID-PI cascade controller with feed-forward approaches.*

4.4 Controller performance comparison

To determine which control systems are better suited to control a turbocharged SOFC system, it is necessary not only to observe the deviation from the $T_{ca,out}$ set-point, but also to guarantee a safe margin on many operative limits (Table 9). At first, the comparison is based on the simulations considered in Section 4.3, where j_{cell} was reduced with a ramp (scenario A). Then, another set of simulations is performed to provide a broader view on the controller features and test their robustness. In these simulations a more aggressive reduction of j_{cell} occurred, followed by an increase back to the initial value (scenario B).

4.4.1 Scenario A: current density reduction

All the simulations, already presented in the previous section and used here for controller comparison, start from an on-design condition. After 60 s, the system is subject to a transient due to a j_{cell} reduction, from 100% to 90% of its nominal

value over 600 s. Reducing the j_{cell}, the fuel mass flow is reduced proportionally, causing a temperature decrease in the SOFC stack. Thus, the control system has to modify the FO_{CBV} to follow the $T_{ca,out}$ set-point.

Here, control system performance is compared in Table 12 for the maximum deviation from the $T_{ca,out,max}$ and for the margins left on the operative limits (Table 9). Moreover, to evaluate controller promptness, a settling time τ_{sett} is defined as the time necessary to bring the $T_{ca,out}$ permanently within a range of ±0.5°C from its set-point, measured from the end of the j_{cell} variation (forcing term).

The $T_{ca,out}$ trends obtained during the simulations, which were already presented in Figure 34, Figure 38, Figure 41 and Figure 43, are displayed on the same plot in Figure 45 for immediate comparison. Similarly, Figure 46 shows how the fractional opening of the CBV is modified using all the proposed control systems.

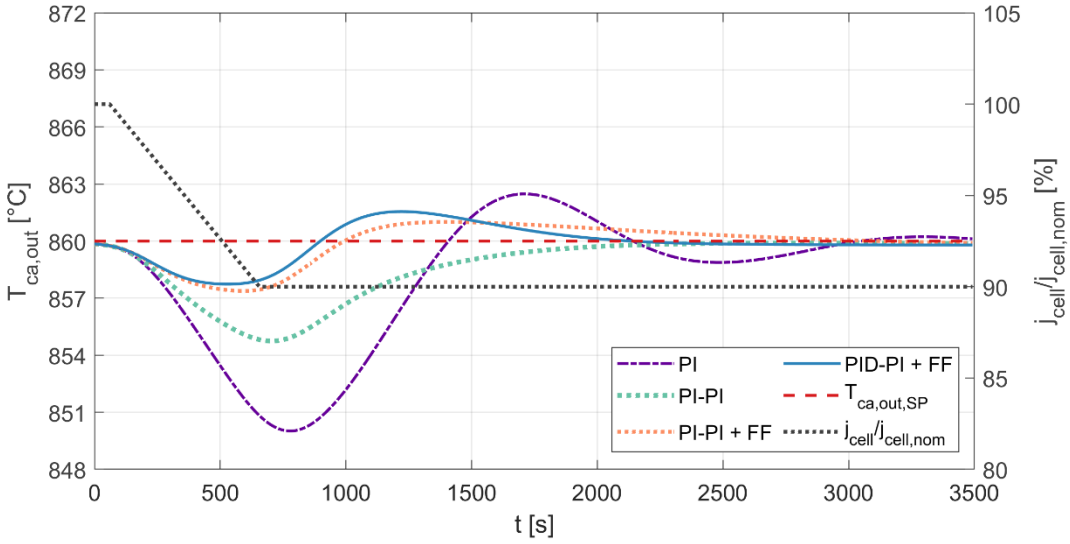

Figure 45. *Comparison of the $T_{ca,out}$ trends during scenario A, using all controllers.*

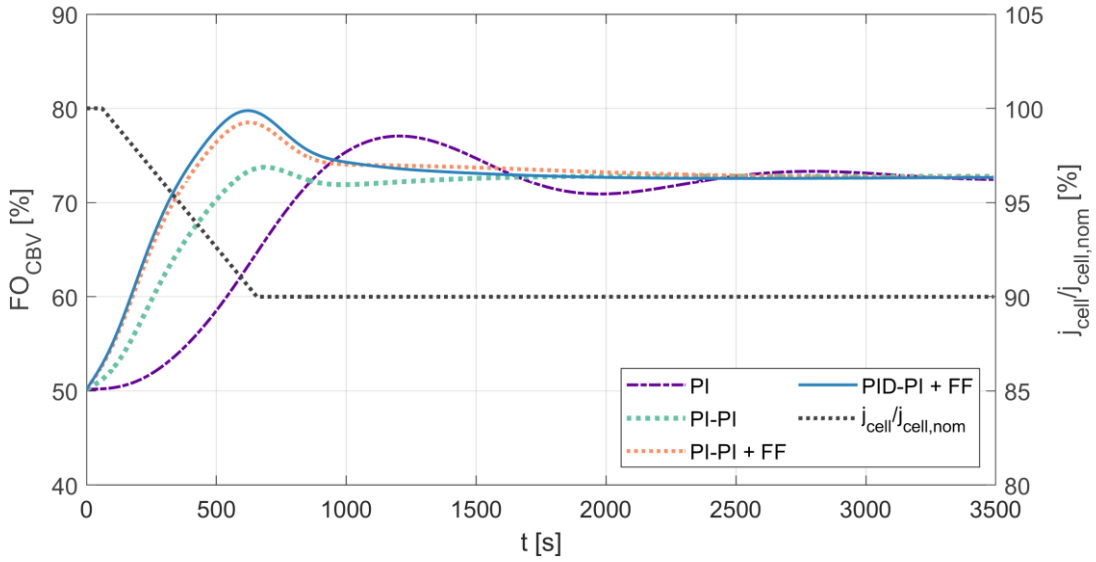

Figure 46. *Comparison of the FO_{CBV} trends during scenario A, using all controllers.*

Table 12. *Control system performance comparison, scenario A.*

Parameter	Unit	Limits	Control System			
			PI	**PI-PI**	**PI-PI + FF**	**PID-PI + FF**
$\Delta T_{cat,out,max}$	°C	-	9.8	5.1	2.5	2.1
τ_{sett}	s	-	2120	1008	1760	1176
$(\Delta T_{cat,out}/\Delta t)_{max}$	°C/min	< 5	1.23	0.69	0.58	0.64
$\Delta p_{SOFC,in,max}$	Pa	< 3000	838.8	800.7	799.0	799.1
$\Delta p_{SOFC,out,max}$	Pa	< 3000	149.0	146.5	149.2	150.5
ω_{max}	rpm	< 2.90 10^5	2.68 10^5	2.68 10^5	2.68 10^5	2.68 10^5
S/C_{min}	-	> 1.8	2.35	2.36	2.35	2.35
$K_{p,min}$	-	> 1.1	1.79	1.79	1.79	1.79

The results in Table 12 show that all the controllers can comply with the system operative constraints, for the entire simulation. The controller that keeps $T_{cat,out}$ closest to 860°C is the PID-PI + FF, with a maximum deviation of 2.1°C, as observed previously. It is also the one with the second lowest value of τ_{sett}, equal to 1176 s. The controller with the shortest settling time is the PI-PI, with only 1008 s, but its $\Delta T_{cat,out,max}$ is significantly higher (5.1°C). The PI-PI + FF has the second smallest $\Delta T_{cat,out,max}$, equal to 2.5°C, but a settling time of 1760 s, which makes it less interesting than the PID-PI + FF. Despite its simplicity, the PI is the controller with the worst performance: both its $\Delta T_{cat,out,max}$ and τ_{sett} are the highest. Pressure gradients are always significantly lower than the 3000 Pa limit for all the controllers tested. The values of turbocharger rotational speed, S/C and surge margin K_p shown in Table 12 are very similar, and they all ensure the proper operation of the system. The value of minimum K_p does not change adopting different control systems, because in this scenario it is always obtained at the starting point.

4.4.2 Scenario B: current density reduction and restoration

Considering only a reduction of j_{cell} (scenario A), a complete overview of the performance of the control systems is not provided. In detail, the results presented so far show that the maximum deviation from the $T_{ca,out,SP}$ is always experienced close to the end of the j_{cell} reduction ramp, but no information is available about controller performance when the j_{cell} is increased. Said transient needs to be investigated because of the strong non-linearities of the plant. Therefore, a new set of simulations is run, according to the following scenario:

- At the beginning, the system operates stably at nominal conditions.
- After 100 s, the j_{cell} starts decreasing linearly for the next 900 s, from 100% to 80% of its design value.
- $j_{cell}/j_{cell,des}$ is kept equal to 80% for 1000 s.
- The j_{cell} is restored to its design value with a ramp of 900 s.

- The system operates with j_{cell} equal to its design value until the end of the simulation (7000 s).

Compared to scenario A, these simulations present a faster and larger variation of j_{cell} (20% variation over 900 s, against the previous 10% over 600 s). Thus, scenario B is expected to better highlight the characteristic features of each controller.

As a first comment, it needs to be mentioned that in this scenario the PI controller was no longer able to ensure the proper operation of the system. In fact, j_{cell} reduction was too steep, and the controller was not responsive enough to contrast the $T_{cat,out}$ decrease. Thus, the energy available at the turbine inlet was lower, and the turbocharger rotational speed kept decreasing, and eventually the system was no longer able to run. Figure 47 shows the progressive decrement of $T_{cat,out}$. The plot is interrupted before the end of the simulation when the turbocharger speed went below 1.35 10^5 rpm.

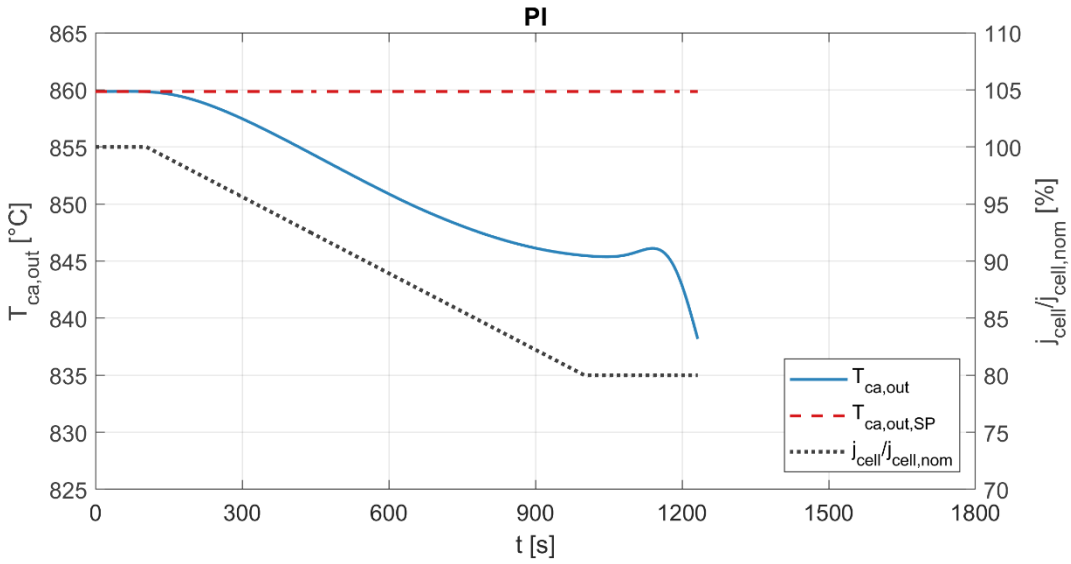

Figure 47. *SOFC cathode outlet temperature trend during scenario B, using the PI controller.*

Such an issue was not present for the other controllers, as shown by Figure 48. Table 13 shows the maximum $T_{cat,out}$ deviations obtained during the simulations of this scenario, the settling times, and also the values of all the parameters

considered critical for the correct operation of the turbocharged SOFC system. In this specific case the maximum $T_{cat,out}$ deviations correspond with the maximum overshoots.

The PID-PI + FF control was the one that showed the best performance in terms of deviation from the $T_{ca,out,SP}$, with a maximum error of 5.6°C, reached between 2000 s and 3000 s, while the j_{cell} was increasing back to its nominal value. Similarly to the previous scenario, the τ_{sett} measurement starts when the j_{cell} variation ends, i.e. at the end of the j_{cell} ramp up (τ = 2900 s). Although the lowest value of τ_{sett}, equal to 1212 s, was obtained again implementing the PI-PI control, the value of 1348 s measured using the PID-PI + FF was also interesting. The PI-PI + FF controller, instead, required a significantly higher time to reach the temperature set-point (τ_{sett} = 2396 s).

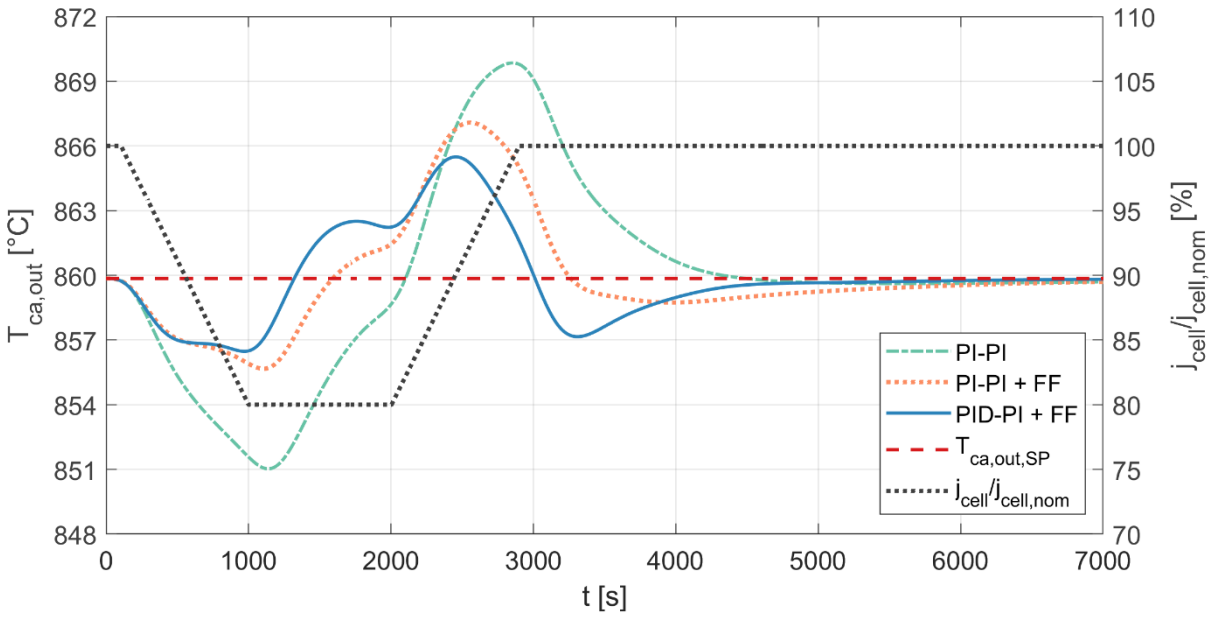

Figure 48. *Comparison of the $T_{ca,out}$ trends during scenario B, using the PI-PI, the PI-PI + FF and the PID-PI + FF controllers.*

Table 13. *Control system performance comparison, during scenario B.*

Parameter	Unit	Acceptable values	Control System		
			PI-PI	PI-PI + FF	PID-PI + FF
$\Delta T_{cat,out,max}$	°C	-	10.0	7.2	5.6
τ_{sett}	s	-	1212	2396	1348
$(\Delta T_{cat,out}/\Delta t)_{max}$	°C/min	< 5	1.33	1.05	0.98
$\Delta p_{SOFC,in,max}$	Pa	< 3000	870.2	945.3	988.3
$\Delta p_{SOFC,out,max}$	Pa	< 3000	153.8	156.5	160.5
ω_{max}	rpm	< 2.90 10^5	2.73 10^5	2.68 10^5	2.68 10^5
S/C_{min}	-	> 1.8	2.32	2.31	2.30
$K_{p,min}$	-	> 1.1	1.76	1.75	1.73

Table 13 shows that all three controllers were able to comply with the SOFC system operative limits, maintaining a proper safe margin during the whole j_{cell} variation. The PID-PI + FF is the controller that caused less stress on the SOFC in terms of temperature variation rate ($(\Delta T_{cat,out}/\Delta t)_{max}$ = 0.98°C/s), while the stress caused by pressure gradients was minimum using the PI-PI control system. The S/C_{min} had minimum variations for the three different control systems, and it was always higher than the 1.8 limit, averting carbon deposition within the SOFC.

The values of ω_{max} and $K_{p,min}$ were similar and ensured the correct operation of the turbocharger. It can be observed in Figure 49 that the turbocharger rotational speed had the most limited variation using the PI-PI, but the values were always acceptable for all the controllers. Figure 50 shows that the widest and most abrupt changes of FO_{CBV} were produced by the PID-PI + FF, but the controller output, which was always between 0.2 and 0.9, was never saturated.

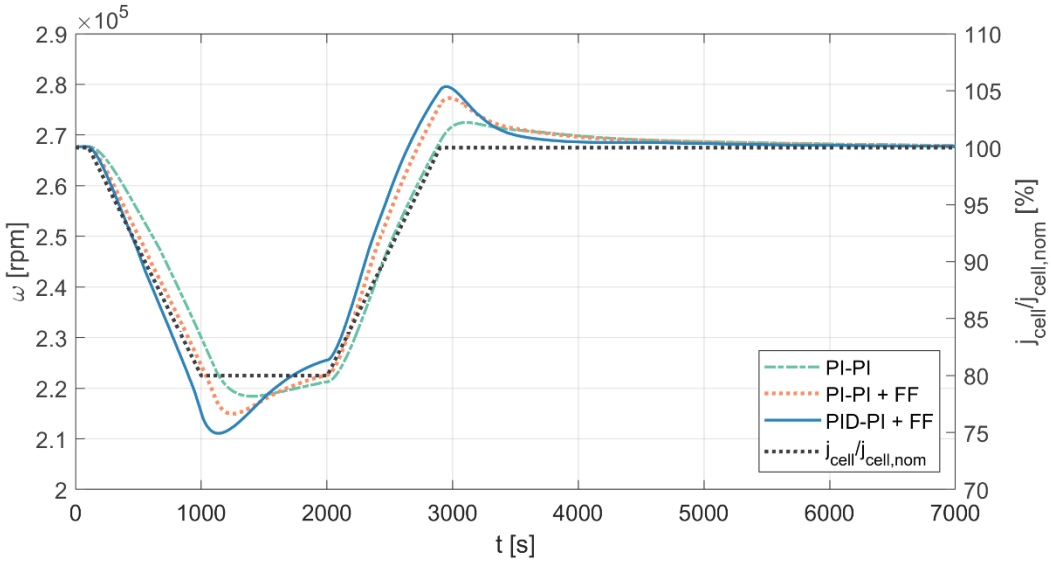

Figure 49. *Comparison of the ω trends during scenario B, using the PI-PI, the PI-PI + FF and the PID-PI + FF controllers.*

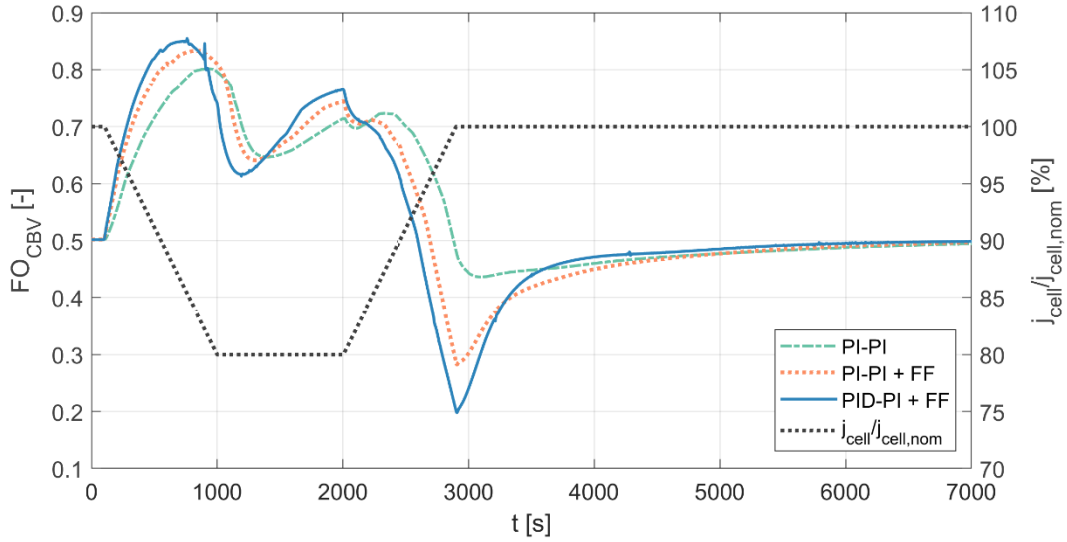

Figure 50. *Comparison of the FO_{CBV} trends during scenario B, using the PI-PI, the PI-PI + FF and the PID-PI + FF controllers.*

The small oscillations observed in Figure 50 for the PI-PID + FF are due to numerical noise generated by the model, having a strong effect on the derivative term of the controller. However, these oscillations have a very limited effect on the system performance and could be further reduced by a filter.

4.5 Concluding remarks

In this chapter, the dynamic model of an innovative turbocharged SOFC system fed by biogas and capable of about 30 kW net power was developed and used to design and test four different controllers, devoted to keeping the fuel cell maximum temperature constant during electrical current variations. At first the model was used to simulate the system steady-state behaviour at ambient temperature (15°C), for current density j_{cell} between 100% and 80% of its nominal value, corresponding to the operating range considered for this analysis. Then, it was used to characterise the system transient response to a CBV opening step variation and to determine which physical quantities should be monitored to develop a responsive controller: the OGB outlet temperature showed the promptest reaction, followed by the SOFC cathode outlet temperature. Four different controllers (PI, PI-PI, PI-PI + FF and PID-PI + FF) were tuned following a consistent procedure and implemented onto the system model. Such controllers were tested on two different j_{cell} variation scenarios: scenario A, where j_{cell} decreased from 100% to 90% over 600 s, and scenario B, where j_{cell} followed a more aggressive saddle in the 80% - 100% range. Finally, their performance was compared in terms of maximum deviation from the set-point, settling time and compliance with the operative constraints. The main outcomes of this analysis are:

- Acting on the CBV without modifying the BV opening is an effective way to comply with all the operative constraints of the biofueled turbocharged SOFC system, while operating at steady-state condition within the range $80\% \leq j_{cell}/j_{cell,des} \leq 100\%$.
- A CBV opening step response analysis showed that the physical quantities that appeared to be more interesting for the development of the control system are the SOFC cathode outlet temperature $T_{ca,out}$, which is also the process variable (set-point equal to 860°C), and the OGB outlet

temperature $T_{OGB,out}$, which was the one with the fastest variation. The SOFC cathode inlet temperature $T_{ca,in}$ had a significantly slower variation, therefore being the least interesting for control.

- In general, the gains obtained applying the Ziegler-Nichols method guaranteed good performance of the control system, but it was always necessary to reduce the proportional gain of the controller driving the FO_{CBV} to avoid instabilities.
- The PI resulted to be the least performing control system in scenario A, with the highest maximum deviation from the $T_{ca,out}$ set-point (9.8°C) and settling time (2120 s). However, all the operative constraints were respected. On the other hand, it was not able to follow the temperature set-point during scenario B, characterised by more aggressive variations of j_{cell}.
- The PI-PI, PI-PI + FF and PID-PI + FF cascade controllers were able to control the SOFC system during both scenarios, thanks to their better performance. The PI-PI is a good improvement from the PI, with a $\Delta T_{ca.out,max}$ of 5.1°C and the shortest τ_{sett} in scenario A (1008 s). The τ_{sett} was the shortest also in scenario B (1212 s), but the maximum deviation from the $T_{ca,out}$ set-point was the highest recorded (10.0°C).
- The addition of the feed-forward to the PI-PI cascade control led to a $\Delta T_{ca,out,max}$ reduction down to 2.5°C and 7.2°C during scenario A and B, respectively. However, in both scenarios it was the cascade controller with the highest τ_{sett} values: 1760 s in scenario A and 2396 s in scenario B.
- The results obtained with the PID-PI + FF cascade control were the most promising, in particular regarding its capacity to keep the $T_{ca,out,max}$ close to its set-point and to reach the desired value within a limited timeframe. This controller was able to keep the $T_{ca,out}$ within 2.1°C of its set-point during scenario A, with the second shortest τ_{sett} (1176 s, corresponding to

an increase of 16% from the PI-PI simulation). The advantages of this controller became more evident in scenario B: the $\Delta T_{ca,out,max}$ was 5.6°C, significantly lower than the 7.2°C obtained with the PI-PI + FF, and the τ_{sett} was equal to 1348 s, with an increase of only 11% from the PI-PI value.

- Compliance with system constraints was guaranteed by all the controllers in scenario A, with higher margins for the cascade controllers. During scenario B, all the cascade controllers were able to respect the operative limits. The PID-PI + FF was the controller that put the SOFC under the smallest thermal stress, while the PI-PI minimised the mechanical stress due to pressure gradients. During both scenarios, S/C, ω_{max} and $K_{p,min}$ had similar values between the different simulations, always far from their limits.

In conclusion, it was demonstrated for the first time that a cascade controller monitoring the off-gas burner outlet temperature is an effective way of controlling a pressurised SOFC system, in this case a biofueled turbocharged SOFC hybrid system, acting only on a cold bypass valve. Amongst the different control systems designed and tested, a cascade control composed of a PID and a PI, integrated with a feed-forward tool showed the best performance in terms of deviation from the SOFC cathode outlet temperature set-point. The results obtained are even more impressive, considering that all the operative constraints of the system are always respected. The deviations from the cathode outlet temperature set-point are always limited and temporary, ensuring the proper operation of the SOFC.

These encouraging results are an important step towards the development of pressurised SOFC systems. Being able to limit the deviation from the standard operation of the system, and to respect its operative constraints, cascade controllers could be implemented on emulator plants and eventually on real prototypes. Moreover, control systems based on cascade controllers could be designed to act simultaneously on the wastegate and cold bypass valves, improving the system performance as explained in Chapter 3.

In the next chapters it will be investigated how to enhance the control system of a pressurized SOFC system by integration with diagnosis systems, in order to prevent compressor surge and to limit degradation of the fuel cell.

5 Surge Prevention and Recovery Techniques for a SOFC-Turbocharger Hybrid System

In the previous chapters, it was highlighted that SOFCs are delicate devices, which should always be working in a limited operative range to avoid degradation. In a pressurized system, the limitations on pressure gradients between cathode and anode sides of the cell are particularly critical. In the turbocharged SOFC system considered for this research activity, the maximum allowed pressure gradient between anode and cathode is assumed to be 3000 kPa, according to the Staxera GmbH system datasheet [86], and the compliance of this limit was one of the specifications for the design of the control system presented in Chapter 4.

Moreover, the presence of the fuel cell stack volume between compressor and turbine alters the behavior of the turbomachinery during transients, raising the risk of compressor surge [93]. It is crucial to avoid this kind of event because the pressure oscillations associated with it would damage permanently the fragile ceramic materials of the fuel cells.

Different solutions were proposed to prevent this issue. An automated compressor surge recovery system for gas turbine based hybrid plants, including the bypass of cold air, was designed and tested on different scenarios in [93]. A model reference adaptive control, acting on air flow rate and motor speed, was implemented on an automotive fuel cell system to avoid compressor surge during transients in [146].

To lower the risk of surge in innovative cycles including turbomachinery, researchers have started to develop various techniques to detect surge precursors [147,148]. Many of these techniques analyze vibro-acoustic data, collected by non-intrusive sensors, to determine if the compressor is approaching surge [149,150].

The information obtained by surge precursors detection methods is extremely valuable. In details, it could be integrated with the control system of a pressurized SOFC system, reducing the risk of surge when the compressor is approaching a dangerous operating condition and therefore increasing greatly the system reliability.

In this chapter the effect of different surge prevention techniques on turbocharged SOFC systems is investigated, and the potential of control systems integrated with surge precursors detection methods is assessed. Many procedures are presented and tested by means of a dynamic model: in particular, an innovative approach employing a special intake ejector is proposed and verified. Their effectiveness is compared in terms of surge margin increase on the short and long term. Then, the most promising procedures are integrated with the control system and tested on a simulated scenario where the compressor is approaching a surge condition.

5.1 Simplified Plant Layout

As mentioned in the previous section, the fuel cell volume increases the risk of compressor surge during the dynamics of pressurized SOFC systems. While the increase of temperature through the SOFC system directly impacts on the energy available to the turbocharger, the chemical and electrochemical reactions occurring in the REF and the SOFC do not affect the compressor behavior. For this reason, in this study the authors consider a simplified layout, that recalls the structure of an emulator plant, where the SOFC stack is replaced by a vessel of equal volume [151]. In this layout, displayed in Figure 51, the air flow is pressurized by the compressor before entering a burner. Here, the oxygen in the air flow takes part into the combustion of methane, emulating the temperature rise of the SOFC system. The exhaust gases enter the vessel, are expanded in the turbine and finally discharged into the ambient.

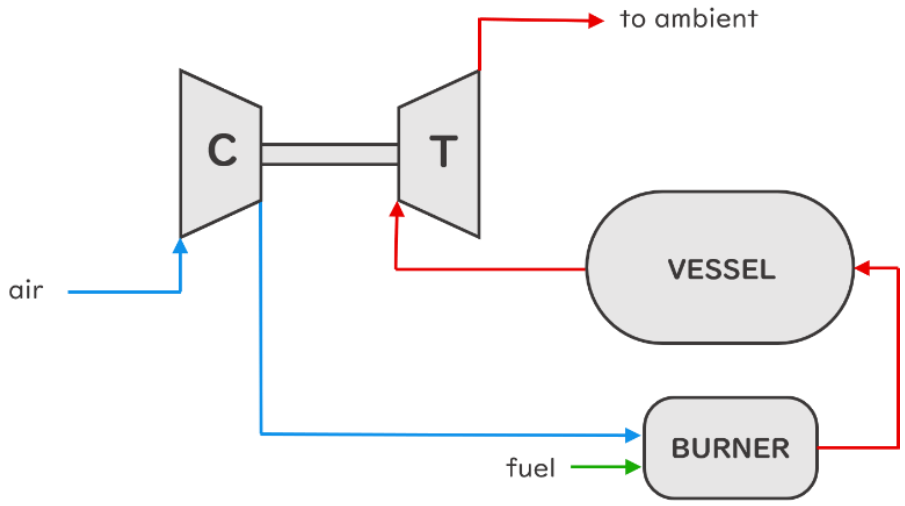

Figure 51. *Simplified turbocharged SOFC layout (blue line for fresh air, green line for fuel, red line for exhausts).*

In nominal conditions (full load and ambient temperature equal to 15°C), a fuel mass flow $\dot{m}_{fuel}$ of 11.2 10^{-3} kg/s is provided to the system to obtain a turbine inlet temperature $T_{T,in}$ of 1035 K, while the turbocharger provides an air mass flow $\dot{m}_{air}$ of 84 10^{-3} kg/s, with a pressure ratio β around 3.4.

5.2 Surge Prevention & Recovery Techniques

Several surge prevention techniques are proposed and compared on the basis of simulation results. Their effectiveness is evaluated observing the surge margin K_p, a parameter introduced in Section 2.8, representing the distance from the compressor operative point and the surge line, which is defined according to Eq. (5). It is useful to recall that values of K_p lower than 1.10 represent dangerous operating conditions [96].

At first, the effect of compressor inlet temperature and pressure on the surge margin will be evaluated. Then, various techniques, which require modifications of the SOFC system layout, will be implemented and tested:

- **Injection of water spray in the compressor inlet air flow**. The injection of water is expected to lower the compressor inlet flow

temperature, reducing the compressor work and increasing the mass flow. This could move the compressor operative point far from the surge line. The amount of water injected is set to never exceed saturation of the air flow, to avoid liquid droplets at compressor inlet.

- **Compressor fogging**. This procedure is similar to the previous one in terms of equipment; however, the amount of water injected exceeds the saturation limit, and liquid droplets enter the compressor. During the compression, the liquid water evaporates, lowering the temperature continuously and reducing the power drawn by the compressor. The drawback of this solution is that the impact of the droplets on the blades might cause damage.
- **Bleed of the compressor outlet flow.** Installing a bleed valve (BV) downstream of the compressor, part of the compressed air flow can be discharged into the ambient. Thus, it is possible to reduce the mass flow circulating in the system and the pressure at the compressor outlet, with a beneficial effect on the surge margin.
- **Recirculation of the compressor flow.** Adding a connection between the compressor outlet and inlet, it is possible to control the partial recirculation of the pressurized air flow acting on a recirculation valve (RV). This procedure causes a pressure reduction at the compressor outlet, similarly to the bleed, but, at the same time, increases the temperature at compressor inlet.
- **Ejector-aided recirculation of the compressor flow.** This solution is conceptually similar to the recirculation, but an ejector is installed before the compressor inlet. The recirculated flow enters the primary nozzle of the ejector where, due to Venturi effect, it draws the air flow from the secondary nozzle. The two flows are mixed before entering the compressor inlet.

A system equipped with water spray, bleed valve and recirculation line is displayed in Figure 52, while Figure 53 shows how the ejector-aided recirculation can be implemented on the turbocharged SOFC system layout.

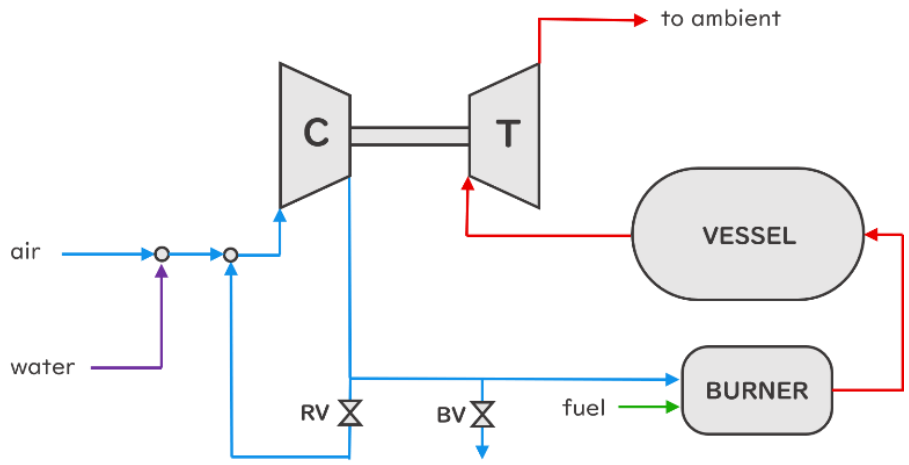

Figure 52. *Simplified turbocharged SOFC layout with bleed valve, recirculation line and water injection at the compressor inlet (colors as in Figure 51, purple line for the water spray).*

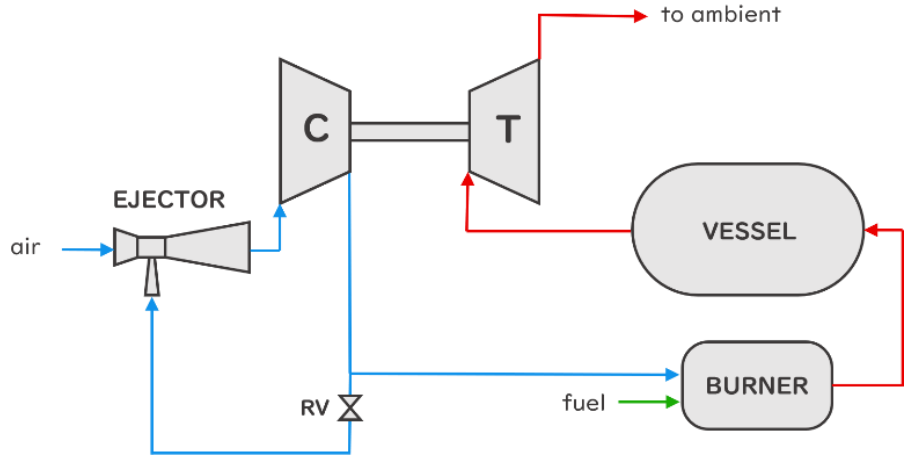

Figure 53. *Simplified turbocharged SOFC layout with recirculation line and ejector at the compressor inlet (colors as in Figure 51).*

5.3 Model Description

To simulate the turbocharged SOFC system, to evaluate the influence of compressor inlet temperature and pressure, and to test the different surge prevention techniques, a dynamic model was developed. The simplified layout presented in the previous section was considered, to take into account the effect of the SOFC volume and thermal output, but without simulating the electrochemical reactions of the fuel cell to reduce the computational effort of the model.

This model was created using the TRANSEO tool and the components of its library, introduced in Section 4.1. For the descriptions of models of turbocharger, ejector, burner and valve the reader is referred to Section 4.1.

Also in this case, most of the TRANSEO components used to create the plant model were already available and validated. In this thesis it was necessary to define the simulation workflow of the model, to interface the various components and to set their characteristic parameters. However, it was necessary to develop the air-water mixer component, based on the modelling approach adopted in [152].

5.3.1 Vessel

The vessel, representing the volume of the fuel cell stack, is simulated using the plenum TRANSEO component [115]. The plenum acts as a rigid volume and it integrates continuity and energy equations, in order to update its internal pressure and temperature on the basis of downstream and upstream mass flow information. In this component the kinetic energy of the mass flow is dissipated through an adiabatic transformation, neglecting heat losses to the ambient. Thus, total and static pressure are assumed to be equal, while the total pressure is conserved. According to the study presented in [96], the volume of the vessel is set equal to 2.8 m^3.

5.3.2 Air-water mixer

The injection of water spray into the air flow is simulated with a 0D air-water mixer model. The mixer updates the air mass flow and composition, simulating the variation of temperature caused by the humidity increase. The computation of psychrometric properties of air are based on the Matlab tool "SI Psychrometric Chart" [152].

5.4 Simulations Results

5.4.1 Effect of inlet air conditions

At first, the effect of different inlet air conditions is evaluated on the dynamic model in two different conditions:

- **Constant turbine inlet temperature.** To keep the $T_{T,in}$ constant, a proportional integrative derivative (PID) controller is implemented on the system. This controller determines the fuel mass flow $\dot{m}_{fuel}$ to the burner in order to match a $T_{T,in}$ setpoint, set equal to 1035 K according to the steady-state analysis presented in Chapter 3.
- **Constant fuel mass flow.** The mass flow of methane to the burner is constant, and the temperature at the turbine inlet may vary during the system operation. The $\dot{m}_{fuel}$ is set to 11.2 10^{-3} kg/s, corresponding to the amount necessary to obtain a $T_{T,in}$ of 1035 K in nominal conditions (T_{amb} =15°C, $\dot{m}_{air}$ = kg/s, $\beta \approx 3.4$).

The first condition is representative of pressurized SOFC systems where the fuel cell exhausts are directly led to the turbine. In details, the fuel cell maximum temperature, which often corresponds to the outlet one, is a critical constraint that must be controlled for the proper operation of the SOFC. The second condition is representative of layouts including other components (e.g. heat exchangers or burners) between the stack outlet and the turbine intake, such as the one introduced in Chapter 2.

All the simulations start in a stable condition with K_p = 1.56, but, after 600 s, the conditions of the compressor inlet air are modified with a step variation of pressure (+10 kPa) or temperature (+5 K). The system is then simulated for 1800 s, in order to reach steady-state conditions.

Figure 54 shows that, when the system runs with constant $T_{T,in}$, the variation of compressor inlet pressure causes a quick growth of K_p, reaching a value of 1.74 after 2 s from the pressure step. However, this is followed by a gradual increase of $p_{C,out}$ and consequently of $p_{T,in}$. The combination of these effects with the action of the temperature controller brings to a similar increase (in percentage) of ω, β and $\dot{m}_C$. Since K_p is directly proportional to $\dot{m}_C$, and inversely proportional to β, its final value is very close to the initial value (K_p = 1.56)

If the fuel mass flow is constant, there is a similar increase of surge margin following the pressure step, with a maximum K_p value of 1.74. Since $T_{T,in}$ is not controlled, its value decreases after the $p_{C,in}$ increase, while the $p_{T,in}$ grows. In comparison with the initial condition, it can be observed that these effects cause a decrease of ω and β, but an increase of $\dot{m}_C$. Consequently, the compressor operative point moves farther from the surge line, and, when the transient is ended, K_p is equal to 1.67.

The early increase of K_p can be explained observing that the air pressure variation is followed by a simultaneous decrease of pressure ratio and increase of mass flow. Observing the example of compressor map in Figure 14, it is evident how this moves the compressor working point far from the surge line.

Figure 55 shows that the increase of $T_{C,in}$ has a similar effect in both conditions (constant $T_{T,in}$ and constant $\dot{m}_{fuel}$). At first there is a small decrement of surge margin: since the air is hotter, it has a lower density, and the mass flow through the compressor decreases, moving the operative point closer to the surge line. Then the K_p increases, because the reduction of pressure ratio becomes prevalent on the decrement of mass flow. When the system reaches a stable point, the K_p is equal to 1.61 for constant $T_{T,in}$, and equal to 1.57 for constant $\dot{m}_{fuel}$.

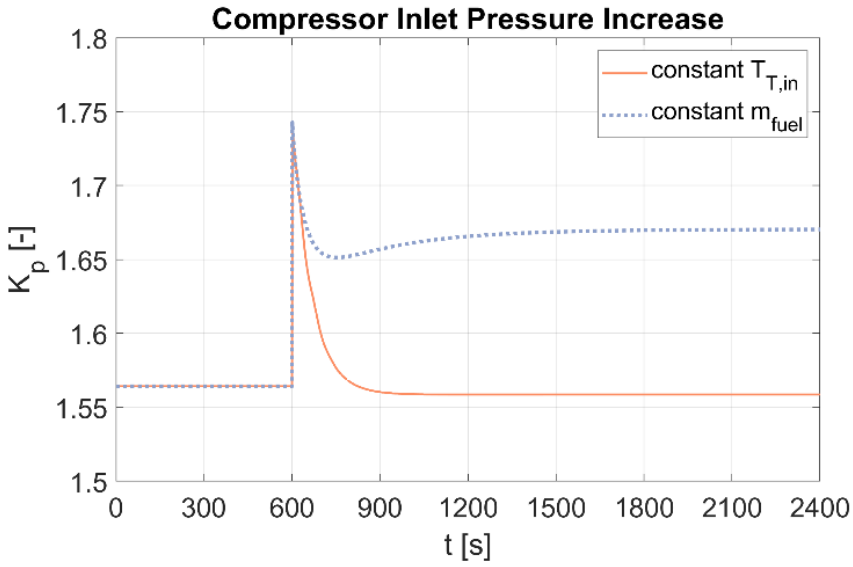

Figure 54. *Variations of K_p caused by a $p_{C,in}$ increase of 10 kPa.*

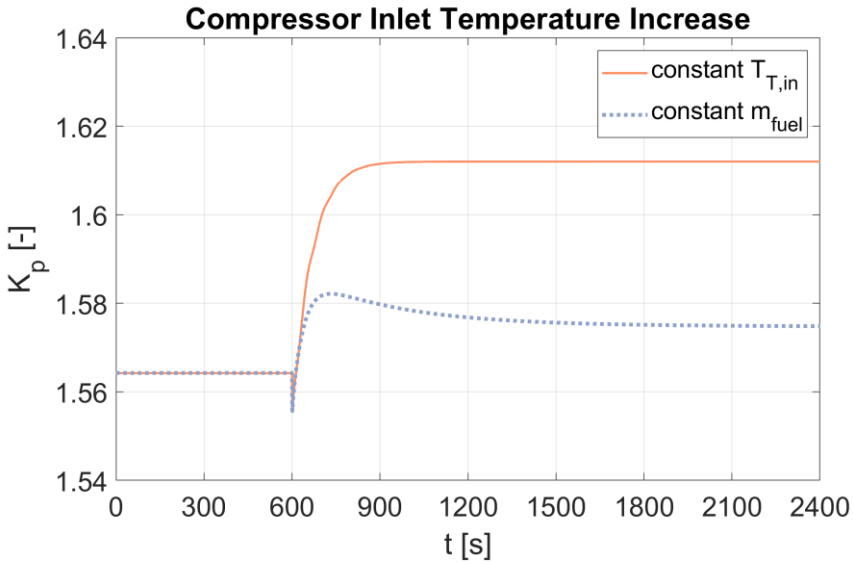

Figure 55. *Variations of K_p caused by a $T_{C,in}$ increase of 5 K.*

5.4.2 Effect of surge prevention & recovery techniques

A second set of simulations is performed to study the effect of the proposed surge prevention techniques (water spray, fogging, bleed, recirculation and ejector-aided recirculation). Similarly to the previous set of simulations, the different procedures are activated after 600 s and observed for the following 1800 s.

The spray at the compressor inlet is simulated assuming an injection of 5.0 10^{-4} kg/s of water at the ambient temperature (288 K). Since the main effect of this procedure is a decrement of about 1.2 K at the compressor inlet, the K_p has an almost symmetrical trend to the one shown in Figure 55, but with a smaller variation in terms of magnitude (Figure 56).

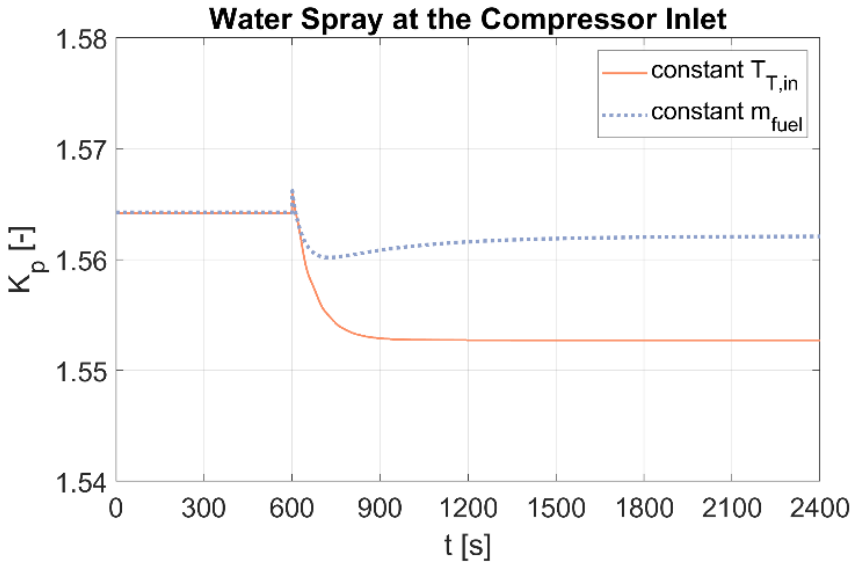

Figure 56: *Variations of K_p caused by a 0.5 10^{-3} kg/s water spray at the compressor inlet.*

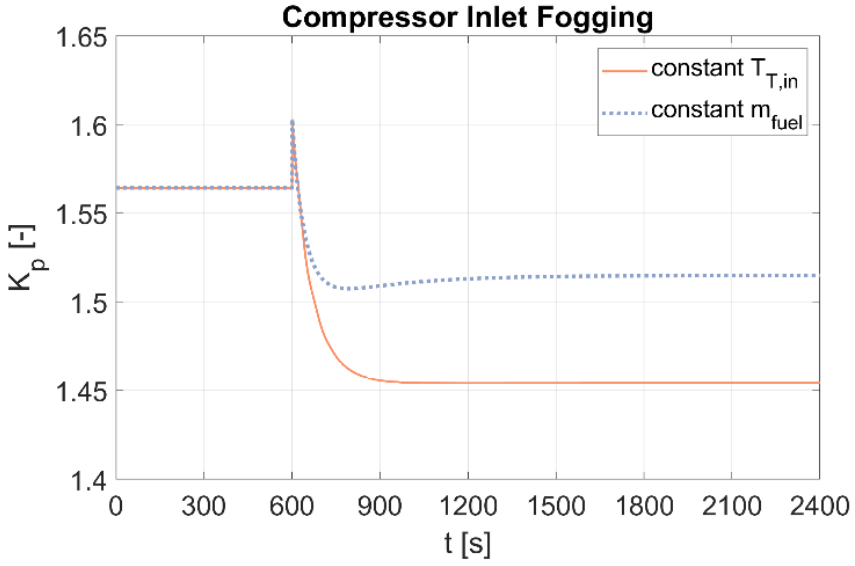

Figure 57: *Variations of K_p caused by compressor inlet fogging.*

Since the TRANSEO compressor model is not able to simulate the presence of liquid water through the impeller, the effect of such fogging is simulated saturating the inlet air flow and reducing of 6% (by assumption) the power drawn by the compressor. Such assumption is in accordance to the analysis presented in [153]. The plot in Figure 57 shows a similar trend to the one observed during the water spray simulation, but the reduction of compressor power consumption, combined with a more substantial injection of water, causes larger variations of K_p. A quick increase of surge margin (K_p = 1.60 after 2 s from the activation of fogging), is followed by a more significant reduction. When the system reaches a stable condition, the turbocharger operates in a different point, characterized by K_p = 1.51 for constant $\dot{m}_{fuel}$ and K_p = 1.45 for constant $T_{T,in}$.

Based on these results, water spray and inlet fogging do not seem to be viable procedures to extend the safe operation range of the SOFC system.

To compare the effectiveness of bleed and recirculation, the openings of both BV and RV are set in order to have 5% of the main air flow diverted through the valve. The opening command of each valve is altered instantaneously, while the variation of mass flow experiences a small time delay.

The variations of K_p caused by these procedures are similar, as shown by Figure 58 and Figure 60, but opening the RV there is a small quick reduction of K_p before it starts growing. This behavior is very similar to the one observed in Figure 55 for the $T_{C,in}$, because recirculation increases the compressor inlet temperature. Also in this case, the cause is the sudden reduction of $\dot{m}_C$ due to the compressor inlet flow density decrease. However, the K_p decrease is just temporary because the effect of the gradual β reduction becomes prevalent very quickly. The values of surge margin at the end of the simulations are significantly higher than the initial value, and the most beneficial effect is achieved opening the RV: K_p = 1.82 for constant $T_{T,in}$ and K_p = 1.68 for constant $\dot{m}_{fuel}$. However, the results obtained opening the BV are still interesting: K_p = 1.75 for constant $T_{T,in}$ and K_p = 1.66 for constant $\dot{m}_{fuel}$. Figure 59 and Figure

61 show how the compressor operative point changes on its maps activating bleed and recirculation, respectively.

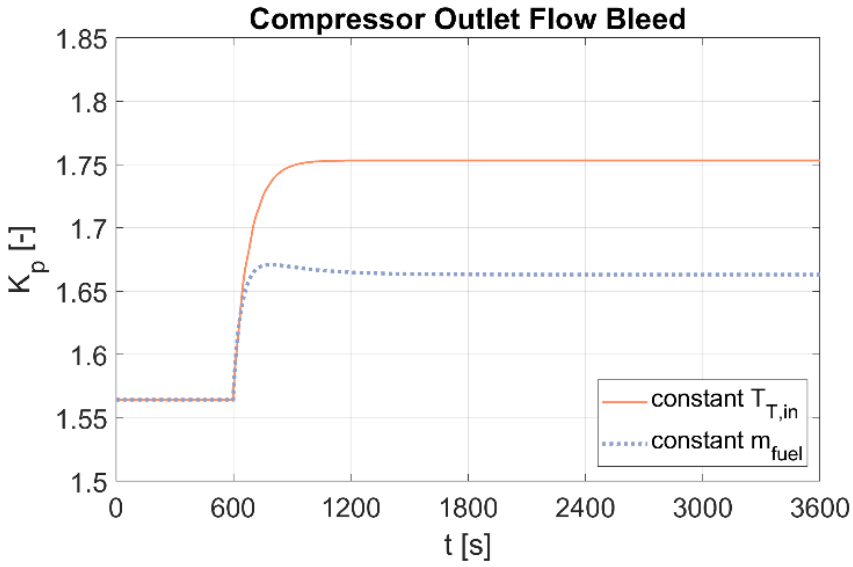

Figure 58: *Variations of K_p caused by compressor outlet flow bleed.*

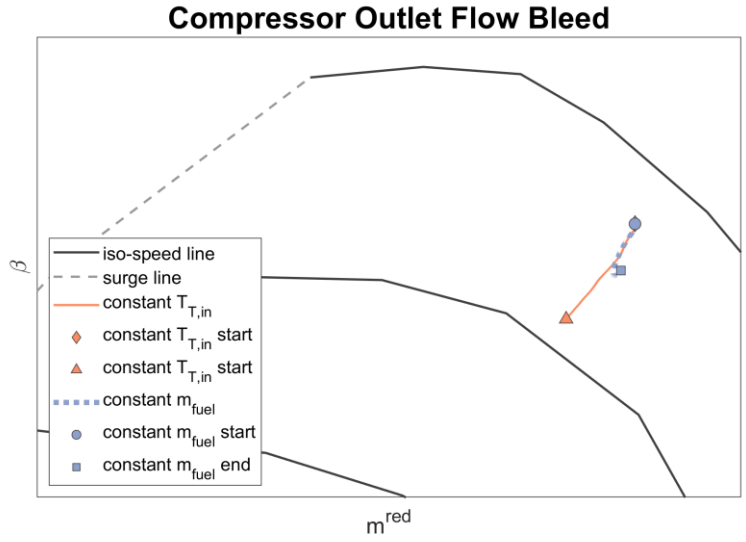

Figure 59: *Variations of the compressor operative point activating compressor outlet flow bleed (the starting point is the same for constant $T_{T,in}$ and constant $\dot{m}_{fuel}$).*

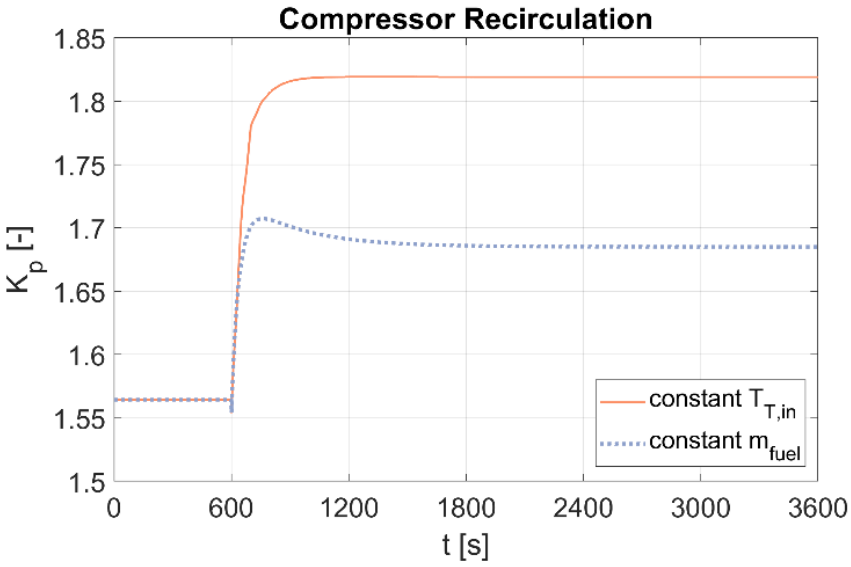

Figure 60: *Variations of K_p caused by compressor outlet flow recirculation.*

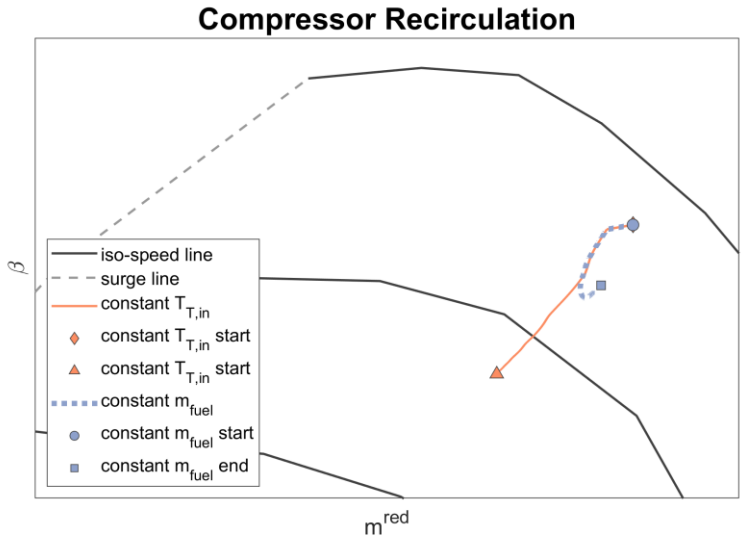

Figure 61: *Variations of the compressor operative point activating compressor outlet flow recirculation (the starting point is the same for constant $T_{T,in}$ and constant $\dot{m}_{fuel}$).*

In both cases, the decrement of mass flow downstream of the compressor lowers the pressure in the system, and consequently the compressor pressure ratio β. Since the mass flow is diverted after the compressor, the reduction of compressor mass flow is limited, and caused only by the smaller power generated by the

turbine. As expected from the performance maps in Figure 14, because of this effect the compressor operative point is moved far from the surge line.

The ejector-aided recirculation is also tested recirculating 5% of the air flow, in order to compare its effect with the standard recirculation. The variations of surge margin observed during the simulations are shown in Figure 62, while the variation of compressor operative point on the maps is shown in Figure 63. Unlike the recirculation case, no reduction of K_p is observed right after the RV opening. This can be explained observing that the ejector-aided recirculation increases $T_{C,in}$, like the recirculation, but also $p_{C,in}$. Figure 54 and Figure 55 showed that an increase of $p_{C,in}$ causes a fast growth of K_p, while increasing $T_{C,in}$ quickly reduces the K_p. Activating the ejector-aided recirculation, these are almost balanced opposite effects, and the K_p does not decrease. The compressor operative point is moved quickly far from the surge line, reaching K_p = 1.82 for constant $T_{T,in}$ and K_p = 1.68 for constant $\dot{m}_{fuel}$. The initial value of K_p is different for the two curves, because the setpoint values of $\dot{m}_{fuel}$ and $T_{T,in}$ are always 11.2 10^{-3} kg/s and 1035 K respectively, but the ejector alters the standard behavior of the system. Therefore, the $T_{T,in}$ obtained with $\dot{m}_{fuel}$ = 11.2 10^{-3} kg/s is different from 1035 K, and values of K_p are different as well.

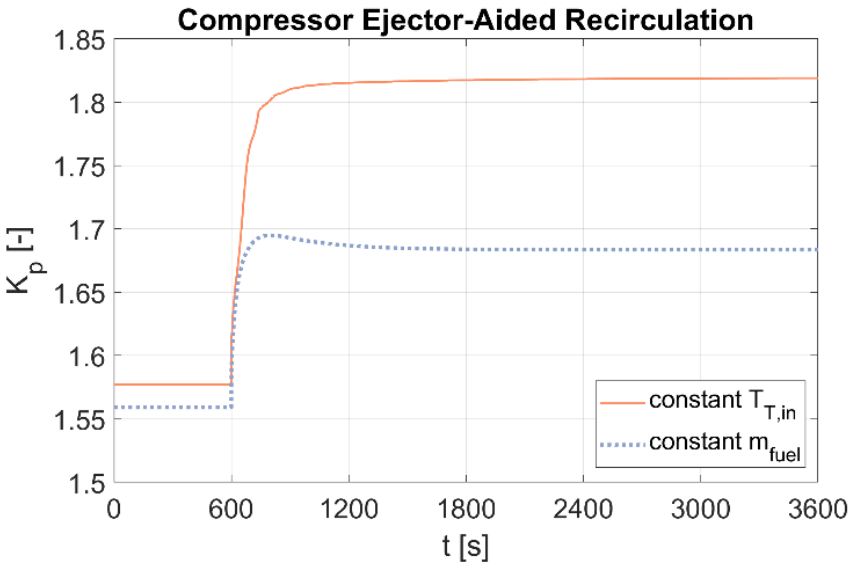

Figure 62: *Variations of K_p caused by compressor outlet flow ejector-aided recirculation.*

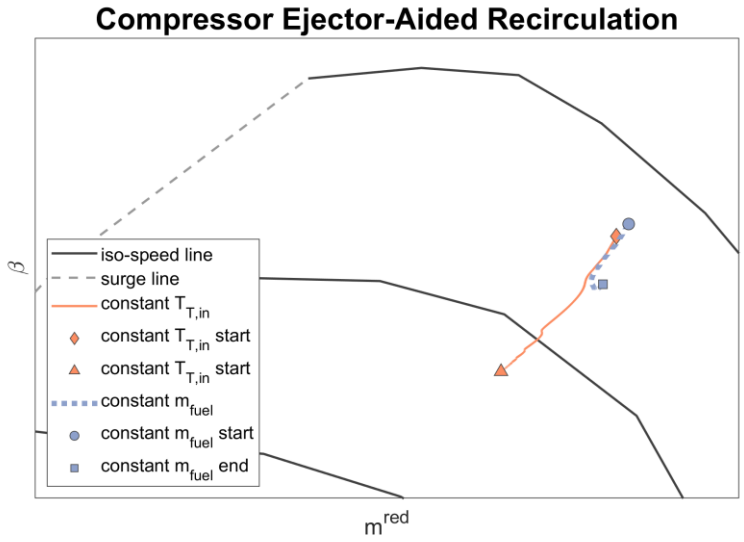

Figure 63: *Variations of the compressor operative point activating compressor outlet flow ejector-aided recirculation.*

This procedure is also more effective than the simple recirculation in terms of responsiveness. Considering the system operating with constant $\dot{m}_{fuel}$, it takes 19 s after the activation of the recirculation to increase of 0.05 the initial value of K_p. Instead, if the ejector-aided recirculation is used, only 8 s are necessary to reach the same increment.

A drawback of this solution is that, when the recirculation is not active, the ejector introduces a pressure loss at the compressor inlet intake, slightly altering the air flow conditions and the compressor operative conditions, as shown in Figure 62.

To compare the effect of all the different procedures on K_p, Table 14 and Table 15 show its maximum increment, maximum reduction and variation at the end of each simulation (in percentage). It is possible to observe that the maximum increase of K_p in steady conditions is achieved by the recirculation for constant $T_{T,in}$ (16.3%), and by the ejector-aided recirculation for constant $\dot{m}_{fuel}$ (8.0%).

Table 14: *Percentage variations of surge margin for constant $T_{T,in}$ (negative values in red).*

Procedure	$\Delta K_{p,max}$	$\Delta K_{p,min}$	$\Delta K_{p,end}$
Water Spray	0.1%	-0.7%	-0.7%
Fogging	2.5%	-7.0%	-7.0%
Bleed	12.1%	0.0%	12.1%
Recirculation	16.3%	-0.7%	16.3%
Ejector-Aided Recirculation	15.3%	0.0%	15.3%

Table 15: *Percentage variations of surge margin for constant $\dot{m}_{fuel}$ (negative values in red).*

Procedure	$\Delta K_{p,max}$	$\Delta K_{p,min}$	$\Delta K_{p,end}$
Water Spray	0.1%	-0.3%	0.1%
Fogging	2.5%	-3.6%	-3.2%
Bleed	6.8%	0.0%	6.3%
Recirculation	9.1%	-0.7%	7.7%
Ejector-Aided Recirculation	8.7%	0.0%	8.0%

On the basis of these results, recirculation and ejector-aided recirculation seem the most promising procedures to prevent & recover compressor surge. In the next section, these techniques will be integrated with the control system of the turbocharged SOFC system and tested in a simulated environment.

5.5 Integration with the Control System

A surge prevention and recovery technique based on compressor recirculation should be activated only when it is necessary, because the reduction of air flow and pressure would negatively affect the SOFC performance.

In a real application, this operation would be possible exploiting a surge precursors detection method, such as those presented in [149,150]. The information provided by one of these tools should be integrated with the SOFC system control strategy in such a way that, when a surge precursor is detected, the recirculation valve is opened.

Since this study is not performed on an experimental prototype, but on a dynamic model, the information from a surge precursor method is not available. Instead, the activation of surge prevention techniques on the model is dependent on the surge margin value: when K_p decreases under a threshold value, set equal to 1.50, the recirculation valve is opened to move the compressor operative point far from the surge line.

It was observed that, for the simplified layout considered in this study, a $\dot{m}_{fuel}$ increase leads to a reduction of K_p. Thus, to prove the effectiveness of the compressor recirculation (with and without ejector), a fuel mass flow variation scenario is simulated. In details, the system runs in nominal conditions for the first 600 s, then the $\dot{m}_{fuel}$ is increased of $2\ 10^{-4}$ kg/s over 900 s. The fuel mass flow is kept constant for the next 900 s and then it is reduced to the initial value with the same slope used previously. Eventually, the system reaches a stable condition, and the simulation ends when t = 4200 s.

Figure 64 shows that the K_p decreases when the $\dot{m}_{fuel}$ is increased, if no surge prevention technique is implemented on the system. Figure 65 shows how the compressor behavior changes if, when the K_p reaches the value of 1.50, the control system activates the surge prevention techniques, i.e. recirculation or ejector-aided recirculation. In both cases 5% of the compressor outlet flow is recirculated through the RV. Even if the K_p grows back to values higher than

1.50, the RV is kept open to avoid oscillations in the system, but it could be closed with a manual reset.

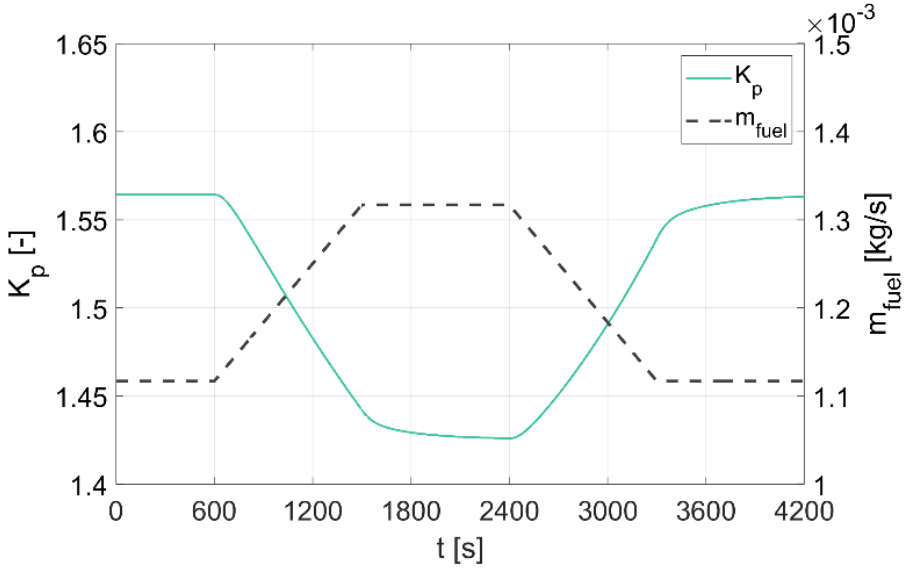

Figure 64: *Variations of K_p (green line) caused by fuel mass flow change (black dashed line), with no active surge prevention technique.*

These simulations confirm the results obtained in the previous Section. The increase of K_p due to the two procedures is similar in steady-state conditions, but there are significant differences during the transients. When the recirculation is activated, the K_p decreases to 1.48 before growing. In this specific case this is not a risk for the safe operation of the compressor, but this behavior must be taken in account for systems designed to operate closer to the surge line. This behavior is not observed during the ejector-aided recirculation simulation, confirming that this solution is also the most responsive of the two: it takes 11 s to increase the K_p of 0.05 after the activation of the ejector-aided recirculation, while il takes 24 s with the recirculation.

Another comparison can be made observing the variations of compressor outlet pressure $p_{C,out}$ (Figure 66) and mass flow $\dot{m}_{C,out}$ (Figure 67), which are parameters impacting on the SOFC performance.

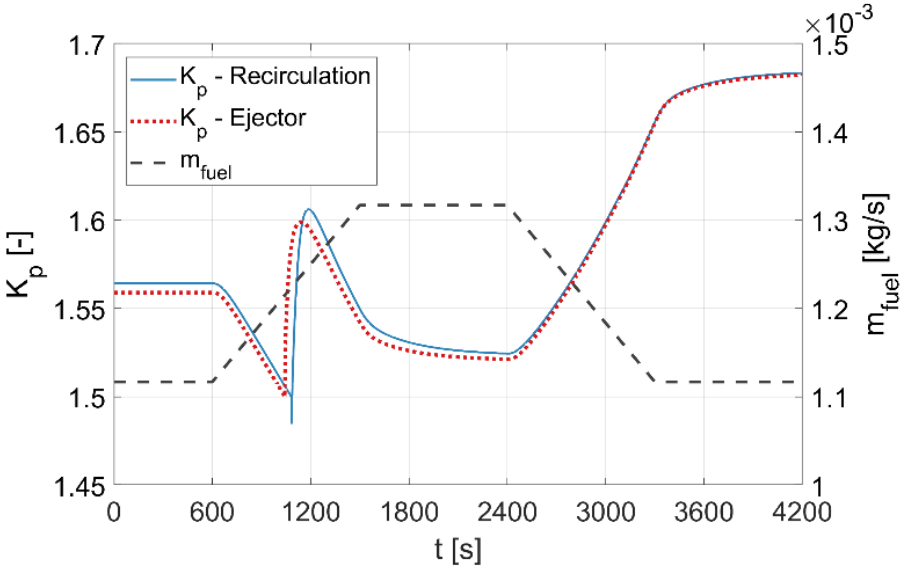

Figure 65: *Comparison between the effect of recirculation (blue line) and ejector-aided recirculation (red dotted line) on the K_p during a fuel mass flow change (black dashed line).*

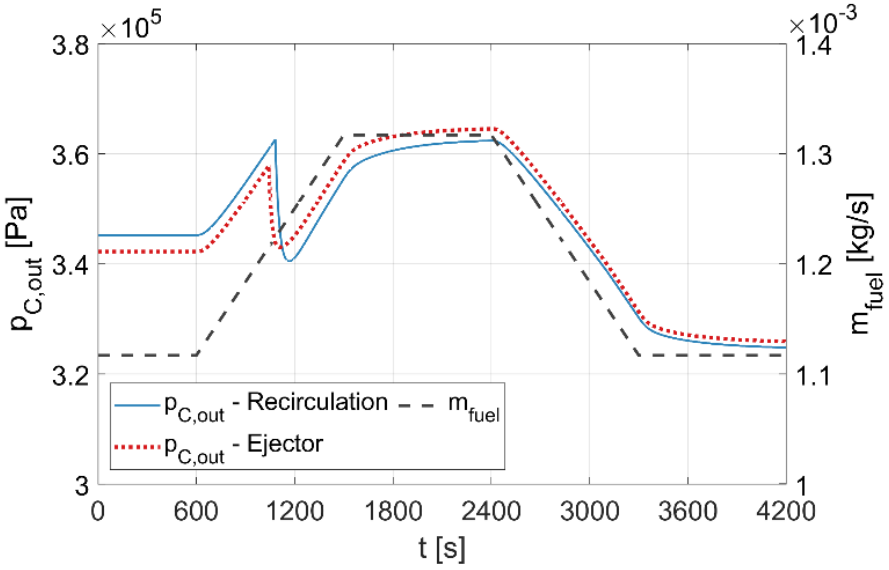

Figure 66: *Comparison between the effect of recirculation (blue line) and ejector-aided recirculation (red dotted line) on the K_p during a fuel mass flow change (black dashed line).*

In standard operating conditions, the ejector pressure loss at the compressor intake has a negative effect on air mass flow (-1.3%), compressor outlet pressure (-0.9%) and surge margin (-0.3%). A lower $\dot{m}_{C,out}$ limits the supply of oxygen at

the SOFC cathode, reducing its capability to oxidize hydrogen and generate power. Instead, lower $p_{C,out}$ reduces the SOFC stack pressure, lowering its power density and efficiency. However, the presence of the ejector mitigates the negative impact of the recirculation on the turbocharger performance, increasing the air mass flow and its pressure. Therefore, as shown in Figure 66 and Figure 67, the values of $p_{C,out}$ and $\dot{m}_{C,out}$ after the opening of the RV are always higher during the simulation with ejector-aided recirculation.

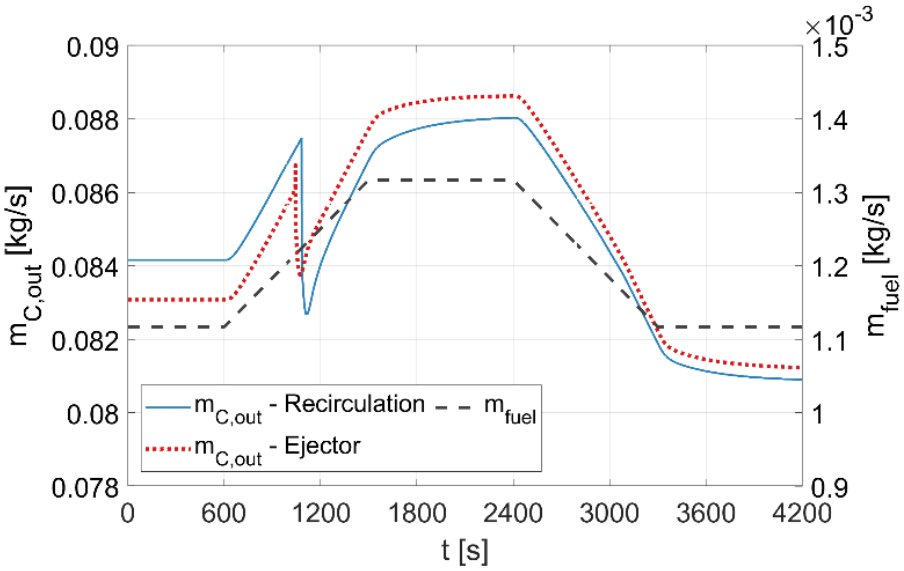

Figure 67: *Comparison between the effect of recirculation (blue line) and ejector-aided recirculation (red dotted line) on the K_p during a fuel mass flow change (black dashed line).*

5.6 Concluding remarks

In this study, many different techniques were tested to prevent or potentially recover compressor surge in a turbocharged SOFC system through a dynamic model developed onto the TRANSEO simulation tool.

Two operating conditions, representative of different pressurized SOFC systems, were considered: (i) constant fuel mass flow and (ii) constant turbine inlet temperature.

A first set of simulations showed the impact of the inlet air conditions on the surge margin. An increase of the $p_{C,in}$ was able to move the compressor operative point farther from the surge line very quickly, but after that the K_p decreased gradually. On the other hand, an increase of $T_{C,in}$ had an almost opposite effect: a quick small reduction of K_p was followed by a gradual increase of its value.

A second set of simulations focused on the effect of the actual surge prevention techniques. Solutions based on the injection of water at the compressor inlet, i.e. water spray and fogging, were not effective. In fact, their main effect was to lower the compressor inlet temperature, leading to a reduction of the K_p after a small quick increment.

On the other hand, techniques based on the partial deviation of the compressor outlet flow (bleed, recirculation and ejector-aided recirculation) were all able to drive a significant growth of the K_p. More in detail, recirculating 5% of the mass flow through the BV caused a K_p increment in stable conditions, equal to +12.1% for constant $T_{T,in}$ and to +6.3% for constant $\dot{m}_{fuel}$. The recirculation, instead, caused an increase of about +16.3% for constant $T_{T,in}$ and of +7.7% for constant $\dot{m}_{fuel}$. In this case, the increase of surge margin was preceded by a quick decrement (-4.8%), which may be detrimental in the short-term.

Ejector-aided recirculation led to similar values of K_p at the end of the transient (increments of +15.3% for constant $T_{T,in}$ and of +8.0% for constant $\dot{m}_{fuel}$), but no reduction of K_p was observed just after the RV opening. This is a remarkable achievement. However, the presence of the ejector at the compressor intake increases pressure losses in normal operation.

From these results, recirculation and ejector-aided recirculation were selected as the most promising surge prevention techniques and integrated with the control strategy of the SOFC system. They were both tested successfully on the TRANSEO model during a $\dot{m}_{fuel}$ variation scenario. The main results of the integrated control hybrid system can be summed up as follows:

- Both the recirculation and ejector-aided recirculation solutions are able to move the compressor operating point far from the surge line, extending its range of safe operation.
- The ejector-aided recirculation avoids temporary reductions of K_p, thus it is more effective to move quickly the compressor operative point far from the surge line.
- The SOFC system equipped with the ejector has slightly lower values of air mass flow, $p_{C,out}$ and K_p during regime operation, due to permanent pressure losses introduced by the ejector itself.
- When activated, the ejector-aided recirculation causes a limited reduction of air mass flow and $p_{C,out}$, which helps a smoother system operation.

In conclusion, both techniques can be effectively implemented to increase the compressor surge margin of a turbocharged SOFC system. The recirculation could be preferred to have a simpler plant layout with better performance in nominal conditions. The ejector-aided recirculation, instead, would be the preferrable solution if it is necessary to increase the K_p quickly, with no temporary reductions during the transients. Despite being a less performing solution, also the compressor bleed could be effectively adopted to prevent surge.

These results are novel for turbocharged SOFC systems, but they could be valuable also for other compressor systems.

The outcomes of this study open the way for future research activities aimed to increase the reliability of turbocharged SOFC hybrid systems. After analyzing the effect of these surge prevention techniques on detailed dynamic models, it will be possible to implement them on emulator plants and, in the future, on a real turbocharged SOFC system prototype. It will also be possible to study more in detail the integration with surge precursors detection tools, for the design of other surge-prevention and surge-recovery strategies and for the validation onto experimental test rigs.

6 Application of Bayesian Networks for Degradation Diagnosis on SOFC-MGT Hybrid Systems

In the previous chapter, the focus was on preventing compressor surge, a fluid-dynamic instability which can heavily damage the SOFC structure. However, this is not the only phenomenon that could compromise the proper operation of the fuel cell in a hybrid system, whether it is an MGT-based or turbocharger-based layout. In details, excessive values of temperature or pressure can cause a structural damage, while feeding the cell with an unsuitable carbon content gas may result in the inhibition of the electrochemical reactions. Therefore, it is crucial to know the degradation level of different components in the hybrid system to improve durability. The status of the main sensors should be also monitored in order to avoid wrong control action, which could be potentially detrimental for the fuel cell.

The development of an accurate diagnosis system for a fuel cell hybrid system is a challenging task due to the high complexity of the system, the interactions between the components and the limited available data compared to large industrial gas turbines or SOFCs applications. For these reasons, only a few studies on diagnostic tools for MGT-based fuel cell hybrid systems are available in literature, while no studies on turbocharged systems currently exist, according to the author's knowledge.

Unlike the other activities carried out for this thesis, the study presented in this chapter considers a SOFC-MGT hybrid system and it aims at developing diagnostic tools based on Bayesian belief networks (BBNs).

When it comes to micro gas turbines, the challenges in fault diagnostics are more than for large units mainly due to the limited number of sensors for cost reduction [154]. Applications of diagnostic methods on micro turbines are limited in the literature [155,156].

Concerning fuel cells diagnostics, several methods have been applied to improve durability and favor fuel cell commercialization; for example, pattern classification was applied to proton exchange membrane fuel cells [157] while quadratic support vector machine was demonstrated successful in diagnosis and prognosis of SOFC [158]. In [159] a fault diagnosis and accommodation system based on fuzzy logic was integrated with neural network augmenters and applied to a SOFC – gas turbine hybrid system. A fuzzy-based failure mode and effect analysis was performed for a molten carbonate fuel cell (MCFC) – gas turbine hybrid system for marine propulsion in [160].

Bayesian belief networks have been used for many decades for fault diagnosis in turbomachinery [161]. Multiple Bayesian models using Bayesian averaging were proved successful in isolating components faults and sensors bias [162]. With a similar approach, a multiple Bayesian network was used to combine additional information such as a degradation model or sensors calibration and enhance diagnosis accuracy [163]. However, the potential of BBNs for the diagnosis of fuel cell hybrid systems has not been investigated yet.

The aim of the study presented in this Chapter is to develop BBNs that could be effectively used for the diagnosis of micro gas turbine (MGT), SOFC and sensors in a SOFC-MGT hybrid system. The study starts focusing on an emulator plant, characterized by a simpler layout, to turn then on a real hybrid system. The BBNs performance is analyzed mainly on steady state simulations results, but a few tests on transient operations data are performed as well. At this stage, validation on experimental results is not possible, because of data unavailability regarding the operation of a real hybrid system in degraded conditions. In fact, fuel cell hybrid systems are still on a research level and, due to their complexity, only a few big companies had the capabilities of developing prototypes [55].

A different layout is considered in this chapter because this work was part of a bi-lateral collaboration project between Università degli Studi di Genova and Mälardalens Högskola, focused on SOFC-MGT hybrid systems. However, the approach adopted here could be extended to different plants and applied to

develop diagnostic systems for a turbocharged SOFC system. The project was funded by the Italian Minister of Education and the Swedish Research Council, and the research activity was carried out by the author of this thesis in 2019, during a period of 4 months with the SOFIA Group of Mälardalens Högskola in Västerås, Sweden.

The outcomes of this work were presented at the ASME Turbo Expo 2020 [164] and will be partially published on the Journal of Engineering for Gas Turbines and Power in 2021.

6.1 Plant Layouts

Since SOFC-MGT hybrid systems are not fully commercial yet and even lab-scale prototypes are not easily available, experimental research was often carried out on system emulators, for example exploiting cyber-physical simulations [165]. For this reason, the diagnostics system was developed and tested on two configurations: a hybrid system emulator and a complete SOFC-MGT hybrid system. The reason for considering first the hybrid system emulator was to neglect at first the fuel cell electrochemistry; results on such system will be essential for future experimental tests on the emulator rig present at University of Genoa. The first diagnosis system is hence applied on the model of the SOFC-MGT emulator test rig of University of Genoa (Figure 8), whose layout was considered as adopted in [166]. This setup is based on a recuperated Turbec T100 – Series 3 unit, able to generate 100kW of electrical net power when operating with natural gas in nominal conditions, with an electric efficiency of 30% [167]. The influence of the fuel cell system volume (including reformer, off-gas burner, and recirculation) on the dynamic behavior of the system is emulated with a pressurized vessel with a volume of $4m^3$, while its thermal output is recreated by a burner. The fuel mass flow is determined by a proportional-integrative (PI) controller to keep the $T_{T,out}$ equal to a set-point, 600°C in this work. Another control loop is used to regulate the power output of

the system according to the load demand as in [166]. This configuration is especially apt for cyber-physical simulations and control development as discussed in [165].

The second application is on the full hybrid system model based on the coupling of a SOFC stack with a MGT, whose layout is shown in Figure 68. This is the layout that was considered to design the emulator plant, and its characteristics were defined in previous studies [72,168]. The stack contains tubular SOFCs with a total area of ~188 m^2. The MGT is again an AE-T100 unit. This system was designed to generate 353kW of electrical net power when operating in nominal conditions, of which 287kW are produced by the SOFC. In nominal conditions, the hybrid system is fed with a biogas, whose chemical composition is reported in Table 16.

The stack exhausts, expanding in the turbine, drive the compressor, pressurizing the SOFC with a positive effect on its performance [45,169]. The MGT is equipped with an electric generator, contributing to the overall system electric power output.

After being compressed, the air flow is pre-heated by a heat exchanger, mixed with part of the cathode outlet flow and lead into the SOFC cathode inlet. The fuel flow goes through the ejector primary nozzle, driving a partial recirculation of the anode outlet flow. At this point the ejector outlet flows enters the stack anode side. Before taking part in the electrochemical reactions, the fuel must be processed. In fact, the fuel considered in this analysis is not H_2, but a biogas composed mainly by CH_4 and CO (Table 16). Thanks to methane steam reforming (MSR) (1) and water gas shift (WGS) (2) reactions [85] occurring in the REF, H_2 is obtained from the biogas. The recirculation of cathode and anode flows is crucial to provide the proper amount of heat and steam necessary to drive these reactions.

In the SOFC the O^{2-} ions move through the electrolyte from the cathode to the anode, where they participate to the electrochemical oxidation of H_2 (3). The

electrons e^- released by this reaction migrate from the anode to the cathode through an electrical connection, generating the electrical power [42].

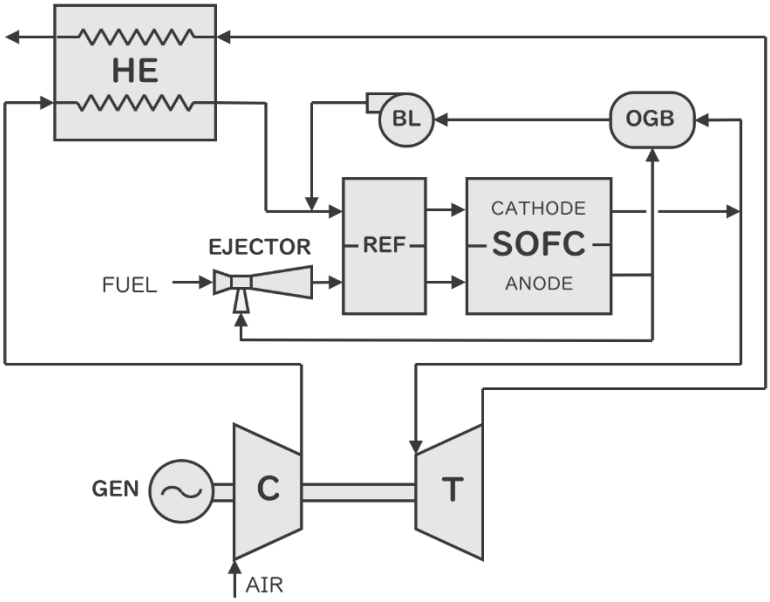

Figure 68. *Plant layout of the SOFC-MGT hybrid system.*

Table 16. *Biogas mass percent composition.*

Substance	Mass fraction
CH_4	71.9%
CO	17.4%
CO_2	5.0%
N_2	3.3%
H_2O	2.4%

The part of anode outlet flow which is not recirculated by the ejector goes into an off-gas burner (OGB), and so does part of the cathode outlet flow. The portion of fuel that did not react in the SOFC is burnt in the OGB and then recirculated to the cathode inlet by a blower.

Part of the cathode outlet flow expands in the turbine, pre-heats the compressed air flow through the heat exchanger (HE) and is finally discharged into the atmosphere. The total electric power generated by the fuel cell stack and the cathode inlet temperature are controlled by two proportional-integrative-derivative (PID) controllers as in [106].

While the hybrid system model represents the real system as shown in Figure 68, in the emulator model, the components SOFC, reformer, ejector, and OGB are simulated simply as mixing volumes and the control of fuel cell parameters (such as power or temperature) is not present.

6.2 Model Description

6.2.1 Component models

The emulator plant and the hybrid system dynamic models were created in Matlab®-Simulink® combining the components of an original Real Time library developed previously at TPG by other researchers. The Real Time library is based on the same logics of the TRANSEO tool introduced in Chapter 4, with some simplifications introduced to reduce the computational demands and achieve real-time capabilities.

The components models are all based on the numerical solution of momentum, energy and mass balance equations [114,165], with the exception of the MGT shaft, the electrical devices and the fuel valve. With the aim of integrating these models with a control system in the future, some simplifications were adopted to be able to run the simulations in real-time. The validation of these tools was performed comparing the simulations results with experimental data in [155,165,170].

The compressor and turbine 0D models are based on the interpolation of steady state maps of rotational speed, mass flow, efficiency and pressure ratio. The rotational speed of the shaft is determined from the MGT power balance

equation, considering mechanical losses and the efficiency of the electrical devices.

The combustor model, used to simulate the OGB, is based on a 0D approach. Its steady state performance calculation relies on the solution of the global energy equation, considering inlet flows properties and combustion efficiency.

The heat exchanger is spatially discretized into 10 sections according to the 1D scheme adopted in [170], taking into account different properties for hot side, cold side and solid structure.

The 0D SOFC model (in the hybrid system model) is based on the approach proposed in [171]. It simulates the fuel cell thermal and electrochemical performance, considering reactions at chemical equilibrium and neglecting the contribution of CO. The real voltage V_{real} is obtained subtracting Ohmic, activation and concentration losses from Nernst's ideal value (23). More details regarding the computation of the losses terms can be found in [171]. The electric power generated by the SOFC is determined as the product between V_{real}, the cell electric current density j_{cell}, the total area of cells in the stack A_{cell} and the inverter efficiency η (40).

The reformer (REF) model, which is based on a 0D approach, computes the anode composition solving MSR and WGS reactions at equilibrium. To be able to achieve real-time performance, the stack heat loss to the ambient is assumed equal to zero.

The ejector model was developed with a lumped volume procedure, taking into account the momentum loss in the primary nozzle, the viscous pressure losses in the diffuser and in the mixing chambers. The transient behavior of the ejector is simulated considering also the heat exchange between the flows, the solid structure and the ambient [125].

The fuel mass flow is determined through a linear relationship with the fuel valve fractional opening. The pipes between the main components are modeled considering both thermal and viscous losses.

The model was validated by other researchers in previous studies, comparing simulation results with experimental data. Most of the components were validated at first in [165], while a detailed validation of recuperator and MGT was performed in [170] and [155] respectively.

6.2.2 Degradation simulation

For this thesis, it was necessary to modify the Real Time models of MGT and SOFC, including many performance deviations parameters to simulate the degradation of the components. The deviation from the standard behavior of the MGT is represented by the flow correction factor (CAW) and the efficiency delta (DAE), defined for both compressor and turbine as in Eq. (50).

$$\mathrm{CAW} = \frac{\dot{m}}{\dot{m}_n} \qquad \mathrm{DAE} = \frac{\eta}{\eta_n} \tag{50}$$

Fuel cell degradation can be caused by many phenomena such as impurities in the fuel, excessive temperatures, fuel starvation etc., but they commonly all have the effect of reducing the operating voltage. Hence, in the model, this effect is represented with the coefficient Fv, defined as in Eq. (51).

$$\mathrm{F_V} = \frac{V_{cell}}{V_{cell,n}} \tag{51}$$

The effect of a sensor degradation is simulated altering the measurement, in order to have a biased result to be processed by control or diagnosis systems.

6.3 Bayesian Belief Networks

A Bayesian belief network is a graphical representation of probabilistic dependency between variables based on Bayesian theory of probability. The structure of a BBN is a direct acyclic graph where nodes represent random variables and are connected by edges, which show probabilistic dependency between the connected variables. Probability distributions need to be known for

each node. If an event X causes the effect Y and Y is observable, the probability of X being the cause of Y can be derived from Eq. (52) according to the Bayesian theory.

$$P(X|Y) = \frac{P(Y|X)}{P(Y)} P(X) \tag{52}$$

In (52), *P(X)* is called a priori probability distribution, and *P(Y|X)* is called conditional probability distribution. In a BBN, both the direct acyclic graph and the probability distributions for each node can be constructed either manually or from data. The most popular techniques for identifying conditional probabilities from data are the maximum likelihood estimation and the Bayesian estimation [172].

An example of BBN structure is depicted in Figure 69, where X_i nodes represent the occurrence of fault type 'i' and Y_j nodes denote the measured deviations 'j' induced by each fault.

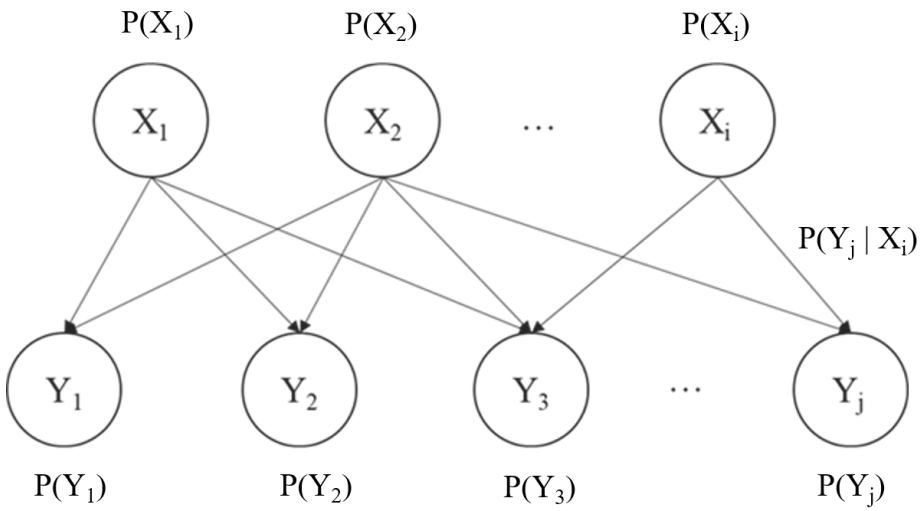

Figure 69: *An example of Bayesian belief network structure, with details of a priori probability distributions for each node and the conditional probability distribution for the j-th event and the i-th cause.*

Bayesian networks have been extensively used fault diagnosis in gas turbines, and multiple examples can be found in the literature of BBNs application to modeling of gas turbine components, anomalies detection, and fault identification [161,162,173].

In this Chapter BBNs will be developed to diagnose the status of turbocharger and SOFC. These components we selected as case studies because they are the main components of the hybrid system. However, the methodology proposed here could be applied also to other components, such as recuperator or reformer.

6.4 MGT Diagnosis in Hybrid System Emulator

The first diagnosis system developed for this study is a BBN aimed at detecting degradation of compressor and turbine in the hybrid system emulator, which does not include the SOFC. In the next paragraphs, the same procedure will be applied to the complete SOFC-MGT hybrid system. The values of CAW and DAE considered are between 1.00 and 0.95 and they were sorted in 3 categories, defined by the author according to the experience of his colleagues, and shown in Table 17.

Table 17. *Maximum and minimum values of degradation parameters categories.*

Category	Description	Max Value	Min Value
H	Healthy	1.000	0.995
d	Minor degradation	0.995	0.980
D	Major degradation	0.980	0.950

The d category includes scenarios where a component is starting to degrade, while the D category includes conditions where maintenance should be performed soon. However, the severity of a condition cannot be determined just by the degradation parameters values, and the possibility of recovering the

component must be evaluated based on the specific degradation phenomenon occurring.

The diagnosis system should be able to predict the status of each degradation parameter based on the measurements collected by sensors installed on the MGT. The measurements that were considered in this case are $\dot{m}_C$, $p_{C,out}$, $T_{C,out}$, $p_{T,in}$, $\dot{m}_{fuel}$, N_{shaft}, $p_{T,out}$, $T_{T,out}$.

Running the emulator model in steady state conditions, two sets of simulations were performed: the first one varying CAW_C and DAE_C and setting CAW_T and DAE_T equal to 1, the second one varying CAW_T and DAE_T and setting CAW_C and DAE_C equal to 1. As example, Figure 70 shows how the ratio $\Delta N_{shaft}/N_{shaft,n}$ changes varying the compressor degradation parameters. In this specific case, the control system must increase the MGT rotational speed when the performance of the compressor decreases for a reduction of CAW_C or DAE_C, leading to the trend shown in Figure 70.

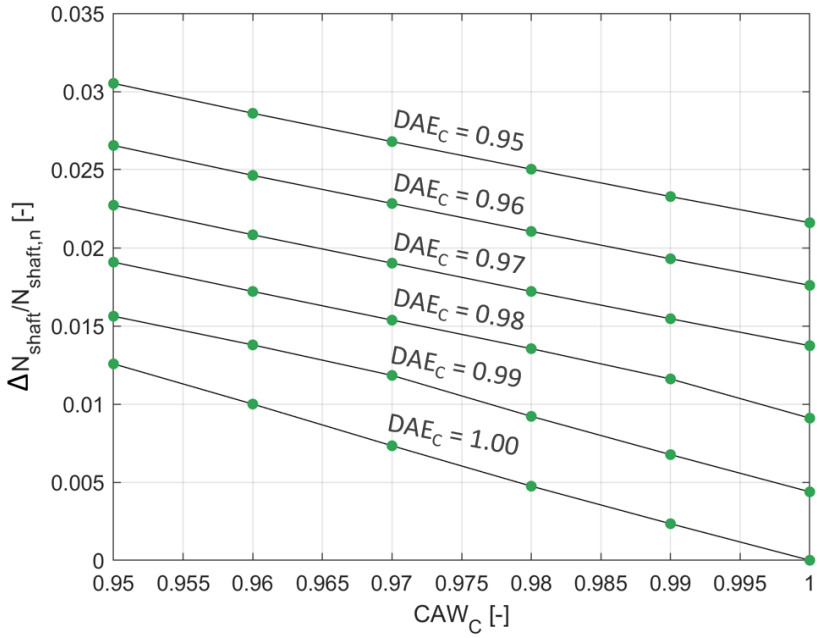

Figure 70. *Trend of $\Delta N_{shaft}/N_{shaft,n}$ varying CAW_C and DAE_C (CAW_T and DAE_T equal to 1.00).*

From the analysis of the results in the considered operating range, it was observed that all the physical quantities vary with a trend that, with good approximation, can be considered linear. Thus, it is possible to perform a linear interpolation between steady state points to generate intermediate points in a sufficient quantity required for the BBN train and test. The linear interpolator accuracy was tested based on the results of 20 simulations: half of them with compressor degradation (CAW_C and DAE_C chosen randomly) and the other half with turbine degradation (CAW_T and DAE_T chosen randomly). The interpolation precision turned out to be always higher than 99.93%. In this way it is possible to generate quickly a big amount of data, which can be used to train and test the BBN.

The training data set is composed by 18000 points, while the test data set by 7200 points, both equally divided between cases where the compressor is degraded and where the turbine is degraded. In order to develop a robust diagnosis system, all these data were altered adding a random noise to take into account deviations from the standard behavior of the system and inaccurate measurements. The maximum values of these noise levels are shown in Table 18.

Table 18. *Maximum values of noise (percentages referred to nominal conditions measurements) on the training and test data sets for MGT diagnosis systems.*

Data	Maximum Noise	Data	Maximum Noise
$\dot{m}_C$	±0.15%	$\dot{m}_{fuel}$	±0.50%
$p_{C,out}$	±0.25%	N_{shaft}	±0.45%
$T_{C,out}$	±0.20%	$p_{T,out}$	±0.25%
$p_{T,in}$	±0.25%	$T_{T,out}$	±0.10%

Since the diagnosis system has to predict the status of the degradation parameters based on the measured quantities, the BBN was created in Hugin Expert according to the scheme showed in Figure 71 and trained on the training

data set. The measurements are not treated as continuous quantities, but they are sorted in intervals. The number of intervals is different for each node (between 5 and 7) and it was selected empirically to have the best performance.

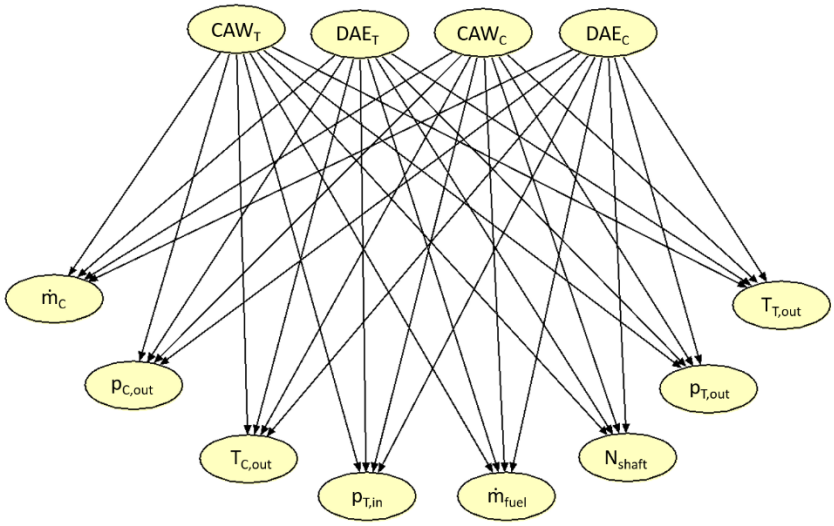

Figure 71. *Structure of the BBN used for the MGT diagnosis.*

Testing the BBN on the whole test data set and comparing the network predictions with the actual values of the degradation parameters, it was possible to compute the exact prediction rate (R_{pred}) for each one of them. R_{pred} is defined as the ratio between the number of correct predictions made by the BBN and the total number of predictions made by the BBN. The values of R_{pred} are showed in Table 19.

Table 19. *Exact prediction rates of the diagnosis system for the emulator plant MGT.*

Degradation Parameter	**R_{pred}**
CAW_C	0.7243
DAE_C	0.9431
CAW_T	0.8547
DAE_T	0.9761

It is worth pointing out that the BBN is very precise in detecting an efficiency reduction in compressor and turbine. The R_{pred} values are lower for the *CAW*s, but still valuable, especially considering that efficiency and flow capacity deviations are likely to occur together in a component (due to fouling, erosion, etc.) So, it is sufficient that one of the two parameters is detected to flag an alarm. To explain why the R_{pred} values are lower for the *CAW*s, it important to remember that in a hybrid system, the air mass flow and the compressor outlet pressure have direct impact on the SOFC performance. However, in the emulator plant, the SOFC is not present, and compressor degradation could have a more limited effect on the system, being thus more difficult to detect.

To analyze more deeply the BBN performance, three possible conditions of the components were defined:

- If at least one of the degradation parameters is in the D category, the component is heavily degraded (D);
- If at least one of the degradation parameters is in the d category, but no parameters are in the D category, the component is slightly degraded (d);
- If all the degradation parameters are in the H category, the component is healthy (H).

Confusion matrices for both compressor and turbine were created to understand how often the condition of these components is properly detected (Table 20).

Table 20. *Confusion matrix of compressor and turbine status detection for the emulator plant MGT (in green exact predictions, in yellow minor mistakes, in red significant mistakes).*

C		**Detected**		
		D	d	H
Real	D	1633	195	172
	d	245	499	456
	H	89	9	3902

T		**Detected**		
		D	d	H
Real	D	1868	132	0
	d	59	1009	132
	H	1	37	3962

It is possible to observe that the BBN makes an exact prediction in 95.00% of the cases for the turbine and in 86.58% for the compressor. The percentage of cases where a healthy condition is diagnosed as heavy degradation or vice versa (red cells in Table 20) is negligible for the turbine (0.1%) and low for the compressor (3.63%).

6.5 MGT Diagnosis in Hybrid System

In the previous section it was proved that a BBN structured according to Figure 71 can be used effectively to diagnose the status of compressor and turbine in a hybrid system emulator plant (where the SOFC is not present) operating in

stationary conditions. Based on these promising results, the same procedure was adopted for the diagnosis of the MGT in the complete hybrid system presented in Section 6.1.

Two sets of simulations were run on the hybrid system model in steady state conditions. In the first set the values of CAW_C and DAE_C vary, while CAW_T and DAE_T are always equal to 1. In the second set the values of CAW_T and DAE_T vary, while CAW_C and DAE_C are always equal to 1. Also in this case it was possible to approximate the system stationary behavior, in terms of $\dot{m}_C$, $p_{C,out}$, $T_{C,out}$, $p_{T,in}$, $\dot{m}_{fuel}$, N_{shaft}, $p_{T,out}$, $T_{T,out}$, with a linear interpolator. Testing it according to the procedure explained in Section 6.4, its precision was always higher than 99.91%. A training data set of 18000 points and a test data set of 7200 points were generated from this interpolator as described in Section 6.4 and altered with random noise (maximum values in Table 18).

To be able to compare the performance of the BBN when implemented on the hybrid system MGT and on the emulator MGT, the same structure shown in Figure 71 was adopted. However, it was necessary to redefine the measurements intervals according to the new simulations results.

The BBN was tested and the R_{pred} values of all the degradation parameters were computed (Table 21).

Table 21. *Exact prediction rates of the diagnosis system for the hybrid plant MGT.*

Degradation Parameter	**R_{pred}**
CAW_C	0.9321
DAE_C	0.8535
CAW_T	0.9458
DAE_T	0.9271

Compared to the emulator MGT analysis, these results show that, using a BBN for the monitoring of a MGT in a hybrid system, it is possible to predict more

accurately the mass flow reduction (higher R_{pred} for CAW_C and CAW_T), but the precision is lower for efficiency losses detection (lower R_{pred} for DAE_C and DAE_T).

Table 22 shows the confusion matrices for compressor and turbine that were created referring to the same conditions defined in Section 6.4.

The percentages of exact predictions are slightly higher than those obtained with the emulator MGT diagnosis system: 90.19% for the compressor and 95.04% for the turbine. The percentage of cases where a healthy condition is diagnosed as heavy degradation or vice versa (red cells in Table 22) are negligible for both compressor (0.03%) and turbine (0.01%).

Table 22. *Confusion matrix of compressor and turbine status detection for the hybrid plant MGT (in green exact predictions, in yellow minor mistakes, in red significant mistakes).*

C		**Detected**		
		D	d	H
Real	D	1833	167	0
	d	62	663	475
	H	2	0	3998

T		**Detected**		
		D	d	H
Real	D	1825	175	0
	d	55	1026	119
	H	1	7	3992

The fact that the diagnosis system performance is better on the hybrid system than on the emulator is an interesting result, and the reasons behind it have been investigated. It was observed that the influence of the degradation parameters on the systems behavior is different, mainly due to differences in

turbine outlet temperature control strategies. In the emulator plant, degradation of turbine and compressor influences in a similar way most of the measurements considered ($\dot{m}_C$, $p_{C,out}$, $T_{C,out}$, $p_{T,in}$, $\dot{m}_{fuel}$, N_{shaft}, $p_{T,out}$, $T_{T,out}$). However, this is not true for the complete hybrid plant and this is helpful to diagnose correctly the system status. For example, varying the values of CAW_C and of CAW_T, the effect on the $p_{C,out}$ is similar in the emulator plant. On the hybrid system, instead, the value of $p_{C,out}$ increases when the CAW_T decreases, while it decreases when CAW_C decreases. Therefore, monitoring the measurement of $p_{C,out}$ provides more information regarding the MGT status in the hybrid system than in the emulator plant.

These results show that, despite the complexity of the hybrid plant considered in this study, using a BBN is an effective way to diagnose the status of an MGT when included in such a system.

6.6 SOFC Diagnosis in Hybrid System

The last BBN developed within this work has the purpose of diagnosing the SOFC status in the hybrid system. If the SOFC degrades, a drop in V_{cell} can be observed. However, this is not the only potential cause of a voltage reduction: if there is a fault in the sensor measuring the $T_{cat,in}$, the action taken by the control system in order to keep this temperature constant will be wrong. More specifically, if the measurement is higher than the real value, the SOFC will be forced to operate at a lower temperature than its design value, decreasing its performance and thus the V_{cell}. A SOFC diagnosis system should be able to understand if a V_{cell} reduction is caused by a cell fault or by a sensor bias, based on other measurements of the system ($T_{cat,in}$, $T_{cat,out}$, $p_{cat,out}$, $\dot{m}_{fuel}$). This information is extremely valuable to ensure proper operation of the system. Knowing the SOFC status, it would be possible to slow down the degradation process acting on the control system, e.g. reducing the power generation, and thus extending the service life of the hybrid system. The detection of a biased

$T_{cat,in}$ measurement, instead, would allow for intervening on the problem, avoiding wrong control actions that may damage the SOFC.

Running the hybrid system model in steady-state conditions, two sets of simulations were performed: the first one reducing the V_{cell} to simulate a SOFC degradation, the second one considering different levels of bias on the $T_{cat,in}$ sensor. For both sets a variation of V_{cell} between 100% and 97% of its nominal value is considered. How the physical quantities of interest vary is shown in Figure 72 for the first set of simulations, and in Figure 73 for the second one. Since a bias on the cathode inlet temperature sensor can be present, both the actual value $T_{cat,in}$ and the one measured by the sensor $T_{cat,in,sens}$ are plotted.

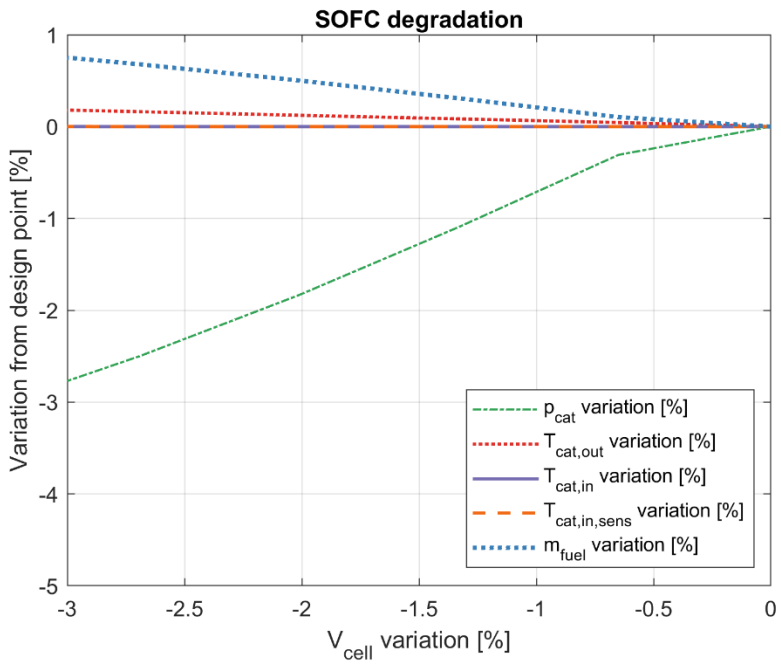

Figure 72. *Variation from design point of hybrid system physical quantities vs V_{cell}, simulating SOFC degradation (values of $T_{cat,in}$ and $T_{cat,in,sens}$ are coincident).*

In Figure 72 it is possible to observe that, when the $T_{cat,in}$ measure is correct, its value does not change due to SOFC degradation, because the control system always manages to keep it equal to the setpoint value.

In both sets all the measurements vary with a monotonous trend. Therefore, it is easy to approximate well the system behavior with fitting curves, which can

be used to generate the data necessary to train and test the BBN, similarly to what was done for the MGT. In this case 4th order polynomials were used as fitting curves and they were tested based on the results of 20 simulations: half of them with SOFC degradation (V_{cell} reduction chosen randomly) and the other half with $T_{cat,in}$ sensor fault (measurement bias chosen randomly). The polynomials precision turned out to be always higher than 99.92%. The diagnosis system is designed in a way that only faults that cause a drop in V_{cell} over 0.5% are considered relevant.

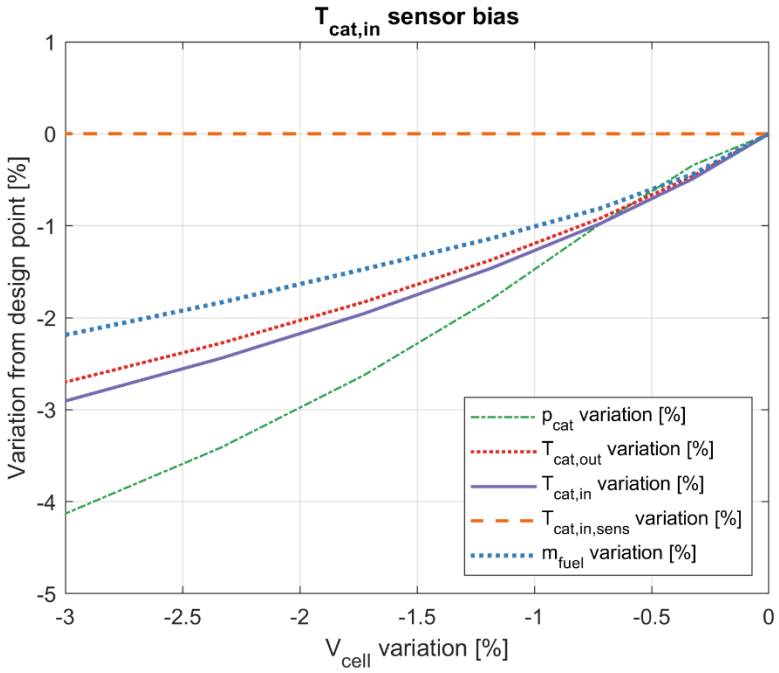

Figure 73. *Variation from design point of hybrid system physical quantities vs V_{cell}, simulating $T_{cat,in}$ sensor bias (values of $T_{cat,in}$ and $T_{cat,in,sens}$ are different).*

The training data set generated in this way is composed by 25000 points, while the test data set by 10000 points, both equally divided between the following cases:

- Healthy system (H);
- SOFC fault with V_{cell} drop under 0.5%, still considered healthy (H);
- SOFC fault with V_{cell} drop over 0.5%, (D);

- Biased temperature sensor with V_{cell} drop under 0.5%, still considered healthy (H);
- Biased temperature sensor with V_{cell} drop over 0.5% (D);

Random noise was added to all these data to develop a robust diagnosis system, considering deviations from the standard behavior of the system and inaccurate measurements. The maximum values of these noise levels are shown in Table 23.

Table 23. *Maximum values of noise on the training and test data sets for SOFC diagnosis system.*

Data	Maximum Noise
V_{cell}	±0.50%
$P_{cat,out}$	±0.25%
$T_{cat,out}$	±0.10%
$\dot{m}_{fuel}$	±0.50%
$T_{cat,in}$	±0.10%

To design the BBN structure, it was necessary to consider that, in this specific case, the diagnosis system must be able to detect the plant status observing how the system behavior is affected by the V_{cell}. After many trials, the structure showed in Figure 74 was selected and the BBN was created in Hugin Expert. All the measurements are sorted in intervals (between 5 and 7 depending on the node).

The diagnosis system was tested on the whole test data set. To analyze its performance, the R_{pred} values for the status of SOFC and temperature sensor were computed (Table 24) and the confusion matrices were created (Table 25).

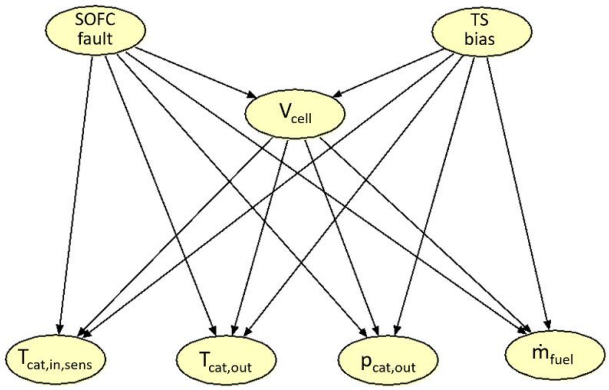

Figure 74. *Structure of the BBN used for the SOFC diagnosis.*

Table 24. *Exact prediction rates of the SOFC diagnosis system.*

Component Status	**R_{pred}**
SOFC degradation	0.9718
$T_{cat,in}$ sensor bias	0.9764

Table 25. *Confusion matrix of SOFC and cathode inlet temperature sensor status detection (in green exact predictions, in red wrong predictions).*

SOFC		**Detected**	
		D	H
Real	D	1764	236
	H	46	7954

$T_{cat,in}$ sensor		**Detected**	
		D	H
Real	D	1943	57
	H	179	7821

From the results of this analysis the BBN seems able to detect the cause of a voltage drop with a high level of precision. More in details, the status of the SOFC is diagnosed correctly on the 97.18% of the cases, while the status of the temperature sensor on the 97.64%.

Based on these promising results, the BBN was tested also on dynamic simulations of the system. In this new setup, the measurements necessary for the BBN prediction are averaged over a time span of 60s and then altered with random noise, always according to Table 23. The capabilities of BBNs for online diagnosis could have been evaluated on the MGT as well. However, only the tests for SOFC degradation are presented in this thesis for the sake of brevity.

During the first simulation, a SOFC degradation occurred after 100 min and the FV decreased over 300 min before stabilizing on a value equal to 0.99. The predictions of the diagnosis system are showed in Figure 75. The performance of the BBN is good, with a SOFC status R_{pred} equal to 0.8860. The temperature sensor was always correctly diagnosed as healthy. It is worth pointing out that the wrong diagnosis concern points are close to the -0.5% V_{cell} variation threshold, which defines healthy and faulty conditions. Considering that the BBN was trained on noisy data, it is reasonable to have some wrong detection close to this threshold. Therefore, these results are very promising, considering that after ~300 min, when the V_{cell} variations are more significant, all the predictions are correct.

In the second simulation, a $T_{cat,in}$ sensor fault occurred after 100 min and the temperature measurement started being overestimated. At 400 min the sensor bias stopped increasing and the system stabilized (V_{cell} variation around -0.7% from the nominal value and $T_{cat,in}$ overestimated by 10K). The predictions of the diagnosis system are shown in Figure 76. The $T_{cat,in}$ sensor R_{pred} is equal to 0.9479 and the SOFC status was always correctly diagnosed as healthy. In this case the system starts detecting the sensor bias as soon as the V_{cell} variation exceeds the -0.5% value, but a few wrong predictions are present when the system behavior stabilized.

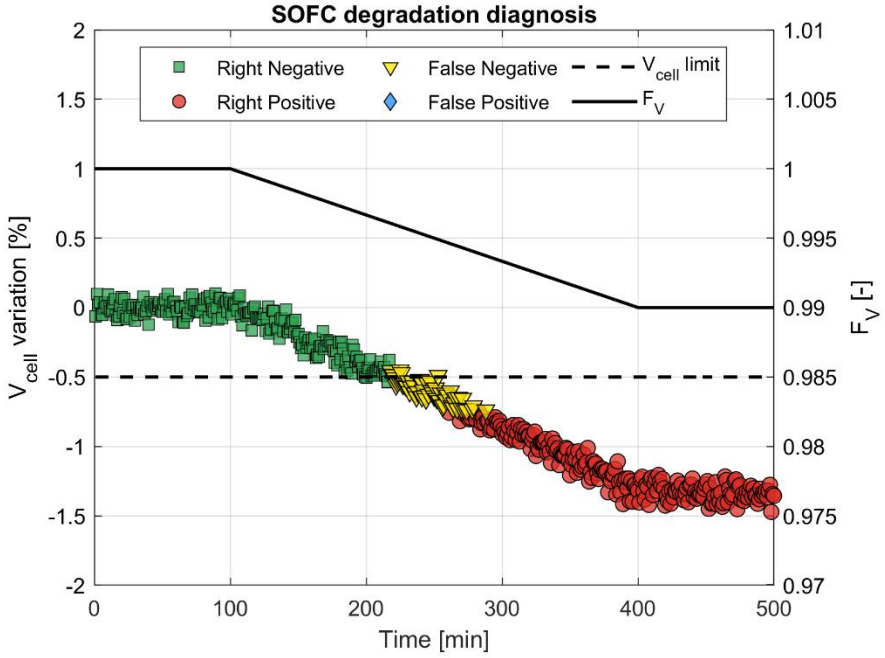

Figure 75. *V_{cell} variation, F_V trend and SOFC degradation diagnosis for the first dynamic simulation.*

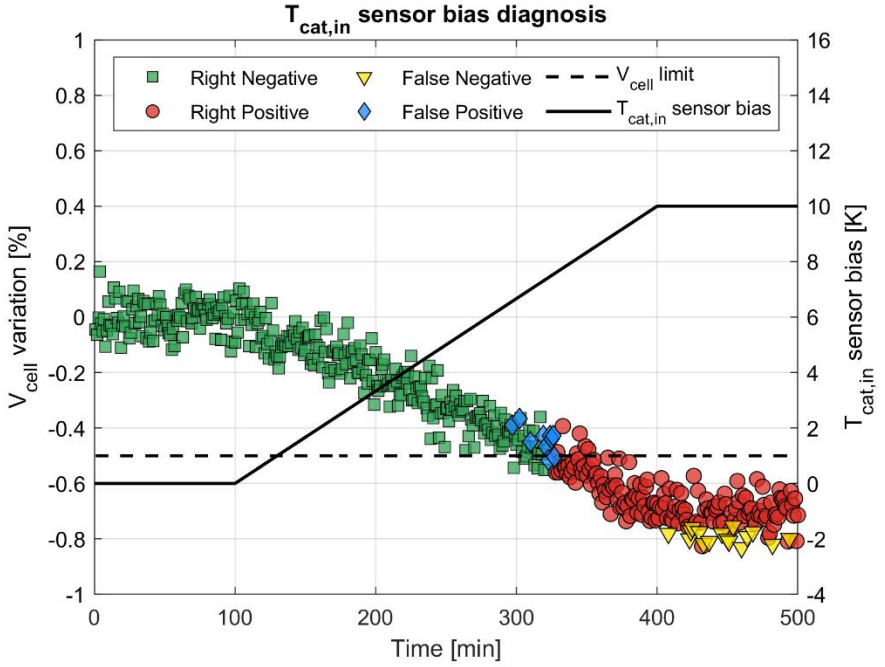

Figure 76. *V_{cell} variation, $T_{cat,in}$ sensor bias trend and temperature sensor diagnosis for the second dynamic simulation.*

Two additional tests were performed to better understand if the wrong predictions are caused by the difference between the dynamic and the steady state behavior of the system.

A first set of 21 simulations was run setting the FV between 1.00 and 0.99 (extreme values in Figure 75). In this case 4 wrong diagnosis about the SOFC status were made for values of V_{cell} close to the -0.5% threshold (Figure 77), similarly to what was observed in Figure 75. Therefore, these mistakes seem to be independent from the transient behavior of the hybrid system during the SOFC degradation. The healthy status of the temperature sensor was always diagnosed correctly also in this case.

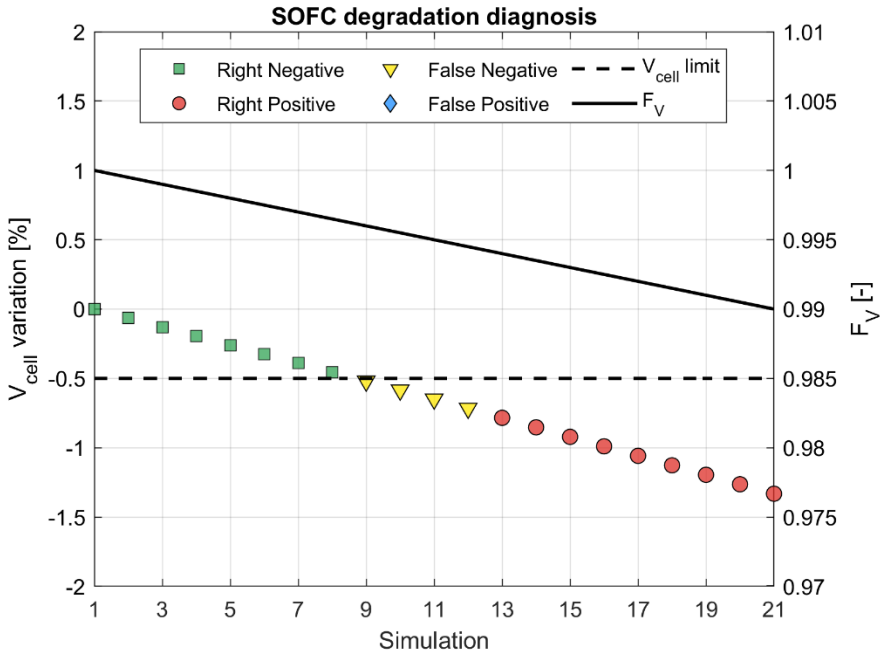

Figure 77. *V_{cell} variation, FV trend and SOFC degradation diagnosis for the first set of steady state simulations.*

A second set of 21 simulations was run setting the $T_{cat,in}$ sensor bias between 0K and 10K (extreme values in Figure 76). In this case no wrong diagnosis were made both for temperature sensor (Figure 78) and for SOFC status. Thus, it is possible to state that the BBN performance is better in this case compared to

the transient behavior diagnosis (Figure 76). However, even in that case the BBN had a high level of accuracy, with a R_{pred} equal to 0.9479.

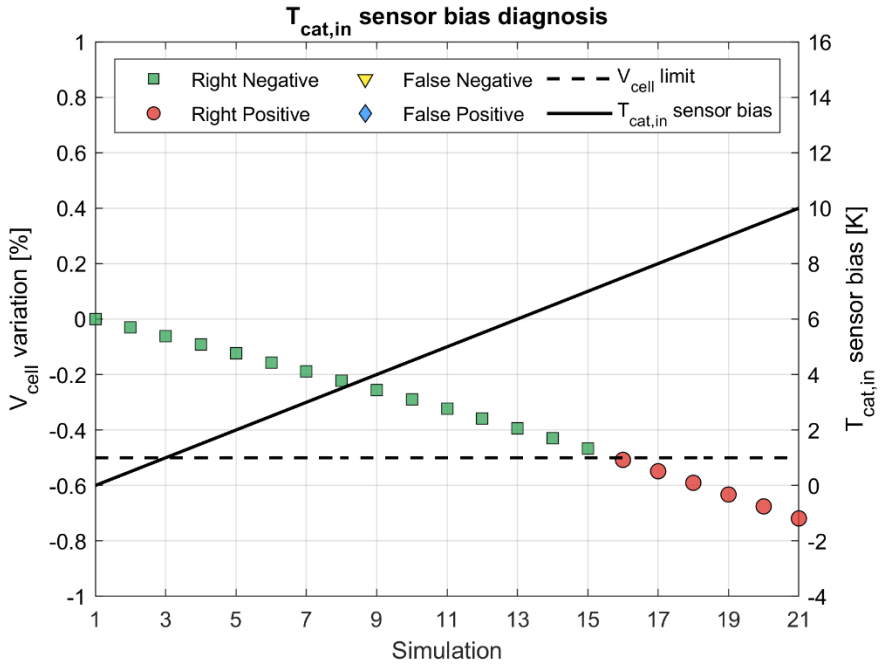

Figure 78. *V_{cell} variation, $T_{cat,in}$ sensor bias trend and temperature sensor diagnosis for the second set of steady state simulations.*

From the results obtained in these tests, it is possible to deduct that a BBN trained on steady state conditions data can be effectively used to monitor the hybrid system also while the degradation of a component is occurring. However, the precision of the BBN is higher when the system is stationary, suggesting that it would be more accurate also if the components degraded more gradually than in the two cases presented in Figure 75 and Figure 76. To increase the accuracy of the diagnostic tool on transient scenarios, it would be necessary to develop a different BBN, using also transient data for training.

6.7 Control Strategies in Hybrid System under Degradation

As stated in Section 6.6, information regarding the status of the components is valuable to avoid wrong control actions that could damage the system. In particular, an unsuitable value of the electric current could accelerate the degradation of the SOFC [109]. The control system was enhanced to take into account diagnostic data of the SOFC and of the $T_{cat,in}$ sensor, and it was tested on two different cases: the first one with a degrading SOFC, and the second one with a biased $T_{cat,in}$ sensor. It is important to point out that, at this stage, the BBN developed on Hugin Expert is not directly linked with the dynamic model, and that these tests have the only purpose of proving the effectiveness of the control strategies. It was assumed that, when the value of V_{cell} decreases under the -0.5% limit, the BBN would correctly diagnose a fault condition.

In the first case, the value of FV was equal to 0.997 for the first 10 minutes, and then it started decreasing gradually over 2 hours, until it was equal to 0.992. To match with the power demand, the default control system would increase the stack current, stressing the cell and intensifying its degradation process [109]. The control strategy of the system was properly modified to deal with this kind of event. If the BBN diagnoses a degraded status of the SOFC, the control system should switch the controlled variable from the power to the V_{cell}, setting its design value as set point. To switch back to the previous control strategy, a manual reset is required; otherwise the power would be set as controlled variable again as soon as the system were controlled properly. It can be observed in Figure 79 that, during the test, the new control system worked as intended. When the SOFC degradation was diagnosed (black line reaching the red line in Figure 79), the V_{cell} increased until it reached its design value. At the same time the power decreased and consequently the j_{cell} decreased as well, reducing the stress on the cell with a positive impact on the SOFC service life.

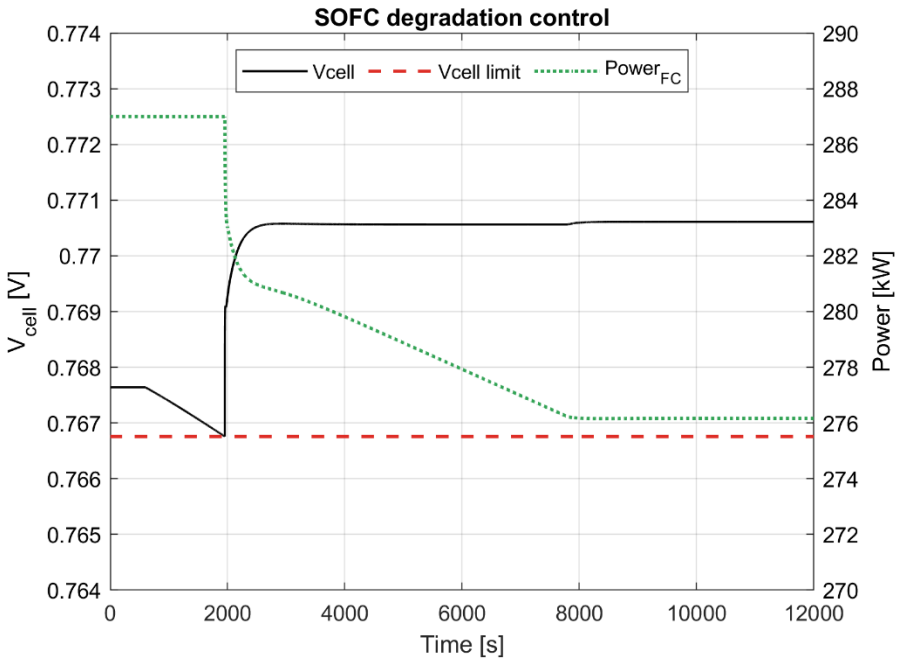

Figure 79: *V_{cell} variation and fuel cell power trend during the first control system test.*

In the second case, the bias of the $T_{cat,in}$ sensor increases up to +15°C over a $4 \cdot 10^4$ s time span, with a trend composed by a series of three consecutive ramps. When the $T_{cat,in}$ measured value is higher than the real one, and the sensor fault is undetected, the $T_{cat,in}$ is below the set point due to the wrong control action. Consequently, the V_{cell} decreases, as showed in Figure 80, and the j_{cell} increases to cope with the power demand. Also in this case, the increase of current density would have a detrimental effect on the SOFC, and it should be avoided. If the $T_{cat,in}$ sensor had a negative bias instead (real temperature higher than the measured one), the control system may keep the SOFC at an excessive temperature, causing thermal stress on the cells. This would eventually damage permanently the fuel cell, and for this reason it is crucial to detect any fault in the $T_{cat,in}$ sensor.

To control properly the system, it is necessary to have a more precise estimate of the $T_{cat,in}$. To obtain this information, the data from the steady simulations was used to create semi-empirical function, that gives the value of $T_{cat,in}$ based on the values of $T_{cat,out}$ and $p_{cat,out}$. When the sensor fault is detected (black line reaching the red line in Figure 80), the control system replaces the controlled

variable from the $T_{cat,in}$ value measured by the sensor to the one computed by the interpolator. Figure 80 shows that, after diagnosing the sensor fault, the control system is able to bring back the V_{cell} on its set point in about half an hour, proving the effectiveness of the new strategy.

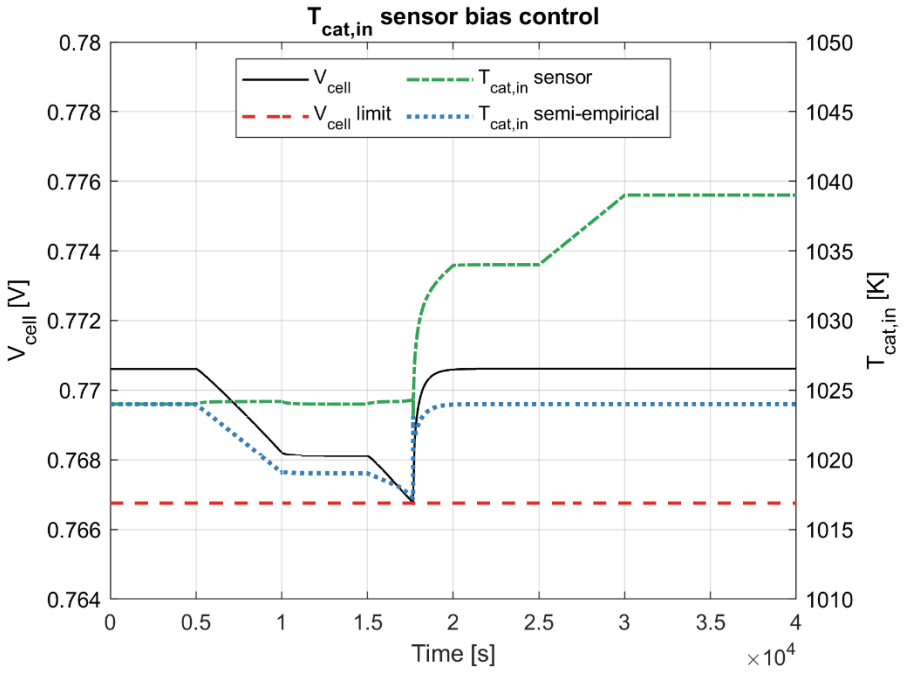

Figure 80. *Trends of V_{cell}, $T_{cat,in}$ sensor measurement and $T_{cat,in}$ computed by the semi-empirical function during the second control system test.*

6.8 Concluding remarks

The potential of BBNs for diagnosis applications on SOFC-MGT hybrid systems was investigated in this Chapter. To obtain the data used to train and test the BBNs, it was necessary to develop dynamic models of both the system considered, i.e. an emulator plant and a complete hybrid system. A high amount of data was generated from the simulation results by use of fitting curves (linear interpolators and polynomials). These data were then altered with noise to develop a more robust diagnosis system.

A BBN designed to detect mass flow reduction and efficiency loss in the MGT showed its efficacy when tested on both the emulator and the hybrid system in steady-state conditions. Despite the higher complexity of the hybrid system, the results were more accurate when compared with the emulator diagnosis. The predictions of the *CAW* were particularly accurate for the hybrid system diagnosis, with R_{pred} values higher than 0.93 for both compressor and turbine. The turbine status was predicted correctly 95.04% of the times, while the compressor status diagnosis accuracy was equal to 90.19%. The number of cases where a healthy condition was diagnosed as heavily degraded and vice versa is negligible.

Another BBN was developed to diagnose the status of SOFC and $T_{cat,in}$ sensor in the hybrid system. This BBN was trained and tested on steady state data, providing very accurate results: the R_{pred} values regarding both SOFC and temperature sensor were higher than 0.97. This tool, useful to understand the cause of a potential voltage drop, can provide also the information necessary to avoid wrong control actions and extend the system service life. The BBN was tested also on two transient scenarios, where a gradual degradation of the components occurred. In this case, the results had a good level of accuracy, even if lower than in the previous tests. Therefore, it could be possible to use a BBN trained on steady state data to monitor the status of a hybrid system while the degradation is occurring.

In conclusion, a control strategy able to avoid wrong actions using the fault detection information was presented and successfully tested.

The promising results obtained from this analysis open the way for many further activities such as real time diagnosis applications, tests of the proposed methodology on experimental data, development of more sophisticated BBN-based diagnostic systems and integration with the control system.

7 Conclusions

This thesis aimed at expanding the knowledge on SOFC hybrid systems based on turbocharger-derived machinery, focusing in particular on an innovative bio-fueled SOFC-turbocharger layout. After three years of work, it is finally possible to answer to all the research questions that were asked at the beginning of this thesis. Due to the novelty, high cost and fragility of such fuel cell systems, the use of simulation tools and numerical models was crucial to achieve this goal.

To study the performance of turbocharged SOFC systems, the research activity started from the development of a detailed steady-state model of the turbocharged SOFC system. This model was used to perform for the first time an off-design performance analysis of a SOFC hybrid system considering at the same time the influence of power load and ambient temperature. The steady-state model was necessary to assess the capabilities of turbocharged SOFC systems, as well as to start the control system design process.

This analysis showed that a biofueled turbocharged SOFC system can operate in a wide range of conditions, with high values of energy conversion efficiency (>50% already at small size of 30kWe). Simulating the system for values of the j_{cell} between 100% and 60% of its nominal value, varying the ambient temperature between 0°C and 30°C, it was found that, acting on the only CBV or with CBV and WGV, it is possible to comply with the many constraints of the small-scale plant considered for this study. Also a control strategy based only on the WGV was tested, but it was unable to comply with the 650°C limit on the maximum recuperator temperature at the hot exhaust side, which is considered essential to keep the plant capital cost within acceptable boundaries.

Adopting the CBV+WGV control strategy, the system was able to generate about 30kW in nominal conditions, with a net efficiency of 50.8%, which is a very interesting value when compared with traditional energy systems. The analysis showed that the SOFC system has a remarkable increase of efficiency at lower

electric current density (up to 57.3% for T_{amb} = 15°C), which makes it particularly interesting for part load operations. Moreover, the system had limited variations of efficiency due to the ambient temperature, showing that it could operate effectively during the whole year and that it can be installed in various environments. Based on this results, turbocharged SOFC systems can be a viable alternative to MGT-based layouts, despite their lower complexity and power density.

The results obtained with the stationary model were used to develop a dynamic model of the same system, to be used for transient analysis and control system development. From the CBV step response of the turbocharged SOFC system, it was possible to characterize its time-dependent behavior and to design different control systems, aimed at controlling the SOFC maximum temperature acting on the CBV valve. The CBV control strategy was preferred to the CBV+WGV not to increase the complexity of the problem. It was observed that the OGB outlet temperature $T_{OGB,out}$ had the fastest variation when the CBV is opened, followed by the SOFC cathode outlet temperature $T_{ca,out}$. The SOFC cathode inlet temperature $T_{ca,in}$ variation was too slow to be considered interesting for control purposes.

Four different controllers (PI, PI-PI, PI-PI + FF and PID-PI + FF) were tuned following a consistent procedure, implemented onto the system model and tested on two different current density variation scenarios. It was observed that a PI acting directly on the CBV to follow the $T_{ca,out}$ setpoint was the least performing controller, causing the widest deviation from the temperature setpoint. On the other hand, cascade controllers observing also the $T_{OGB,out}$ had a better performance and were able to ensure the proper operation of the SOFC system also during quick load variations, respecting all the constraints. The PID-PI + FF cascade control was the most promising, in particular regarding its capacity to keep the cell temperature close to its set-point and to reach the desired value within a limited timeframe. In conclusion, this study showed that a control system designed to act only the cold bypass valve can comply with all the system

constraints in stationary conditions. However, a simple PI would not be effective to control the system during quick load transients, while a more sophisticated control algorithm based on cascade controllers and feed-forwards would ensure responsiveness and limited oscillations.

The final part of the thesis focused on designing tools and solutions that, after being integrated with the control system of a SOFC hybrid system, could protect the integrity of the fuel cell from anomalous events and extend the lifetime of the whole plant. For this purpose, the research activity focussed on surge prevention techniques and Bayesian belief network.

Many different techniques were tested to prevent compressor surge in a turbocharged SOFC system. Solutions based on the injection of water at the compressor inlet, i.e. water spray and fogging, were not effective. In fact, their main effect was to lower the compressor inlet temperature, leading to a reduction of the surge after a small quick increment. Instead, techniques based on the partial deviation of the compressor outlet flow (bleed, recirculation and ejector-aided recirculation) were all able to drive a significant growth of the surge margin. Since recirculation and ejector-aided recirculation were the most promising techniques, they were integrated with the control strategy of the SOFC system. They were both successfully tested during a transient scenario characterized by a surge margin decrement. Analysing the results of these simulations, it was observed that recirculation is preferrable to have a simpler plant layout with better performance during standard operations. On the other hand, the ejector-aided recirculation, should be adopted if it is necessary to have more responsiveness. The outcomes of this study open the way for integration with surge precursor detection tools, in order to improve the reliability of turbocharged SOFC hybrid systems.

In order to detect degradation and faults of the most critical components in a SOFC hybrid system, some diagnosis tools based on Bayesian belief networks were developed and tested. For this activity, a SOFC-MGT hybrid system and an emulator plant were considered. BBNs were trained and tested in Hugin

Expert on simulation data, obtained from dynamic models of both systems and altered with random noise to increase the system robustness. A BBN designed to detect mass flow reduction and efficiency loss in the compressor and turbine achieved high accuracy when tested on both emulator and hybrid system. Another BBN was developed to diagnose the status of SOFC and detect faults of the cathode inlet temperature sensor in the hybrid system. Tests on this BBN produced high accuracy results as well. A control strategy able to avoid wrong actions using the diagnosis of the BBN was presented and successfully tested in a simplified setup, while simulating SOFC degradation and $T_{cat,in}$ sensor fault.

Both tools developed in the final part of this thesis were proved to be effective to avoid risky scenarios. Surge prevention techniques based on recirculation appeared to be a simple and effective solution to move the compressor operative point far from the surge line. Diagnostic BBNs, instead, could accurately detect degradation of components and sensors, avoiding wrong and potentially detrimental control actions.

7.1 Contribution to knowledge

In conclusion, it is possible to state that, thanks to the work carried out during this thesis, it is now possible to have a better understanding of innovative SOFC hybrid systems based on turbocharger-derived machinery, and to assess their capabilities. In particular, the large literature gap on turbocharged SOFC systems was partially filled and the knowledge on SOFC hybrid systems was expanded. The main outcomes of this thesis are the following:

- Turbocharged SOFC systems can operate in a wide range in terms of power load and ambient temperature. Growing efficiencies at part loads and the possibility of using biofuels make them extremely interesting as power generation systems with a small environmental impact.
- Turbocharged SOFC systems can be effectively controlled acting only on one or two valves installed on the plant. Cascade controllers integrated

with feed-forwards are particularly effective to reduce the SOFC maximum temperature deviations during transients, ensuring high responsiveness and limited oscillations.

- The reliability of SOFC hybrid systems can be enhanced integrating their control algorithm with diagnostic tools and compressor surge prevention techniques. For diagnostic purposes, BBNs can be used to detect accurately components degradation and biased sensors. Instead, surge can be prevented adopting procedures based on compressor recirculation or ejector-aided recirculation.

7.2 Future work

The control system and the tools developed for this thesis were able to guarantee the proper operation of SOFC hybrid systems on many different scenarios and increase their reliability. These results are expected to open the way for more studies on SOFC hybrid plants, in particular turbocharged-based systems.

In the future, the behaviour of turbocharged SOFC systems could be investigated with regards to many other variables, such as biofuel composition and degradation parameters. For sure it would be possible to develop and test more sophisticated controllers, such as model predictive controls, in order to act on multiple variables and improve system performance. Unfortunately, the TPG emulator was under development for most of these three years, but the controllers could be tested on it in the future, and eventually on real prototypes. The surge prevention techniques proposed in this thesis could be integrated with a surge precursor detection tool and implemented on a test rig for experimental validation. Also the diagnostic systems based on BBN could be tested on emulators and real plants, and more complex tools based on this approach could be designed.

Hopefully, the promising results obtained on SOFC hybrid systems based on turbocharger-derived machinery will motivate academia and industry to focus on these highly efficient energy systems and to invest on their development.

Bibliography

[1] International Energy Agency, 2017, *World Energy Outlook 2017*.

[2] Blunden, J., Arndt, D. S., Hartfield, G., Weyhenmeyer, G. A., and Ziese, M. G., 2018, *State of the Climate in 2017*.

[3] Manabe, S., 2019, "Role of Greenhouse Gas in Climate Change**," Tellus A Dyn. Meteorol. Oceanogr., **71**(1), p. 1620078.

[4] Dyurgerov, M. B., and Meier, M. F., 2000, "Twentieth Century Climate Change: Evidence from Small Glaciers," Proc. Natl. Acad. Sci. U. S. A., **97**(4), pp. 1406–1411.

[5] Burrell, A. L., Evans, J. P., and De Kauwe, M. G., 2020, "Anthropogenic Climate Change Has Driven over 5 Million Km2 of Drylands towards Desertification," Nat. Commun., **11**(1), pp. 1–11.

[6] Wright, L. P., Zhang, L., Cheng, I., Aherne, J., and Wentworth, G. R., 2018, "Impacts and Effects Indicators of Atmospheric Deposition of Major Pollutants to Various Ecosystems-A Review," Aerosol Air Qual. Res., **18**, pp. 1953–1992.

[7] Barna, C., 2020, "Current Socio-Economic Challenges. Approaching Sustainability and Social Economy," Manag. Dyn. Knowl. Econ., **8**(1), pp. 7–9.

[8] European Commission, 2019, *The European Green Deal*.

[9] Hainsch, K., Göke, L., Kemfert, C., Oei, P.-Y., and Von Hirschhausen, C., 2020, "European Green Deal: Using Ambitious Climate Targets and Renewable Energy to Climb Out of the Economic Crisis," DIW Wkly. Rep., **28+29**(28/29), pp. 303–310.

[10] Sun, K., Xiao, H., Liu, S., You, S., Yang, F., Dong, Y., Wang, W., and Liu, Y., 2020, "A Review of Clean Electricity Policies—From Countries to Utilities," Sustainability, **12**(19), p. 7946.

[11] Amin, A. Z., 2014, "Renewable Energy Prospects: China," /publications/2014/Nov/Renewable-Energy-Prospects-China, (November), p. 102.

[12] Bilgili, M., Ozbek, A., Sahin, B., and Kahraman, A., 2015, "An Overview of Renewable Electric Power Capacity and Progress in New Technologies in the World," Renew. Sustain. Energy Rev., **49**, pp. 323–334.

[13] Perez-Arriaga, I. J., and Batlle, C., 2012, "Impacts of Intermittent Renewables on Electricity Generation System Operation," Econ. Energy Environ. Policy, **1**(2), pp. 3–17.

[14] Chalk, S. G., and Miller, J. F., 2006, "Key Challenges and Recent Progress in Batteries, Fuel Cells, and Hydrogen Storage for Clean Energy

Systems," J. Power Sources, **159**(1 SPEC. ISS.), pp. 73–80.

[15] Leonard, M. D., Michaelides, E. E., and Michaelides, D. N., 2020, "Energy Storage Needs for the Substitution of Fossil Fuel Power Plants with Renewables," Renew. Energy, **145**, pp. 951–962.

[16] Haseli, Y., 2018, "Maximum Conversion Efficiency of Hydrogen Fuel Cells," Int. J. Hydrogen Energy, **43**(18), pp. 9015–9021.

[17] Trendewicz, A. A., and Braun, R. J., 2013, "Techno-Economic Analysis of Solid Oxide Fuel Cell-Based Combined Heat and Power Systems for Biogas Utilization at Wastewater Treatment Facilities," J. Power Sources, **233**, pp. 380–393.

[18] Chan, S. H., and Wang, H. M., 2000, "Thermodynamic Analysis of Natural-Gas Fuel Processing for Fuel Cell Applications," Int. J. Hydrogen Energy, **25**(5), pp. 441–449.

[19] Turco, M., Ausiello, A., and Micoli, L., 2016, "Fuel Cells Operating and Structural Features of MCFCs and SOFCs," *Green Energy and Technology*, Springer Verlag, pp. 31–76.

[20] Kirubakaran, A., Jain, S., and Nema, R. K., 2009, "A Review on Fuel Cell Technologies and Power Electronic Interface," Renew. Sustain. Energy Rev., **13**(9), pp. 2430–2440.

[21] Weidner, E., Ortiz Cebolla, R., and Davies, J., 2019, *Global Deployment of Large Capacity Stationary Fuel Cells*.

[22] Nielsen, E. R., Prag, C. B., Bachmann, T. M., Carnicelli, F., Boyd, E., Walker, I., Ruf, L., and Stephens, A., 2019, "Status on Demonstration of Fuel Cell Based Micro-CHP Units in Europe," Fuel Cells, **19**(4), p. fuce.201800189.

[23] Grand View Research, 2020, *Fuel Cell Market Size & Share | Industry Growth Report, 2027*.

[24] National Fuel Cell Research Center, 2018, *Stationary Fuel Cell Cost Trends*.

[25] Zhang, X., Chan, S. H., Ho, H. K., Tan, S. C., Li, M., Li, G., Li, J., and Feng, Z., 2015, "Towards a Smart Energy Network: The Roles of Fuel/Electrolysis Cells and Technological Perspectives," Int. J. Hydrogen Energy, **40**(21), pp. 6866–6919.

[26] Olabi, A. G., Wilberforce, T., and Abdelkareem, M. A., 2021, "Fuel Cell Application in the Automotive Industry and Future Perspective," Energy, **214**, p. 118955.

[27] van Biert, L., Godjevac, M., Visser, K., and Aravind, P. V., 2016, "A Review of Fuel Cell Systems for Maritime Applications," J. Power Sources, **327**, pp. 345–364.

[28] Baroutaji, A., Wilberforce, T., Ramadan, M., and Olabi, A. G., 2019,

"Comprehensive Investigation on Hydrogen and Fuel Cell Technology in the Aviation and Aerospace Sectors," Renew. Sustain. Energy Rev., **106**, pp. 31–40.

[29] 2013, "EBay Turns on First Fuel Cell Powered Data Centre, Has Bloom Tech," Fuel Cells Bull., **2013**(10), pp. 3–4.

[30] 2020, "Microsoft Claims a First in Hydrogen-Fueled Data Center Test" [Online]. Available: https://www.datacenterknowledge.com/microsoft/microsoft-claims-first-hydrogen-fueled-data-center-test. [Accessed: 07-Jan-2021].

[31] FuelCellsWorks, 2020, "Plug Power Expands Hydrogen and Fuel Cell Solutions into Walmart ECommerce Applications - FuelCellsWorks" [Online]. Available: https://fuelcellsworks.com/news/plug-power-expands-hydrogen-and-fuel-cell-solutions-into-walmart-ecommerce-applications/. [Accessed: 12-Jan-2021].

[32] 2020, "Doosan Fuel Cell - Media Center - News" [Online]. Available: https://www.doosanfuelcell.com/en/media-center/medi-0101_view?id=62&page=0&. [Accessed: 08-Jan-2021].

[33] Das, H. S., Tan, C. W., and Yatim, A. H. M., 2017, "Fuel Cell Hybrid Electric Vehicles: A Review on Power Conditioning Units and Topologies," Renew. Sustain. Energy Rev., **76**, pp. 268–291.

[34] Papagianni, A., Kalfas, A., Aslanidou, I., Kavvalos, M. D., and Kyprianidis, K., *Conceptual Design of a Hybrid Gas Turbine-Solid Oxide Fuel Cell System for Civil Aviation*.

[35] 2016, "First Flight of DLR's HY4 Fuel Cell Light Aircraft," Fuel Cells Bull., **2016**(10), p. 1.

[36] Mekhilef, S., Saidur, R., and Safari, A., 2012, *Comparative Study of Different Fuel Cell Technologies*, Elsevier Ltd.

[37] Larminie, J., and Dicks, A., 2013, *Fuel Cell Systems Explained: Second Edition*.

[38] Hoogers, G., 2002, *Fuel Cell Technology Handbook*.

[39] Zeng, H., Wang, Y., Shi, Y., and Cai, N., 2017, "Biogas-Fueled Flame Fuel Cell for Micro-Combined Heat and Power System," Energy Convers. Manag., **148**, pp. 701–707.

[40] Lackey, J., Champagne, P., and Peppley, B., 2017, "Use of Wastewater Treatment Plant Biogas for the Operation of Solid Oxide Fuel Cells (SOFCs)," J. Environ. Manage., **203**, pp. 753–759.

[41] Xu, H., Chen, B., Liu, J., and Ni, M., 2016, "Modeling of Direct Carbon Solid Oxide Fuel Cell for CO and Electricity Cogeneration," Appl. Energy, **178**, pp. 353–362.

[42] Stambouli, A. B., and Traversa, E., 2002, "Solid Oxide Fuel Cells (SOFCs):

A Review of an Environmentally Clean and Efficient Source of Energy," Renew. Sustain. Energy Rev., **6**(5), pp. 433–455.

[43] Palsson, J., Selimovic, A., and Sjunnesson, L., 2000, "Combined Solid Oxide Fuel Cell and Gas Turbine Systems for Efficient Power and Heat Generation," J. Power Sources, **86**(1), pp. 442–448.

[44] Milewski, J., Miller, A., and Sałaciński, J., 2007, "Off-Design Analysis of SOFC Hybrid System," Int. J. Hydrogen Energy, **32**(6), pp. 687–698.

[45] Henke, M., Kallo, J., Friedrich, K. A., and Bessler, W. G., 2011, "Influence of Pressurisation on SOFC Performance and Durability: A Theoretical Study," *Fuel Cells*, pp. 581–591.

[46] Breeze, P., 2019, *Power Generation Technologies*, Elsevier.

[47] Calebfinch, 2014, "C65 Cutaway" [Online]. Available: https://commons.wikimedia.org/wiki/File:C65_Cutaway.jpg. [Accessed: 07-May-2021].

[48] Montero Carrero, M., De Paepe, W., Parente, A., and Contino, F., 2016, "T100 MGT Converted into MHAT for Domestic Applications: Economic Analysis Based on Hourly Demand," Appl. Energy, **164**, pp. 1019–1027.

[49] De Paepe, W., Montero Carrero, M., Bram, S., Contino, F., and Parente, A., 2017, "Waste Heat Recovery Optimization in Micro Gas Turbine Applications Using Advanced Humidified Gas Turbine Cycle Concepts," Appl. Energy, **207**, pp. 218–229.

[50] Lanchi, M., Montecchi, M., Crescenzi, T., Mele, D., Miliozzi, A., Russo, V., Mazzei, D., Misceo, M., Falchetta, M., and Mancini, R., 2015, "Investigation into the Coupling of Micro Gas Turbines with CSP Technology: OMSoP Project," *Energy Procedia*, Elsevier Ltd, pp. 1317–1326.

[51] De Paepe, W., Carrero, M. M., Giorgetti, S., Parente, A., Bram, S., and Contino, F., 2016, "Exhaust Gas Recirculation on Humidified Flexible Micro Gas Turbines for Carbon Capture Applications," *Proceedings of the ASME Turbo Expo*, American Society of Mechanical Engineers (ASME).

[52] Pantaleo, A. M., Camporeale, S. M., and Shah, N., 2013, "Thermo-Economic Assessment of Externally Fired Micro-Gas Turbine Fired by Natural Gas and Biomass: Applications in Italy," Energy Convers. Manag., **75**, pp. 202–213.

[53] Bao, C., Wang, Y., Feng, D., Jiang, Z., and Zhang, X., 2018, "Macroscopic Modeling of Solid Oxide Fuel Cell (SOFC) and Model-Based Control of SOFC and Gas Turbine Hybrid System," Prog. Energy Combust. Sci., **66**, pp. 83–140.

[54] Hassmann, K., 2001, "SOFC Power Plants, the Siemens-Westinghouse Approach," Fuel Cells, **1**(1), pp. 78–84.

[55] Damo, U. M., Ferrari, M. L., Turan, A., and Massardo, A. F., 2019, "Solid

Oxide Fuel Cell Hybrid System: A Detailed Review of an Environmentally Clean and Efficient Source of Energy," Energy, **168**, pp. 235–246.

[56] McLarty, D., Kuniba, Y., Brouwer, J., and Samuelsen, S., 2012, "Experimental and Theoretical Evidence for Control Requirements in Solid Oxide Fuel Cell Gas Turbine Hybrid Systems," J. Power Sources, **209**, pp. 195–203.

[57] Summers, R., 2016, *GE-FUEL CELLS THE POWER OF TOMORROW*.

[58] DeBellis, C. L., 2019, *DE-FE0031180 Final Report - LGFCS Prototype System Testing - R0*, Pittsburgh, PA, and Morgantown, WV (United States).

[59] Nichols, D. K., Agnew, G., and Strickland, D., 2008, "Outlook and Application Status of the Rolls-Royce Fuel Cell Systems Sofc," *IEEE Power and Energy Society 2008 General Meeting: Conversion and Delivery of Electrical Energy in the 21st Century, PES*.

[60] Mitsubishi Power, "Fuel Cells - Hybrid System of Solid Oxide Fuel Cells (SOFC) and Micro Gas Turbines (MGT)" [Online]. Available: https://power.mhi.com/products/sofc.

[61] Rossi, I., Sorce, A., and Traverso, A., 2017, "Gas Turbine Combined Cycle Start-up and Stress Evaluation: A Simplified Dynamic Approach," Appl. Energy, **190**, pp. 880–890.

[62] Zaccaria, V., Tucker, D., and Traverso, A., 2016, "Transfer Function Development for SOFC/GT Hybrid Systems Control Using Cold Air Bypass," Appl. Energy, **165**, pp. 695–706.

[63] Stiller, C., Thorud, B., Bolland, O., Kandepu, R., and Imsland, L., 2006, "Control Strategy for a Solid Oxide Fuel Cell and Gas Turbine Hybrid System," J. Power Sources, **158**(1), pp. 303–315.

[64] Hauptmeier, K., Penkuhn, M., and Tsatsaronis, G., 2016, "Economic Assessment of a Solid Oxide Fuel Cell System for Biogas Utilization in Sewage Plants," Energy, **117**, pp. 361–368.

[65] Damo, U. M., Ferrari, M. L., Turan, A., and Massardo, A. F., 2015, "Test Rig for Hybrid System Emulation: New Real-Time Transient Model Validated in a Wide Operative Range," Fuel Cells, **15**(1), pp. 7–14.

[66] Abrassi, A., Traverso, A., Tucker, D., and Liese, E., 2020, "Impact of Different Volume Sizes on Dynamic Stability of a Gas Turbine-Fuel Cell Hybrid System," J. Eng. Gas Turbines Power, **142**(5).

[67] Hashimoto, S., Nishino, H., Liu, Y., Asano, K., Mori, M., Funahashi, Y., and Fujishiro, Y., 2008, "Development of Evaluation Technologies for Microtubular SOFCs Under Pressurized Conditions."

[68] Ferrari, M. L., Pascenti, M., Bertone, R., and Magistri, L., 2009, "Hybrid Simulation Facility Based on Commercial 100 KWe Micro Gas Turbine," J. Fuel Cell Sci. Technol., **6**(3), pp. 0310081–0310088.

[69] Tucker, D., Lawson, L., and Gemmen, R., 2003, "Preliminary Results of a Cold Flow Test in a Fuel Cell Gas Turbine Hybrid Simulation Facility," *American Society of Mechanical Engineers, International Gas Turbine Institute, Turbo Expo (Publication) IGTI*, American Society of Mechanical Engineers Digital Collection, pp. 281–287.

[70] Hohloch, M., Huber, A., and Aigner, M., 2016, "Experimental Investigation of a Sofc/Mgt Hybrid Power Plant Test Rig - Impact and Characterization of a Fuel Cell Emulator," *Proceedings of the ASME Turbo Expo*, American Society of Mechanical Engineers (ASME).

[71] Metten, M., Tomberg, M., Heddrich, M. P., and Friedrich, K. A., "Analysis of Experimental Results of a Pressurized Solid Oxide Fuel Cell System Simulating a Hybrid Power Plant."

[72] Ferrari, M. L., Pascenti, M., Magistri, L., and Massardo, A. F., 2010, "Hybrid System Test Rig: Start-up and Shutdown Physical Emulation," J. Fuel Cell Sci. Technol., **7**(2), pp. 0210051–0210057.

[73] Bio-Hypp Consortium, 2019, "Bio-HyPP Project Website - Stakeholders' Meeting and Onsite Visit – (DLR Stuttgart, 8/5/2019)" [Online]. Available: http://www.bio-hypp.eu/stakeholders-meeting-and-onsite-visit-dlr-stuttgart-852019/.

[74] Oh, S. R., Sun, J., Dobbs, H., and King, J., 2011, "Performance Evaluation of Solid Oxide Fuel Cell Engines Integrated with Single/Dual-Spool Turbochargers," J. Fuel Cell Sci. Technol., **8**(6).

[75] Lee, K., Kang, S., and Ahn, K. Y., 2017, "Development of a Highly Efficient Solid Oxide Fuel Cell System," Appl. Energy, **205**, pp. 822–833.

[76] "How Does A Turbocharger Work? | Turbo Dynamics.Co.Uk" [Online]. Available: https://www.turbodynamics.co.uk/technical/understanding-turbochargers/. [Accessed: 12-Jan-2021].

[77] Ferrari, M. L., De Campo, M., and Magistri, L., 2018, "Design and Emulation of a Turbocharged Bio-Fuelled SOFC Plant," *ASME Turbo Expo 2018: Turbomachinery Technical Conference and Exposition*, Oslo, Norway, p. V003T06A001--V003T06A001.

[78] Bo, T., Zhu, X., Zhang, L., Tao, Y., He, X., Li, D., and Yan, Z., 2014, "A New Upgraded Biogas Production Process: Coupling Microbial Electrolysis Cell and Anaerobic Digestion in Single-Chamber, Barrel-Shape Stainless Steel Reactor," Electrochem. commun., **45**, pp. 67–70.

[79] Rathod, V., and Bhale, P. V., 2014, "Experimental Investigation on Biogas Reforming for Syngas Production over an Alumina Based Nickel Catalyst," *Energy Procedia*, Elsevier Ltd, pp. 236–245.

[80] Rasi, S., Veijanen, A., and Rintala, J., 2007, "Trace Compounds of Biogas from Different Biogas Production Plants," Energy, **32**(8), pp. 1375–1380.

[81] Honeywell, 2018, *2018 Global Turbo Forecast*.

[82] Staunton, R. H., and Ozpineci, B., 2003, *MICROTURBINE POWER CONVERSION TECHNOLOGY REVIEW*.

[83] Visser, W. P. J., Shakariyants, S. A., and Oostveen, M., 2011, "Development of a 3 KW Microturbine for CHP Applications," J. Eng. Gas Turbines Power, **133**(4).

[84] Liu, M., Lanzini, A., Halliop, W., Cobas, V. R. M., Verkooijen, A. H. M., and Aravind, P. V., 2013, "Anode Recirculation Behavior of a Solid Oxide Fuel Cell System: A Safety Analysis and a Performance Optimization," Int. J. Hydrogen Energy, **38**(6), pp. 2868–2883.

[85] Venkataraman, K., Wanat, E. C., and Schmidt, L. D., 2003, "Steam Reforming of Methane and Water-Gas Shift in Catalytic Wall Reactors," AIChE J.

[86] Staxera, *SOFC Stack - Mk200, Product Data Sheet, Article 186*.

[87] Costamagna, P., Magistri, L., and Massardo, A. F., 2001, "Design and Part-Load Performance of a Hybrid System Based on a Solid Oxide Fuel Cell Reactor and a Micro Gas Turbine," J. Power Sources.

[88] Campanari, S., 2000, "Full Load and Part-Load Performance Prediction for Integrated SOFC and Microturbine Systems," J. Eng. Gas Turbines Power, **122**(2), pp. 239–246.

[89] Marsano, F., Magistri, L., and Massardo, A. F., 2004, "Ejector Performance Influence on a Solid Oxide Fuel Cell Anodic Recirculation System," J. Power Sources, **129**(2), pp. 216–228.

[90] Lingstädt, T., Grimm, F., Kutne, P., and Aigner, M., 2019, "Design and Setup of a Low Calorific SOFC Off-Gas Combustion Chamber for a Pressurized MGT Hybrid Power Plant Test Rig," E3S Web Conf., **113**, p. 02016.

[91] Mantelli, L., De Campo, M., Ferrari, M. L., and Magistri, L., 2019, "Fuel Flexibility for a Turbocharged SOFC System," *Energy Procedia*.

[92] Farrahi, G. H., Tirehdast, M., Masoumi Khalil Abad, E., Parsa, S., and Motakefpoor, M., 2011, "Failure Analysis of a Gas Turbine Compressor," Eng. Fail. Anal., **18**(1), pp. 474–484.

[93] Tucker, D., Shadle, L., Harun, N. F., and Farida Harun, N., 2017, "Automated Compressor Surge Recovery with Cold Air Bypass in Gas Turbine Based Hybrid Systems," *International Symposium on Transport Phenomena and Dynamics of Rotating Machinery*, pp. 1–5.

[94] Chen, J., Li, J., Zhou, D., Zhang, H., and Weng, S., 2018, "Control Strategy Design for a SOFC-GT Hybrid System Equipped with Anode and Cathode Recirculation Ejectors," Appl. Therm. Eng., **132**, pp. 67–79.

[95] Ratz, J., Leichtfuß, S., Beck, M., Schiffer, H.-P., and Fröhlig, F., 2019, "Surge Margin Optimization of Centrifugal Compressors Using a New Objective Function Based on Local Flow Parameters," Int. J.

Turbomachinery, Propuls. Power, **4**(4), p. 42.

[96] Mantelli, L., Ferrari, M. L., and Magistri, L., 2021, "Off-Design Performance Analysis of a Turbocharged Solid Oxide Fuel Cell System," Appl. Therm. Eng., **183**, p. 116134.

[97] Massardo, A. F., and Lubelli, F., 2000, "Internal Reforming Solid Oxide Fuel Cell-Gas Turbine Combined Cycles (IRSOFC-GT): Part A- Cell Model and Cycle Thermodynamic Analysis," J. Eng. Gas Turbines Power, **122**(1), pp. 27–35.

[98] Chen, J., Gao, K., Liang, M., and Zhang, H., 2019, "Performance Evaluation of an SOFC-GT Hybrid System With Ejectors for the Anode and Cathode Recirculations," J. Electrochem. Energy Convers. Storage, **16**(4).

[99] Cuneo, A., Zaccaria, V., Tucker, D., and Sorce, A., 2018, "Gas Turbine Size Optimization in a Hybrid System Considering SOFC Degradation," Appl. Energy, **230**, pp. 855–864.

[100] Hajabdollahi, Z., and Fu, P. F., 2017, "Multi-Objective Based Configuration Optimization of SOFC-GT Cogeneration Plant," Appl. Therm. Eng., **112**, pp. 549–559.

[101] Wongchanapai, S., Iwai, H., Saito, M., and Yoshida, H., 2013, "Performance Evaluation of a Direct-Biogas Solid Oxide Fuel Cell-Micro Gas Turbine (SOFC-MGT) Hybrid Combined Heat and Power (CHP) System," J. Power Sources, **223**, pp. 9–17.

[102] Lv, X., Ding, X., and Weng, Y., 2019, "Performance Analysis of an Intermediate-Temperature-SOFC/Gas Turbine Hybrid System Using Gasified Biomass Fuel in Different Operating Modes," J. Eng. Gas Turbines Power, **141**(1).

[103] Facchinetti, E., Gassner, M., D'Amelio, M., Marechal, F., and Favrat, D., 2012, "Process Integration and Optimization of a Solid Oxide Fuel Cell - Gas Turbine Hybrid Cycle Fueled with Hydrothermally Gasified Waste Biomass," Energy, **41**(1), pp. 408–419.

[104] Patel, H. C., Woudstra, T., and Aravind, P. V., 2012, "Thermodynamic Analysis of Solid Oxide Fuel Cell Gas Turbine Systems Operating with Various Biofuels," Fuel Cells, **12**(6), pp. 1115–1128.

[105] Cordiner, S., Feola, M., Mulone, V., and Romanelli, F., 2007, "Analysis of a SOFC Energy Generation System Fuelled with Biomass Reformate," Appl. Therm. Eng., **27**(4), pp. 738–747.

[106] Larosa, L., Traverso, A., and Zaccaria, V., 2015, "Ambient Temperature Impact on Pressurized Sofc Hybrid Systems," *Proceedings of the ASME Turbo Expo*, American Society of Mechanical Engineers (ASME).

[107] Song, T. W., Sohn, J. L., Kim, T. S., and Ro, S. T., 2006, "Performance Characteristics of a MW-Class SOFC/GT Hybrid System Based on a

Commercially Available Gas Turbine," J. Power Sources, **158**(1), pp. 361–367.

[108] Mueller, F., Jabbari, F., Brouwer, J., Roberts, R., Junker, T., and Ghezel-Ayagh, H., 2007, "Control Design for a Bottoming Solid Oxide Fuel Cell Gas Turbine Hybrid System," J. Fuel Cell Sci. Technol., **4**(3), pp. 221–230.

[109] Zaccaria, V., Tucker, D., and Traverso, A., 2017, "Operating Strategies to Minimize Degradation in Fuel Cell Gas Turbine Hybrids," Appl. Energy, **192**, pp. 437–445.

[110] Çengel, Y. a., 2004, *Thermodynamics: An Engineering Approach*, McGraw Hill.

[111] Green, D. W., and Perry, R. H., 2019, *Perry's Chemical Engineers' Handbook*.

[112] Trasino, F., Bozzolo, M., Magistri, L., and Massardo, A. F., 2011, "Modeling and Performance Analysis of the Rolls-Royce Fuel Cell Systems Limited: 1 MW Plant," J. Eng. Gas Turbines Power, **133**(2).

[113] Traverso, A., Massardo, A. F., and Scarpellini, R., 2006, "Externally Fired Micro-Gas Turbine: Modelling and Experimental Performance," Appl. Therm. Eng., **26**(16), pp. 1935–1941.

[114] Traverso, A., 2005, "TRANSEO Code for the Dynamic Performance Simulation of Micro Gas Turbine Cycles," *Proceedings of the ASME Turbo Expo*, pp. 45–54.

[115] Traverso, A., 2004, "TRANSEO: A New Simulation Tool For Transient Analysis Of Innovative Energy Systems," University of Genoa.

[116] Mengual, J. I., Khayet, M., and Godino, M. P., 2004, "Heat and Mass Transfer in Vacuum Membrane Distillation," Int. J. Heat Mass Transf., **47**(4), pp. 865–875.

[117] Sorce, A., Greco, A., Magistri, L., and Costamagna, P., 2014, "FDI Oriented Modeling of an Experimental SOFC System, Model Validation and Simulation of Faulty States," Appl. Energy, **136**, pp. 894–908.

[118] Ahmed, K., and Föger, K., 2017, "Analysis of Equilibrium and Kinetic Models of Internal Reforming on Solid Oxide Fuel Cell Anodes: Effect on Voltage, Current and Temperature Distribution," J. Power Sources, **343**, pp. 83–93.

[119] Ferrari, M. L., Traverso, A., and Massardo, A. F., 2004, "Transient Analysis of Solid Oxide Fuel Cell Hybrids Part B: Anode Recirculation Model," *Proceedings of the ASME Turbo Expo 2004*, pp. 399–407.

[120] Blomen, L. J. M. J., and Mugerwa, M. N., 1993, *Fuel Cell Systems*, Springer US.

[121] Saravanamuttoo, H. I. H., Rogers, G. F. C., and Cohen, H., 2009, *Gas Turbine Theory*.

[122] Costamagna, P., 1998, "Modeling of Solid Oxide Heat Exchanger Integrated Stacks and Simulation at High Fuel Utilization," J. Electrochem. Soc., **145**(11), p. 3995.

[123] Greco, A., Sorce, A., Littwin, R., Costamagna, P., and Magistri, L., 2014, "Reformer Faults in SOFC Systems: Experimental and Modeling Analysis, and Simulated Fault Maps," Int. J. Hydrogen Energy.

[124] Magistri, L., Bozzo, R., Costamagna, P., and Massardo, A. F., 2004, "Simplified Versus Detailed Solid Oxide Fuel Cell Reactor Models and Influence on the Simulation of the Design Point Performance of Hybrid Systems," J. Eng. Gas Turbines Power.

[125] Ferrari, M. L., Pascenti, M., and Massardo, A. F., 2008, "Ejector Model for High Temperature Fuel Cell Hybrid Systems: Experimental Validation at Steady-State and Dynamic Conditions," J. Fuel Cell Sci. Technol., **5**(4).

[126] Azizi, M. A., and Brouwer, J., 2018, "Progress in Solid Oxide Fuel Cell-Gas Turbine Hybrid Power Systems: System Design and Analysis, Transient Operation, Controls and Optimization," Appl. Energy, **215**, pp. 237–289.

[127] Cuneo, A., Mantelli, L., Giugno, A., and Traverso, A., 2019, "Uncertainty Quantification Analysis of a Pressurised Fuel Cell Hybrid System," *Proceedings of ASME Turbo Expo 2019: Turbomachinery Technical Conference and Exposition*, Phoenix, pp. 1–15.

[128] Giugno, A., Mantelli, L., Cuneo, A., and Traverso, A., 2019, "Robust Design of a Hybrid Energy System," *E3S Web of Conferences*.

[129] Riensche, E., Stimming, U., and Unverzagt, G., 1998, "Optimization of a 200 KW SOFC Cogeneration Power Plant Part I: Variation of Process Parameters," J. Power Sources, **73**(2), pp. 251–256.

[130] Chen, J., Liang, M., Zhang, H., and Weng, S., 2017, "Study on Control Strategy for a SOFC-GT Hybrid System with Anode and Cathode Recirculation Loops," Int. J. Hydrogen Energy, **42**(49), pp. 29422–29432.

[131] Oh, S. R., Sun, J., Dobbs, H., and King, J., 2012, "Model-Based Predictive Control Strategy for a Solid Oxide Fuel Cell System Integrated with a Turbocharger," *Proceedings of the American Control Conference*, pp. 6596–6601.

[132] Plianos, A., Chaudhari, A. R., and Stobart, R. K., *Modelling and Control of a Novel SOFC-IC Engine Hybrid System*.

[133] Mantelli, L., Ferrari, M. L., and Traverso, A., 2021, "Dynamics and Control of a Turbocharged Solid Oxide Fuel Cell System," Appl. Therm. Eng., **191**, p. 116862.

[134] Traverso, A., Magistri, L., Scarpellini, R., and Massardo, A., 2003, "Demonstration Plant and Expected Performance of an Externally Fired Micro Gas Turbine for Distributed Power Generation," *American Society of Mechanical Engineers, International Gas Turbine Institute, Turbo Expo*

(Publication) IGTI, American Society of Mechanical Engineers Digital Collection, pp. 191–199.

[135] Dixon, S. L., and Hall, C. A., 2013, *Fluid Mechanics and Thermodynamics of Turbomachinery, 7th Edition*.

[136] White, F. M., *Fluid Mechanics*.

[137] Ferrari, M. L., 2015, "Advanced Control Approach for Hybrid Systems Based on Solid Oxide Fuel Cells," Appl. Energy, **145**, pp. 364–373.

[138] Torreglosa, J. P., Jurado, F., Garca, P., and Fernndez, L. M., 2011, "Application of Cascade and Fuzzy Logic Based Control in a Model of a Fuel-Cell Hybrid Tramway," Eng. Appl. Artif. Intell., **24**(1), pp. 1–11.

[139] Belhaj, F. Z., El Fadil, H., Tahri, A., Gaouzi, K., Rachid, A., and Giri, F., 2018, "Sliding Mode Control of a Cascade Boost Converter for Fuel Cell Energy Generation System," *Proceedings of 2017 International Conference on Electrical and Information Technologies, ICEIT 2017*, Institute of Electrical and Electronics Engineers Inc., pp. 1–6.

[140] Romdlony, M. Z., Trilaksono, B. R., and Ortega, R., 2012, "Experimental Study of Extremum Seeking Control for Maximum Power Point Tracking of PEM Fuel Cell," *Proceedings of the 2012 International Conference on System Engineering and Technology, ICSET 2012*.

[141] Zhong, Z. dan, Huo, H. bo, Zhu, X. jian, Cao, G. yi, and Ren, Y., 2008, "Adaptive Maximum Power Point Tracking Control of Fuel Cell Power Plants," J. Power Sources, **176**(1), pp. 259–269.

[142] Ziegler, J. G., and Nichols, N. B., 1993, "Optimum Settings for Automatic Controllers," J. Dyn. Syst. Meas. Control. Trans. ASME, **115**(2B), pp. 220–222.

[143] Åström, K. J., and Hägglund, T., 2004, "Revisiting the Ziegler-Nichols Step Response Method for PID Control," J. Process Control, **14**(6), pp. 635–650.

[144] Franks, R. G., and Worley, C. W., 1956, "Quantitative Analysis of Cascade Control," Ind. Eng. Chem., **48**(6), pp. 1074–1079.

[145] Knospe, C., 2006, "PID Control," IEEE Control Syst., **26**(1), pp. 30–31.

[146] Han, J., Yu, S., and Yi, S., 2017, "Adaptive Control for Robust Air Flow Management in an Automotive Fuel Cell System," Appl. Energy, **190**, pp. 73–83.

[147] Marelli, S., Misley, A., Taylor, A., Silviestri, P., Capobianco, M., and Canova, M., 2018, "Experimental Investigation on Surge Phenomena in an Automotive Turbocharger Compressor," *SAE Technical Papers*, SAE International.

[148] Liśkiewicz, G., Horodko, L., Stickland, M., and Kryłłowicz, W., 2014, "Identification of Phenomena Preceding Blower Surge by Means of

Pressure Spectral Maps," Exp. Therm. Fluid Sci., **54**, pp. 267–278.

[149] Ferrari, M. L., Silvestri, P., Reggio, F., and Massardo, A. F., 2018, "Surge Prevention for Gas Turbines Connected with Large Volume Size: Experimental Demonstration with a Microturbine," Appl. Energy, **230**, pp. 1057–1064.

[150] Munari, E., D'Elia, G., Morini, M., Mucchi, E., Pinelli, M., and Spina, P. R., 2018, "Experimental Investigation of Vibrational and Acoustic Phenomena for Detecting the Stall and Surge of a Multistage Compressor," J. Eng. Gas Turbines Power, **140**(9).

[151] Ferrari, M. L., Pascenti, M., and Abrassi, A., 2019, "Test Rig for Emulation of Turbocharged SOFC Plants," E3S Web Conf., **113**, p. 02001.

[152] Ali, M. T., "SI Psychrometric Chart," MATLAB Cent. File Exch. [Online]. Available: https://it.mathworks.com/matlabcentral/fileexchange/49154-si-psychrometric-chart. [Accessed: 20-Nov-2020].

[153] Sanaye, S., and Tahani, M., 2010, "Analysis of Gas Turbine Operating Parameters with Inlet Fogging and Wet Compression Processes," Appl. Therm. Eng., **30**(2–3), pp. 234–244.

[154] Rahman, M., Zaccaria, V., Zhao, X., and Kyprianidis, K., 2018, "Diagnostics-Oriented Modelling of Micro Gas Turbines for Fleet Monitoring and Maintenance Optimization," Processes, **6**(11), p. 216.

[155] Mahmood, M., Martini, A., Massardo, A. F., and De Paepe, W., 2018, "Model Based Diagnostics of AE-T100 Micro Humid Air Turbine Cycle," ASME International.

[156] Davison, C. R., and Birk, A. M., 2006, "Automated Fault Diagnosis of a Micro Turbine with Comparison to a Neural Network Technique," *Proceedings of the ASME Turbo Expo*, pp. 795–804.

[157] Li, Z., Outbib, R., Giurgea, S., Hissel, D., Giraud, A., and Couderc, P., 2019, "Fault Diagnosis for Fuel Cell Systems: A Data-Driven Approach Using High-Precise Voltage Sensors," Renew. Energy, pp. 1435–1444.

[158] Wu, X., and Ye, Q., 2016, "Fault Diagnosis and Prognostic of Solid Oxide Fuel Cells," J. Power Sources, **321**, pp. 47–56.

[159] Yang, W., Lee, K. Y., Junker, S. T., and Ghezel-Ayagh, H., 2008, "Fault Diagnosis and Accommodation System with a Hybrid Model for Fuel Cell Power Plant," *IEEE Power and Energy Society 2008 General Meeting: Conversion and Delivery of Electrical Energy in the 21st Century, PES*.

[160] Ahn, J., Noh, Y., Park, S. H., Choi, B. Il, and Chang, D., 2017, "Fuzzy-Based Failure Mode and Effect Analysis (FMEA) of a Hybrid Molten Carbonate Fuel Cell (MCFC) and Gas Turbine System for Marine Propulsion," J. Power Sources, **364**, pp. 226–233.

[161] Romessis, C., and Mathioudakis, K., 2006, "Bayesian Network Approach for Gas Path Fault Diagnosis," J. Eng. Gas Turbines Power, **128**(1), pp.

64–72.

[162] Lee, Y. K., Mavris, D. N., Volovoi, V. V., Yuan, M., and Fisher, T., 2010, "A Fault Diagnosis Method for Industrial Gas Turbines Using Bayesian Data Analysis," J. Eng. Gas Turbines Power, **132**(4).

[163] Kestner, B. K., Lee, Y. K., Voleti, G., Mavris, D. N., Kumar, V., and Lin, T. P., 2011, "Diagnostics of Highly Degraded Industrial Gas Turbines Using Bayesian Networks," *Proceedings of the ASME Turbo Expo*, pp. 39–49.

[164] Mantelli, L., Zaccaria, V., Kyprianidis, K., and Ferrari, M. L., 2020, "A Degradation Diagnosis Method for Gas Turbine – Fuel Cell Hybrid Systems Using Bayesian Networks," ASME International.

[165] Pezzini, P., Caratozzolo, F., and Traverso, A., 2011, "Real-Time Simulation of an Experimental RIG with Pressurized SOFC," *Proceedings of the ASME Turbo Expo*, pp. 113–121.

[166] Zaccaria, V., Ferrari, M. L., and Kyprianidis, K. G., 2019, "Adaptive Control of Micro Gas Turbine for Engine Degradation Compensation," J. Eng. Gas Turbines Power.

[167] De Paepe, W., Coppitters, D., Abraham, S., Tsirikoglou, P., Ghorbaniasl, G., and Contino, F., 2019, "Robust Operational Optimization of a Typical Micro Gas Turbine," *Energy Procedia*, Elsevier Ltd, pp. 5795–5803.

[168] Ferrari, M. L., Pascenti, M., Traverso, A. N., and Massardo, A. F., 2012, "Hybrid System Test Rig: Chemical Composition Emulation with Steam Injection," Appl. Energy, **97**, pp. 809–815.

[169] Gandiglio, M., Lanzini, A., Leone, P., Santarelli, M., and Borchiellini, R., 2013, "Thermoeconomic Analysis of Large Solid Oxide Fuel Cell Plants: Atmospheric vs. Pressurized Performance," Energy, **55**, pp. 142–155.

[170] Larosa, L., Traverso, A., and Massardo, A. F., 2016, "Dynamic Analysis of a Recuperated Mgt Cycle for Fuel Cell Hybrid Systems," *Proceedings of the ASME Turbo Expo*, American Society of Mechanical Engineers (ASME).

[171] Magistri, L., Trasino, F., and Costamagna, P., 2006, "Transient Analysis of Solid Oxide Fuel Cell Hybrids - Part I: Fuel Cell Models," J. Eng. Gas Turbines Power, **128**(2), pp. 288–293.

[172] Heckerman, D., Geiger, D., and Chickering, D. M., 1995, "Learning Bayesian Networks: The Combination of Knowledge and Statistical Data," Mach. Learn., **20**(3), pp. 197–243.

[173] Romessis, C., Stamatis, A., and Mathioudakis, K., 2001, "Setting up a Belief Network for Turbofan Diagnosis with the Aid of an Engine Performance Model," *15th International Symposium on Air Breathing Engines, (Bangalore, India), International Society for Air Breathing Engines*, pp. 19–26.

Appendix

In this Appendix it is possible to find the Matlab code used to simulate the SOFC, the functions used to initialize the code and to compute various physical properties, as well as the values of the parameters set in the model.

```
%=========================================================================
% SOLID OXIDE FUEL CELL MODEL
%=========================================================================
% Function
%=========================================================================
function
[Results,AnodeOut,CathodeOut,Tsolid,Tanode,Tcathode,currDistr,Nernst,...
xtemp,xcurr,xtime]= SOFCstack(time,simstart,AnodeIn,CathodeIn,...
Data,ndiscr,x0temp,x0curr,x0time)
%#codegen
coder.extrinsic('warning');

%===STRUCTURES INITIALISATION=============================================
par=struct('kk',0,'current',0,'currdistr',zeros(1,ndiscr),'curr',zeros(1,
ndiscr));

%---PARAMETERS READING--------------------------------------------------
par.kk=ndiscr;          % Single cell discretisation

%---INPUT PORTS READING-------------------------------------------------
qinan=AnodeIn(1);       % Anode flow in [Nl/min]
pinan=AnodeIn(2);       % Anode inlet pressure [Pa]
Tfuelin=AnodeIn(3);     % Anode Temperature [K]
xAnin=AnodeIn(4:9);     % Anode Compositions: H2 H2O CH4 CO2 CO N2

qincat=CathodeIn(1);    % Cathode flow in [Nl/min]
pincat=CathodeIn(2);    % Cathode inlet pressure [Pa]
Tcat=CathodeIn(3);      % Cathode Temperature [K]
xCatin=CathodeIn(4:8);  % Cathode Compositions: H2O CO2 N2 O2 Ar /
                        % previous O2 N2 CO2 H2O Ar
```

```
par.current=Data(1);     % Stack current [A]
kasr=Data(2);            % Losses calculation mode
tsolid=Data(3);          % Solid temperature initialisation
Kcont=Data(4);           % Contact losses trim constant
Katan=Data(5);           % Anode activation losses trim constant
Katca=Data(6);           % Cathode activation losses trim constant
Kohm=Data(7);            % Ohmic losses trim constant
Kdiff=Data(8);           % Diffusion losses trim constant
Qlosses_stack=Data(9);   % Q_losses
n_cell_stack=Data(10);   % Number Of Cells into the stack

%---TIMESTEP INITIALIZATION-----------------------------------------------
actualtime=time;
dtime=0;
xtime=actualtime;
if actualtime <=0
    dtime=0.1;
elseif actualtime>0
    dtime=actualtime-x0time;
end

%---INITIALISATION OF PERSISTENT DATA VARIABLES--------------------------
persistent sd
sd=struct('nelect',0,'faraday',0,'rgas',0,'pfact',0,'LHV',zeros(1,6),...
'nusselt',0,'A',1,'B',1,'C',1,'D',1,'E',1,'F',1,'G',1,'H',1,...
'ancomp',1,'MMan',zeros(1,6),'anhmat',zeros(6,7),'refHan',zeros(6,1),...
'catcomp',1,'MMcat',zeros(1,5),'cathmat',zeros(5,7),'refHcat',...
zeros(5,1),'react',1,'hmat',zeros(6,7),'refH',zeros(6,1),'anlmat',...
zeros(6,7),'catlmat',zeros(5,7),'anmumat',zeros(6,7),'catmumat',...
zeros(5,7),'anhd',0,'cathd',0);
% if isempty(sd)
    sd=initialize(sd);
% end

%---INITIALIZATION OF ARRAY VARIABLES-------------------------------------
%___Temperature initialization
tc=zeros(1,ndiscr+1);                  % Cathode temperature
                                       % distribution
```

```
tc(1)=Tcat;                                % Cathode distribution inlet
                                           % value
tcm=zeros(1,par.kk);                       % Average cathode temperature
                                           % distribution
ta=zeros(1,ndiscr+1);                      % Anode temperature distribution
ta(1)=Tfuelin;                             % Anode distribution inlet value
tam=zeros(1,par.kk);                       % Average anode temperature
                                           % distribution
%___Flow initialization
qcat=zeros(1,par.kk+1);                    % Cathode flow distribution
qcat(1)=qincat/n_cell_stack/22.414/60;     % Cathode distribution inlet
                                           % value [mol/s]
qan=zeros(1,par.kk+1);                     % Anode flow distribution
qan(1)=qinan/n_cell_stack/22.414/60;       % Anode distribution inlet value
                                           %[mol/s]
%___Composition initialization
xcat=zeros(5,par.kk+1);                    % Cathode composition
                                           % distribution
xcat(:,1)=xCatin;                          % Cathode distribution inlet
value
xan=zeros(6,par.kk+1);                     % Anode composition distribution
xan(:,1)=xAnin;                            % Anode distribution inlet value

%___Solid temperature & current distribution initialization
if actualtime<=0    % First instant
    if simstart==1
        tpen=tsolid*ones(1,ndiscr);          % Solid T distribution
        par.currdistr=ones(1,par.kk)/par.kk; % Non-dimensional current
                                              % distribution
        par.curr=par.currdistr*par.current;  % Current distribution
    else
        tpen=x0temp;             % Solid T from states
        par.currdistr=x0curr';   % Non-dimensional current from states
                                 % $(1:par.kk)$
        par.curr=par.current*par.currdistr; % Current distribution
    end
else
    tpen=x0temp;             % Solid T from states
    par.currdistr=x0curr';   % Non-dimensional current from states
```

```
                                % $(1:par.kk)$
    par.curr=par.current*par.currdistr; % Current distribution
end
%___E-chem variables initializations
o2cons=zeros(1,par.kk);
h2cons=zeros(1,par.kk);
ch4ref=zeros(1,par.kk);
nsh=zeros(1,par.kk);
vnernst=zeros(1,ndiscr);
polconc=zeros(1,par.kk);
polca=zeros(1,par.kk);
polan=zeros(1,par.kk);
polohm=zeros(1,par.kk);
polcont=zeros(1,par.kk);
poltot=zeros(1,par.kk);
vreal=zeros(1,par.kk);

%___Thermals variables initialisation
hcin=zeros(1,par.kk+1);
hain=zeros(1,par.kk+1);
hconvc=zeros(1,par.kk);
hconva=zeros(1,par.kk);
cathconv=zeros(1,par.kk);
anhconv=zeros(1,par.kk);
hh2out=zeros(1,par.kk);
hh2oin=zeros(1,par.kk);
hch4out=zeros(1,par.kk);
hco2in=zeros(1,par.kk);
hcoout=zeros(1,par.kk);
ho2out=zeros(1,par.kk);
Qreact=zeros(1,par.kk);
% AA=zeros(1,par.kk);
% BB=zeros(1,par.kk);
% CC=zeros(1,par.kk);
% Dd=zeros(1,par.kk);

%************************************************************************
% Geometry of the cell%
%************************************************************************
```

```
LENGTH=0.1;          % [m] cell lenght
WIDTH=0.1278;        % [m] cell width
ANTHICK=40.E-6;      % [m] zan - Anode thickness
CATTHICK=40.E-6;     % [m] zca - Cathode thickness
ELTHICK=95.E-6;      % [m] zel - Electrolyte thickness
ANCOLTHICK=0.25E-3; % [m] zcca - Anode current collector thickness
CATCOLTHICK=0.25E-3;% [m] zccc - Cathode current collector thickness
ANCHATH=2.5e-3;      % [m] Anodic channel heigth [thickness]
CATCHATH=2.5e-3;     % [m] Cathodic channel thickness heigth [thickness]
ANPOR=0.4E0;         % [-] porean - anodic porosity
CATPOR=0.4E0;        % [-] poreca - cathodic porosity
ANCOLPOR=0.3E0;      % [-]porecca - anodic current collector porosity
CATCOLPOR=0.3E0;     % [-] poreccc - cathodic current collector porosity
POREDIAM=1.E-6;      % [m] dpore - mean diameter of pores
ANTORT=3.E0;         % [-] tauan - anodic tortuosity
CATTORT=3.E0;        % [-] tauca - cathodic tortuosity
ANCOLTORT=3.E0;      % [-] taucca - anodic current collector tortuosity
CATCOLTORT=3.E0;     % [-] tauccc - cathodic current collector tortuosity

%************************************************************************
% Parameters and coefficients
%************************************************************************
GIBBS1=-245255.E0;  % [J/mol] ug1 - coeff. for Gibb's free energy
GIBBS2=49.925E0;    % [J/mol] ug2 - coeff. for Gibb's free energy
GIBBS3=2.625E-3;    % [J/mol] ug3 - coeff. for Gibb's free energy
ROAN=20000.E0;      % [1/ohm m] - an. electronic conductivity
ROCA=2500.E0;       % [1/ohm m] - cat. electronic conductivity
ROEL1=28333.E0;     % [1/ohm m] - coeff. for electrolyte ionic
                    % conductivity
ROEL2=11000.E0;     % [K] - coeff. for electrolyte ionic conductivity
KAN=5.5E8;          % [A/m2] - an. preexp. factor (eq. Rechenauer)
EAN=1.E5;           % [J/mol] - an. activation en. (eq. Rechenauer)
MAN=1.0E0;          % [-] - an. exponential factor (eq. Rechenauer)
KCA=7.E8;           % [A/m2] - cat. preexp. factor (eq. Rechenauer)
ECA=1.2E5;          % [J/mol] - cat. activation en. (eq. Rechenauer)
MCA=0.25E0;         % [-] - cat. exponential factor (eq. Rechenauer)
TETAAN1=2.E0;       % [-] - an. electron transfer coeff.
                   % (eq. Butler-Volmer)
TETAAN2=1.E0;       % [-] - an. electron transfer coeff.
```

```
                    % (eq. Butler-Volmer)

TETACA1=0.6E0;      % [-] - cat. electron transfer coeff.
                    % (eq. Butler-Volmer)
TETACA2=1.4E0;      % [-] - cat. electron transfer coeff.
                    % (eq. Butler-Volmer)

%**************************************************************************
% Solid Properties
%**************************************************************************
ROSOLID=7700.E-1;   % 7700/5200 [kg/m3] - Solid density, FeCrAlloy
CPSOLID=660.E-1;    % 660/430 [J/kg K] - Solid specific heat, FeCrAlloy
kcon=24;            % [W/m K] cell thermal conductivity

**************************************************************************
% Geometry Initialization
%**************************************************************************
% positive-electrolyte-negative (PEN)
% PAB is the ionic bond strength
% Active electrolyte area equal to total area [m2]
elaa=LENGTH*WIDTH;
% Lenght of integration element [m]
xcell=LENGTH/par.kk;
% Area of each integration element (cell) and total area (tube) [m2] [m2]
area=elaa/par.kk;
% Anodic channel geometry [m] [m2] and hydraulic diameters [m] = 4*p/A
anchp=2*ANCHATH+2*WIDTH;    % Anode Perimeter
ancha=ANCHATH*WIDTH;        % Anode Area
sd.anhd=4*ancha/anchp;
% Cathodic channel geometry [m] [m2] and hydraulic diameters [m]
catchp=2*WIDTH+2*CATCHATH;
catcha=WIDTH*CATCHATH;
sd.cathd=4*catcha/catchp;
% Solid geometry
solthick=ANTHICK+CATTHICK+ELTHICK+ANCOLTHICK+CATCOLTHICK;
soltrasvarea=WIDTH*solthick;

% ELECTROCHEMICAL PERFORMANCE CALCULATION ================================
isoVerr=10;
```

```
while isoVerr>0.001
    for i=1:(par.kk)
        %---CATHODE REACTION-----------------------------------------------
        %___O2 current
        o2cons(i)=par.curr(i)/(2*sd.nelect*sd.faraday);
        o2react=[0 0 0 -o2cons(i) 0];
        %___Next cell flowrate [mol/s]
        qcat(i+1)=qcat(i)-par.curr(i)/(2*sd.nelect*sd.faraday);
        %___Next cell composition
        xcat(:,i+1)=(xcat(:,i)*qcat(i)+o2react')/qcat(i+1);
        xO2cm=(xcat(4,i)+xcat(4,i+1))/2;

        %---ANODE REACTION-------------------------------------------------
        %___H2 current
        h2cons(i)=par.curr(i)/(sd.nelect*sd.faraday);
        h2react=[-h2cons(i) +h2cons(i) 0 0 0 0];
        %___Complete reforming of residual methane
        ch4ref(i)=qan(i)*xan(3,i);
        ch4react=[+3*ch4ref(i) -ch4ref(i) -ch4ref(i) 0 +ch4ref(i) 0];
        %___Single species flows [mol/s] at inlet of integration element
        inflows=qan(i)*xan(:,i);
        %___Single species at shifting after reforming and e-chem
        % reaction
        shiftflows=inflows+h2react'+ch4react';
        %___Shifting constant
        Is=-5.0927801e0;
        HOs=-4.182e4;
        DAs=-9.125e-1;
        DBs=2.382e-2;
        DCs=-1.219e-5;
        LGs=Is-HOs/(sd.rgas*tpen(i))+(DAs/sd.rgas)*log(tpen(i))+...
        (DBs/(2*sd.rgas))*tpen(i)+(DCs/(6*sd.rgas))*(tpen(i)^2);
        KS=exp(LGs);
        %___Shifting reaction
        A=(KS-1);
        B=-(KS*(shiftflows(5)+shiftflows(2))+shiftflows(1)+...
        shiftflows(4));
        C=KS*shiftflows(5)*shiftflows(2)-shiftflows(1)*shiftflows(4);
        if(A==0)
```

```
    nsh(i)=-C/B;
else
    sol1=(-B+sqrt((B^2)-4*A*C))/(2*A);
    sol2=(-B-sqrt((B^2)-4*A*C))/(2*A);
    if A*C>=0 && -B/A>0
        nsh(i)=min(sol1,sol2);
    elseif A*C>=0 && -B/A<0
        nsh(i)=max(sol1,sol2);
    elseif A*C<0 && -B/A>0
        nsh(i)=min(sol1,sol2);
    elseif A*C<0 && -B/A<0
        nsh(i)=max(sol1,sol2);
    end
end
coreact=[nsh(i) -nsh(i) 0 nsh(i) -nsh(i) 0];
outflows=shiftflows+coreact';
%___Next cell flowrate [mol/s]
qan(i+1)=sum(outflows);
%___Next cell composition
xan(:,i+1)=outflows/qan(i+1);
if i==1 %assign to the first cell average composition the outlet
        % one
    xH2am=xan(1,i+1);
    xH2Oam=xan(2,i+1);
else
    xH2am=(xan(1,i)+xan(1,i+1))/2;
    xH2Oam=(xan(2,i)+xan(2,i+1))/2;
end

%---ELECTROCHEMISTRY----------------------------------------------
%___Gibbs potential [V]
UG=-(GIBBS1+GIBBS2*tpen(i)+GIBBS3*(tpen(i)^2))/...
(sd.nelect*sd.faraday);
%___Nernst's open circuit voltage [V]
cost=sd.rgas*tpen(i)/(sd.faraday*sd.nelect);
pga_an=pinan/sd.pfact; % P is in [atm] in Nernst's voltage
                       % formula
pga_cat=pincat/sd.pfact; % P is in [atm] in Nernst's voltage
                         % formula
```

```
if(xH2Oam<=0)
    xH2Oam=1e-5;
end
CG=(pga_an*xH2am)*sqrt(pga_cat*xO2cm)/(pga_an*xH2Oam);
vnernst(i)=UG+cost*log(CG);
%___Overpotentials
if(kasr==1) % Simplified calculation
    iASR=0.505/0.847*exp(1.080*sd.faraday/(sd.rgas)*...
    (1/tpen(i)-1/(860+273.15)))+0.125;
    poltot(i)=par.curr(i)/(area*1e4)*iASR;
else        % Detailed calculation
    % ionic conductivities [S/m] (Bossel)
    roel=ROEL1*exp(-ROEL2/tpen(i));
    eqvr2=ANTHICK/ROAN+CATTHICK/ROCA+ELTHICK/roel;

    %___Diffusion Losses [V]_____________________________________
    MH2H2O=((1/sd.MMan(1)+1/sd.MMan(2))^-1);
    MO2N2=((1./sd.MMcat(4)+1/sd.MMcat(3))^-1);
    %   Collision Diameters [A°] (1A°=1.E-10m)
    %   R.A.Svehla:NACA Tech.Rep. R-132,
    %   Lewis Research Center, Cleveland, Ohio USA 1962
    SIH2=2.915;
    SIH2O=3.737;
    SIO2=3.433;
    SIN2=3.681;
    EKH2=38;
    EKH2O=32;
    EKO2=113;
    EKN2=91.5;
    SIH2H2O=(SIH2+SIH2O)/2;
    SIO2N2=(SIO2+SIN2)/2;
    EKH2H2O=(EKH2*EKH2O)^(1/2);
    EKO2N2=(EKO2*EKN2)^(1/2);
    KBH2H2O=tpen(i)/EKH2H2O;
    KBO2N2=tpen(i)/EKO2N2;
    OMH2H2O=sd.A./KBH2H2O.^sd.B+sd.C./exp(sd.D.*KBH2H2O)...
    +sd.E./…exp(sd.F.*KBH2H2O)+sd.G./exp(sd.H.*KBH2H2O);
    OMO2N2=sd.A./KBO2N2.^sd.B+sd.C./exp(sd.D.*KBO2N2)...
    +sd.E./exp(sd.F.*KBO2N2)+sd.G./exp(sd.H.*KBO2N2);
```

```
% Ordinary diffusion coefficients for binary gas mixtures
% [m2/s] (Hirschfelder,Bird & Spotz)
DH2H2O=1.8583E-7*(tpen(i)^1.5)/(pga_an*(SIH2H2O^2)...
*sqrt(MH2H2O)*OMH2H2O);                                    %
DO2N2=1.8583E-7*(tpen(i)^1.5)/(pga_cat*(SIO2N2^2)...
*sqrt(MO2N2)*OMO2N2);
% Knudsen diffusion coefficients for H2 and O2 [m2/s]
DH2K=2/3*POREDIAM*sqrt(8*sd.rgas*tpen(i)/(pi*sd.MMan(1)));
DO2K=2/3*POREDIAM*sqrt(8*sd.rgas*tpen(i)/(pi*sd.MMcat(4)));
% Effective diffusion coefficients [m2/s] (Bosanquet)
deffan=(ANPOR/ANTORT)*((1/DH2H2O+1/DH2K)^-1);
deffca=(CATPOR/CATTORT)*((1/DO2N2+1/DO2K)^-1);
deffcca=(ANCOLPOR/ANCOLTORT)*((1/DH2H2O+1/DH2K)^-1);
deffccc=(CATCOLPOR/CATCOLTORT)*((1/DO2N2+1/DO2K)^-1);
% Anodic and cathodic concentration polarization
dra=(par.curr(i)/area)*sd.rgas*tpen(i)*...
(ANCOLTHICK/deffcca+ANTHICK/deffan)/...
(sd.nelect*sd.faraday*pinan);
coa=(sd.rgas*tpen(i)/(sd.nelect*sd.faraday))*...
log((1+dra/xH2Oam)/(1-dra/xH2am));
drc=(par.curr(i)/area)*sd.rgas*tpen(i)*(CATCOLTHICK/...
deffccc+CATTHICK/deffca)/(2*sd.nelect*sd.faraday*pincat);
coc=(sd.rgas*tpen(i)/(2*sd.nelect*sd.faraday))*...
log((1/xO2cm-(1/xO2cm-1)*exp(drc))^-1);
polconc(i)=coc+coa;
% H2 and H2O cocentration at anode/electrolyte interface
% [mol/mol]
xH2ai=xH2am-dra;
xH2Oai=xH2Oam+dra;
% O2 concentration at the cathode/electrolyte interface
% [mol/mol]
xO2ci=1-(1-xO2cm)*exp(drc);
%___Activation Losses [V]_____________________________________
% anodic activation resistance [ohm]
% (Rechenauer and linear Butler-Volmer)
anexcurr=(KAN*(xH2ai*xH2Oai*(pga_an^2))^MAN)*...
exp(-EAN/(sd.rgas*tpen(i)))*area;
actan=cost/((TETAAN1+TETAAN2)*anexcurr);
```

```
% cathodic activation resistance [ohm] (Rechenauer and linear
% Butler-Volmer)
caexcurr=(KCA*(xO2ci*pga_cat)^MCA)*...
exp(-ECA/(sd.rgas*tpen(i)))*area;
actca=cost/((TETACA1+TETACA2)*caexcurr);
% Activation polarization
polan(i)=actan*par.curr(i);
if(polan(i)>0.1)
    polan(i)=cost*log(par.curr(i)/anexcurr)/TETAAN1;
end
polca(i)=actca*par.curr(i);
if(polca(i)>0.1)
    polca(i)=cost*log(par.curr(i)/caexcurr)/TETACA1;
end
erran=5;
errca=5;
while((erran>1.e-4)||(errca>1e-4))
    corran=anexcurr*(exp(TETAAN1*polan(i)/cost)-...
    exp(-TETAAN2*polan(i)/cost));
    deran=anexcurr*(TETAAN1*exp(TETAAN1*polan(i)/cost)/...
    cost+TETAAN2*exp(-TETAAN2*polan(i)/cost)/cost);
    if par.curr(i)>0
        erran=abs((corran-par.curr(i))/par.curr(i));
    else
        erran=abs(corran-par.curr(i));
    end
    corrca=caexcurr*(exp(TETACA1*polca(i)/cost)-...
    exp(-TETACA2*polca(i)/cost));
    derca=caexcurr*(TETACA1*exp(TETACA1*polca(i)/cost)/...
    cost+TETACA2*exp(-TETACA2*polca(i)/cost)/cost);
    if par.curr(i)>0
        errca=abs((corrca-par.curr(i))/par.curr(i));
    else
        errca=abs(corrca-par.curr(i));
    end
    %Newton-Raphson's method
    if(erran>1e-4)
        polan(i)=polan(i)+0.5*(par.curr(i)-corran)/deran;
    end
```

```
                if(errca>1e-4)
                    polca(i)=polca(i)+0.5*(par.curr(i)-corrca)/derca;
                end
            end
            %___Ohmic Losses [V]_____________________________________________
            polohm(i)=eqvr2*par.curr(i)/area;
            %___Contact Losses [V]____________________________________________
            rcontact=0.0031169E0;
            polcont(i)=rcontact*par.curr(i);
            %___Total Losses [V]______________________________________________
            poltot(i)=(polan(i)*Katan+polca(i)*Katca+...
            polohm(i)*Kohm+polconc(i)*Kdiff+polcont(i)*Kcont);
        end
        %___Cell voltage [V]_____________________________________________
        vreal(i)=vnernst(i)-poltot(i);
    end
    %---UNIFORM VOLTAGE ON CELL PLATE-----------------------------------
    par=equipotential(vreal,par);
    meanvolt=mean(vreal);
    isoVerr=max(abs(vreal-meanvolt)/meanvolt);
    if par.current<=0.7
        isoVerr=0;
    end
end

% === END ELECTROCHEMICAL PERFORMANCE CALCULATION ======================

% === THERMALS CALCULATIONS ============================================

%Estimation of Q_losses as function of Stack_Power and cathode flow rate
%Qlosses_stack=205.2502+ 7.5949*par.current -0.6165*qincat; %[W]
Qlosses_cell=Qlosses_stack/n_cell_stack; %[W]
%Parabolic distribution
x=0.5/par.kk:1/par.kk:1-0.5/par.kk;
y=12*x.^2-12*x+3;
Area=sum(y*1/par.kk);
Q_losses=y*1/par.kk*Qlosses_cell/Area; %correction due to
                                       % finite number of par.kk
U=(kcon/xcell)*soltrasvarea; %[W/K]
```

```
    R=1/U; %[K/W]
    AA=zeros(1,ndiscr);
BB=zeros(1,ndiscr);
CC=zeros(1,ndiscr);
Dd=zeros(1,ndiscr);
for i=1:par.kk

    % --- CATHODE ------------------------------------------------------
    % Convective heat transfer coefficient [W/m2 K]
    cathconv(i)=sd.nusselt*catcond(tc(i),xcat(:,i)',sd)/sd.cathd;
    % Cathode enthalpy @ integration element inlet
    hcin(i)=qcat(i)*cath(tc(i),xcat(:,i),sd);
    % Reacting streams enthalpies @ Tpen
    hTpen=hreactants(tpen(i),sd);
    o2out=o2cons(i);
    tc(i+1)=0.5*(tc(i)+tpen(i));
    errc=1.0;
    tpos=0;
    tneg=0;
    w=1;
    while abs(errc)>1e-6
        % Cathode enthalpy @ integration element outlet
        hcin(i+1)=qcat(i+1)*cath(tc(i+1),xcat(:,i+1),sd);
        % Mean cathode temperature
        tcm(i)=0.5*(tc(i)+tc(i+1));
        % Reacting streams enthalpies @ average Tcat
        hTcat=hreactants(tcm(i),sd);
        % Reacting O2 enthalpy according to reaction sign
        hTotal=hTcat+hTpen;
        ho2out(i)=o2out*0.5*(hTotal(6)+hTcat(6)*...
        sign(o2out)-hTpen(6)*sign(o2out));
        hconvc(i)=cathconv(i)*area*(tpen(i)-tcm(i));
        errc=(hcin(i+1)+ho2out(i)-hcin(i)-hconvc(i))/abs(hcin(i));
        tpos=tc(i+1)*(errc>0)+tpos*(errc<=0);
        tneg=tc(i+1)*(errc<0)+tneg*(errc>=0);
        if tpos==0 || tneg==0
            if errc<0
                tc(i+1)=tc(i+1)+w*10;
            elseif errc>0
```

```
                tc(i+1)=tc(i+1)-w*10;
            end
            if tc(i+1)<288.15 || tc(i+1)>1750
                warning(['MATLAB: Initialisation Overflow.',...
                ' No first guess found in cathode thermal...
                  for element %d.'],i);
                break;
            end
        else
            tc(i+1)=(tpos+tneg)/2;
        end
        w=w+1;
        if w>=200
            break;
        end
    end

% --- ANODE ------------------------------------------------------------
    % Convective heat transfer coefficient [W/m2 K]
    anhconv(i)=sd.nusselt*ancond(ta(i),xan(:,i)',sd)/sd.anhd;
    % Anode enthalpy @ integration element inlet
    hain(i)=qan(i)*anh(ta(i),xan(:,i),sd);
    % Reacting streams enthalpies @ Tpen
    hTpen=hreactants(tpen(i),sd);
    h2out=h2cons(i)-3*ch4ref(i)-nsh(i);
    h2oin=h2cons(i)-ch4ref(i)-nsh(i);
    ch4out=ch4ref(i);
    co2in=nsh(i);
    coout=nsh(i)-ch4ref(i);
    ta(i+1)=0.5*(ta(i)+tpen(i));
    erra=1.0;
    tpos=0;
    tneg=0;
    w=1;
    while abs(erra)>1e-6
        % Anode enthalpy @ integration element outlet
        hain(i+1)=qan(i+1)*anh(ta(i+1),xan(:,i+1),sd);
        % Mean anode temperature
        tam(i)=0.5*(ta(i)+ta(i+1));
```

```
    % Reacting streams enthalpies @ average Tan
    hTan=hreactants(tam(i),sd);
    % Reacting streams enthalpies according to reaction sign
    hTotal=hTan+hTpen;
    hh2out(i)=h2out*0.5*(hTotal(1)+hTan(1)*sign(h2out)...
    -hTpen(1)*sign(h2out));
    hh2oin(i)=h2oin*0.5*(hTotal(2)- ...
    hTan(2)*sign(h2oin)+hTpen(2)*sign(h2oin));
    hch4out(i)=ch4out*0.5*(hTotal(3)+hTan(3)*sign(ch4out)-...
    hTpen(3)*sign(ch4out));
    hco2in(i)=co2in*0.5*(hTotal(4)-...
    hTan(4)*sign(co2in)+hTpen(4)*sign(co2in));
    hcoout(i)=coout*0.5*(hTotal(5)+hTan(5)*sign(coout)-...
    hTpen(5)*sign(coout));
    hconva(i)=anhconv(i)*area*(tpen(i)-tam(i));
    erra=(hain(i+1)+hh2out(i)+hch4out(i)+hcoout(i)-...
    hain(i)-hh2oin(i)-hco2in(i)-hconva(i))/abs(hain(i));
    tpos=ta(i+1)*(erra>0)+tpos*(erra<=0);
    tneg=ta(i+1)*(erra<0)+tneg*(erra>=0);
    if tpos==0 || tneg==0
        if erra<0
            ta(i+1)=ta(i+1)+w*10;
        elseif erra>0
            ta(i+1)=ta(i+1)-w*10;
        end
        if ta(i+1)<288.15 || ta(i+1)>1750
            warning(['MATLAB:InitialisationOverflow.',...
            ' No first guess found in anode thermal...
            for element %d.'],i);
            break;
        end
    else
        ta(i+1)=(tpos+tneg)/2;
    end
    w=w+1;
    if w>=200
        break;
    end
end
```

```
    % --- electrochemical, reforming and shifting reactions [W]
    Qreact(i)=hh2out(i)+hch4out(i)-hh2oin(i)-...
    hco2in(i)+hcoout(i)+ho2out(i)-vreal(i)*par.curr(i);
    %Solution Matrix
    A(i)=(ROSOLID*CPSOLID*soltrasvarea*xcell/dtime)+(2/R)+...
    area*(anhconv(i)+cathconv(i));
    BB(i)=-1/R;
    CC(i)=-1/R;
    Dd(i)=anhconv(i)*area*tam(i)+cathconv(i)*area*tcm(i)+...
    Qreact(i)+(tpen(i)*ROSOLID*CPSOLID*soltrasvarea*...
    xcell/dtime)-Q_losses(i);
end
%Vectors for k+1 and k-1 for Upper and Lower diagonals
AA(1)=AA(1)-1/R;
AA(par.kk)=AA(par.kk)-1/R;
Bi=BB(1,1:par.kk-1);
Ci=CC(1,2:par.kk);
%Matrix
maindiagonal=diag(AA);
lower=diag(Bi,1);
upper=diag(Ci,-1);
M=maindiagonal+upper+lower;
dD=Dd';
tpennew=(M\dD)';
tpen(1:par.kk)=tpennew;

% === END THERMALS CALCULATIONS ==========================================

% === LAST CALCULATIONS ==================================================

Uf=(par.current*n_cell_stack/(sd.nelect*sd.faraday))/...
(qinan/60/22.414*(xan(1,1)+4*xan(3,1)+xan(5,1)));
Lambda=1/((par.current/(sd.nelect*2*sd.faraday))/...
(qcat(1)*(xcat(4,1))));
UO2=(par.current*n_cell_stack/(2*sd.nelect*sd.faraday))/...
(qincat/22.414/60*(xCatin(4)));
SteamToCarbon=xAnin(2)/(xAnin(3)+xAnin(5));
 %Efficiency
LHVin=qan(1)*sd.LHV*xan(:,1);
```

```
eff=(par.current*vreal(end)/LHVin);
% Average values
vrealm=mean(vreal);
% Thermal balance
ThermalBalError=(hain(par.kk+1)+hcin(par.kk+1)-hain(1)-...
hcin(1)+par.current*vrealm+Qlosses_cell)/(hain(1)+hcin(1));
CellCurrentDensity=par.current/elaa/1e4;
Power=par.current*vrealm*n_cell_stack;
qoutcat=qcat(par.kk+1)*n_cell_stack*22.414*60;

% -----WORKING VECTORS STATES UPDATE-----------------------------------
xtemp=tpen;
xcurr=par.currdistr;
% Fixed output update
Results=[ThermalBalError;Qlosses_stack;UO2;n_cell_stack;...
SteamToCarbon;mean(tpen);ta(end);tc(end);CellCurrentDensity;...
-1;-1;vrealm;mean(vnernst);SteamToCarbon;-1;...
qincat/n_cell_stack;tpen(end);Uf;eff;Lambda;Power];
% Anode output update
AnodeOut=[qan(par.kk+1)*n_cell_stack*22.414*60;...
pinan;ta(par.kk+1);xan(:,par.kk+1);0];
% Cathode output update
CathodeOut=[qoutcat;pincat;tc(par.kk+1);xcat(:,par.kk+1)];
% Solid T distribution
Tsolid=tpen;
% Anode T distribution
Tanode=ta;
% Cathode T distribution
Tcathode=tc;
% Current distribution
currDistr=par.curr;
% Nernst Voltage distribution
Nernst=vnernst;

% ===CUSTOM FUNCTIONS=================================================

%____Initialisation_____________________________________________________
function sd=initialize(sd)
% --- Properties & Constants ----------------------------------------
```

```
sd.nelect=2.;           % [-] ne - number of electrons transferred
sd.faraday=96485.3399;  % [C/mol] fc - Faraday's constant
sd.rgas=8.3145E0;       % [J/mol K] rg - perfect gases constant
sd.pfact=101325.E0;     % [Pa/atm] pcfact - pressure conversion factor
sd.LHV=[241820.0 0.0 802620.0 0.0 283000.0 0.0];
sd.nusselt=4.E0;            % [-] - Nusselt number

% The interpolation of collision integrals has been superseded by the use
% of the analytical formula found in "The Properties of Gases and
% Liquids"
% by Poling, Prausnitz & O'Connell, 5th Edition -------------------------

% Coefficients for collision integrals analytical expression
sd.A=1.06036;
sd.B=0.15610;
sd.C=0.19300;
sd.D=0.47635;
sd.E=1.03587;
sd.F=1.52996;
sd.G=1.76474;
sd.H=3.89411;

% --- REFERENCE ENTHALPY -----------------------------------------------
% Reference enthalpy [kJ/kmol]=enthalpy at reference temperature + the
% standard enthalpy of formation of each specie
reftred=298.15/1000;
reftredvect=1000*[reftred^1 reftred^2 reftred^3 reftred^4 reftred^5
reftred^6 reftred^7];
hcoeffh2=[21.157/1 56.036/2 -150.55/3 199.29/4...
-136.15/5 46.903/6 -6.4725/7];       % H2
hcoeffh2o=[37.373/1 -41.205/2 146.01/3 -217.08/4...
181.54/5 -79.409/6 14.015/7];      % H2O
hcoeffch4=[47.964/1 -178.59/2 712.55/3 -1068.7/4...
856.93/5 -358.75/6 61.321/7];      % CH4
hcoeffco2=[4.3669/1 204.60/2 -471.33/3 657.88/4...
-519.9/5 214.58/6 -35.992/7];       % CO2
hcoeffco=[30.429/1 -8.1781/2 5.2062/3 41.974/4...
-66.346/5 37.756/6 -7.6538/7];       % CO
hcoeffn2=[29.027/1 4.8987/2 -38.040/3 105.17/4...
```

```
-113.56/5 55.554/6 -10.350/7];       % N2
hcoeffo2=[34.850/1 -57.975/2 203.68/3 -300.37/4...
231.72/5 -91.821/6 14.776/7];       % O2
hcoeffar=[20.786/1 0.0 0.0 0.0 0.0 0.0 0.0];  % Ar
% Anode
sd.ancomp=6;
sd.MMan=[2.016 18.015 16.043 44.009 28.01 28.013];
refAnHform=[0 241814 74520 393510 110530 0];
sd.anhmat=[hcoeffh2;hcoeffh2o;hcoeffch4;hcoeffco2;hcoeffco;hcoeffn2];
sd.refHan=sd.anhmat*reftredvect'+refAnHform';
% Cathode
sd.catcomp=5;
sd.MMcat=[18.015 44.009 28.013 31.998 39.948];
refCatHform=[241814 393510 0 0 0];
sd.cathmat=[hcoeffh2o;hcoeffco2;hcoeffn2;hcoeffo2;hcoeffar];
sd.refHcat=sd.cathmat*reftredvect'+refCatHform';
% Reactants
sd.react=6; % Number of reactants stream considered in solid & gases
            % energy balance.
refHform=[0 241814 74520 393510 110530 0];
sd.hmat=[hcoeffh2;hcoeffh2o;hcoeffch4;hcoeffco2;hcoeffco;hcoeffo2];
sd.refH=sd.hmat*reftredvect'+refHform';

% --- THERMAL CONDUCTIVITY MATRIX -------------------------------------
lcoeffh2=[1.5040 62.892 -47.190 47.763 -31.939 11.972 -1.8954];
lcoeffh2o=[2.0103 -7.9139 35.922 -41.390 35.993 -18.974 4.1531];
lcoeffch4=[0.4796 1.8732 37.413 -47.440 38.251 -17.283 3.2774];
lcoeffco2=[2.8888 -27.018 129.65 -233.29 216.83 -101.12 18.698];
lcoeffco=[-0.2815 13.999 -23.186 36.018 -30.818 13.379 -2.3224];
lcoeffn2=[-0.3216 14.810 -25.473 38.837 -32.133 13.493 -2.2741];
lcoeffo2=[-0.1857 11.118 -7.3734 6.7130 -4.1797 1.4910 -0.2278];
lcoeffar=[-0.1331 10.404 -18.610 26.039 -20.573 8.5311 -1.4444];
sd.anlmat=[lcoeffh2;lcoeffh2o;lcoeffch4;lcoeffco2;lcoeffco;lcoeffn2];
sd.catlmat=[lcoeffh2o;lcoeffco2;lcoeffn2;lcoeffo2;lcoeffar];

%% --- ABSOLUTE VISCOSITY MATRIX ---------------------------------------
mucoeffh2o=[-6.7541 244.93 419.50 -522.38 348.12 -126.96 19.591];
mucoeffco2=[-20.434 680.07 -432.49 244.22 -85.929 14.450 -0.4564];
mucoeffn2=[1.2719 771.45 -809.20 832.47 -553.93 206.15 -32.430];
```

```
mucoeffo2=[-1.6918 889.75 -892.79 905.98 -598.36 221.64 -34.754];
mucoeffar=[-3.0982 978.51 -922.67 912.64 -593.76 217.79 -33.919];
mucoeffh2=[15.553 299.78 -244.34 249.41 -167.51 62.966 -9.9892];
mucoeffch4=[-9.9989 529.37 -543.82 548.11 -367.06 140.48 -22.920];
mucoeffco=[-4.9137 793.65 -875.90 883.75 -572.14 208.42 -32.298];
sd.anmumat=[mucoeffh2;mucoeffh2o;mucoeffch4;mucoeffco2;...
mucoeffco;mucoeffn2];
sd.catmumat=[mucoeffh2o;mucoeffco2;mucoeffn2;mucoeffo2;mucoeffar];
return

%_____Enthalpy_____________________________________________________________
function anhmolar=anh(tflow,compflow,sd)
% This function returns the enthalpy in [J/mol] at a given temperature in
% [K] of an anode gas mixture molar composition including the following
% gases [H2 H2O CH4 CO2 CO N2 Ar].
% Temperature T can be a vector with [M,1]=size(T) and compositon C
% can be a matrix with [N,M]=size(C) where N is the number of elements in
% the composition array (7).
% The third input, sd, is the structure used to pass extra data to the
% function:
%   1) Enthalpies of formation of each component;
%   2) Matrix of coefficients for the calculation of single component
%   enthalpies in [kJ/kmol].

% Reduced temperature vector
tredvect=1000*[(tflow/1000).^1 (tflow/1000).^2 (tflow/1000).^3
(tflow/1000).^4 (tflow/1000).^5 (tflow/1000).^6 (tflow/1000).^7];
len=size(tredvect,1);
% Enthalpy of mixture
h=zeros(sd.ancomp,len);
anhmolar=zeros(1,size(tredvect,1));
for q=1:size(tredvect,1)
    h(:,q)=sd.anhmat*tredvect(q,:)'-sd.refHan;
    anhmolar(q)=compflow(:,q)'*h(:,q);  %   [J/mol]
end
return
function cathmolar=cath(tflow,compflow,sd)

% This function returns the enthalpy in [J/mol] at a given temperature in
```

```
% [K] of a cathode gas mixture molar composition including the following
% gases [H2O CO2 N2 O2 Ar].
% Temperature T can be a vector with [M,1]=size(T) and compositon C
% can be a matrix with [N,M]=size(C) where N is the number of elements in
% the composition array (5).
% The third input, sd, is the structure used to pass extra data to the
% function:
%   1) Enthalpies of formation of each component;
%   2) Matrix of coefficients for the calculation of single component
%   enthalpies in [kJ/kmol].

% Reduced temperature vector
tredvect=1000*[(tflow/1000).^1 (tflow/1000).^2 (tflow/1000).^3
(tflow/1000).^4 (tflow/1000).^5 (tflow/1000).^6 (tflow/1000).^7];
% Enthalpy of mixture
h=zeros(sd.catcomp,size(tredvect,1));
cathmolar=zeros(1,size(tredvect,1));
for q=1:size(tredvect,1)
    h(:,q)=sd.cathmat*tredvect(q,:)'-sd.refHcat;
    cathmolar(q)=compflow(:,q)'*h(:,q);%    [J/mol]
end
return

function reactH=hreactants(tflow,sd)
% This function returns the enthalpy in [J/mol] at a given temperature in
% [K] of the following set of reacting gases [H2 H2O CH4 CO2 CO O2].
% Temperature T can be a vector with [M,1]=size(T).
% The second input, sd, is the structure used to pass extra data to the
% function:
%   1) Enthalpies of formation of each component;
%   2) Matrix of coefficients for the calculation of single component
%   enthalpies in [kJ/kmol].

% Reduced temperature vector
tredvect=1000*[(tflow/1000).^1 (tflow/1000).^2 (tflow/1000).^3
(tflow/1000).^4 (tflow/1000).^5 (tflow/1000).^6 (tflow/1000).^7];
reactH=zeros(sd.react,size(tredvect,1));
for q=1:size(tredvect,1)
    reactH(:,q)=sd.hmat*tredvect(q,:)'-sd.refH;
```

```
end
return
%_____Thermal Conductivity_____________________________________________
function anlamda=ancond(tflow,compflow,sd)
% This function returns the thermal conductivity in [W/m K] at a given
% temperature in [K] of an anode gas mixture molar composition including
% the following gases [H2 H2O CH4 CO2 CO N2 Ar].
% Temperature T can be a vector with [1,1]=size(T) and compositon C
% can be a matrix with [1,N]=size(C) where N is the number of elements in
% the composition array (7).
% The third input, sd, is the structure used to pass extra data to the
% function:
%   1) Matrix of coefficients for the calculation of single component
%   thermal conductivity in [W/m K];
%   2) Matrix of coefficients for the calculation of single component
%   absolute viscosity in micro Poise [microP] = 10-7 [Pa*s].

% Reduced temperature vector
tredvect=[(tflow/1000)^0 (tflow/1000)^1 (tflow/1000)^2 (tflow/1000)^3
(tflow/1000)^4 (tflow/1000)^5 (tflow/1000)^6];
% Pure gas thermal conductivity [W/m K]
tvectlamda=0.01*tredvect;
lamda=sd.anlmat*tvectlamda';
% Pure gas absolute viscosity in micro Poise [microP] = 10-7 [Pa*s]
tvectmu=tredvect;
mu=sd.anmumat*tvectmu';
% Thermal conductivity of mixture by the Wassiljewa's method in[W/m K]
MM=[2.016;18.015;16.043;44.009;28.01;28.013];
eps1=1;    % This constant is near unity but is taken as unity
lamdaratio=zeros(sd.ancomp);
AA=(mu./MM)*ones(1,sd.ancomp);
MMratio=zeros(sd.ancomp);
MMmat=MM*ones(1,sd.ancomp);
for i=1:sd.ancomp
    ab=AA(1:sd.ancomp,i);
    ba=AA(i,1:sd.ancomp)';
    lamdaratio(1:sd.ancomp,i)=ab./ba;
    bc=MMmat(1:sd.ancomp,i);
    cb=MMmat(i,1:sd.ancomp)';
```

```
    MMratio(1:sd.ancomp,i)=bc./cb;
end
AIJ=(eps1*(ones(sd.ancomp,sd.ancomp)+lamdaratio.^0.5.*...
MMratio.^0.25).^2)./((8*(1+MMratio)).^0.5);
mixmix=AIJ*compflow';
lamdamix=compflow*(lamda(1:sd.ancomp)./mixmix(1:sd.ancomp));
anlamda=lamdamix;   %   [W/m K]
return

function catlamda=catcond(tflow,compflow,sd)
% This function returns the thermal conductivity in [W/m K] at a given
% temperature in [K] of a cathode gas mixture molar composition including
% the following gases [H2O CO2 N2 O2 Ar].
% Temperature T can be a vector with [1,1]=size(T) and compositon C
% can be a matrix with [1,N]=size(C) where N is the number of elements in
% the composition array (5).
% The third input, sd, is the structure used to pass extra data to the
% function:
%   1) Matrix of coefficients for the calculation of single component
%   thermal conductivity in [W/m K];
%   2) Matrix of coefficients for the calculation of single component
%   absolute viscosity in micro Poise [microP] = 10-7 [Pa*s].

% Reduced temperature vector
tredvect=[(tflow/1000)^0 (tflow/1000)^1 (tflow/1000)^2...
(tflow/1000)^3 (tflow/1000)^4 (tflow/1000)^5 (tflow/1000)^6];
% Pure gas thermal conductivity [W/m K]
tvectlamda=0.01*tredvect;
lamda=sd.catlmat*tvectlamda';
% Pure gas absolute viscosity in micro Poise [microP] = 10-7 [Pa*s]
tvectmu=tredvect;
mu=sd.catmumat*tvectmu';
% Thermal conductivity of mixture by the Wassiljewa's method in[W/m K]
MM=[18.015;44.009;28.013;31.998;39.948];
eps1=1.;    % This constant is near unity but is taken as unity
lamdaratio=zeros(sd.catcomp);
AA=(mu./MM)*ones(1,sd.catcomp);
MMratio=zeros(sd.catcomp);
MMmat=MM*ones(1,sd.catcomp);
```

```
for i=1:sd.catcomp
    ab=AA(1:sd.catcomp,i);
    ba=AA(i,1:sd.catcomp)';
    lamdaratio(1:sd.catcomp,i)=ab./ba;
    bc=MMmat(1:sd.catcomp,i);
    cb=MMmat(i,1:sd.catcomp)';
    MMratio(1:sd.catcomp,i)=bc./cb;
end
AIJ=(eps1*(ones(sd.catcomp,sd.catcomp)+...
lamdaratio.^0.5.*MMratio.^0.25).^2)./((8*(1+MMratio)).^0.5);
mixmix=AIJ*compflow';
lamdamix=compflow*(lamda(1:sd.catcomp)./mixmix(1:sd.catcomp));
catlamda=lamdamix;  %   [W/m K]
return

%_____Equipotential cell_____________________________________________
function par=equipotential(vreal,par)
% Function help
if par.current>0
    equires=vreal./par.curr;
    refvolt1=ones(1,par.kk);
    voltmatrix1=diag(refvolt1);
    refvolt2=zeros(1,par.kk-1);
    for q=1:par.kk-1
        refvolt2(q)=-equires(q+1)/equires(q);
    end
    voltmatrix2=diag(refvolt2,1);
    voltmatrix=voltmatrix1+voltmatrix2;
    refcurr=ones(1,par.kk);
    voltmatrix(par.kk,:)=refcurr;
    currsol=zeros(1,par.kk);
    for j=1:par.kk-1
        currsol(j)=par.curr(j)-equires(j+1)/equires(j)*par.curr(j+1);
    end
    currsol(1,par.kk)=0;
    currcorr1=voltmatrix\currsol';
    par.currdistr=(par.curr+currcorr1')/par.current;
    par.curr=par.current*par.currdistr;
else
```

```
    par.currdistr=par.currdistr;
    par.curr=par.current*par.currdistr;
end
return
```